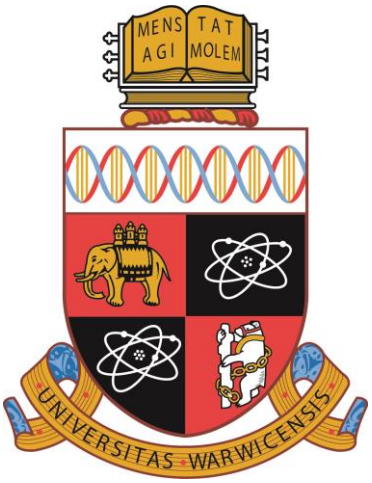

Silicon Germanium Materials for Terahertz Emission

by

John E. Halpin

Thesis

Submitted to the University of Warwick

in partial fulfilment of the requirements

for admission to the degree of

Doctor of Philosophy

Department of Physics

THE UNIVERSITY OF WARWICK

Declaration

This thesis is submitted to the University of Warwick in support of my application for the degree of Doctor of Philosophy. All experimental work presented was carried out by the author, or (where stated) by specialists under the author's direction.

Acknowledgments

I would like to thank the EPSRC for funding this study.

This work would not have been completed without the help, guidance and patience of my supervisors, Prof. David Leadley and Dr. Maksym Myronov. Especially, I am grateful to Dr Maksym Myronov for proposal, design and growth by RP-CVD of all structures researched in this work and given me an amazing opportunity to acquire hands on experience and knowledge in epitaxy of SiGe materials.

I am deeply indebted to Vishal Shah and Stephen ‘Warrior of the Flame’ Rhead for their help with the suspended structures work.

I would like to thank everyone I have worked with in the physics department, Dr Alan ‘turbo’ Burton, Alistair Julian, Dr Chris Morrison, Dr Martin Prest, Dr "Ti" Van Huy Nguyen, James Richardson-Bullock, Phil Allred, Jamie Foronda, David Patchett, Gerard Colston, James Finch, Dr. Amna Hassan, Dr Catarina Castelerio, Dr Richard Beanland, Dr Anna Sanchez (for HRTEM and STEM measurements), Dr. Richard Morris (for SIMs measurements), Josh Cowell, Dr Andrew Dobbie, Dr David Walker (for help with XRD), Yuji Kuribara, Haitham Alabdulali, Prof. Evan Parker, Prof. Terry Whall and Tim Naylor.

I would like to thank my collaborators in the QCL project at the University of Leeds and the University of Glasgow. This includes Prof. Robert Kelsall, Prof. Douglas J. Paul and Dr. Pavlo Ivanov.

I would like to thank Yasuo Shimizu, Masaki Shimodaira, Hisashi Takamizawa, Koji Inoue and Yasuyoshi Nagai for APT performed at Tohoku University.

I am very grateful to those who have helped me with outreach and the Cycling Physicist project, this includes Ally Caldicote, Dr. Emilio Jimenez-Roldan, Dr. Rachel Edwards, Prof. Mark Dowsett.

I would like to thank my friends, Alex Hilton, Danny Foulstone, Alex Barton, Joe Wilson, Sarah-Beth Gilbert, Kyly Wilson, Michael Ratledge, Cait Buckley, Michelle Bailey, Nessa Saniee, Natalia Parzyk, Nina Milan, Dr. Stepan Rudzika, Helen Wishart, Eva Brown and Emma Edgecombe.

Finally I would like to thank my family, parents Nigel Halpin, Margaret Halpin and sister Fiona Halpin for their support and giving me an interest in science in the first place.

Abstract

Terahertz radiation has many uses in a broad range of fields including medicine and healthcare security, earth science, production monitoring and astronomy. The use of terahertz in many of these applications has been precluded by the lack of an inexpensive source that can operate without cryogenic cooling. If a Si-based terahertz quantum cascade laser could be developed, it is a likely candidate to fill this role. It is possible that the largest challenge facing the development of a Si-based quantum cascade laser is that of the demand requiring epitaxial growth. The main achievement of this study is the growth of challenging n-type $Ge/Si_{1-x}Ge_x$ superlattice structures which are intended for terahertz emission. Comprehensive materials characterisation is presented for the structures. The final structures have been sent to collaborators for further characterisation and to be processed into devices. The results of which will be used to optimise future growth of Si-based QCL structures. The effects of the low temperature used in the growth of the QCL structures on the critical thickness is investigated and $Si_{0.4}Ge_{0.6}/Si$ layers grown far beyond the critical thickness predicted by theory are presented. These layers have applications in electronic devices such as field effect transistors (FETs).

The fabrication and characterisation of flat, single crystal Ge membranes is presented. The strain, membrane thickness, crystalline tilt and crystalline quality are determined by micro-diffraction, performed on the membranes at Beamline B16 at the Diamond Light Source. These membranes are shown to be of high crystal quality which gives them many applications, including as a possible platform for Si-based quantum cascade laser structures.

Publications and Presentations

Refereed Publications

S. D. Rhead, **J. E. Halpin**, V. A. Shah, M. Myronov, D. H. Patchett, P. S. Allred, V. Kachkanov, I. P. Dolbnya, J. S. Reparaz, N. R. Wilson, C. M. Sotomayor Torres, and D. R. Leadley, "Tensile strain mapping in flat germanium membranes," *Applied Physics Letters*, vol. 104, no. 17, p. 172107, Apr. 2014.

T. Ulyanenkova, M. Myronov, A. Benediktovitch, A. Mikhalychev, **J. Halpin**, and A. Ulyanenkov, "Characterization of SiGe thin films using a laboratory X-ray instrument," *Journal of Applied Crystallography*, vol. 46, no. 4, pp. 898–902, Jun. 2013.

M. Myronov, C. Morrison, **J. Halpin**, S. Rhead, C. Casteleiro, J. Foronda, V.A. Shah, and D.R. Leadley "An extremely high room temperature mobility of two-dimensional holes in a strained Ge quantum well heterostructure grown by reduced pressure chemical vapor deposition" *Japanese Journal of Applied Physics*, vol 53, 04EH02, 2014.

O. Trushkevych, V. A Shah, M. Myronov, **J. E Halpin**, S. D Rhead, M. J Prest, D. R Leadley, and R. S Edwards, "Laser-vibrometric ultrasonic characterization of resonant modes and quality factors of Ge membranes," *Science and Technology of Advanced Materials*, vol. 15, no. 2, p. 025004, Apr. 2014.

V. A. Shah, S. D. Rhead, **J. E. Halpin**, O. Trushkevych, E. Chávez-Ángel, A. Shchepetov, V. Kachkanov, N. R. Wilson, M. Myronov, J. S. Reparaz, R. S. Edwards, M. R. Wagner, F. Alzina, I. P. Dolbnya, D. H. Patchett, P. S. Allred, M. J. Prest, P. M. Gammon, M. Prunnila, T. E. Whall, E. H. C. Parker, C. M. Sotomayor Torres, and D. R. Leadley, "High quality single crystal Ge nano-membranes for opto-electronic integrated circuitry," *Journal of Applied Physics*, vol. 115, no. 14, p. 144307, Apr. 2014.

V.A. Shah, M. Myronov, A. Shchepetov, **J. Halpin**, S. Rhead, M.J. Prest, M. Prunnila, P. M. Gammon, T.E. Whall, E.H.C. Parker, and D.R. Leadley "Flat Single Crystal Ge Membranes for Sensors and Opto-Electronic Integrated Circuitry" *Solid State Electronics*, vol 98, pp 93-98, Aug 2014

C. Casteleiro**, J. E. Halpin**, V. A. Shah, M. Myronov, and D. R. Leadley, "Thermally grown GeO2 on epitaxial Ge on Si(001) substrate," in *2013 14th International Conference on Ultimate Integration on Silicon (ulis)*, New York: Ieee, pp. 170–173, 2013.

A. H. A. Hassan, O. A. Mironov, A. Dobbie, J. H. Morris, **J. E. Halpin**, V. A. Shah, M. Myronov, D. R. Leadley, S. Gabani, A. Feher, E. Cizmar, V. V. Andrievskii, and I. B. Berkutov, "Structural and Electrical Characterization of SiGe Heterostructures Containing a Pure Ge Strained Quantum Well", *Electronics and Nanotechnology (ELNANO), 2013 IEEE XXXIII International Scientific Conference*, pp51-55, 2013, 2013.

T. Ulyanenkova, A. Benediktovitch, M. Myronov, **J. Halpin**, S. Rhead, and A. Ulyanenkov, "Stress of Homogeneous and Graded Epitaxial Thin Films Studied by Full-Shape Analysis of High Resolution Reciprocal Space Maps," *Materials Science Forum*, vol. 768–769, pp. 249–256, Sep. 2013.

R. W. Kelsall, V. T. Dinh, P. Ivanov, A. Valavanis, L. J. M. Lever, Z. Ikonic, P. Velha, D. Dumas, K. F. Gallacher, D. J. Paul, **J. Halpin**, M. Myrnov, and D. R. Leadley, "(Invited) Germanium/Silicon Heterostructures for Terahertz Emission," *ECS Transactions*, vol. 50, no. 9, pp. 763–771, Mar. 2013.

Oral Presentations

M. Myronov, **J. Halpin (presenter)**, H.A.A. Alabdulali and D.R. Leadley "A new approach to grow very thin, smooth and relaxed SiGe epilayers on a Si(100) substrate" *E-MRS 2012 Spring Meeting, Strasbourg*, France, 15-17 May, 2012.

M. Myronov , C. Morrison, **J. Halpin**, S.D. Rhead, J. Foronda, and D.R. Leadley "Revealing ground breaking room temperature 2DHG mobility in a strained Germanium Quantum Well" *32nd Intl. Conf. on the Physics of Semiconductors, ICPS*, Austin, Texas Aug 10-15, 2014.

M. Myronov, C. Morrison, **J. Halpin**, S. Rhead, J. Foronda, D.R. Leadley, "Extremely high room temperature mobility of 2D holes in a compressive strained Ge quantum well heterostructure grown by RP-CVD on a standard Si(001) substrate" *E-MRS Spring Meeting*, Lille 26-30 May , 2014.

S.D. Rhead, J.E. Halpin, V.A. Shah, M. Myronov, D.H. Patchett, P.S. Allred, V. Kachkanov, I.P. Dolbnya, N.R. Wilson and D.R. Leadley "Tensile Strain Mapping in Flat Germanium Membranes" 7th Intl. Silicon-Germanium Technology and Device Meeting (ISTDM) Singapore, June, 2014.

Poster Presentations

J.E. Halpin, S.D. Rhead, M. Myronov, P. Velha, K.F. Gallacher, V.T. Dinh, P. Ivanov, Z. Ikonic, D.J. Paul, R.W. Kelsall and D.R. Leadley "Creation of Silicon-based Quantum Cascade Laser Structures" *UK Silicon Photonics Conference*, Southampton, Nov, 2013.

J. Halpin, V. Shah, M. Myronov**,** and D. Leadley "Epitaxial growth of highly strained SiGe layers directly on Si(001) substrate" *2012 International Silicon-Germanium Technology and Device Meeting (ISTDM)* UC Berkeley, Berkeley, CA, USA, 4-6 June, 2012.

J. Foronda, C. Morrison, M. Myronov, **J. E. Halpin**, S. D. Rhead , and D.R. Leadley "Weak Anti-Localization Behavior of a High Mobility 2D Hole Gas in a Strained Ge QW Heterostructure" *7th Intl. Silicon-Germanium Technology and Device Meeting (ISTDM)* Singapore, June, 2014.

V.A. Shah, O. Trushkevych, M. Myronov, S. Rhead, **J. Halpin**, R. Edwards, and D.R. Leadley "Tensile strained Ge membranes" *ULIS 2014*, Stockholm, Sweden, April, 2014.

Van Huy Nguyen, M. Myronov, P. Allred, **J. Halpin** A. Dobbie and D.R. Leadley "Developments in germanium-on-silicon epitaxy by reduced pressure chemical vapour deposition" *ULIS 2014*, Stockholm, Sweden, April, 2014.

C. Morrison, M. Myronov, J. Foronda, C. Casteleiro, **J.E. Halpin**, S.D. Rhead, D.R. Leadley "Quantum transport of a high mobility two dimensional hole gas in a strained Ge quantum well" *7th Intl. Silicon-Germanium Technology and Device Meeting (ISTDM)* Singapore, June, 2014.

J. Foronda, C. Morrison, M. Myronov, **J. E. Halpin**, S. D. Rhead , and D. R. Leadley." Weak Anti-Localization Behaviour of High Mobility 2D Hole Gas in a Strained Ge QW Heterostructure" *Magnetism 2014*, 7-8 April, Manchester, 2014.

M. Myronov, **J. Halpin**, S. Rhead, Van Huy Nguyen, D. Patchett, P. Allred, J. Foronda, V. Shah, C. Morrison, G. Colston, V. Sivadasan, D.R. Leadley "Silicon-based epitaxy capability at the University of Warwick" *UK Silicon Photonics Conference*, Southampton, Nov, 2013.

S.D. Rhead, M. Myronov, V.A. Shah, **J.E. Halpin** and D.R. Leadley "Ge-on-Si Selective Epitaxy" *UK Silicon Photonics Conference*, Southampton, Nov, 2013.

C. Casteleiro, **J. Halpin**, V.A. Shah, M. Myronov and D.R. Leadley "Electrical and Structural Characterization of Thermally Grown GeO2 on Epitaxial Ge on Si(001) Substrate" *International Conference on Silicon Epitaxy and Heterostructures (ICSI-8)*, Fukuoka, Japan, June, 2013.

O.A. Mironov, A.H.A. Hassan, A. Dobbie, R.J.H. Morris, A. Feher, E. Cizmar, S. Gabani, I.B. Berkutov, **J.E. Halpin**, S.D. Rhead, P. Allred, and D.R. Leadley "New RP CVD grown ultra-high performance selectively B-doped pure-Ge 20 nm QWs on (100)Si as basis material for post-Si CMOS technology" *E-MRS Spring Meeting*, Strasburg, May, 2013.

A.H.A. Hassan, O.A. Mironov, A. Dobbie, R.J.H. Morris, **J.E. Halpin**, V.A. Shah, M. Myronov, D.R. Leadley, A. Feher, E. Cizmar, S. Gabani, V.V. Andrievskii and I.B. Berkutov "Structural and Electrical Characterization of SiGe Heterostructures Containing a Pure Ge Strained Quantum Well" *IEEE XXXIII International Scientific Conference, Electronics and Nanotechnology (ELNANO)*, Kiev, April, 2013.

R. Kelsall, V. Dinh, P. Ivanov, A. Valavanis, L. Lever, Z. Ikonic, P. Velha, D. Dumas, K. Gallacher, D. Paul, **J. Halpin**, M. Myronov, and D. Leadley "Germanium/Silicon Heterostructures for Terahertz Emission" *Pacific Rim Meeting on Electrochemical and Solid State Science (PRiME 2012)*, Hawaii, October 7-12, 2012.

C. Casteleiro, M. Myronov, **J. Halpin**, V. A. Shah, and D. R. Leadley, "Electrical and structural properties of thermally grown GeO2 on epitaxial Ge on Si(001) substrate" *Condensed Matter and Materials Physics*, CMMP Edinburgh, 3-7 Sept, 2012.

J. Halpin, M. Myronov, and D.R. Leadley "Epitaxial growth of highly strained SiGe layers directly on Si", *International SiGe Technology and Device Meeting (ISTDM 2012)*, Berkeley, June 4-6, 2012.

Table of Contents

List of Figures

1 Introduction

1.1 Terahertz Radiation

Terahertz (THz) radiation describes frequencies of electromagnetic radiation between 3×10^{11} Hz (0.3 THz), the high end of the millimetre wave band, to 3×10^{13} Hz (30 THz), the low end of the far-infrared band (Figure 1-1). Traditionally, terahertz radiation has had little study outside of astronomy and analytical science [1], when compared to other regions of the electromagnetic spectrum; however, with the recent development of new terahertz sources, a wide range of new applications of terahertz radiation are rapidly being developed. In the following section, some of the main applications of terahertz radiation are given in order to highlight the benefits of the development of cheap, room temperature terahertz source.

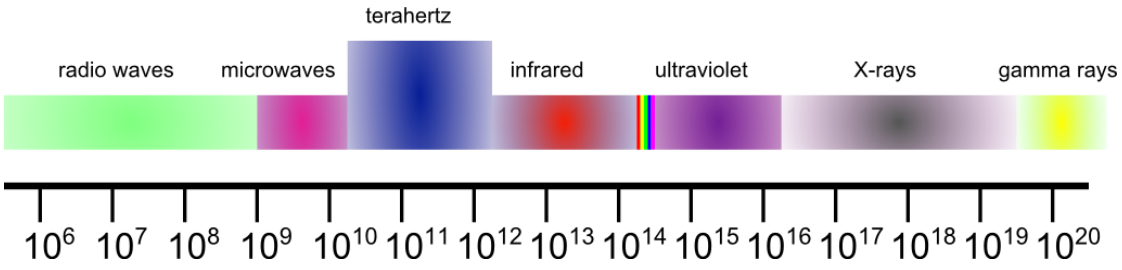

Figure 1-1: Electromagnetic spectrum in Hz showing the location of the terahertz region

1.2 Uses of Terahertz Radiation

1.2.1 Medicine and Health Care

One of the most promising fields for terahertz radiation is in medicine, for both imaging and spectroscopy. Unlike X-rays, terahertz radiation does not pose an ionization risk to tissue, due to the lower energy of its quanta [2]. When compared to visible light and near infrared, terahertz radiation can penetrate much further into the body, since its longer wavelengths are less affected by Rayleigh scattering. Pulses of terahertz radiation have been detected through up to 1.5 mm of skin. This longer penetration depth gives terahertz applications in novel medical imaging techniques. The energy of terahertz radiation corresponds to the energy of rotational and vibrational transitions of molecules, including hydrogen bonds and so can be used in spectroscopy to differentiate between materials. Terahertz radiation is strongly attenuated by water, so terahertz imaging is strongly sensitive to tissue water content. This sensitivity to water acts as contrast mechanism in terahertz medical imaging.

One of the medical applications of THz radiation is in dentistry, where it is possible that it may be able to replace or at the very least support X-rays for imaging. Early studies have shown that terahertz pulse imaging can distinguish between the tooth enamel and softer tissue can be used for early detection of dental carries [3].

Another medical application of terahertz radiation is in the diagnosis of skin cancer [4]. Research has shown that some types of cancer tumour typically have increased water content when compared to surrounding tissue. Since water has strong terahertz absorption, diseased tissue will exhibit different terahertz properties, such as altered

refractive index and absorption coefficient [5]. *Ex vivo* measurements have been performed where terahertz imaging was able to detect basal cell carcinoma, the most common form of skin cancer [6]. Regions of increased absorption agreed well with the tumour site locations. Due to its penetration depth, terahertz radiation is better suited to detecting tumours close to the tissues surface. This is advantageous for imaging during surgery for tumour removal, such as in breast-conserving surgery where knowledge of the position of the tumour is important to save removing tissue unnecessarily. Fitzgerald *et al* have carried out *ex vivo* studies into the possibility of using terahertz radiation to assist with the removal of breast cancer during an operation and have found that the size and shape of the tumour as imaged in the terahertz region agrees with other more established techniques.

The development of a cheap, room temperature terahertz source will aid the uptake of terahertz radiation in medicine. Medicine is not the only field where terahertz radiation can be used for imaging and spectroscopy; it also has applications in security.

1.2.2 Security

In the last 5 years, there has been a significant interest in the use of THz radiation for security applications [7]. Terahertz is ideal for detecting concealed weapons since non-metallic, non-polar materials are relatively transparent to terahertz, allowing imaging of concealed weaponry through clothing, packing material etc. Many substances such as certain drugs and explosives have distinct terahertz spectra [8], which enables them to be rapidly fingerprinted and identified using terahertz

radiation. As previously discussed, since terahertz radiation is non-ionising, its use carries a low health risk to both operators and those being scanned by the terahertz system. This is in contrast to X-rays which are currently used in many security applications, where a health risk due to the ionising nature of X-rays is present.

Relatively intense terahertz sources are needed for security imaging, the power required can be estimated [9]. For an array of cells required for imaging, the minimum detectable energy of a low-temperature terahertz detecting cell can be approximated as ~1 fJ (10^{-15} J) and this is required over a 2D array of pixels ~100x100 (10^4). The absorption and terahertz loses in the detection media can be approximated as ~10^9 with a signal to noise ratio of 100. This gives a minimum source power of around 1 W.

1.3 Sources of Terahertz Radiaition

The terahertz spectrum has traditionally been known as the 'Terahertz Gap'. This name comes from the exponential drop in output power from electronic microwave sources as their frequency is increased towards the terahertz regime and the exponential drop in output power from laser diodes as their frequency is decreased toward the terahertz region [10]. The terahertz gap is slowly being filled with devices that can output in the terahertz region, with currently available terahertz sources summarised in figure 1-2 where the outputs power versus frequency are plotted for each. Since the major obstacle to the uptake of applications of terahertz radiation has been the lack of cheap, commercially available sources, the development of new sources is a topic of active research. In the following sections, more information is given on some of the currently available sources of terahertz radiation able to emit

with reasonable intensity, with the aim of illustrating the lack of a cheap, room temperature terahertz source.

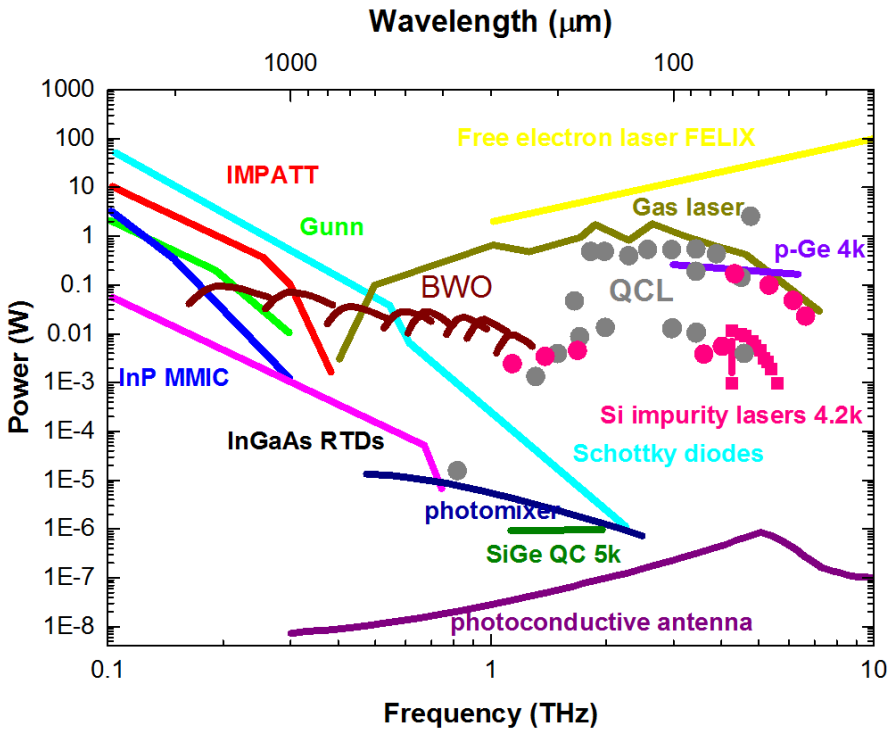

Figure 1-2 - Frequency vs output power for terahertz source technologies. Adapted from [10]. Original sources of technology output power can be found in references [11-27].

1.3.1 Free Electron Lasers

Free electron lasers offer the highest output power available from any terahertz source, they are also easily tuneable. Operation occurs by sending a beam of relativistic electrons through an undulator, which is a side to side magnetic field created by arranging magnets periodically with alternating poles. Radiation is emitted with the frequency of the electrons oscillation in the undulator [24]. The frequency range of free electron lasers extends from microwaves, through the

terahertz spectrum to visible frequencies and X-ray. Free electron lasers are capable of providing very short pulses of radiation, with the pulse time reducing with frequency, with a typical pulse of approximately 2 ps at 1 THz. Unfortunately free electron lasers are both very bulky and expensive due to requiring a source of accelerated electrons such a synchrotron. A powerful, but smaller and cheaper source of terahertz radiation is the gas laser which is discussed in the next section.

1.3.2 Gas Lasers

Powerful mid and high terahertz emission can be produced using a gas laser (figure 1-2). A CO_2 laser is used to optically pump a mixture of gases which has vibrational states in the THz. While lasers of this kind have existed for decades in research laboratories, it is only in the last 10 years that turn-key versions have become commercially available [28]. Gases used as gain media in terahertz gas lasers are molecular gases such as CH_3F, CH_3OH, NH_3 and CH_2F_2, with the terahertz radiation coming from the rotational transitions of the molecules [29] . Gas lasers are still large and expensive, but fortunately, in recent years a powerful solid state source of terahertz radiation has been developed, the quantum cascade laser.

1.3.3 III-V Terahertz Quantum Cascade Lasers

It can be argued that quantum cascade lasers (QCLs) are the only practical solid state terahertz source, small and inexpensive when compared with other sources, with optical power output sufficient for terahertz imaging applications. QCLs operate by intersubband transitions in a multiple quantum well semiconductor structure repeated many times to form a superlattice. This is in contrast to a standard semiconductor

laser in which emission comes from a p-n junction where electrons and holes recombine.

Since the demonstration of the first working terahertz QCL demonstrated by Köhler *et al*. in 2002 from a AlGaAs/GaAs heterostructure [30], there have been many technological advancements. Output power and operating temperature have both increased and coverage of the entire terahertz spectrum has improved. At the time of writing, the most powerful III-V terahertz QCL has been demonstrated by the University of Leeds, with an output power in excess of 1 W [31]. The device uses a AlGaAs/GaAs heterostructure, emits at ~3.4 terahertz and has a maximum operating temperature of 123 K. Unfortunately, III-V terahertz QCLs still require cryogenic temperatures to operate and are difficult to integrate into existing facilities for mass fabrication. A possible method for increasing the operating temperature of QCLs and making them easy to integrate into mass fabrication facilities is to develop a Si based QCL.

1.4 Si terahertz quantum cascade lasers

Si is by far the most commonly used semiconductor in microelectronics, with Si technology dominating. For this reason, the integration of a semiconductor laser with Si has been a long standing goal, facilitating the combination of optical and microelectronic components on the same die. Si has an indirect band gap and so it cannot be used for a conventional semiconductor laser. For QCLs, a direct band gap is not a necessity (QCL operation is discussed in section 2.1.2) and so the development of a Si QCL is a possibility for a Si based laser.

Si offers many potential advantages over III–V technologies, especially in the terahertz frequency range. The thermal conductivity of Si substrates is roughly three times that of III–V substrates, with the bulk thermal conductivity at 300 K for Si $\sim 1.5\ \mathrm{W/(cm \cdot K)}$ [32] and $\sim 0.55\ \mathrm{W/(cm \cdot K)}$ for GaAs [33]. The higher thermal conductivity substrate is advantageous in that it can easily dissipate excess heat. Si also offers mature processing techniques and is compatible with existing facilities for mass fabrication

Si offers significantly higher operating temperatures for terahertz QCLs since, as opposed to III–Vs, Si is a non-polar material; this is due to the nature of the IV- IV bond. In non-polar semiconductors, polar optical phonon scattering is negligible when compared with polar semiconductors. This reduced polar optical phonon scattering gives greatly enhanced intersubband lifetimes in SiGe, which have been measured experimentally [34]. For a Ge/SiGe QW system, it is shown that the relaxation time is greater than 10 ps, including for transition energies above the Ge optical phonon energy up to 300 K. This is an improvement of at least an order of magnitude over GaAs, for which phonon scattering dominates the intersubband lifetimes above 40 K [35], giving Si based terahertz QCL devices the possibility of higher operating temperatures than III–V based terahertz QCL devices.

Despite the many advantages that constructing a terahertz QCL from a Si based heterostructure could bring, to date, no Si based QCL has been realised, with all structures produced so far exhibiting gain below the threshold required for lasing. The aim of this study is to work toward a lasing Si based laser structure, with a focus

on the growth of n-type $Ge/Si_{0.15}Ge_{0.85}$ superlattice designs for terahertz emission (for reasons discussed in section 2.1.4). For QCL operation, it is necessary to create an optical cavity, and one of the most effective ways to do this for a terahertz QCL involves the removal of the substrate from the laser, leaving just the active region. The removal of the substrate from a Ge layer creating a Ge suspended membrane is discussed in the next section, both in the context of the development of a Si based QCL optical cavity and also more general applications.

1.5 Suspended Ge membrane Structures

In the context of realising a Si based QCL structure, Ge membranes can bring two advantages. For QCL operation, it is necessary to create an optical cavity using a waveguide. The optical cavity/waveguide is designed to confine the optical mode in the vertical direction with a low loss, surrounding the active region and providing feedback of the laser light. Two kinds of waveguide are commonly used for terahertz lasers, the single plasmon waveguide and the more recent double-metal waveguide which offers better high temperature performance [36,37]. The single plasmon waveguide is constructed by sandwiching the active region between a highly conducting layer, such as a metal and a dielectric, such as a semiconductor. If the imaginary part of the refractive index of the conducting layer is bigger than both the real part and that of the dielectric, then electron waves known as plasmons will be created at the interface between the materials and propagate along the interface. The double-metal waveguide is constructed by depositing single plasmon waveguides directly above and below the active region. This is obviously more complicated to construct than the single plasmon waveguide since it requires the substrate to be

removed from the back of the active QCL region, to provide access to the rear of this region, and difficult metal bonding. The Si-based QCL structures to be presented in this work use virtual substrates as a platform for growth, which begin with a layer of Ge-on-Si. If this Ge-on-Si layer which supports the QCL structure is fabricated into a membrane, and possibly given an additional etch to remove the virtual substrate, a suspended QCL structure will remain that is ideal for the fabrication of a double-metal waveguide since it is exposed from both sides.

Semiconductor membranes are one of the basic micro-electro-mechanical systems (MEMS) components. Their many applications include capacitive pressure sensors [38,39], gas flowmeters [40], high performance tactile imagers [41], micropower thermoelectric generators [42] and mirrors for optical sensor applications [43]. Single crystal Si membranes have been reported, with thicknesses as low as 10 nm and areas around 1 mm^2 [44]. While Si membranes have been the subject of much research, relatively little work has been done on Ge membranes. High quality, easy to produce Ge membranes can find uses in applications that currently use Si membranes, due to the different mechanical and electrical properties offered by Ge. Also, the additional functionality that epitaxial Ge-on-Si brings to the Si platform (such as Ge-on-Si photodetectors [45], optoelectronic modulators [46], lasers [47] and solar cells [48]) could benefit from high quality, easy to produce Ge membranes. High quality layers of III-V materials can be grown on Ge-on-Si [49], these layers could be turned into membranes by adapting the Ge membrane process.

1.6 Summary

Terahertz radiation has a wealth of application which can benefit from the development of a cheap, practical, room temperature source of terahertz radiation. Currently, the most practical terahertz source is the III-V terahertz QCL. If a Si-based terahertz QCL could be demonstrated, it would offer many potential advantages over its III-V based counterparts. In order for a Si-based terahertz QCL to lase, it will require an optical cavity/waveguide - the basis for this could be a suspended Ge membrane structure.

In this work, progress is made towards the demonstration of a Si based QCL with the growth of high Ge content n-type Si based QCL structures. These structures will be fabricated into devices by collaborators, which when tested, should exhibit electroluminescence and possibly lasing. Even if these structures do not function as lasers, then the knowledge gained from their materials characterisation can be fed into the design of future Si based QCL structures. Work on suspended Ge membrane structures is also presented, which has applications in the construction of the optical cavity/waveguide for a Si based QCL.

2 Theoretical Discussion

In this chapter the theory which is relevant to the rest of this study is discussed. The theory behind QCL operation is first given and then progress of p-type and n-type Si QCLs reported on. N-type Si terahertz QCLs, the most likely candidate for a Si-based QCL are discussed. Background theory for the growth of single crystal superlattice structures required for QCL operation is then given. This includes the basic properties of silicon, germanium and SiGe, the theory of epitaxial growth, precursors and chemical reactions, dislocations, critical thickness, diffusion, segregation and virtual substrates.

2.1 Quantum cascade lasers

2.1.1 Interband laser operation

It is helpful to first understand the operation of the standard interband semiconductor laser diode before that of the intraband laser, the QCL. If an incident photon has energy near that of the separation between energy levels, $E_{21} = E_2 - E_1$ (figure 2-1), then it can strongly interact with the electrons in these levels. The interaction depends on the initial state of the electron. If the electron lies in the lower energy level, E_1 (figure 2-1), then the photon can be absorbed and the electron excited to the upper energy level E_2. If the electron occupies the upper energy level, E_2 (figure 2-1) then the photon causes the electron to drop to the lower energy level, E_1, and a new photon is emitted. The emitted photon has a time and phase relation to the incident photon and so the two photons are highly coherent. This process is known as

stimulated emission. When a system is in thermodynamic equilibrium, there will always be fewer electrons in the lower energy level than in the higher energy level, so the majority of incident photons are absorbed as they travel through the system.

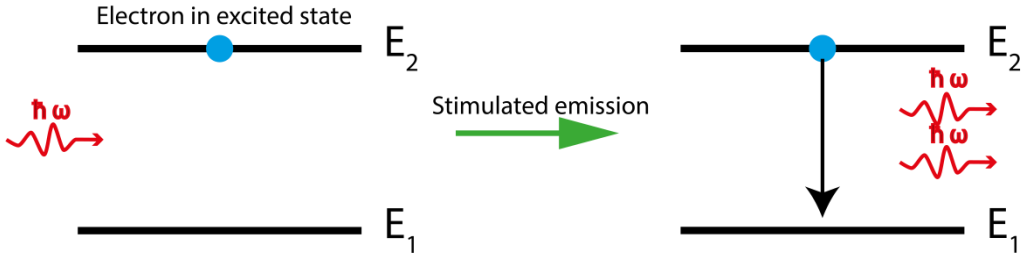

Figure 2-1 - Photon interacting with excited electron to give stimulated emission

In a laser the electrons are pumped into the higher energy level, this is achieved either by an electric current or an external light source. The situation where more electrons exist in the higher energy level than the lower energy level is known as population inversion. Due to the population inversion, when photons travel through the system, stimulated emission occurs more frequently than absorption resulting in light amplification and the production of coherent light.

For a standard interband laser diode, the electrons are pumped into the conduction band and the optical transition occurs in the energy bandgap between the conduction and the valence band. Since this transition is between bands it is known as an interband transition and its energy is limited to the range of energy bandgaps available in semiconducting materials. Quantum well (QW) lasers have also been developed where layers of different semiconducting material (having different energy bandgaps) create a potential well in the conduction band that traps electrons. Since the QW is narrow, the electrons can only occupy quantised energy subbands

inside it. The energy between the lowest conduction subband and the highest valence subband minima can be changed by varying the size of the QW giving a tuneable emission frequency, however the bandgap of the semiconductor still places a low frequency limit on the emission from the laser. A way to remove the limit placed by the bandgap on the emission frequency is to utilise QCLs, which are described in the next section.

2.1.2 Quantum cascade laser operation

In QCLs, transitions between subbands are used as opposed to transitions between the conduction band and valence band. This allows for low energy transitions and hence low frequency laser emission.

The building block of the QCL is the QW. Semiconductor QWs are one dimensional potential wells of finite depth with wave functions that penetrate into the surrounding barriers. For multiple quantum wells, if the barrier thickness is sufficiently reduced, the tails of QW wave functions can reach across and experience the potential confinement of adjacent QWs. In the most basic case of two identical QWs with a thick barrier, the wave functions are the same in each QW and the wells are not coupled. As the thickness of the barrier between the two QWs is reduced, the wave functions become degenerate in energy with an energy gap between them. This can be extended to multiple QWs. The wave functions can be delocalised over many QWs with a small emery gap between each, forming a broad energy continuum called a miniband. This is important for QCL design.

The idea behind QCL operation, was originally proposed by R.F. Kazarinov and R.A. Suris in 1971 [50]. This was the use of a staircase of QWs for light amplification. The staircase is created by applying an electric field to a multiple QW structure. Electrons can cascade down the QWs with a photon emitted at each step. Unfortunately, lasing was not observed experimentally from this design. This was due to non-uniform uniform electric field formation and the emission of longitudinal optical-phonons (LO-phonons).

A benefit of using intersubband transitions in a laser is that that the active region can be easily cascaded. Carriers travel from period to period as they cascade through the structure. The cascade has two significant advantages. A single carrier has the potential to emit a number of photons equivalent to the number of periods in the cascade, increasing the devices efficiency. Also, less population inversion is required per period for a cascade, since the gain is occurring over a larger area. This gives a lower threshold current for the device.

Despite the many challenges, the use of a biased superlattice for light amplification has gone on to be the foundation of the QCL. Lasing in QCLs has been achieved by using multiple coupled QWs to form a miniband in each period of the active region as opposed to the single QW that was used in each period of the early biased superlattices intended for light emission. This is the reason behind the complex designs seen in QCL structures.

The QCL period can be split into the following regions, an active region, where light is emitted by an optical transition between subband energy levels and a

injector/extractor region which is responsible for quickly extracting the electrons from the lowest lasing level in the active region and injecting them into the top of the next active region. These regions are illustrated in figure 2-2. It is important that that correct electric field is applied to a QCL structure to give the band-alignment required in the regions for radiative transitions in the active region.

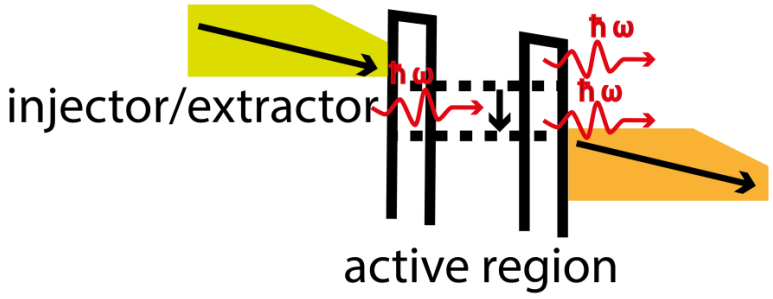

Figure 2-2 - Simplified schematic diagram of regions in a QCL structure period. The energy levels indicated all lie within the conduction band. Adapted from [51]

Intersubband emission was first observed in 1988 in the terahertz spectrum from a GaAs/AlGaAs superlattice grown by organometallic chemical vapour deposition [52]. Due to the many challenges present in fabrication a functioning QCL, it was not until 1994 that lasing was observed in a quantum cascade structure, at Bell Labs at a frequency of 75 THz [53] by Faist *et al*. This was achieved in a AlInAs-GaInAs superlattice grown by MBE. The active region in this design utilised fast optical phonon (LO-phonon) scattering to quickly remove carriers from the lowest lasing level. In 1997, a new bound-to-continuum (BTC) QCL active region design was presented [54]. In this structure, the laser transition is between two minibands and the rapid carrier scattering within a superlattice is utilised to give population inversion.

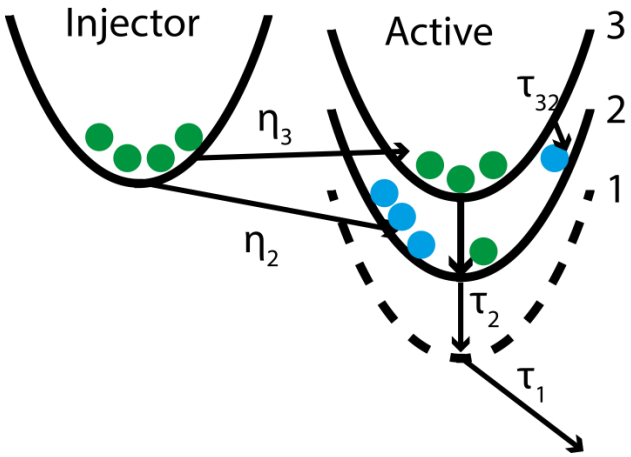

Figure 2-3 - Schematic diagram of the relevant levels and injection efficiencies in a cascade laser. Adapted from [55]

For a QCL, gain, G, is proportional to the population inversion, Δn, that exists between the upper radiative state, $n = 3$ and the lower radiative state, $n = 2$. If, as is shown in figure 2-3, a fraction η_3 of the current flow is injected into the upper state of the active region and a fraction η_2 into the lower state, the gain can be described by equation 2-1 [56], where τ_2, τ_3 are the total lifetimes, τ_{32} the intersubband scattering time between the $n = 3$ and $n = 2$ states and σ the transition cross section.

$$G = \sigma \Delta n = \sigma \frac{J}{q_0}\left(\tau_3 \eta_3 \left(1 - \frac{\tau_2}{\tau_{32}}\right) - \eta_2 \tau_2\right). \qquad 2\text{-}1$$

It can be seen from equation 2-1 that the gain of the laser is strongly dependant on the efficiency of the injector region and the ratio of the lifetimes. If the injector region is efficient, a large fraction of the carriers is injected into the upper state, creating a large population inversion. Also, if the carriers have a long lifetime before being non-radiatively scattered between the upper and lower states, and a short lifetime before being removed from the lower state, a large population is created. A QCL design must aim to maximise ($\tau_3 \eta_3$ - $\eta_2 \tau_2$) and minimise $\frac{\tau_2}{\tau_{32}}$ if it is to give a

reasonable gain. Since the injection efficiencies and lower state lifetimes are difficult to both predict and measure [55], equation 2-1 is not ideal for predicting device gain, however it is useful in explaining the different strategies employed in QCL design.

The two QCL designs which have come to be accepted as the most successful in the THz regime GaAs QCLs [10] are the bound-to-continuum and the phonon depopulation design. Bound-to-continuum designs use radiative transitions between an isolated state and a miniband. The miniband both quickly depopulates the lower laser level by electron-electron scattering and then acts as an injector into the single bound state. The efficiency of the injection into the upper radiative subband is intended to be maximised by this design [56]. In the phonon depopulation design fast electron–optical-phonon scattering is utilised to depopulate the lower laser level [14,57].

An example of the simulated bandstructure in a bound-to-continuum $Si/Si_{0.15}Ge_{0.85}$ QCL design is given in figure 2-4 for the L-valley (conduction band minima at the L-symmetry point of the Brillouin zone [192]). The design has been calculated by Dinh *et al* [60] using a density matrix method which includes coherent transport and electron scattering effects.

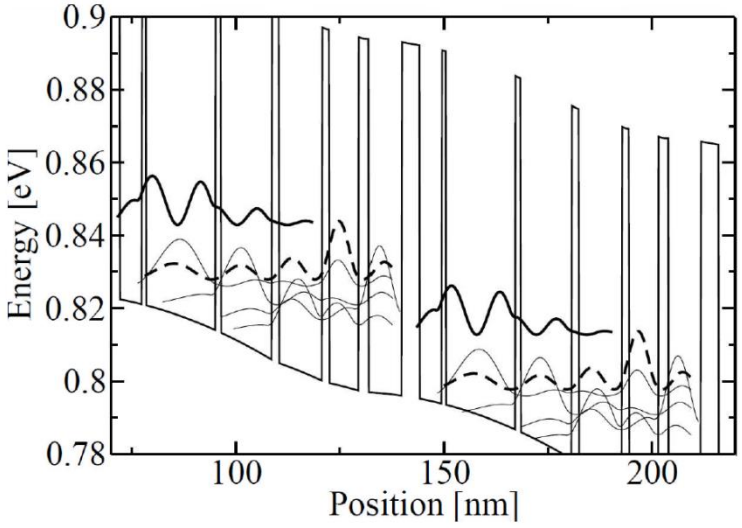

Figure 2-4 – Example of bound-to-continuum Ge/$Si_{0.15}Ge_{0.85}$ QCL design adapted from [59]. The simulated conduction band profile and electron wavefunctions are shown for two periods of the structure. The design has a repeating period of 6 QW's, with thicknesses (in nm) from the left of the figure of 5.0/*1.2*/14.3/*1.3*/12.9/*1.6*/7.9/*1.8*/7.1/*2.5*/7.8/4.3 where the italic font represents $Si_{0.15}Ge_{0.85}$ barriers, the standard font Ge QW's and the underlined sections regions doped at 8 x 10^{18} cm^{-2}. The wave functions in bold lines are the upper laser states and the wavefunctions in dotted lines the lower laser states.

The lasing transition in figure 2-4 is between the two states in the widest quantum well, the main QW, with a frequency of 4 THz. The barrier to the left of the main QW is known as the injection barrier, since it is the main factor in determining the injection efficiency into the upper radiative subband in the main QW. A miniband is formed by the wave functions from the QWs between the main QWs. Due to the lattice mismatch of Si and Ge, a structure of this kind must be grown on a virtual substrate (discussed in section 2.5).

2.1.3 Si QCL Material Configurations

When deciding the best material system with which to construct a QCL, the following parameters must be considered; the band structure of the material, electron effective mass *m**, mobility and most importantly (and the subject of this work) the ease with which the structure can be grown to the operating tolerances of the design.

Since QCL operation relies on quantum mechanical tunnelling, the effective mass is an important parameter. For an electron with energy E impinging on a barrier with height ΔE_c and width b, the transmission coefficient T can be approximated by equation 2-2 [58].

$$T \sim \frac{16E}{\Delta E_c} e^{\left[-2\sqrt{\frac{2m^*(\Delta E_c - E)}{\hbar}}b\right]}. \qquad 2\text{-}2$$

From equation 2-2 it can be seen that the quantum mechanical tunnelling coefficient decreases exponentially with effective mass, so low effective mass is required for QCLs to give sufficient tunnelling between states for operation. Larger effective masses can be compensated for by reducing the barrier thickness, however this can cause difficulties with growth due to the very high tolerance needed for growth of thin barriers.

A number of different material configurations have been explored in the Ge/Si material system. The predicted peak optical gain per unit length for different material configurations is given in figure 2-5 for bound-to-continuum QCLs. For lasing to be achieved, the gain must be greater than the waveguide losses, which are illustrated by the dashed yellow line in figure 2-5. This lasing threshold is reached when the gain provided by the active region is balanced by the cumulative losses for a round trip of

light in the optical cavity of the QCL. If the gain is below this threshold, the optical output will be dominated by spontaneous emission as opposed to stimulated emission and only electroluminescence (EL) will be observed. It can be seen that the Si-based system with the largest simulated gain is the n-type Ge/SiGe cascade laser with high Ge content barriers grown on (001) substrates. Since a low effective mass is an important consideration when choosing a material system for a QCL, tunnelling effective masses (m*) for the relevant lowest subband states are given for different material configurations are given in table 1. For a comprehensive review on Si-based QCLs see Paul [10].

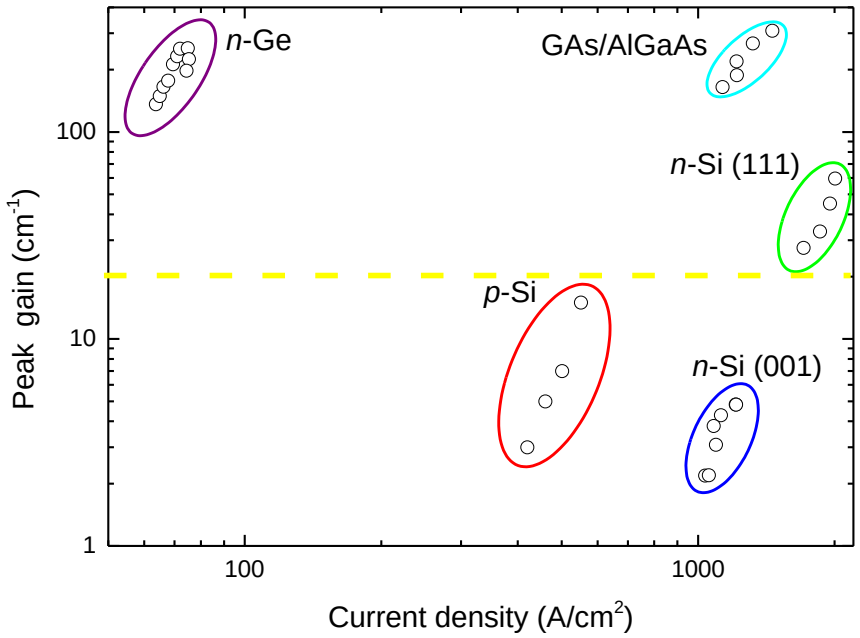

Figure 2-5 - The predicted maximum gain vs. current density (at peak gain) for bound-to-continuum QCLs fabricated from diferent Ge/Si materials systems. Where: "n-Si (001)" and "n-Si (111)" represents n-type Si/SiGe csascades with Si-rich alloy barriers, grown on (001) and (111) substrates respectively; “p-Si” represents p-type Si/SiGe cascades with Ge-rich barriers grown on (001) substrates; “n-Ge” represents n-type Ge/SiGe cascades with high Ge content barriers grown on (001) Si substrates. For comparison, simulation results are also shown for GaAs/AlGaAs bound-to-continuum cascades. Simulations were performed using a self-consistent rate equation model. Figure adapted from [59]. The dashed yellow line corresponds to the minimum waveguide losses, above which, devices should produce lasing.

Material system	Ground state m*
n-GaAs (001)	0.067 m_0
p-$Si_{0.7}Ge_{0.3}$ (001)	0.35 m_0
p-$Si_{0.2}Ge_{0.8}$ (001)	0.16 m_0
p-Ge	0.284 m_0
n-Si (001)	0.93 m_0
n-Si (111)	0.26 m_0
n-Ge	0.113 m_0

Table 1 - Tunnelling effective mass (m*) for the relevant lowest subband state. Adapted from [10]

2.1.4 Previous SiGe QCLs (p-type Si QCLs) and n-type Si QCLs

The prevalent Si-based QCL design demonstrated to date has been p-type. In p-type QCLs, hole transitions in the valence band are used for operation. The preference for p-type comes from holes having a lower effective mass than electrons in the tunnelling direction for the Δ-valley (conduction band minima at the Δ-symmetry point of the Brillouin zone [192]) for Si-like band structures (for $Si_{1-x}Ge_x$, $x<0.85$, the lowest valleys exist in the Δ directions and so the majority of the electron population lies here). The high segregation of n-type dopants in $Si_{1-x}Ge_x$ when compared to p-type dopants also made p-type designs more attractive. Examples of p-type Si-based QCL structures are given in [61-63], for mid-infrared emission and for THz in [19,64,65].

All p-type designs so far have produced a relatively low level of gain, below the minimum waveguide losses which must be exceeded for lasing. This is mainly due to extreme sensitivity of p-type designs to small deviations in grown thickness, leading to states being misaligned and also due to the relatively large effective mass which limits the gain.

Past research has generally focused on p-type Si based QCL designs instead of n-type. This is partly due to p-type designs requiring high Ge composition $Si_{1-x}Ge_x$ structures with pure Ge quantum wells, for which the growth technology is comparatively immature when compared to that for low Ge composition $Si_{1-x}Ge_x$. It is also due to the negligibly small conduction band offset of ~10 meV, which is most likely to be too low for a functioning QCL device. For comparison, a typical value for the conduction-band offset in AlGaAs terahertz QCLs is around 130 meV. However, recent work on n-type Si based QCL designs have shown these to be very promising, with the potential for high gain devices.

In references [66] and [67] an n-type structure with pure Ge QWs grown on a $Si_{1-x}Ge_x$ virtual substrate with a final composition of $x \geqslant 0.85$ is proposed by Driscoll and Paella. The structure uses the L-valleys (for $Si_{1-x}Ge_x$, $x<0.85$, the lowest valleys exist in the L-directions and so the majority of the electron population is in this valley) of the Ge QWs for operation, which as can be seen in Table 1 have a relatively low effective mass, which is ideal for QCL operation. In [68] it is shown that the maximum usable energy range of ~90 meV is available if a Ge fraction of 0.85 is used for the barriers. As can be seen in Figure 2-4, simulation of n-type QCLs with Ge QWs predicts high gain - above all other Si-based materials systems and

almost on a par with GaAs/AlGaAs devices. This makes n-type designs the most likely candidate for a Si-based QCL. The design and growth of an n-type Si based QCL requires good knowledge of the properties of Si/Ge/$Si_{1-x}Ge_x$ material system, the basics of which are described in the next section.

2.2 Basic Properties of Silicon Germanium

Silicon and germanium both share the same crystal structure, that of the diamond lattice. The diamond lattice is comprised of two face centred cubic lattices, displaced by a quarter of the diagonal across the cube. The unit cell contains 8 atoms with each atom bonded to four nearest neighbour atoms (figure 2-6) by covalent bonding. The distance between each atom and its nearest neighbours is $\sqrt{3} \times {}^{a}/_{4}$, where a is the lattice parameter.

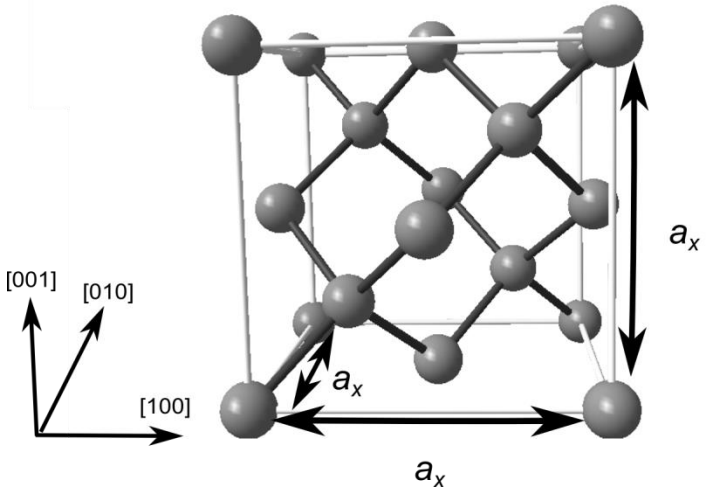

Figure 2-6 - Diagram of face centred diamond cubic crystal structure. Bonds between atoms are given by thick black lines and a_n is the lattice parameter.

When unstrained, the lattice exhibits cubic symmetry and a_n=a_x=a_y=a_z. Silicon has a bulk lattice parameter (a_{si}) of 5.43102 Å [69] and germanium has a bulk lattice

parameter (a_{Ge}) of 5.6579 Å [69]. The silicon and germanium lattice parameters have a 4.17% mismatch. Lattice mismatch (f_m) can be calculated from equation 2-3, where a_s is the substrate lattice parameter and a_l the lattice parameter of the layer.

$$f_m = \frac{(a_s - a_{l(bulk)})}{a_s}. \qquad 2\text{-}3$$

Vegard's law states that the lattice parameter of a solid varies linearly with composition. For a relaxed SiGe alloy, the variation in lattice parameter with composition is accurately fitted with the corrected-Vegard's law, equation 2-4, which was experimentally derived by measuring the alloy lattice parameter by X-ray diffraction and the alloy composition by Rutherford Backscattering [69].

$$a_{Si_{1-x}Ge_x} = a_{Si}(1-x) + a_{Ge}x + 0.02733x^2 - 0.02733x. \qquad 2\text{-}4$$

The phase diagram for SiGe is given in figure 2-7. The diagram was initially calculated by Stöhr and Klemm [70] and has been refined in references [71] and [72]. It can be seen from figure 2-7 that the liquid and solid states have a large gap of coexistence. For a given temperature, the compositions of the solid and liquid phases are different, for example at 1200 ^{o}C the solid is ~33% Ge while the liquid is ~64% Ge. This explains why the conventional Czochralski technique is unsuitable for the production of bulk SiGe. As the SiGe solidifies, the melt is depleted in Si, changing the alloy composition of the growing crystal [73]. The growth interface can also be destabilised by the variation in alloy composition [73].

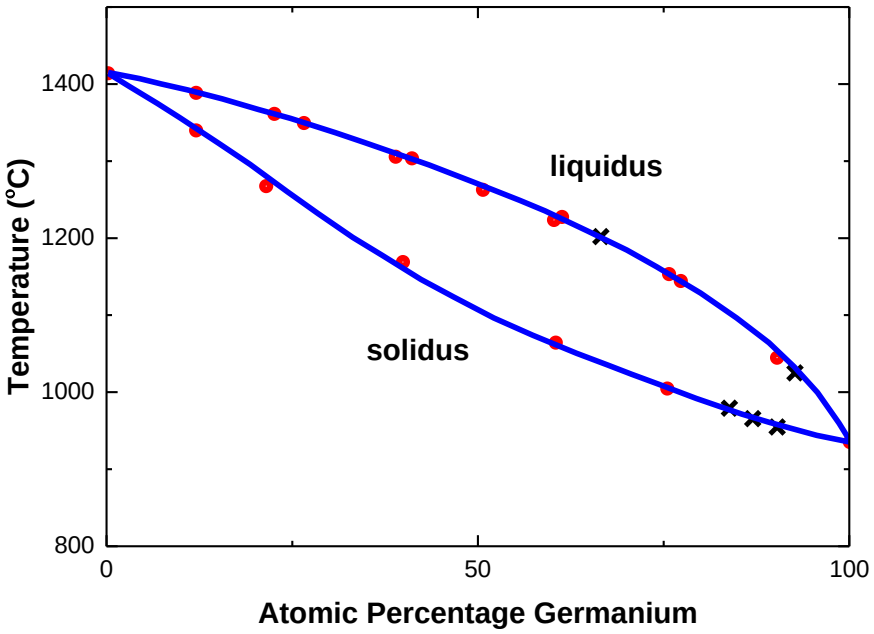

Figure 2-7 - Liquidus-solidus for $Si_{1-x}G_x$ adapted from [74]. Blue lines are from [71] and crosses and circles from [72], [70] respectively.

In Table 2, the properties for bulk Si and Ge are given, along with those for $Si_{1-x}Ge_x$. A crystal growth technique is needed to produce the complex superlattice structure of a QCL whilst remaining a single crystal, such that crystal defects and dislocations that would lead to non-radiative recombination are eliminated. Single crystal growth is the subject of the next section.

	Silicon (Si)	**Germanium (Ge)**	**$Si_{1-x}Ge_x$**
Lattice parameter (Å) [69]	5.43102	5.6579	2-4
Elastic constants (GPa) [75]			
C_{11}	165.8	128.8	$165.8 - 37x$
C_{12}	63.9	48.3	$63.9 - 15.6x$
C_{44}	79.6	66.8	
Poisson Ratio ((100) Orientation) [75]	0.28	0.26	0.28-0.02x
Melting point (K)[76]	1687	1210	Figure 2-7
Linear thermal expansion coefficient (k^{-1}) [76] [75]	2.92×10^{-6} (293 K)	5.9×10^{-6} (300 K)	$(2.6 + 2.55x) \times 10^{-6}$ (x <0.85, 300 K) $(-0.89 + 7.53x) \times 10^{-6}$ (x >0.85, 300 K)
			(2.6+2.55x) x 10-6
Density at 298 K (g/cm^3) [76]	2.3290	5.3234	
Refractive index [77] **(E_0=photon energy in eV, 0 to ~0.5eV)** **(1 terahertz = 0.004 eV)**	$n(E_0) = n_0 + n_1 E_0^2$ $n_0(x) = 3.423$ $n_1(x) = 0.0933$	$n(E_0) = n_0 + n_1 E_0^2$ $n_0(x) = 4.006$ $n_1(x) = 0.217$	$n(E_0) = n_0 + n_1 E_0^2$ $n_0(x) = 4.01 - 0.81x + 0.22x^2$ $n_1(x) = 0.216 - 0.211x + 0.089x^2$
Energy band gap (eV) [76]	1.1242 (between $\Gamma_{25'V}$ and Δ_{1C}) (at 300 K)	0.664 (between Γ_{8V} and L_{6C}) (at 291 K)	
Mobility ($cm^2V^{-1}s^{-1}$) [76]			
Electrons	1450 (300 K)	3800 (300 K)	
Holes	370 (300 K)	1800 (300 K)	
effective mass (m*)	See Table 1	See Table 1	

Table 2 - Properties of bulk Si, Ge and $Si_{1-x}Ge_x$

2.3 Epitaxial growth

Epitaxy is the process of growth of a single-crystal film on a crystalline substrate, where the film adopts the crystalline structure and orientation of the substrate. Homoepitaxy is when epitaxy is performed with only one material. Heteroepitaxy, which will be the basis of this work, is when epitaxy is performed with different materials. Methods typically used for epitaxy are molecular beam epitaxy (MBE) and chemical vapour deposition (CVD). For all epitaxial growth in this work, CVD was used and it is described in depth in the next section.

2.3.1 Chemical Vapour Deposition

CVD is growth by chemical process. The semiconductor industry uses CVD as the preferred process for the deposition of thin crystalline films. This preference comes from CVD's ability to give fast, reproducible growth with uniformity over large wafers. CVD was chosen as the growth technique for this work for a number of reasons. CVD growth of $Ge/Si_{1-x}Ge_x$ has a low interfacial roughness when compared with other techniques such as MBE [10]. In MBE electron beam evaporation is used as the source of Si due to the extreme reactivity of molten Si with the crucible in thermal evaporation sources. Electron beam evaporators struggle to provide constant growth rates, since the growth rate changes as the source is used up and the amount of molten material changes. CVD is able to provide constant growth rates for long periods. 'Spitting' can also occur in MBE when flakes of Si deposited in the growth chamber fall back into the fall electron beam evaporator. Also, any contaminates

present in the growth chamber can become charged which can cause deflection towards the substrate.

2.3.2 Reduced Pressure Chemical Vapour Deposition

All epitaxial growth in this study was performed using reduced pressure chemical vapour deposition (RP-CVD) with an ASM Epsilon 2000 reduced pressure reactor. This is an industry standard growth tool, with many similar systems manufactured by ASM installed in commercial semiconductor foundries and fabrication facilities.

Figure 2-8 shows a typical reactor used for RP-CVD. First, precursors and dopants are fed into the quartz reaction chamber. The flow rate of precursor/dopant gas into the chamber is controlled by mass flow controllers (MFCs). Since the precursor/dopant gas flow affects growth rate and doping level, precise control is important. The gas then flows over the substrate, which is heated by infrared radiation generated by lamps. Temperature is monitored via thermocouples underneath the substrate. The reaction chamber is designed to give a uniform flow over the entire substrate via adjustment of gas flow and temperature profiles. Finally, the remaining gas is vented from the chamber where it is sent to chemical scrubbers to remove any dangerous gases from the exhaust flow. Growth by RP-CVD can be split into stages, given in figure 2-9.

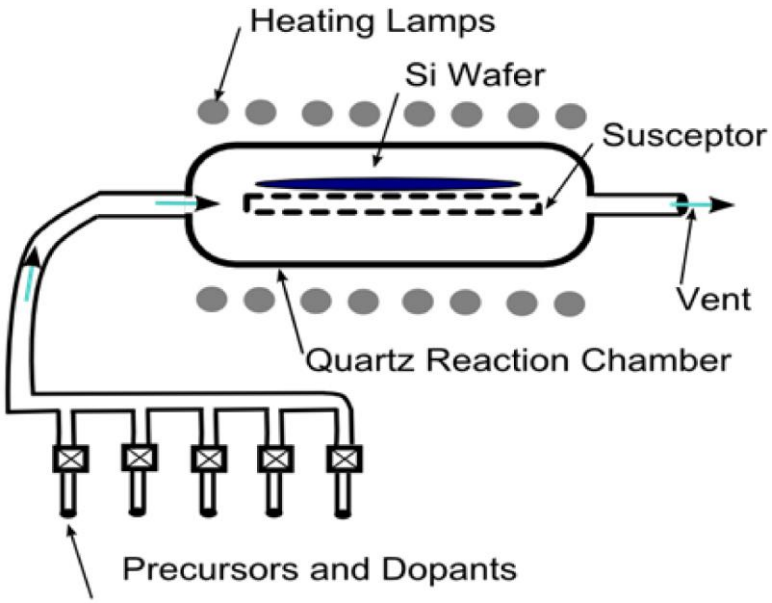

Figure 2-8 - Simplified diagram of RP-CVD reactor

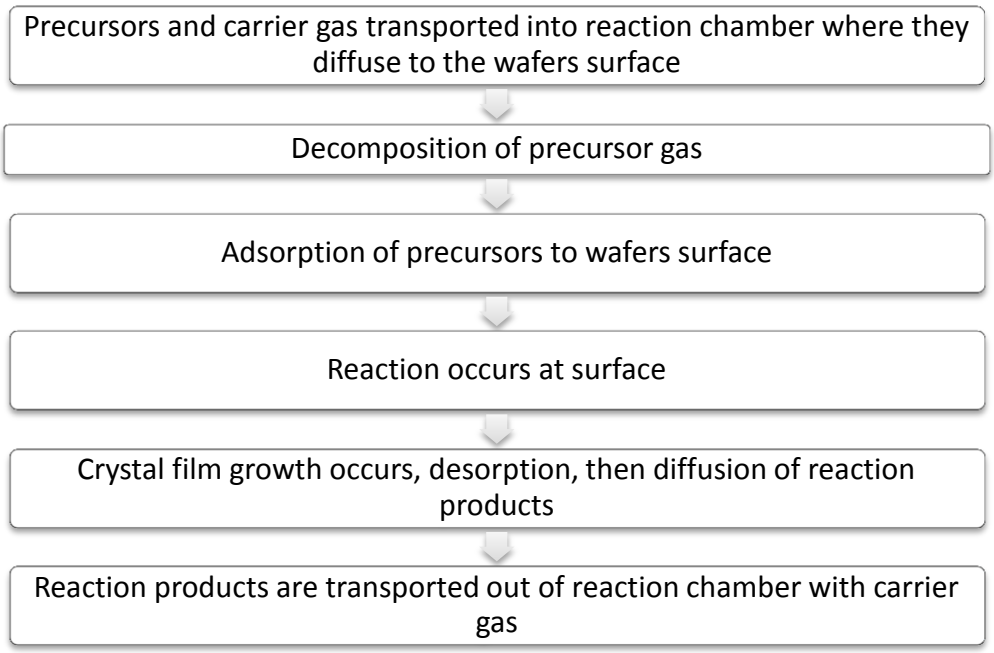

Figure 2-9 - Steps of deposition in RP-CVD

The correct choice of precursor gas is very important when growing a structure by RP-CVD since it effects the growth. The precursors used for the growth in this work are discussed in the next section.

2.3.3 Precursors and chemical reactions

For all epitaxial Si growth, disilane (Si_2H_6) was used as a precursor. Disilane was chosen over silane (SiH_4) because it enables faster growth rates at lower temperatures (~2 nm min^{-1} at 500^{o}C). This is due to the Si-Si bond strength (226 kJ mol^{-1}) being weaker than the Si-H bond strength (318 kJ mol^{-1}) making it easier to form sylil, SiH_3 [78]. This means growth can be performed with a lower thermal budget and use less precursor gas.

Equations 2-5 - 2-8 can be considered the main steps in the deposition of Si with disilane for temperatures $T \leq 575^{\circ}C$ [79], where (g) is a gaseous state, (a) is an absorbed species, $X*$ a chemical species which is bonded to a surface site and * a free surface site.

Molecules of disilane are absorbed onto Si(001) according to

$$Si_2H_6(g) + 2* \rightarrow 2SiH_3*. \qquad 2\text{-}5$$

The sylil then decomposes to silylene and surface hydrogen through

$$SiH_3* + 2* \rightarrow SiH_2* + H*. \qquad 2\text{-}6$$

The surface then becomes mobile along underlying Si dimer rows, reacting to form Si monohydride through

$$2SiH_2 * \rightarrow 2SiH * + H_2(g). \quad \text{2-7}$$

Finally the remaining hydrogen atoms are desorbed through

$$2SiH * \rightarrow 2Si * + H_2(g). \quad \text{2-8}$$

For all epitaxial Ge growth in this study, germane (GeH_4) was used as a precursor. At approximately 280 ^{o}C, germane begins to thermally decompose on a surface giving Ge deposition [80]. Equations 2-9 and 2-10 can be considered the main steps in the deposition of Ge with germane.

$$GeH_4(g) + 2 * \rightarrow H_2(g) + 2H * + Ge(b) * + 2(b), \quad \text{2-9}$$

$$2H * + 2(b) \leftrightarrow H_2 + 2 *. \quad \text{2-10}$$

All doping was n-type phosphorus provided by phosphine, PH_3 . The initial adsorption reaction for phosphine is given by equation 2-8 [81].

$$PH_3(g) + 4 * \rightarrow p * + 3H *. \quad \text{2-11}$$

For exchange of material between the gaseous phase and the solid, crystal phase, a number of atomic scale processes occur. These can be split into two categories, the processes occurring in the bulk phases and the processes on the substrate growing

surface. The processes occurring at the substrate surface are responsible for the morphology of the growth.

2.3.4 Growth Morphology

Epitaxial growth morphology can be divided into three distinct types , Frank-van der Merwe morphology, Volmer-Weber morphology and Stranski-Krastanov morphology. The different growth morphologies can be explain using the concept of free energies, of the substrate σ_s, interface σ_i, and of the layer σ_l, if the assumption of thermodynamic equilibrium is used. When the system reaches thermodynamic equilibrium, the free energy is at a minimum. Epitaxy is often under dynamic equilibrium, but it is still useful to consider the thermodynamic case.

If the free energy of the substrate is larger than that of the combined free energies of the interface and layer:

$$\sigma_s > \sigma_i + \sigma_f, \qquad 2\text{-}12$$

then growth proceeds layer by layer, resulting in a single crystal, 2D flat film (figure 2-10). This 2D growth occurs due to the atoms attaching preferentially to surface sites and is known as Frank-van der Merwe morphology.

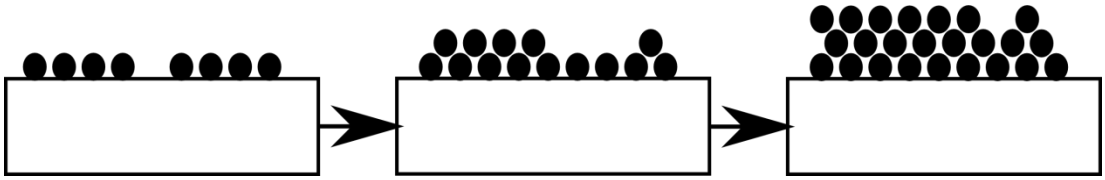

Figure 2-10 - Frank-van der Merwe morphology

If the free energy of the substrate is smaller than that of the combined free energies of the interface and layer:

$$\sigma_s < \sigma_i + \sigma_f, \qquad 2\text{-}13$$

then growth proceeds in 3-dimensional islands (figure 2-11), resulting in a rough surface. This 3D growth occurs due to attractions between adatoms being stronger than those between adatoms and the surface and is known as Volmer-Weber morphology.

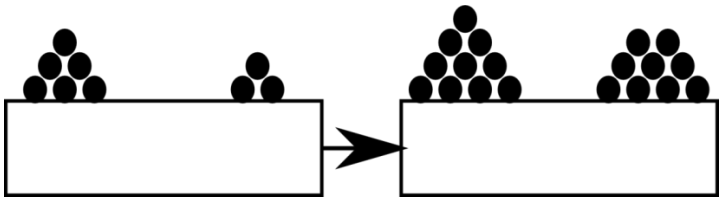

Figure 2-11 - Volmer-Weber morphology

Stranski-Krastanov (SK) morphology is a combination of the two previously mentioned growth modes (figure 2-12). It commonly occurs when there is a lattice mismatch between the growing layer and the substrate. The SK morphology can be

split into three stages, initial growth is layer by layer, forming what is known as the wetting layer on the substrate. Due to the lattice mismatch between the layer and substrate causing strain in the wetting layer, when the film thickness reaches a certain point, island growth begins. As growth progresses, the islands begin to coalesce.

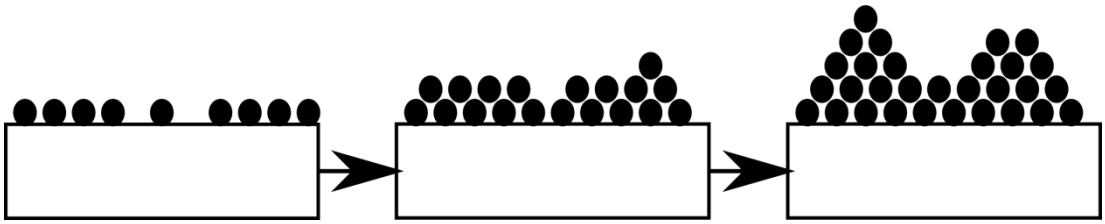

Figure 2-12 - Stranski-Krastanov morphology

If there is a lattice mismatch between the growing layer and the substrate, it can lead to build up of strain in the layer, which can in turn lead to a degradation of the crystal quality of the layer through strain relief by dislocation formation. This is discussed in the next section.

2.3.5 Relaxation and Critical Thickness

If growth is performed on a substrate with a different lattice parameter to the epitaxial layer and growth proceeds pseudomorphically (the layer is forced to adopt the same out in-plane lattice parameter as the substrate) then strain will build up in the layer as the growth thickness increases. The magnitude of the strain is equal to the additive inverse of the lattice mismatch, f_m. The strain will be bi-axial in the

growth plane, with the [100] and [010] directions assumed to be equal, giving the in-plane lattice parameters as $a_x = a_y$. For a strained layer, the out-of-plane lattice parameter will be tetragonally distorted compared to the in-plane lattice parameter (figure 2-13, figure 2-14). The relationship between the in-plane lattice parameters and the out-of-plane lattice parameter is given by equation 2-14, where C_{11} and C_{12} are the elastic moduli, the values of which are given for Si, Ge and SiGe in Table 2, a_{bulk} is the layers bulk lattice parameter, a_z the lattice parameter in the <001> direction and a_x the lattice parameter in the <100> or <010> directions.

$$a_z = a_{bulk} + \frac{2C_{11}}{C_{12}}(a_{bulk} - a_x). \qquad 2\text{-}14$$

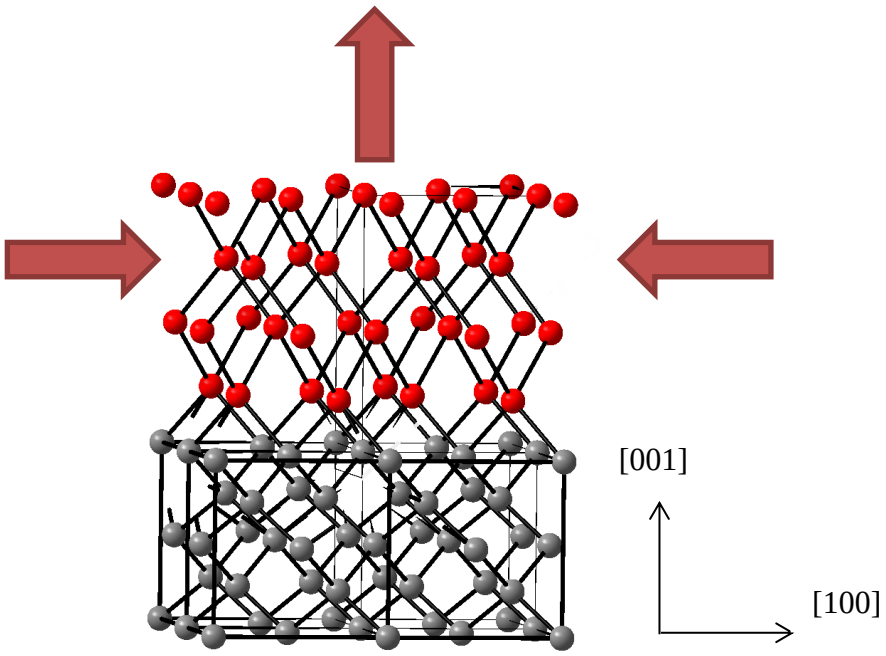

Figure 2-13 - Epitaxial layer under compressive strain

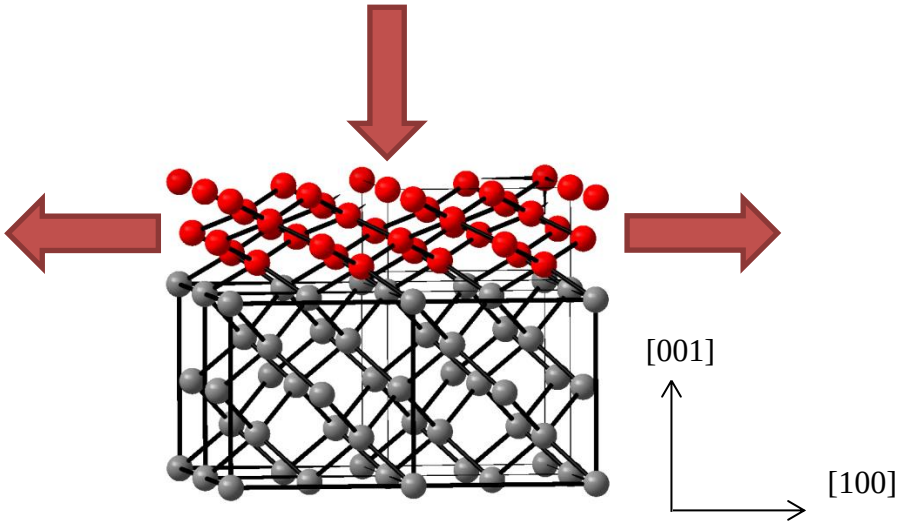

Figure 2-14 - Epitaxial layer under tensile strain

The strain, ε, in a layer with respect to its substrate can be found with equation 2-15, where R is the relaxation of the layer, a_l the in-plane lattice parameter of the layer and $a_{l(bulk)}$ is the bulk lattice parameter of the layer.

$$\varepsilon = f(1 - R) = \frac{a_l - a_{l(bulk)}}{a_s}. \qquad 2\text{-}15$$

Relaxation is defined by equation 2-16 and is commonly given as a percentage.

$$R = \frac{a_s - a_l}{a_s - a_{l(bulk)}}. \qquad 2\text{-}16$$

If the in-plane lattice parameter of a layer is larger than its value in bulk material $a_l > a_{l(bulk)}$, the strain is positive (ε>0) and the layer is tensile strained. If the in-plane lattice parameter of the layer is smaller than the bulk value, $a_l - a_{l(bulk)}$, the strain is negative (ε<0) and the layer is compressively strained. When the relaxation, *R*, is greater than 100% the layer is described as being over-relaxed and if $a_l > a_{l(bulk)}$, the layer is tensile strained. Layer relaxation can occur through the formation of dislocations.

2.3.6 Defects and Dislocations

A dislocation represents a defect or irregularity in the structure of a crystal. The strain accumulated as the pseudomorphic layer thickness increases can be relieved by the formation of dislocations and by surface roughening. Dislocations can be thought of as the termination of a plane of atoms in the crystal lattice and can be divided into two main types, edge dislocations and screw dislocations. Edge dislocations can be visualised as an extra half plane of atoms inserted into the crystal lattice (figure 2-15 a)). Screw dislocations can be visualised as a cube of crystal lattice with a shear stress applied at the top of the cube, such that it has started to rip (figure 2-15 b)). The 'ripped' atoms will have re-established bonds in their new position, but atoms in the process of moving will have broken bonds, forming a dislocation. The dislocations observed experimentally are generally a mixture of these two kinds, edge and screw.

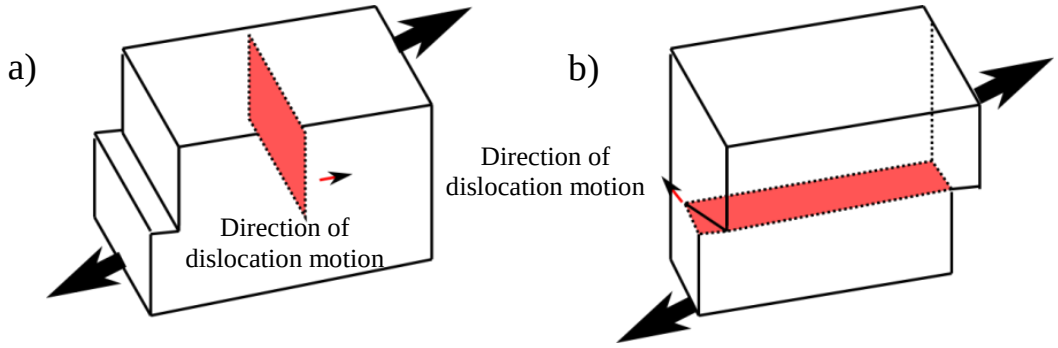

Figure 2-15 - Schematic of a) edge dislocation b) Screw dislocation with large black arrows showing direction of stress casusing dislocation motion and small arrows showing direction of dislocation motion.

The Burgers circuit can be used to define a dislocation. A Burgers circuit is an atom-to-atom path in a crystal lattice that contains dislocations and completes a closed loop [82]. A path of this kind is illustrated in figure 2-16. When the same atom-to-atom path is made in a perfect crystal lattice containing no dislocations and the circuit is unable to close (figure 2-17), then the circuit in the imperfect crystal must contain one or more dislocations. The additional vector required to complete the circuit is called the Burgers vector, $\boldsymbol{b}$. The Burgers vector describes both the magnitude and the direction of lattice distortion of a dislocation. The energy of a dislocation is proportional to the square of the Burgers vector, $\boldsymbol{b}^2$.

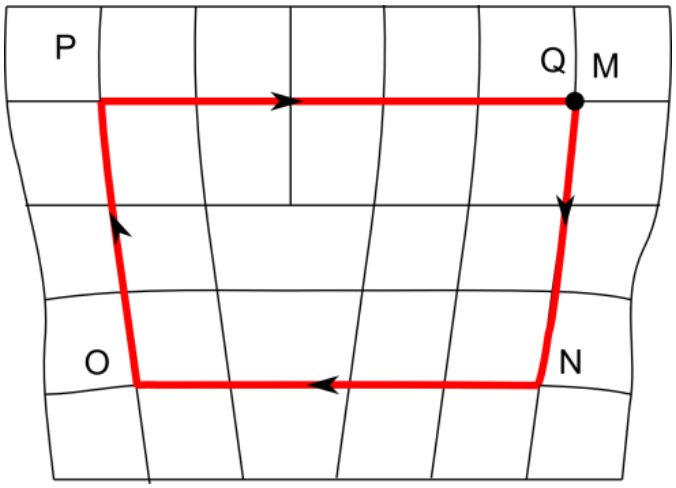

Figure 2-16 - Burgers Circuit around edge dislocation

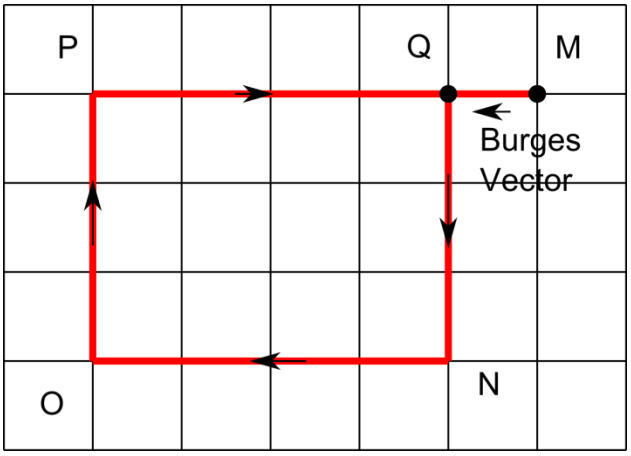

Figure 2-17 - Burgers circuit from previous figure in a perfect, dislocation free lattice. The failure to close the circuit is the Burgers vector, MQ.

The Burgers vector around an edge dislocation is given in figure 2-16. It can be seen that the Burgers vector is at a right angle to the dislocation line in figure 2-17.

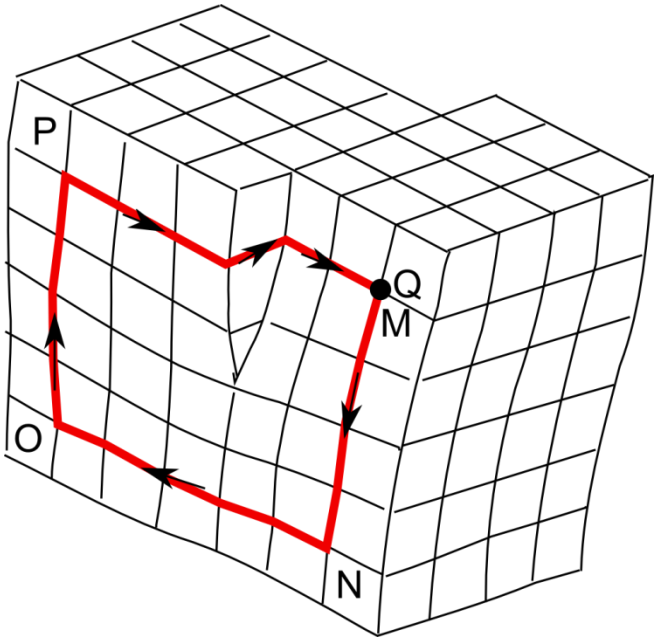

Figure 2-18 - Burgers circuit around screw dislocation

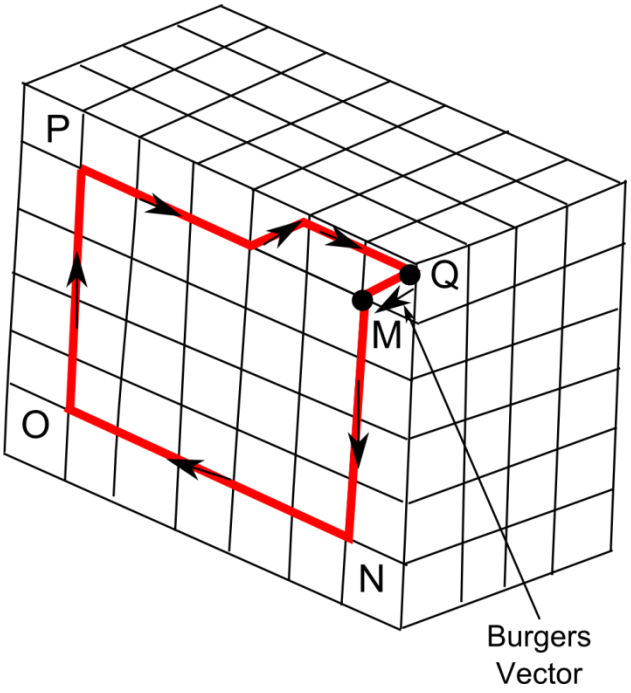

Figure 2-19 - Burgers circuit from previous figure in a perfect, dislocation free lattice. The failure to close the circuit is the Burgers vector.

The Burgers vector around a screw dislocation is given in figure 2-18. It can be seen that the Burgers vector is parallel to the dislocation line (figure 2-19). If a dislocation is combination of edge and screw, then the dislocation line will lie at an arbitrary angle to its Burgers vector and the dislocation is said to be mixed in character.

Since a dislocation causes a distortion of the crystal lattice, if a body contains a dislocation it will have additional strain energy. The total energy contained in a mixed dislocation is given by the sum of its screw and edge components. The total energy per unit length of a mixed dislocation is given by equation 2-17. For an explanation and derivation of 2-17 the author recommends the book by Hirth [83].

$$E_L = \frac{Gb^2(1 - \nu\, cos^2\theta)}{4\pi(1 - \nu)}\left[\ln\left(\frac{R\alpha}{\boldsymbol{b}}\right)\right]. \qquad 2\text{-}17$$

2.3.7 Dislocations in the SiGe system

For lattice mismatched SiGe on Si(001), strain relaxation occurs mainly through the formation of misfit dislocations with a Burgers vector of $\boldsymbol{b}_{60} = \frac{a}{2} < 011 >$, where the 60 refers to the dislocation orientation. These dislocations are oriented at a 60^o angle with the <110> direction and are hence known as 60^o dislocations. Edge misfit dislocations can also be formed, with a Burgers vector of $\boldsymbol{b}_{edge} = \frac{a}{2} < 1 - 10 >$. These dislocations are oriented at a 90^o angle with the <110> direction and are hence

referred to as 90^o dislocations. The fraction of 90^o dislocations increases with the lattice mismatch in the system and the degree of stress relaxation [84].

Dislocation motion can be divided into two basic types, glide motion and climb motion [82]. In glide motion, the dislocation moves in the surface containing both its line and Burgers vector. The glide of many dislocations in a crystal causes slip, which is the most common form of plastic deformation in crystalline solids. The glide planes for Si, Ge and SiGe are the [111] planes (figure 2-20).

Slip can be visualised as the sliding of one plane of atoms over another. The favoured plane for slip is known as the slip plane and is generally the plane with the highest density of atoms. This occurs because in the plane with the highest atomic density, the distance between atoms is on average shorter than in other planes. Slip occurs in the direction with the highest linear density of atoms. The slip planes are the same as the glide planes for Si, Ge and SiGe, [111] (figure 2-20).

In climb motion, the dislocation moves out of the glide surface normal to its Burgers vector, however there is a higher energy barrier for dislocation climb over dislocation glide for the SiGe system, thus strain relaxation proceeds by the glide of 60^o dislocations. Dislocation glide is thermally activated and thus can be supressed at low temperature.

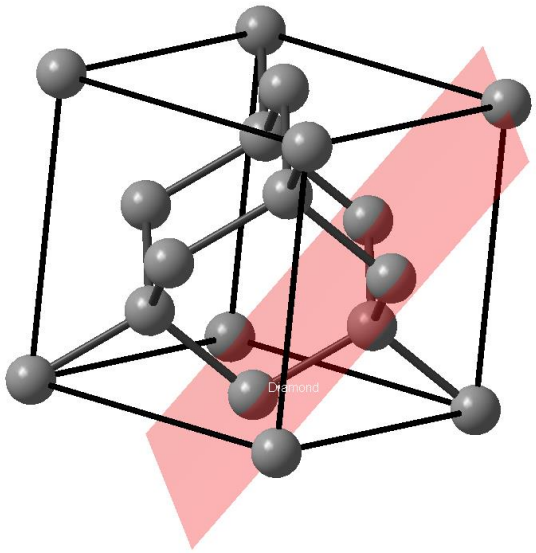

Figure 2-20 - [111] glide plane for Si, Ge and SiGe (red) overlaid on unit cell. On this [111] plane dislocation motion occurs.

2.3.8 Dislocation nucleation and critical thickness

During epitaxial layer growth, assuming a lattice mismatch between the layer and that the substrate, strain energy increases proportionally to the layer thickness. The strain energy cannot increase beyond a certain point before the layer begins to relax. The relaxation occurs by the introduction of dislocations at the layer/substrate interface and by an increase in the surface roughness of the layer.

For a cubic, biaxially strained pseudomorphic layer which is allowed to relax according to the Poisson ratio, the areal elastic energy density (E/A) is given by equation 2-18 [85].

Here t is the strained layer thickness, G is the shear modulus, $\epsilon_{\parallel}$ the in-plane strain parallel to the interface and v is the poisons ration of the layer. It can be seen that

(E/A) increases linearly with the layer thickness and quadratically with $\epsilon_{\parallel}$, which is given by the lattice misfit for the strained layer.

For plastic relaxation by the introduction of dislocations, strained epitaxial layers have a certain *critical thickness*, beyond which the layer begins to relax. Critical thickness for a strained layer was first discussed by Frank and van der Merwe in 1949 [86] for one dimension. This led to the development of the most commonly cited critical thickness model by Matthews and Blakeslee [87].

2.3.8.1 Matthews and Blakeslee model for critical thickness

The Matthews and Blakeslee (MB) model gives a value for critical thickness by balancing the effective stress acting on a pre-existing threading dislocation against that of the line tension in the dislocation. This model makes the assumption that the threading dislocations are present in the layer before strain relaxation begins. When the force on the threading dislocation, F_h, is sufficient, the threading dislocation will glide to relieve strain, forming a misfit dislocation. This is shown in figure 2-21.

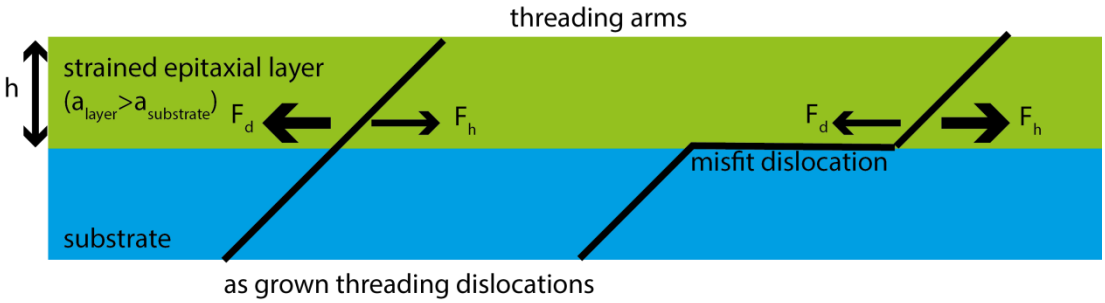

Figure 2-21 Matthews-Blakeslee model for the generation of misfit dislocations. Cross-sectional diagram of substrate/layer showing forces acting on a threading dislocation during glide.

The strain energy, E_r, relieved by a dislocation is given by equation 2-19 where σ is the layers stress, A is the area of the slipped plane perpendicular to the strain direction and $\boldsymbol{b}_{eff}$ the effective Burgers vector of the dislocation. The effective Burgers vector is the component of the Burgers vector in the interface plane in the direction perpendicular to a misfit dislocation [88], defined as $\boldsymbol{b}_{eff} = \boldsymbol{b}\cos(\lambda)$, where $\boldsymbol{b}$ is the Burgers vector of the dislocation and λ the angle between $\boldsymbol{b}$ and the direction within the interfacial plane perpendicular to the line direction.

$$E_r = \sigma A \boldsymbol{b}_{eff} \,. \qquad 2\text{-}19$$

The layer strain ϵ is related the stress by equation 2-20, where G is the shear modulus.

$$\sigma = 2G\epsilon\left(\frac{1+v}{1-v}\right). \qquad 2\text{-}20$$

From equations 2-19 and 2-20 it can be seen that the strain energy relieved by a dislocation can be written as equation 2-21, where the area A is given by $A=hl$.

$$E_r = 2G\epsilon\left(\frac{1+v}{1-v}\right) b\cos(\lambda)\, hl\,. \qquad 2\text{-}21$$

For dislocations to be energetically favoured in the layer, $E_r > E_L$. The critical thickness can then be defined as $E_r = E_L$., which is given in equation 2-22.

$$\frac{G\boldsymbol{b}^2(1-v\,cos^2\theta)}{4\pi(1-\,v)}\left[\ln\left(\frac{h\alpha}{\boldsymbol{b}}\right)\right] = 2G\epsilon\left(\frac{1+v}{1-v}\right)\boldsymbol{b}\cos(\lambda)\, hl\,. \qquad 2\text{-}22$$

Equation 2-22 can then be rearranged to give the Matthews and Blakeslee critical thickness model, equation 2-23.

$$h_c = \frac{\boldsymbol{b}(1-v\,cos^2(\theta))}{8\pi(1+v)\epsilon\cos(\lambda)}\ln\left(\frac{h_c\alpha}{\boldsymbol{b}}\right). \qquad 2\text{-}23$$

Equation 2-23 can be solved numerically and is plotted for a $Si_{1-x}Ge_x$/Si heterostructure in figure 2-23. The following parameters were used, $\boldsymbol{b} = 3.9\,nm$, $cos(\theta)$=0.5, (λ)=0.5 (for 60° dislocations), a from equation 2-4, ϵ from equation 2-15 and v, the Poisson ratio from table 2.

2.3.8.2 People and Bean model for critical thickness

Following the initial work of Matthews and Blakeslee, fully-strained $Si_{1-x}Ge_x$ on Si (001) layers have been grown far beyond the critical thickness predicted by the Matthews-Blakeslee model [89]. This is in part due to the crystal quality of Si substrates increasing, with fewer pre-existing dislocations. This has increased the experimental critical thickness by reducing the number of dislocations grown into the layer.

To accommodate the difference between the Matthews-Blakeslee model and the experimental results, People and Bean developed a critical thickness model that requires no pre-existing dislocations. In the People and Bean model (figure 2-22), strain relaxation occurs by formation of a misfit dislocation from the homogenous (spontaneous formation of a dislocation within the semiconductor material) nucleation of a dislocations loop from a point source. This process requires a higher energy than the creation of a misfit dislocation from the glide of a pre-existing threading dislocation.

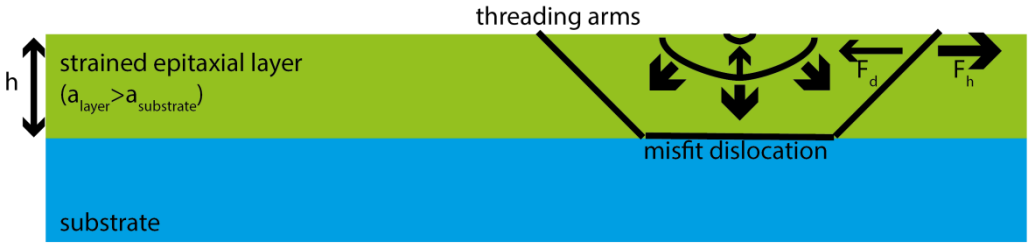

Figure 2-22 The People and Bean model

To nucleate a single screw dislocation, the areal energy density,E_d, is approximately given by equation 2-24 ([90]) where a is the bulk lattice constant of the strained layer. The energy densities of edge and-half loop dislocations were also calculated in reference [90] and the screw dislocation was found to have the minimum energy density.

$$E_d \approx \left(\frac{Gb^2}{8\pi\sqrt{2a}}\right)\ln\left(\frac{h_c}{\boldsymbol{b}}\right). \qquad 2\text{-}24$$

When the areal elastic energy density contained in the layer (equation 2-18) is equated with that necessary to nucleate a dislocation (equation 2-24), giving E_d=E_d, the People and Bean critical thickness is obtained:

$$h_c \approx \left(\frac{1-v}{1+v}\right)\left(\frac{\boldsymbol{b}^2}{16\pi\sqrt{2a}\varepsilon^2}\right)\ln\left(\frac{h_c}{b}\right). \qquad 2\text{-}25$$

In figure 2-23, both the People and Bean and Matthews and Blakeslee critical thickness models are plotted. The following parameters were used for the people and Bean model, ***b***=3.9 nm, *a* from equation 2-4, ϵ from equation 2-15 and *v*, the Poison ratio from table 2. It can be seen that the People and Bean critical thickness is significantly larger than that given by the Matthews and Blakeslee model. It is possible to grow layers above their predicted critical thickness without strain relaxation occurring, these layers are known as metastable.

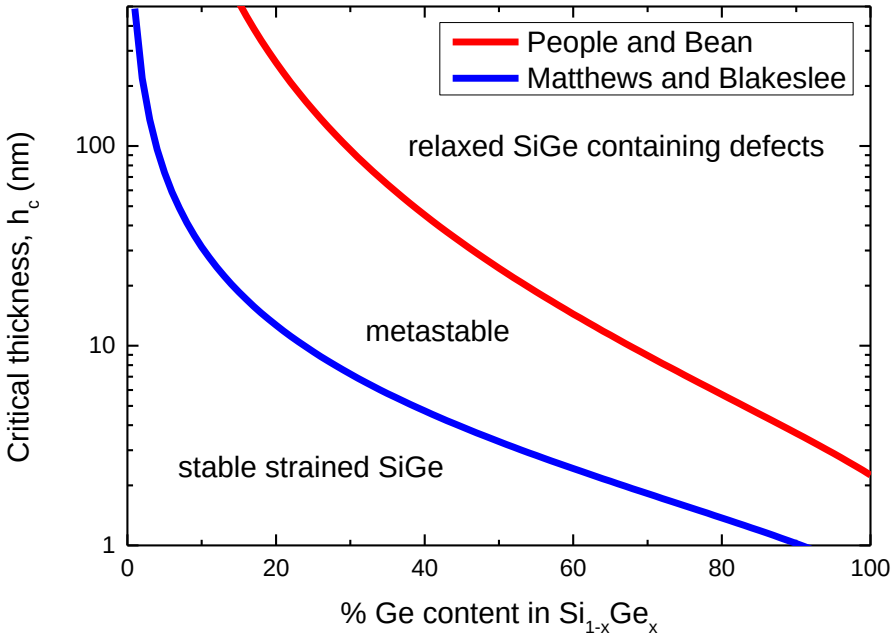

Figure 2-23 - Critical thickness as a function of Ge concentration for a $Si_{1-x}Ge_x$/Si heterostructure

2.3.8.3 Metastable layers

Fully-strained SiGe on Si layers with a thickness greater than their critical thickness have been frequently reported [91]. Below the critical thickness, the mismatch strain should be entirely accommodated by the strain in the film and above the critical thickness the strain is relieved to an extent by the generation of misfit dislocations. Unfortunately, experimental limitations make determining the exact thickness at which misfits are first introduced to the layer/substrate interface difficult [92]. The practical resolution of misfit dislocations gives a minimum detectable relaxation of around 10^{-3} [93], giving one possible reason why the measured critical thickness is generally higher than that predicted by theory. Another explanation is that strain relaxation depends on the kinetics of plastic deformation, the speed of which is reduced at lower growth temperatures. This gives the possibility of growing strained layers well beyond their critical thickness at low growth temperature.

2.4 Superlattice strain balance criteria and strain relaxation

Only single strained layers have so far been discussed, however a Si based QCL will require many strained layers in the form of a superlattice. Strain relaxation must be avoided in a superlattice structure designed for QCL applications, because it introduces dislocations into the superlattice that reduce the crystalline quality. The change in strain can affect key parameters such as the energy offsets between states in the QWs. Any roughness introduced will also affect the shape of the QWs and hence the energy levels therein.

For a strained layer superlattice system, there are two possible strain relaxation methods, both of which are illustrated in figure 2-24. In the first instance, each strained layer adds to the overall stress of the entire superlattice. If the overall stress causes a lattice mismatch between the superlattice and its supporting layer (and capping layer), then strain relaxation can occur at the bottom (and top) of the superlattice [94]. The superlattice lattice parameter then tends towards that of the superlattice structure were it unsupported. This is shown in the left of figure 2-24. In the second instance, the thickness of any individual layer in the superlattice can exceed its critical thickness. If this occurs, misfit strain relief occurs inside the superlattice structure with individual layers relaxing towards their bulk lattice parameters. This is shown on the right of figure 2-24.

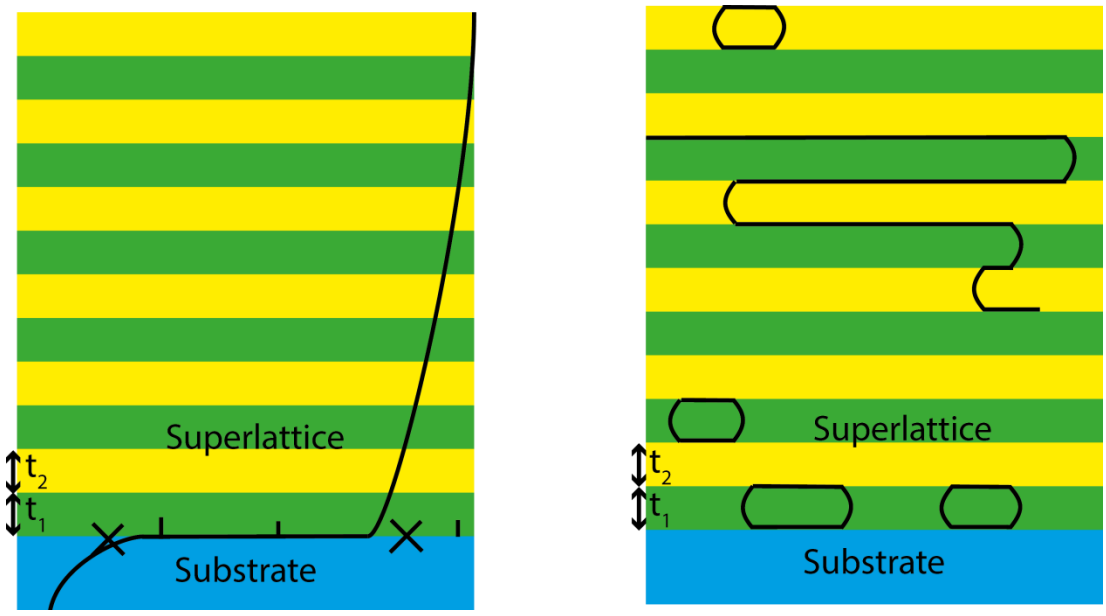

Figure 2-24 - Schematic diagram of possible strain relaxation methods for strained layer superlattices. Left, superlattice with lattice mismatch between substrate causing dislocations to be introduced at the base of the superlattice. Right, superlattice with individual layers grown beyond their critical thickness causing paired dislocations and loops to be introduced in individual strained layers. Adapted from [95].

2.4.1 Criteria for superlattice strain balance

In reference [96], different approaches to developing a criteria for superlattice strain balance are examined. A zero-stress method is proposed as the most accurate approach for designing strain balanced structures. The model is based on the requirement of zero average in-plane stress for the tensile/compressive strained layer combination. The zero-stress method is given in equations 2-26 and 2-27. Equation 2-27 gives the corresponding substrate lattice parameter were it unsupported. If this does not match the lattice parameter of the substrate used for the superlattices growth, then relaxation will begin if it is grown beyond a certain thickness. The thickness at which relaxation begins can then be calculated by using the standard critical thickness models for strained SiGe layers.

$$t_1 A_1 \epsilon_1 a_2 + t_2 A_2 \epsilon_2 a_1 = 0 \qquad \text{2-26}$$

$$a_0 = \frac{A_1 t_1 a_1 a_2^2 + A_2 t_2 a_2 a_1^2}{A_1 t_1 a_2^2 + A_2 t_2 a_1 a_1^2} \qquad \text{2-27}$$

Here $a_1$and a_2 are the lattice parameters of the compressive and tensile layers, t_1 and t_2 the thickness of the compressive and tensile layers, ϵ_1 and ϵ_2 the lattice mismatch/strain of the compressive and tensile layers, a_0 the corresponding substrate lattice parameter, and A_1 and A_2 are constants for each layer given by equation 2-28, where $C_{11}$and C_{12} are the elastic stiffness coefficients of the layers.

$$A = C_{11} + C_{12} - \frac{2C_{12}^2}{C_{11}} \qquad 2\text{-}28$$

It can be seen that the lattice parameter of a superlattice must be lattice matched with the substrate that it is grown on to avoid strain relaxation. The superlattice designs for a n-type Si based QCL which are reported on in this work are comprised of Ge and $Si_{0.15}Ge_{0.85}$ and have a superlattice lattice parameter of $Si_{0.05}Ge_{0.95}$.To avoid strain relaxation, these superlattices must be grown on a substrate of $Si_{0.05}Ge_{0.95}$. Starting from the ubiquitous Si (100) this can be achieved through the use of a virtual substrate.

2.5 Virtual substrates

A virtual substrate is an intermediary layer that allows strained layers with a different lattice parameter to the original substrate to be grown. In this study, a virtual substrate design with a final composition of $Si_{0.05}Ge_{0.95}$ has been used, which has been proposed and designed by M. Myronov. This design is similar to the reverse linearly graded (RLG) design (figure 2-25) originally reported by Shah et al [97] for a final Ge composition of $Si_{0.2}Ge_{0.8}$ and is shown to be highly suitable as a platform for high-quality strain-symmetrized multiple quantum well structures in reference [98]. The design in reference [96] (with a thin, total thickness of 2.4 μm) can give a relaxed, high Ge composition final layer, with a threading dislocation density (TDD) of 4×10^6 cm^{-2} and surface roughness of 3 nm [99]. When compared with other virtual substrate designs, such as linearly graded [100], these results are very good.

The virtual substrate design begins with a high quality 1 μm Ge layer grown on a Si (001) substrate using the two temperature method described in reference [101]. This comprises first growing a Ge layer at low temperature in the range of (300^{o}C-400^{o}C) in which dislocations nucleate but surface roughness remains low due to the low temperature suppressing 3D growth. A high temperature Ge layer is then grown at 670^{o}C which reduces the TDD and also reduces the overall growth time. The structure is then annealed at 830 ^{o}C for 10 min to further reduce the TDD. Ge grown by the two temperature method is generally found to be under tensile strain. Ge has a larger coefficient of thermal expansion than Si (table 2) and when the layers are heated during growth, the Ge layer expands more than the Si substrate, but the additional thermal energy allows the atoms to rearrange themselves to be commensurate with the substrate. As the Ge layer cools, it contracts more than the Si substrate but now the atoms do not have the freedom to move. The over relaxation occurs when the bonds between the substrate and Ge layer prevent the Ge layer from fully relaxing.

Following the 1 μm Ge layer, the graded region is grown. Using a reverse graded, as opposed to forward graded, region gives a thinner virtual substrate and a smoother surface due to the structure relaxing under tensile as opposed to compressive strain [102]. It can be seen in figure 2-25 that the majority of dislocations are confined within this sacrificial layer. Finally, the structure is capped with $Si_{0.05}Ge_{0.95}$ to give a high quality final layer.

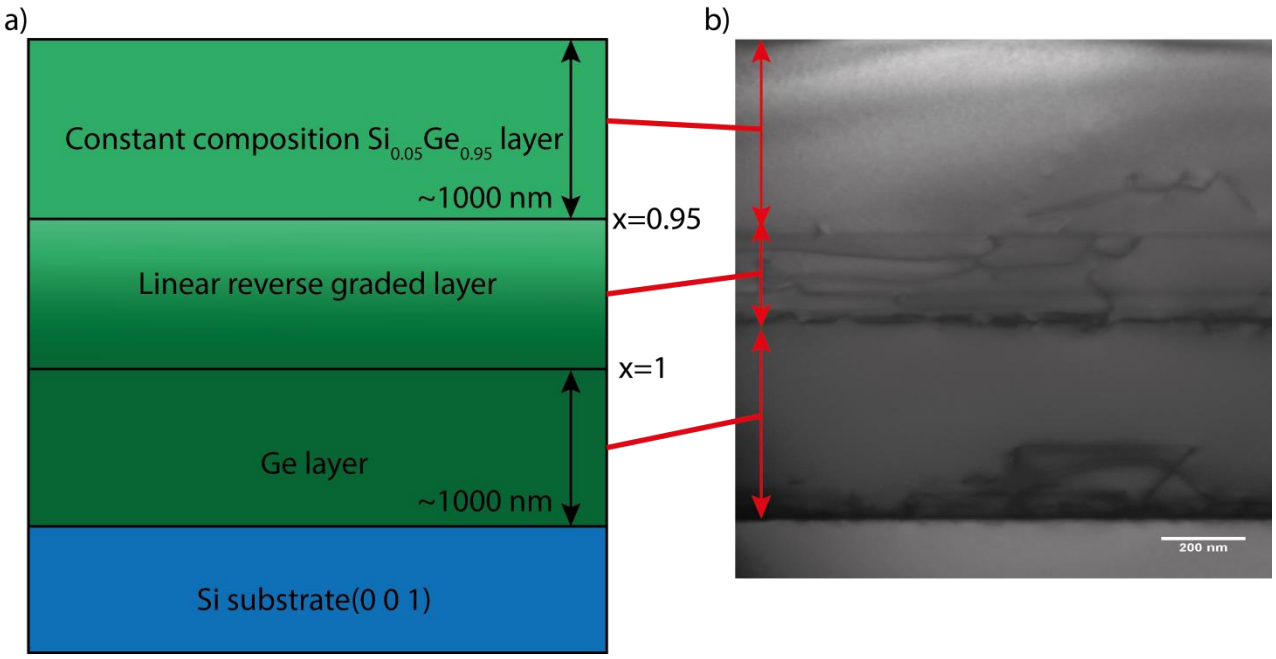

Figure 2-25 –a) Schematic design of the reverse linearly graded $Si_{0.05}Ge_{0.95}$/RLG/Ge/Si(001) virtual substrate b) Cross-sectional TEM micrograph of $Si_{1-x}Ge_x$/RLG/Ge/Si(001) virtual substrate.

Dislocation introduction through strain relaxation is not the only growth issue that has the possibility to adversely affect the electronic behaviour of a Si-based QCL. Diffuse Ge profiles can change the subband spacings in the QWs and also the scattering rates between wells. One of the main factors in determining interface quality is diffusion, which is discussed for the Si/Ge/$Si_{1-x}Ge_x$ material system in the next section.

2.6 Diffusion

Diffusion can be described by a diffusivity or diffusion coefficient, *D*. It is the proportionality constant that relates the molar flux to the concentration gradient for a species. During diffusion, an atom moves between sites and crosses an energy barrier

with the movement being assisted by thermal energy. The diffusion coefficient is commonly given via an Arrhenius expression, equation 2-29. Where D_0 is the pre exponential factor, H the activation enthalpy, k_B the Boltzmann constant and T the temperature.

$$D = D_0 \exp(-H/k_B T) \qquad 2\text{-}29$$

2.6.1 Si and Ge Diffusion

In figure 2-26 the diffusion coefficients for Si and Ge in $Si_{1-x}Ge_x$ (for x=0 to x=1) are given in a Arrhenius plot. It can be seen that diffusion increases with Ge concentration and that Ge diffusion is favoured more by a high Ge content than Si. This is explained by the increasing contribution of vacancies to self-diffusion with increasing Ge content [103]. Figure 2-26 illustrates why low growth temperature is important for high Ge content SiGe heterostructures if diffusion is to be minimised. While the data given in figure 2 21 is for temperatures higher than those used in this study, it can be seen in [104] that the self-diffusivity for Ge can be given by a single Arrhenius equation from 429^{o}C and 904^{o}C (H= 3.13±0.03 eV, D_0=2.54x10^{-3} m^{2}s^{-1}), and so the trends in Arrhenius plot in figure 2-26 can confidently be extended to lower temperatures, at least for Ge and high Ge composition SiGe.

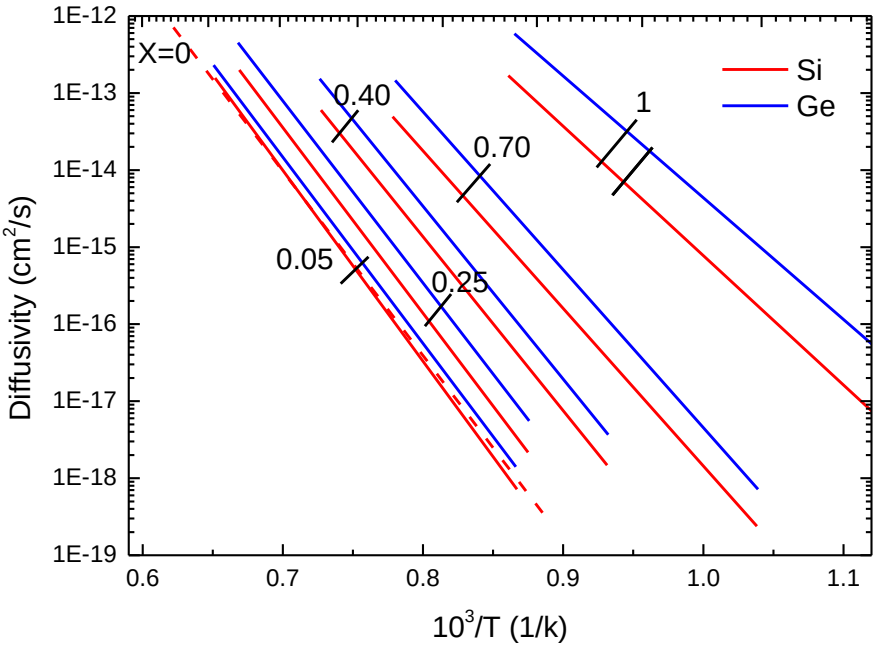

Figure 2-26 - Arrhenius plot of diffusion coefficient in $Si_{1-x}Ge_x$ for a number of alloy concentrations against inverse temperature. Adapted from Kube et al [103]

Dopant profiles are also strongly affected by diffusion. In the next section the diffusion of common dopants for the Si/Ge/$Si_{1-x}Ge_x$ material system is discussed.

2.6.2 Dopant diffusion

In figure 2-27 the diffusion coefficients for dopants P, As, B in Ge and self-diffusivity are given in an Arrhenius plot. While this data is for higher temperatures than those used for growth in this study, little information is available for lower temperatures. It can be seen that while the diffusivity for B, a p-type dopant is relatively low, the diffusivities for the n-type dopants, P and As, are both relatively high, exceeding the Ge self-diffusivity. This is one of the reasons why preference has been given to p-type Si based QCL structures in previous work on Si based QCLs, since attaining sharp doping profiles in n-type structures is difficult. A low growth temperature will be required for a n-type structure to minimise dopant diffusion.

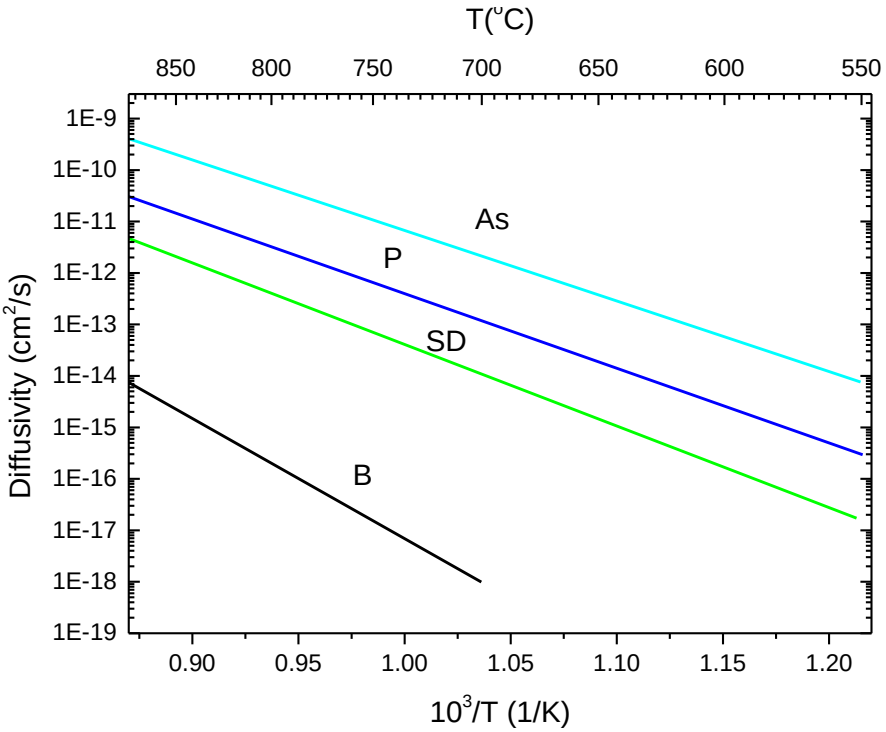

Figure 2-27 - Arrhenius plot of intrinsic diffusivities of P, As, B in Ge. Ge self-diffusivity, SD is also included. Adapted from Shiraki and Usami [74].

Another factor affecting interface quality in the Si/Ge/$Si_{1-x}Ge_x$ materials system is Ge surface diffusion. This segregation must be minimised in order to give sharp interfaces in an n-type Si based QCL superlattice structure.

2.6.3 Ge Surface Segregation

During the growth of $Si_{1-x}Ge_x$ and Si/Ge layers, the surface concentration of Ge has been found to be higher than the rest of the layer [105-106]. This is due to the preferential surface segregation of Ge atoms over Si atoms. Ge surface segregation is driven by a difference in the elements surface tension and by the difference in atomic size (The atomic radius of Ge is 0.137 nm and for Si is 0.132 nm) [107]. In CVD growth, Ge segregation can be supressed by surface passivation by hydrogen [108].

To give sharp interfaces in the superlattice structures in this work, with minimal Ge surface segregation, all growth is being performed in a hydrogen atmosphere.

.

2.7 Summary and outlook

From section 2.1.4 it can be seen that the most likely candidate for a Si-based QCL is an n-type Ge/SiGe structure with high Ge content barriers. A structure of this kind is particularly challenging from a growth perspective. This is due to the requirement for a high Ge composition virtual substrate to achieve strain balance (section 2.5), which in turn presents higher diffusion than for lower Ge content structures leading to barrier degradation (section 2.6), and in addition the high diffusivity of n-type dopants when compared to p-type dopants (section 2.6.2).

3 Experimental Techniques

In this chapter, the techniques used are first compared and contrasted, then described in detail. The techniques are high resolution X-ray diffraction, microbeam X-ray diffraction, atomic force microscopy, transmission electron microscopy, scanning transmission electron microscopy, secondary ion mass spectrometry and atom probe tomography. The simplified theory and experimental method are given for each technique.

3.1 Introduction to characterisation techniques

In order to perform comprehensive structural characterisation on structures designed to operate as QCLs it is necessary to use a number of complementary characterisation techniques. In the context of producing a functioning QCL structure, the structural parameters that are important to measure include alloy composition, strain state, layer thickness, interface quality, surface morphology, dopant concentration, and crystal quality. The choice of characterisation techniques must be capable of measuring these parameters.

The most frequently used technique in this this work is X-ray diffraction. X-ray diffraction is highly suitable as a probe for measurements on the QCL structures since the wavelengths of X-rays are on the order as the atomic spacing in the structures. X-ray diffraction is a fast and non-destructive technique. Structural parameters that can be extracted from X-ray diffraction measurements include alloy composition, strain state, layer thickness, interface quality and crystal quality.

Electron microscopy is also a highly suitable technique for characterising the structures presented in this work and is complementary to X-ray diffraction. X-ray diffraction gives information from a relatively large volume of the sample whereas electron microscopy is able to probe a much smaller volume. Unfortunately electron microscopy is a destructive technique and producing the high quality specimens required is very time consuming.

Both X-ray diffraction and electron microscopy struggle to resolve small changes in alloy concentration within a multilayer structure (such as that from segregation/diffusion at interfaces) and neither can measure dopant concentration. To measure these parameters, it is necessary to use either secondary ion mass spectrometry (SIMS) or atom probe tomography (APT). Both are destructive techniques. Secondary ion mass spectrometry is only able to produce a dopant/alloy concentration profile in one direction through a sample, with the profile averaged over a large area while atom probe tomography has the advantage of being able to provide it in 3D. However, since atom probe tomography has a considerably longer sample preparation time, it is the more difficult of the two techniques.

Finally, a technique is needed to measure the surface morphology of the samples, from which the surface roughness and long and short range order through the structure can be inferred. This can be performed using atomic force microscopy, which is both fast and non-destructive.

3.2 Atomic Force Microscopy

All the atomic force microscopy (AFM) results presented in this work were produced using a Veeco Multimode AFM (see figure 3-1, 3-2) with a Nanonis SPM controller operating in both contact and tapping mode. The surface morphology of a sample can be recorded with AFM with very high vertical (*z*) resolution.

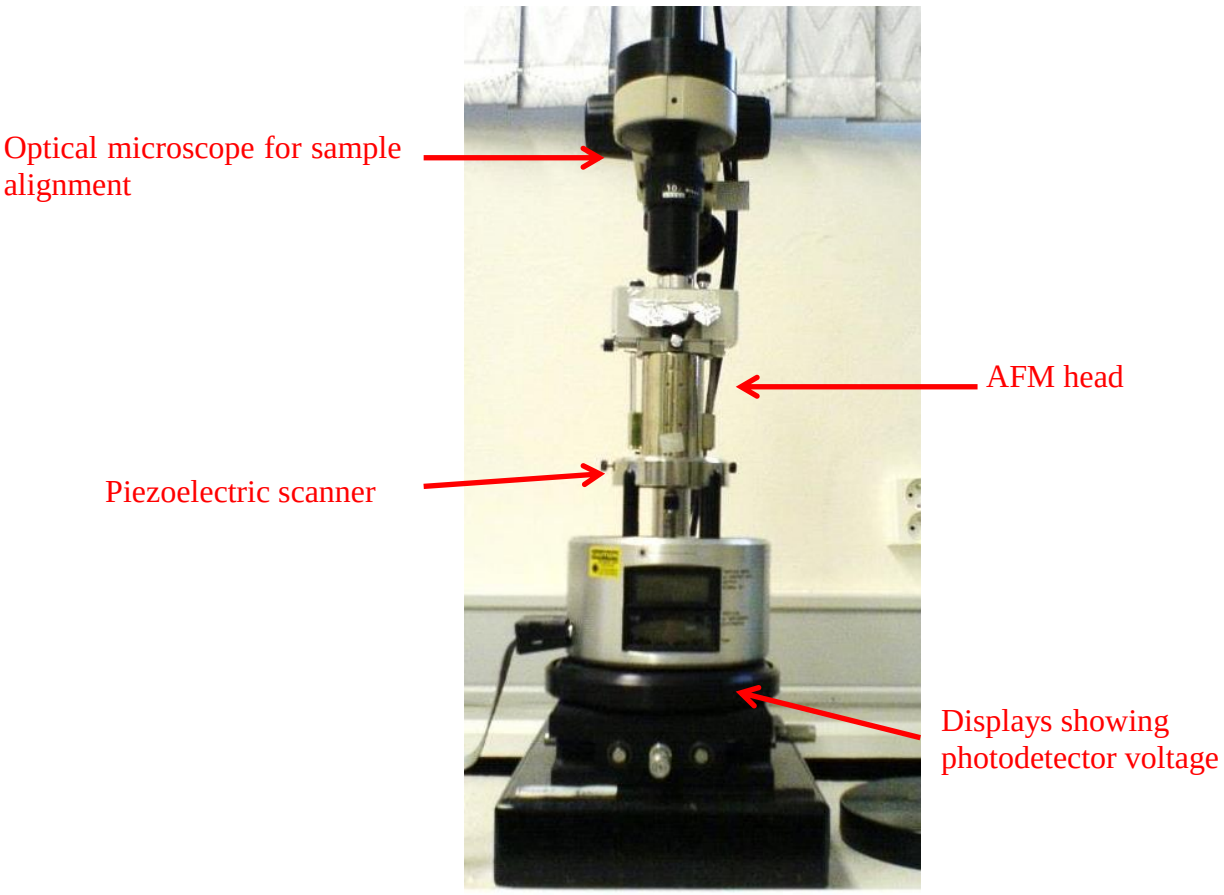

Figure 3-1 - Veeco Multimode AFM

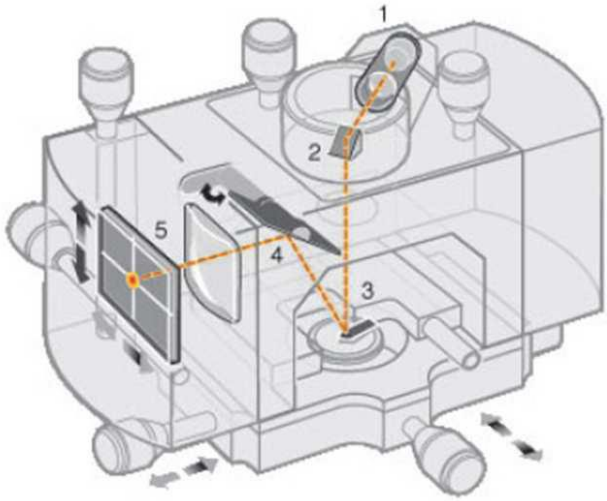

Figure 3-2- AFM head of Veeco multimode AFM. The labelled parts are 1) Laser, 2)Mirror, 2)Mirror, 3)Cantilever, 4)Tilt Mirror and 5)Photo-detector. Reproduced from [109].

3.2.1 Contact Mode

The operation of the AFM in contact mode can be described by the following: The sample is placed on a sample stage mounted on a piezoelectric scanner. The piezoelectric scanner is capable of moving the sample in the *x*, *y* and *z* planes, where *x* and *y* are parallel to the samples surface and *z* is perpendicular to the surface. A silicon nitride tip mounted on a thin, flexible cantilever is lowered towards the sample surface. When the tip nears the sample, forces occurring between the tip and the sample surface cause the cantilever to bend, according to Hooke's law. The tip is observed to 'snap-in' towards the sample surface. A laser beam is directed at the back of the cantilever and is deflected towards a split photo-diode detector, as can be seen in figure 3-2. From the voltage output of the photo-diode, both the lateral flex and the twist of the cantilever can be determined. Feedback from the photodiode is

used to maintain a constant laser deflection by changing the height of the sample using the piezoelectric scanner. A constant laser deflection implies that the cantilever flex remains constant and so the force between the tip and the sample remains constant. The sample is rastered (the sample is moved, the tip stays stationary) over an area defined by the AFM software and, via the AFM controller, a computer records the height or *z* position of the sample at each (*x*,*y*) position. From the *x*, *y* and *z* positions, the computer constructs an image of the sample's surface morphology.

3.2.2 Tapping Mode

AFM in contact mode suffers effects from degradation of both the sample and the tip as the tip is rastered across the sample. Non-contact mode AFM utilizes the attractive inter-atomic force occurring between the tip and sample surface. Unfortunately, in non-contact mode, the meniscus force can cause the sample to stick to the tip and when it is freed by the piezoelectric stage, the cantilever flicks vertically causing a glitch in the image recorded. A solution to this is to perform the scan in tapping mode which was introduced by Zhong *et al* [110].

In tapping mode the tip is rastered across the surface of the sample, just as in contact mode; however, the cantilever is driven to oscillate at a frequency near its resonant frequency. The cantilever oscillation is driven using a piezoelectric element at the base of the cantilever inside the tip holder. As the oscillating tip approaches the surface, the oscillation amplitude is decreased. Whereas in contact mode the *z* height is constantly adjusted to maintain a constants cantilever flex, in tapping mode, the sample *z* height is constantly adjusted to maintain a constant oscillation amplitude.

Tapping mode reduces the damage to the sample surface and tip when compared to contact mode.

3.2.3 AFM Image Analysis

All AFM images presented in this work were analysed and processed using the Gwyddion SPM software. Many artefacts (caused by tip shape, piezoelectric scanner hysteresis, dirt on the sample, etc.) are present in unprocessed AFM images and these must be removed before extracting data, such as RMS surface roughness, from the images. Information can be lost during processing, so care must be taken during its application.

The image is first levelled by the *mean plane subtraction* function. This function computes a plane from all of the image points and subtracts this from the data. The image is then processed with the *remove polynomial background* function. This function fits an *n*th order polynomial to both the horizontal and vertical directions and subtracts this from the data. If the image has horizontal lines running across it (an artefact from rastering the tip line by line across the sample) they are removed with the *correct lines by matching height medium* tool. Additionally, if the image has any artefacts from dirt on the sample, they can be excluded from the analysis by using the *mask* function.

The use of AFM to record the surface morphology of a sample with very high vertical (*z*) resolution has been described. While much information about a sample can be inferred from its surface morphology, to fully characterise a QCL structure it is necessary to look beyond the samples surface and to measure parameters such as

doping and alloy concentration through the structure. These material parameters can be resolved through the structure by the technique described in the next section, secondary ion mass spectrometry

3.3 Secondary Ion Mass Spectrometry

Secondary ion mass spectrometry (SIMS) is a destructive technique with a high sensitivity to impurities in the sample under investigation. The technique involves accelerating a beam of ionised particles into the sample causing ions to be sputtered from the sample surface (figure 3-3). The sputtered ions are known as the secondary ions. The secondary ions are directed into a mass spectrometer where their masses are recorded as a function of erosion time. From the mass spectrometer data, the sputtered ions species and quantity can be determined as a function of time. The depth of the crater produced by the sputtering is then measured and if the sputtering rate is assumed to be constant, then the erosion rate of the sample can be combined with the mass spectrometer data to produce a mass vs. depth profile. The scale in a SIMS profile is not absolute and needs careful calibration for alloy content and depth. This is due to the ion yields and erosion rates varying with the composition of the sample material.

A number of effects can affect the resolution of SIMS analysis. Due to the high energy of the incident ion beam, surface atoms can be forced deeper into the sample (figure 3-3), where they are then sputtered and recorded as secondary ions, causing a boarding of the profile. If the sample has a high surface roughness it can cause broadening in the profile since the ions are sputtered from a large area (a few hundred μm across) on the sample surface and then averaged. If the sample has a

high dislocation density it can affect the erosion rates, introducing a distortion to the profile. It is shown by Morris *et al* [111], that high depth resolution can be obtained for multiple $Ge/Si_{1-x}Ge_x$ QW structures (similar to those presented in this study), if O_2^+ ions are used with an energy below 500 eV and care is taken to adjust for the changes in erosion rate between layers of different composition.

The high resolution SIMS in this study was performed both by Evans Analytical group and by Dr . Richard Morris using a Atomika – 4500 SIMS Profilometer. The Atomika–4500 is capable of detecting dopant concentrations down to 5×10^{16} cm^{-3}, depending on their species.

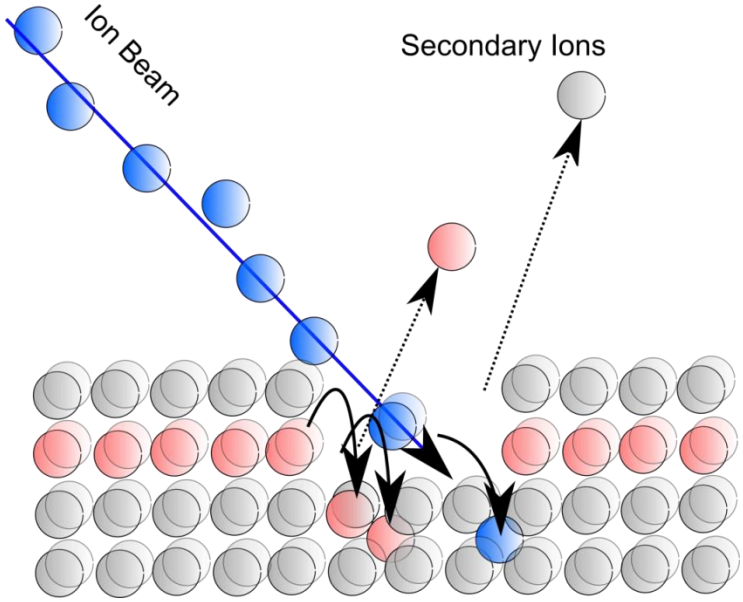

Figure 3-3 - SIMS sputtering process. The primary ion beam sputters secondary ions from the surface. The high energy of the ion beam is causing intermixing.

The use of SIMS to measure dopant/alloy concentration profile through a structure has been described. However, this is only in in one direction. The technique

described in the next section, atom probe tomography, shares the ability of SIMS to measure chemical species, but is able to do so in 3D.

3.4 Atom probe tomography

In atom probe tomography (APT), a time-of-flight mass spectrometer is used in conjunction with a point projection microscope to give atomic scale imaging [112] (figure 3-4). A high voltage (~10 kV) is applied between a needle shaped specimen cooled to cryogenic temperature and a local electrode. Since the sample has an extremely small tip radius <100 nm, a high electric field is created at its point (~10^{10} V/m) [113]. This high electric field causes atoms on the tip to be field evaporated. The tip evaporation is pulsed by modulating the high voltage so that the time of flight between each ion leaving the tip and interacting with the detector can be measured. Since the sharp tip point is projected onto the relatively large (~100 mm diameter) detector, a high magnification of 10^6 is achieved. A computer is used to combine the detected position and time of flight of each ion (from which the element can be found) and the sequence of the evaporation steps (provides depth information). This gives a 3D reconstruction of the sample complete with elemental distributions.

Fabrication of the fine, needle like samples required for APT has traditionally been a difficult task, performed by electropolishing techniques. However, recently sample preparation by focused ion beam (FIB) techniques have been established which extend the range of materials suitable for APT to include electronic device structures [114].

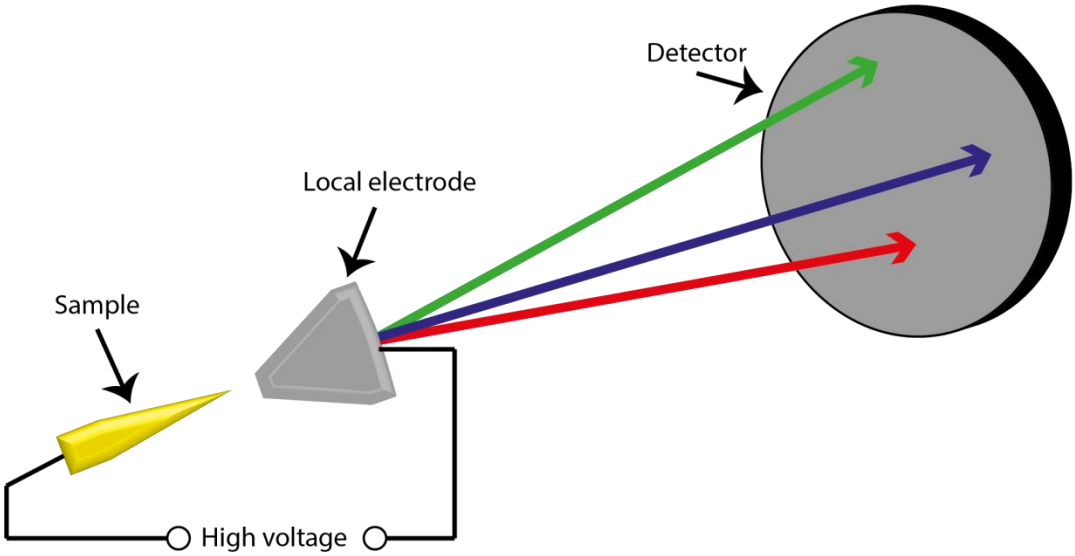

Figure 3-4 - Schematic diagram of three dimensional local electrode atom probe.

Adapted from [113]

Since APT is highly sensitive to chemical species and has 3D spatial resolution, it is an excellent tool for the materials characterisation of semiconductor structures. In the context of the semiconductor superlattice structures studied in this work, APT is well suited to analysis of interface quality, dopant diffusion and alloy distribution. The depth resolution is higher than SIMS, so it is a useful tool for characterising thin layers that SIMS would struggle to resolve. An example atom probe tomograph for a section of a Ge/SiGe superlattice structure with Ge quantum wells and $Si_{0.15}Ge_{0.85}$ barriers is given in figure 3-5. Each dot represents the detection of an atom. It can be seen that the interfaces between the layers are sharp and uniform across the interface.

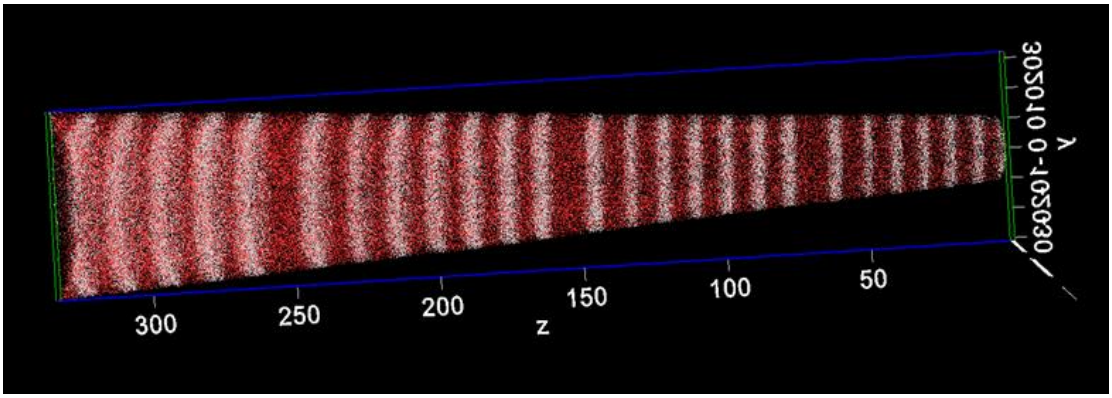

Figure 3-5 – Example APT atom map image of Ge/SiGe superlattice structure showing distribution of Si atoms (red) and Ge atoms (white). Z is the distance through the sample in nm. From APT performed at Tohoku University with credit to Yasuo Shimizu, Masaki Shimodaira, Hisashi Takamizawa, Koji Inoue and Yasuyoshi Nagai.

The use of APT to give a 3D reconstruction of the sample with elemental distributions has been described. While this can be used to give the samples interface quality, dopant diffusion and alloy distribution, it does not give any information on the samples crystal structure. This can obtained using the technique described in the next section, X-ray diffraction.

3.5 X-ray diffraction

High resolution X-ray diffraction (XRD) can be used to find the in- and out- of growth plane lattice parameter with a high degree of precision and find the composition of the layer grown, along with the degree of strain and relaxation. The lyer thickness can also be calculated if thickness fringes are present. All laboratory based X-ray diffraction in this study was carried out using a Panalytical X'Pert PRO Materials Research Diffractometer (MRD), the key components of which are shown in figure 3-6. The diffractometer features a horizontal, high resolution $\omega - 2\Theta$ goniometer, with a radius of 320 mm. The sample is mounted in an open Eulerian

cradle which gives two additional axis of rotation, ($-90^{o} < \psi < 90^{o}$) and ($-460^{o} < \phi < 360^{o}$) which can be seen in figure 3-6. The sample stage can also be moved in the *x*, *y* and *z* axis. The X-rays are generated by a water cooled, ceramic X-ray tube with a Cu anode, operating at 45 kV and 40 mA.

.

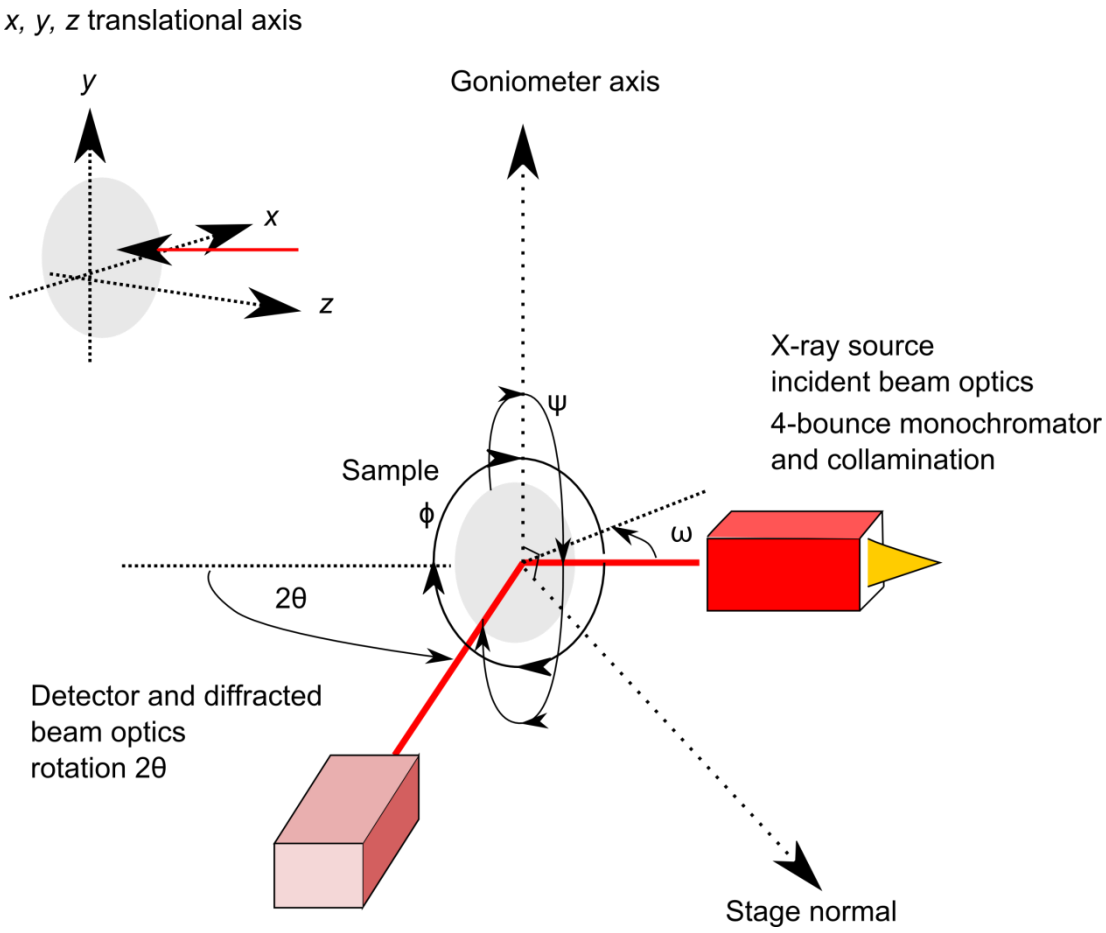

Figure 3-6 - Key components of PANalytical X'Pert diffractometer. The diagram in the top left shows x, y and z translation axis of the sample stage. In the centre the ϕ and ψ axis of the Eulerian cradle and incident and diffracted optics are shown. The path of the X-ray beam is drawn in red.

The incident beam passes through a collimating slit and a germanium Bartells 4-bounce (220) monochromator. An automatic beam attenuator is positioned in front of the monochromator, which when the beam hits the detector with sufficient intensity to damage the detector, moves a nickel window into the beam path to reduce the intensity. Two receiving optics are available, a sealed Xe proportional counter detector with a collimating slit or a sealed Xe proportional counter detector with a germanium crystal positioned in front of it as an analyser crystal. The Ge crystal narrows the angular acceptance of the detector and when combined with the collimator slit, defines a small volume of reciprocal space. This is technique is called triple-axis diffractometry [115]. The relationship between reciprocal space and real space is described in the next section.

3.5.1 Reciprocal space

If the Fourier transform is taken of the crystal lattice, it produces a new lattice where each point, instead of corresponding to an array of atoms, is associated with a particular set of crystal planes. This is known as the reciprocal lattice. The reciprocal lattice axis basis vectors b_i can be expressed in terms of the lattice bases vectors by equations 3-1 - 3-3.

$$b_1 = 2\pi \frac{a_2 \times a_3}{a_1 \cdot (a_2 \times a_3)}, \qquad 3\text{-}1$$

$$b_2 = 2\pi \frac{a_3 \times a_1}{a_2 \cdot (a_3 \times a_1)}, \qquad 3\text{-}2$$

$$b_3 = 2\pi \frac{a_1 \times a_2}{a_3 \cdot (a_1 \times a_2)}. \qquad 3\text{-}3$$

Since the silicon/germanium system has a face centred diamond cubic structure, with a cubic unit cell, the angle between all of the unit cell lattice vectors is $\alpha, \beta, \gamma = 90°$. For two vectors with an angle of 90°, the cross product is 1. If this result is used in equations 3-1 - 3-3 then they can be simplified to the following:

$$b_1 = \frac{2\pi}{a_1}, \qquad 3\text{-}4$$

$$b_2 = \frac{2\pi}{a_2}, \qquad 3\text{-}5$$

$$b_3 = \frac{2\pi}{a_3}. \qquad 3\text{-}6$$

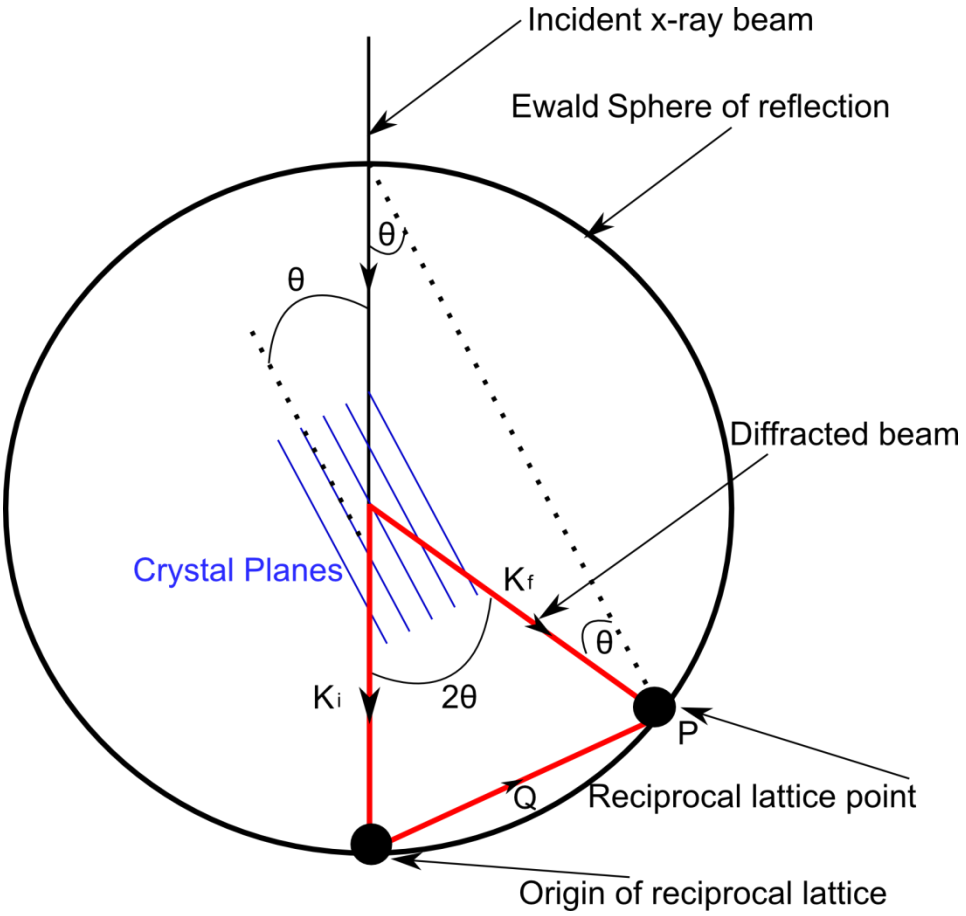

Figure 3-7 - The Ewald Sphere of reflection showing the process of diffraction geometrically.

A geometrical construct, called the Ewald Sphere, is useful in understanding diffraction in reciprocal space, (figure 3-7). The radius of the Ewald sphere is $2\pi/\lambda$. Its circumference passes through the origin of the reciprocal lattice. Incident X-rays enter the sphere along a radius of the sphere. When a reciprocal lattice point lies on the circumference of the sphere, the conditions for Bragg's law are met and diffraction occurs.

For diffraction to occur:

$$K_f - K_i = Q\ , \qquad 3\text{-}7$$

where K_f is the wave vector of the diffracted wave, K_i the wave vector of the incident wave and Q is defined as the scattering vector. This is equivalent to the conditions for Bragg's law being met, as is shown by the following:

From figure 3-7 and its radius, $2\pi/\lambda$:

$$Sin\theta = \left(\frac{|Q|}{2}\right) / \left(\frac{2\pi}{\lambda}\right)\ . \qquad 3\text{-}8$$

From equation 3-4 to equation 3-6, it can be seen that $|Q|$ is related to real space by:

$$|Q| = \frac{2\pi}{d}. \qquad 3\text{-}9$$

When this is substituted into equation 3-8, it results in Bragg's law (equation 3-10).

$$Sin\theta = \frac{\lambda}{2d}. \qquad 3\text{-}10$$

If θ satisfies Braggs law and diffraction occurs, the amplitude of the reflection is expressed by a quantity known as the structure factor which is discussed in the next section.

3.5.2 Structure Factors

The resultant wave scattered by the collective atoms in a unit cell is called the structure factor, $F(Q)$. Knowledge of the structure factor for a particular diffraction

(Bragg peak) from a material is important when working with XRD, since the structure factor determines the scattering intensity from a set of crystal planes.

$F(Q)$ can be found by integrating over the total charge distribution of the unit cell (*UC*). This is given in equation 3-11, where $\rho_e(r)$ is the charge density, Q the scattering vector and r the radius.

$$F(Q) = \int_{UC} \rho_e(r) e^{(-iQr)} dr \, . \qquad 3\text{-}11$$

Equation 3-11 can be approximated by summing over all of the waves scattered by individual atoms in the unit cell [116]. For an isolated atom (*at*), the measure of the scattering amplitude is given by the atomic form factor, f, defined in equation 3-12.

$$f = \int_{at} \rho_e(r) e^{(-iQr)} dr \, . \qquad 3\text{-}12$$

For the collective atoms in a unit cell, since equation 3-12 is the wave scattered by an individual atom, this gives equation 3-13, where *N* is the sum of all the atoms in the unit cell, numbered by *n*, counted from 1 to *N*.

$$F(Q) = \sum_{n=1}^{N} \int_{at} \rho_e(r) e^{(-iQ(r-r_n))} \mathrm{dr} \, . \qquad 3\text{-}13$$

The integration over a single atom's charge distribution is already known from the atomic form factor given in equation 3-12. This can be used to rewrite equation 3-13 as, where f_i is the atomic form of the n^{th} and r_n is the vector for the position of each atom in the unit cell (calculated by $r_n = u_a + v_n b + w_n c$, where u, v and w are the atoms positions, measured in unit cell vectors) giving equation 3-14.

$$F(Q) = \sum_{n=1}^{N} f_n e^{(-iQr_n)} dr \qquad 3\text{-}14$$

The Laue conditions state that:

$$Q \cdot (a + b + c) = (h + k + l). \qquad 3\text{-}15$$

The proof of the Laue equations has been excluded, but is available in reference [116]. When the Laue conditions and the full expression for r_n are substituted into equation 3-14, a final expression for a crystals structure factor is found,

$$F_{hkl} = \sum_{n=1}^{N} f_n e^{(i(hx_n + ky_n + lz_n))} dr \ . \qquad 3\text{-}16$$

The crystal structure of Si and Ge is based on the face centred cubic lattice. The face centred cubic lattice contains atoms located at (0,0,0), $(\frac{1}{2}, 0, \frac{1}{2})$, $(\frac{1}{2}, \frac{1}{2}, 0)$ and $(0, \frac{1}{2}, \frac{1}{2})$. These positions can be substituted into equation 3-16 giving equation 3-17.

$$F_{hkl} = f_n\big(1 + e^{(i(h+l))} + e^{(i(h+k))} + e^{(i(h+l))}\big)\begin{cases} 3f, all\ hkl\ even\ or\ odd \\ 0, n\ mixed \end{cases}. \qquad 3\text{-}17$$

If equation 3-17 is to give a non-zero structure factor, then h, k, l must either all be even or all odd. This is the first condition for the visibility of a Bragg peak in Si or Ge.

There are also atoms attached to the basis of the lattice points at (0,0,0), $(\frac{1}{4},\frac{1}{4},\frac{1}{4})$ in the unit cells of Si and Ge. If these positions are substituted into equation 3-16 it gives equation 3-18.

$$F_{hkl} = f_n\left(1 + e^{\left(\frac{1}{2}i(h+k+l)\right)}\right) = \begin{cases} 2f, & h+k+l = 2n \\ 0, & 0\ otherwise \end{cases}. \qquad 3\text{-}18$$

If equation 3-18 is to give a non-zero structure factor then $h + k + l$ must not be an odd multiple of two. This is the second condition for the visibility of a Bragg peak in Si or Ge. In table 3 the exact structure factors are given. The square of the structure factor gives the intensity of the diffracted Bragg peak. For XRD from silicon and germanium, to yield structural information, the Bragg peaks from the symmetric (004) (figure 3-11) and asymmetric (224) (figure 3-12) planes are most commonly used, with both giving a large scattered intensity when compared with other peaks (table 3). In the next section, a method of recording X-ray scans around the symmetric [0 0 4] Bragg peaks of silicon and germanium is discussed.

Reflection	**$\lvert F_{hkl} \rvert$ V in electron units per Å^3 for one crystal of silicon [115]**
001	0
002	0
004	0.39
111	0.38
222	0
333	0.24
011	0
022	0.45
044	0.31
112	0
224	0.35
113	0.30
115	0.24

Table 3 –Values of $\lvert F_{hkl} \rvert$ V in electron volts for silicon for a number of useful reflections.

3.5.3 X-ray ω-2θ scans

For measurement of an ω-2θ scan, ω is fixed relative to 2Θ and scanned around a Bragg peak in a fixed ratio of 1:2. All the ω-2θ scans in this study have been recorded around the symmetric [0 0 4] Bragg peaks. As can be seen from figure 3-11, the Bragg peak from the (004) planes only carries information about the out of plane

lattice parameter, a_z. Since the out of plane lattice parameter, a_z is determined by layer strain and composition, (004) ω-2θ scans are unable to give independent measures of strain and composition. However, they are useful since they require far less time to obtain than a full (004) and (224) reciprocal space map (discussed in section 3.5.4).

The X-ray ω-2θ scans featured in this study can be divided into those performed on two different kinds of heterostructure, strained/partially relaxed $Si_{0.4}Ge_{0.6}$ on Si (001) and Ge/$Si_{0.15}Ge_{0.85}$ superlattices with reverse graded virtual substrates on Si (001). Since the $Si_{0.4}Ge_{0.6}$ on Si (001) ω-2θ scans are easiest to interpret, in figure 3-8 one is given as an example for a fully strained 21 nm layer of $Si_{0.4}Ge_{0.6.}$ To the right of the ω-2θ scan is the narrow, intense Si (004) peak from the substrate. The position of this peak is used as a reference for all scans. To the left of the ω-2θ scan the $Si_{0.4}Ge_{0.6}$ layer peak is seen. The position of this peak is determined by the strain in the layer and its composition. If the Ge content in the layer is increased, a_z will increase and the layer peak will move to the left. If the Si content in the layer is increased, a_z will decrease and the layer peak will move to the right. To either side of the $Si_{0.4}Ge_{0.6}$ peak and interference fringes are visible. These are called thickness fringes and can be used to measure the thickness of the layer using equation 3-20 [117] (only for a symmetrical ω-2θ scan), where t is the layer thickness, λ.the wavelength, θ_B the Bragg angle and $\Delta\theta_p$ the fringe separation.

$$t = \frac{\lambda}{2\Delta\theta_p cos\theta_B}. \qquad 3\text{-}19$$

The presence of thickness fringes indicates that the layer is of high quality for SiGe on Si. In this case, the ω-2θ scan can be used to find layer composition since the layer will share the same in-plane lattice parameter as the Si substrate as it has not undergone strain relaxation.

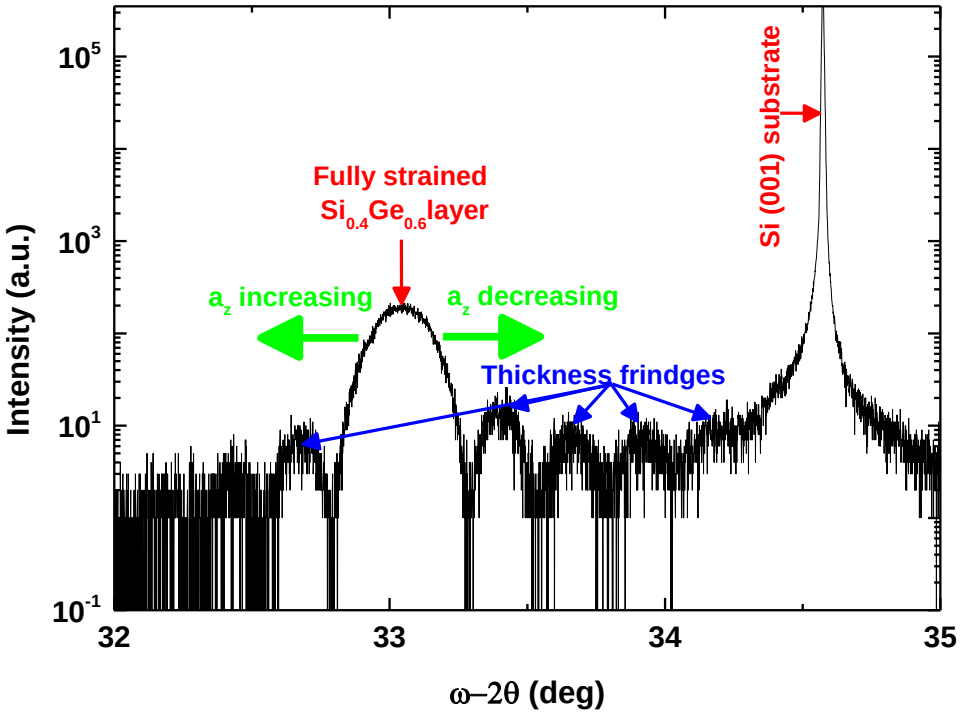

Figure 3-8 - Example ω-2θ scans around the symmetric (004) Bragg peak for a 21 nm $Si_{0.4}Ge_{0.6}$ layer. Distinct thickness fringes can be seen.

For all X-ray ω-2θ scans in this study, the simulation function was used in the PANalytical X'Pert Epitaxy software package. The simulation function is based on the Takagi-Taupin equations of dynamical X-ray scattering [188-190]. To extract information from the ω-2θ scans a fitting algorithm known as Smoothfit, first described by Klappe and Fewster for ion implanted samples was used [191]. This fitting algorithm works by first smoothing the measured and simulated scans then matching major peaks. Initially fitting is performed on heavily smoothed data, this

highlights only the major peaks allowing parameters describing these peaks to be fitted. With subsequent iterations of fitting the measured and simulated scans are progressively smoothed less, so that finer details can be fitted. The simulated data is compared to the measured data using the least squares method. For every data point in the simulation, the difference between the log intensity of the simulation and the log intensity of the measured scan is squared. A fit value is then calculated by dividing the sum of the squared values by the number of data points in the simulated scan. The Smoothfit algorithm finds the parameter that gives the largest change in fit value and adjusts it until no further improvement in fit value is seen. This process is then repeated for subsequent next most significant parameter. The process continues until no change in any of the fitting parameters gives an improved fit value. So that the algorithm can converge on realistic values, constraints must be applied to the parameters.

As previously mentioned, (004) ω-2θ scans are unable to give independent measures of strain and composition. However, this can be achieved by (004) and (224) reciprocal space mapping which is discussed in the next section.

3.5.4 Reciprocal Space Maps (RSMs)

When the diffractometer is in the triple-axis configuration (described in section 3.5), it defines a small volume of reciprocal space. This enables the mapping out of reciprocal space, including the scatter surrounding a reciprocal lattice point. Reciprocal space maps are measured by the diffractometer by collecting a series of ω-2θ scans over a range of ω.

In figure 3-9, the directions moved in reciprocal space by the θ and ω diffractometer axis can be seen. If the incident beam is rotated through 180^{o} from parallel to the sample surface in one direction to parallel in the other direction, a range of reciprocal space can be probed. This area is given by the large white semicircle in figure 3-9. The small semicircle on the left is forbidden in reflection due to the incident beam entering below the surface of the sample. The small semicircle on the right is forbidden in reflection due to the diffracted beam exiting below the surface of the sample. The dotted arrow is for when $\omega \neq 2\theta/2$.

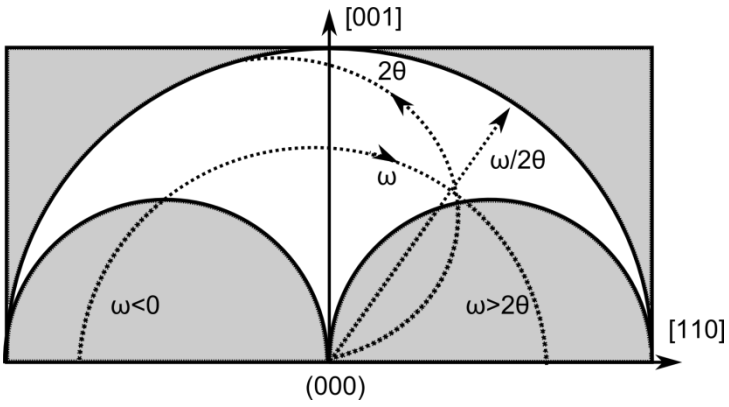

Figure 3-9 Schematic diagram showing directions moved in reciprocal space by θ and ω diffractometer axis. Adapted from Bowen [115]

In figure 3-10, the reciprocal lattice points accessible by the lab based diffractometer are given for Si and Ge. It can be seen that the Ge peaks (pink) are closer to the origin of reciprocal space due to Ge having a larger lattice parameter.

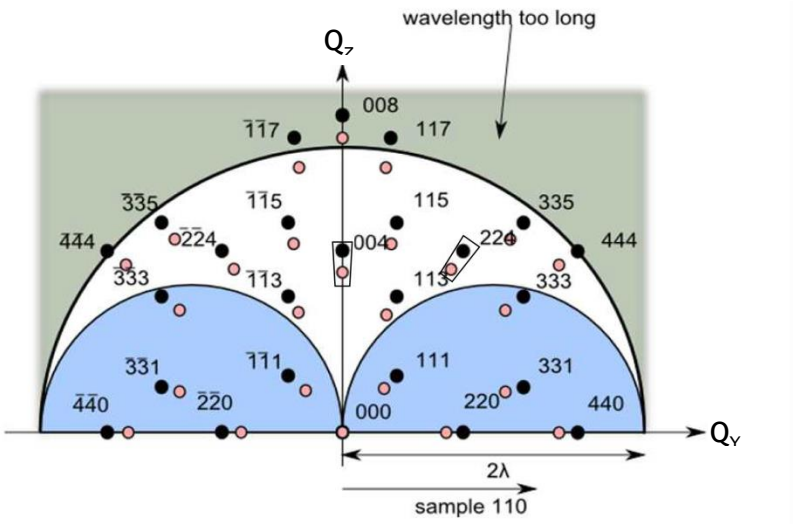

Figure 3-10 – Accessible reciprocal lattice points for Si (black) and Ge (Pink). The Miller indices refer to the adjacent Si peaks, with their Ge counterparts displaced towards the origin. Adapted from [115].

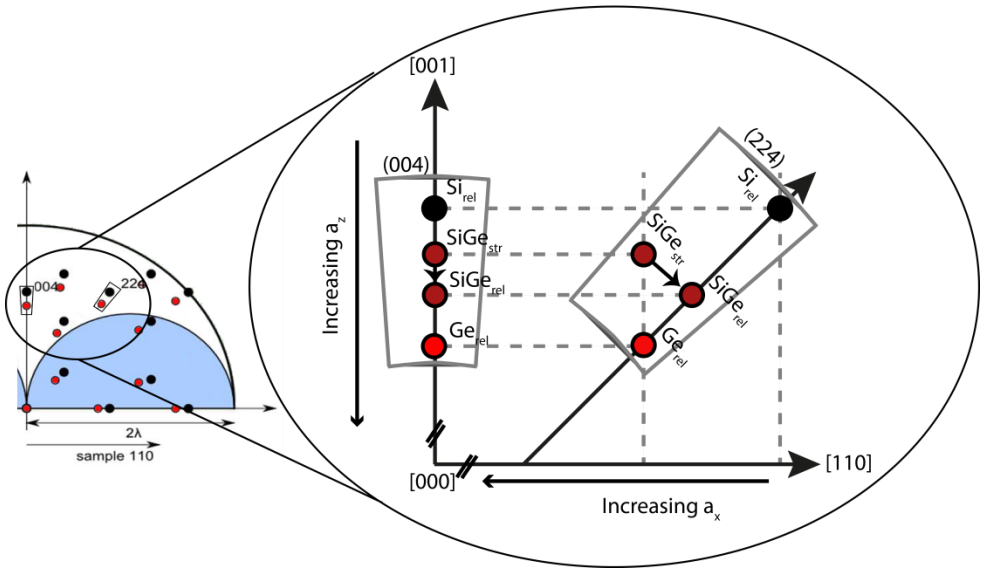

Figure 3-11 - Schematic diagram of (004) and (22) RSMs for Si, Ge and a generic SiGe alloy. Adapted from [115] and [119]

Figure 3-11 is given to aid RSM interpretation for the SiGe system. Bragg peak positions are illustrated in the (004) and (224) RMS for a relaxed Si substrate (Si_{rel}), a relaxed Ge layer (Ge_{rel}), a generic layer of SiGe which is strained to the Ge layer ($SiGe_{str}$) and a SiGe layer with the same alloy composition as the first which is fully

relaxed. If the Si composition of the SiGe layer is increased (decreasing the layers lattice parameter), the Bragg peak associated with the SiGe layer will move along the black arrows towards the Si substrate peak. If the Ge composition of the SiGe layer is increased (increasing the layers lattice parameter), the SiGe peak will move along the black arrows towards the Ge peak.

It can be seen when the SiGe layer is strained to the Ge layer, ($SiGe_{str}$), its Bragg peak is shifted horizontally in reciprocal space, lying directly above the Ge peak in the (224) RSM. This indicates that it has the same in-plane, a_x and a_y, lattice parameters. The strained SiGe peak is also shifted vertically in reciprocal space, which is due to tetragonal distortion of the lattice.

The Bragg peak from the (004) (figure 3-12) planes carry information about the out of plane lattice parameter and the (224) (figure 3-13) set of planes carries information about both the in-plane, a_x and a_y, and out-of-plane lattice parameters a_z, composition and strain can be determined independently using (004) and (224) reciprocal space mapping. A comprehensive guide to lattice calculation can be found in Capewell [118]. Layer tilt can also be determined using (004) and (224) reciprocal space mapping and is the angle between the normal to the layer surface and the normal to the substrate surface.

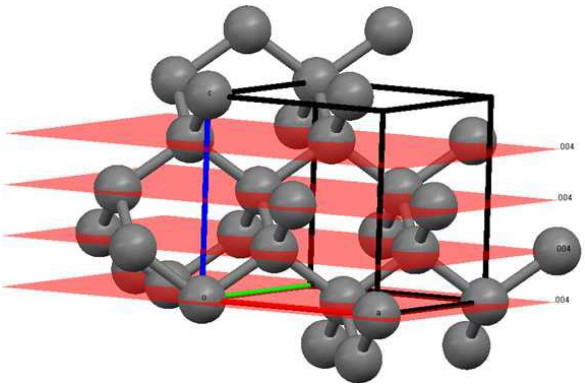

Figure 3-12 - (004) crystal planes (red) overlaid on silicon/germanium structure. The distance between (004) planes is determined by the out of plane lattice parameter a_z

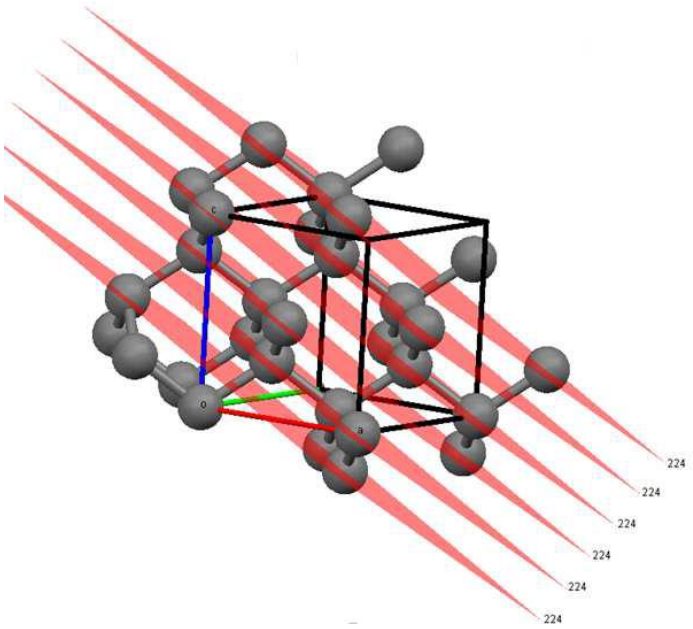

Figure 3-13 - (224) crystal planes (red) overlaid on silicon/germanium structure. The distance between (224) planes is determined by the out of plane lattice parameter a_z and the in plane lattice parameters a_z and a_z.

The X-ray diffraction technique described so far has been laboratory based. Laboratory diffractometers use X-ray tubes as the X-ray source and this limits them in both intensity and wavelength. The low intensity makes diffraction with a small

X-ray spot size difficult using laboratory diffractometers, since the intensity becomes too low for practical applications after focusing. Far higher X-ray intensity's can be obtained using synchrotrons and so much smaller spot sizes can be obtained. In the next section a technique for sample characterisation using microfocus HR-XRD at a synchrotron is given.

3.6 Microfocus X-ray diffraction on suspended structures

The following section describes the technique used for strain mapping by microfocus HR-XRD of Ge membranes using Beamline B16 at the Diamond Light Source.

The X-ray beam size for a typical lab based source is on the order of several hundreds of microns in diameter. This means that lab based HR-XRD is insensitive to localized, real-space changes in crystal properties. Fortunately, in the last decade there has been considerable progress in the focusing of X-rays, leading to X-ray spot sizes smaller than 100 nm [120]. The small X-ray beam can be used as a local probe by scanning the beam over the sample, similar to various scanning microscopy techniques. This has opened up a wide range of possibilities for both micro- and nano-diffraction on different materials. The strain and composition of single micron sized SiGe islands has been determined [121-122], the degree of strain relief in single patterned SiGe nanostructures[123], silicon-on-insulator deformation induced by stressed linear structures [124] and the strain fields in a single SiGe island which is acting as the stressor for a Si channel for a functioning Si metal oxide semiconductor field-effect transistor [125]. X-ray micro-diffraction has also been performed on a suspended Ge bridge [126], but unlike this work, the sample was one dimensional and so has uniaxial strain, it was also thick ($\sim 2\mu m$) and cracked.

3.6.1 Experimental technique

The 3 GeV Diamond Light Source (DLS) is a third generation synchrotron light source facility based at Harwell in the UK. Beamline B16 (figure 3-14) is a test beamline at DLS set up on a bending magnet source. B16 works over a 2 – 25 keV energy range with an acceptance of 3 mrad (h) x 0.5 mrad (v) [127]. For this study, X-rays with an energy of 12.4 keV (λ = 1 Å) were used. A schematic diagram of the beamline is given in Figure 3-14. The main beamline optics are comprised of a double crystal monochromator, a toroidal mirror, a double multilayer monochromator and a set of Be compound refractive lenses CRLs [127], which are used for micro-focusing of the X-ray beam. Beam sizes of 1-5 μm are achievable with focal lengths adjustable from a few 100 mm to several meters.

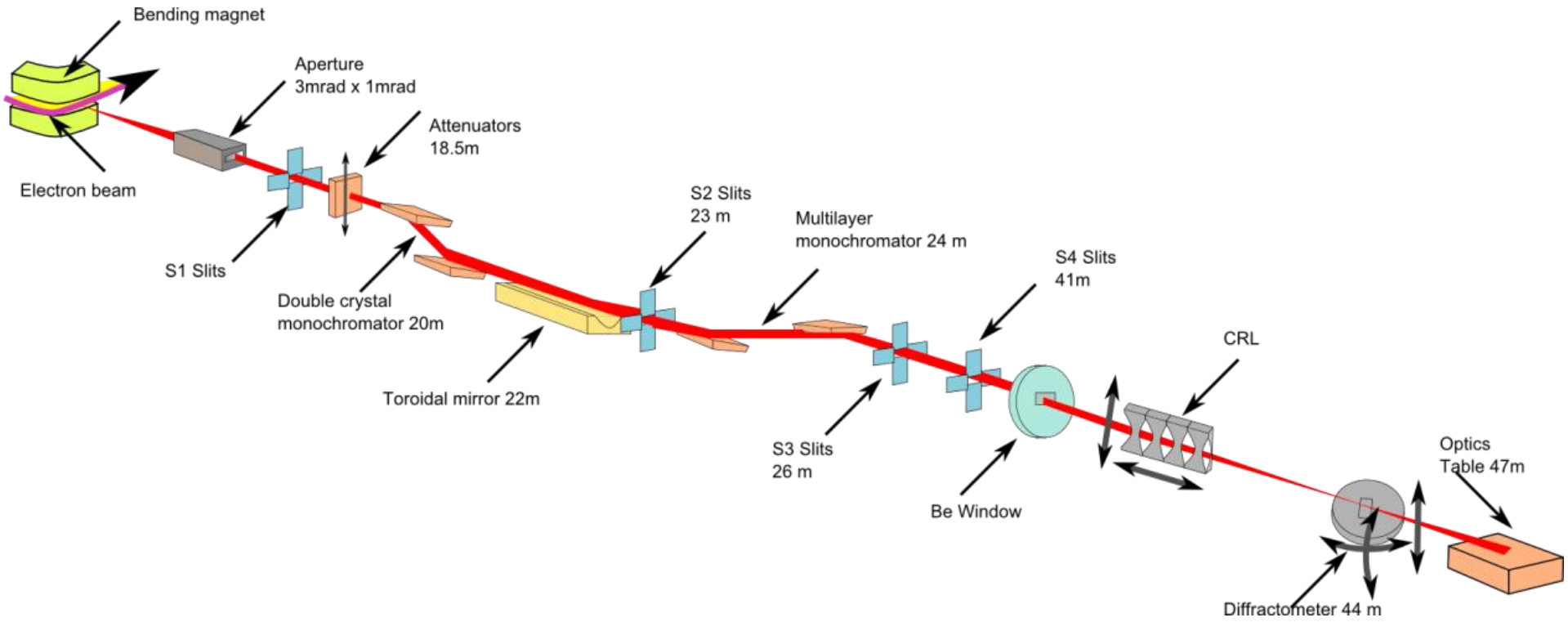

Figure 3-14 - Schematic for Beamline 16 at Diamond Light Source. Adapted from [128].

3.6.1.1 Micro-focus and CRLs

Focusing X-rays using refractive lenses had long been dismissed as unfeasible. Refractive lenses for visible light are viable because they have an index of refraction significantly larger than 1 and only weak absorption. However for X-rays, refraction in condensed matter is weak and absorption is very strong, giving an unfeasibly long focal length for a standard lens. This refractive focusing problem was solved by Snigirev *et al* with the development of compound refractive lenses (CRLs) [129].

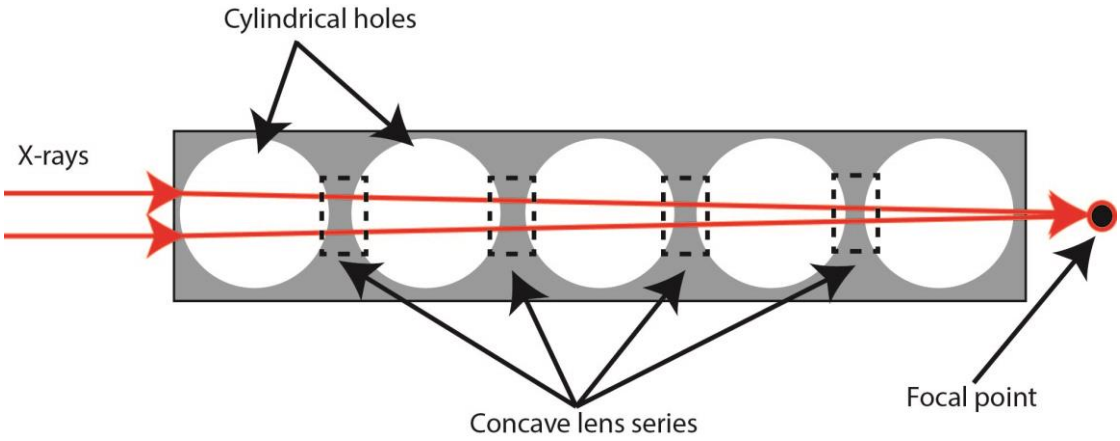

Figure 3-15 - Schematic diagram of CRLs manufactured by drilling in an aluminium block demonstrated in [129]

CRLs are a series of individual concave lenses in a linear array (figure 3-15). Concave lenses are used as opposed to convex ones since for X-rays, the index of refraction is slightly smaller than 1inside the material. CRLs do reduce the beam intensity, but it is still sufficient for most applications. Elements with a low X-ray attenuation coefficient such as Be are generally used for CRLs to minimise the loss in intensity.

At B16, CRLs were used to provide a micro-focused beam with a spot size of 3.72 μm x 1.85 μm (horizontal x vertical). Since the beam does not hit the sample parallel to the surface normal, its footprint is approximately circular with a diameter of ~4 μm for the (004) reflection of Si. The use of CRLs for microfocus at Beamline 16 at Diamond Light Source has been reported on in a number of studies [130-131] using a 1 Å wavelength.

3.6.1.2 Sample mounting and cooling

Membranes were attached to aluminium SEM stubs using sticky, conducting rubber pads. The SEM stub is mounted on a stage with *XYZ* translation having a precision of 0.5 μm (figure 3-16). Since the X-ray flux hitting the sample may cause some local heating, resulting in sample damage or sample distortion caused by strain from thermal expansion, an Oxford Cryosystems Cryostream Plus sample cooler is mounted above the sample. The sample cooler uses a low flow liquid nitrogen jet to maintain the sample temperature at 20 ^{o}C.

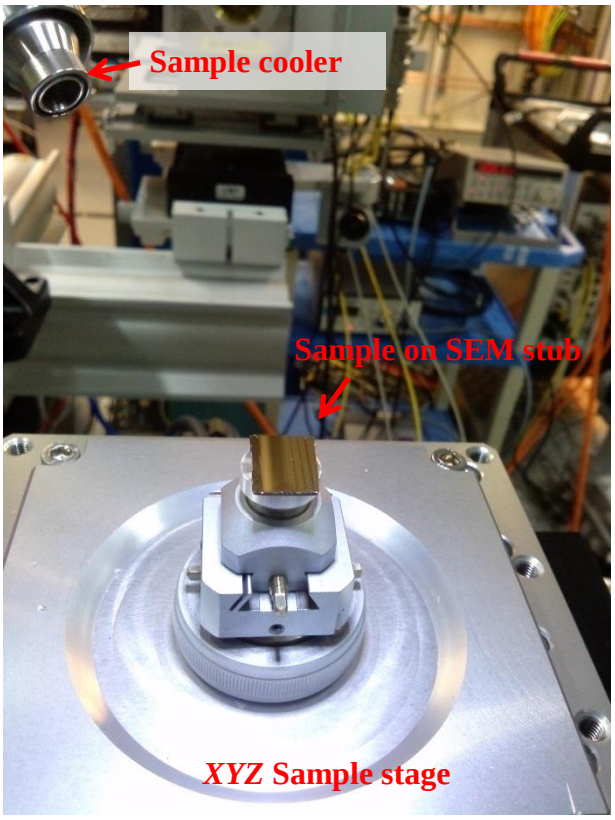

Figure 3-16 - Image of sample mounted on SEM stub on *XYZ* stage with cryocooling

The *XYZ* sample stage is mounted on a 5-circle Huber diffractometer (figure 3-17, 3-18). The detector arm of the diffractomter has a helium filled tube with a Kapton foil window at both ends, travelling the length of the arm from near the sample to the detector. This is to reduce signal loss from X-ray scattering in air. A Pilatus 300K area detector is used, with an array of 487 x 619 pixels, each having a size of 172×172μm² [132]. The Pilatus detector has silicon pixel detectors, in which X-rays are converted to an electrical signal by the photoelectric effect when a bias voltae is applied. Each pixel on the detector has its own electronics for counting X-ray events. CCD area detectors are also available at beamline B16, but the Pilatus detector offers the following advantages: The area of Pilatus dectector is relatively large, which means that the detector did not need to be moved during scans and so reduces the

time taken to aquire RSMs. The Pilatus detector is energy discriminating, with an adjustable energy threshold value for events to exceed before they are detected, effectively giving a zero noise measurement.

3.6.1.3 (0 0 4) reciprocal space mapping using micro-focus diffraction

The sample is first moved up in the *Z* direction, to its half cut position (*Z* position where the sample cuts the X-ray beam intensity in half), then rocked in the ω-circle to give the position at which it is parallel to the X-ray beam. Since the half cut position changes with ω if the sample is not completely parralel to the beam, *Z* and ω are changed through a number of iterations, until the sample is both in the half cut position and completely parallel to the beam.

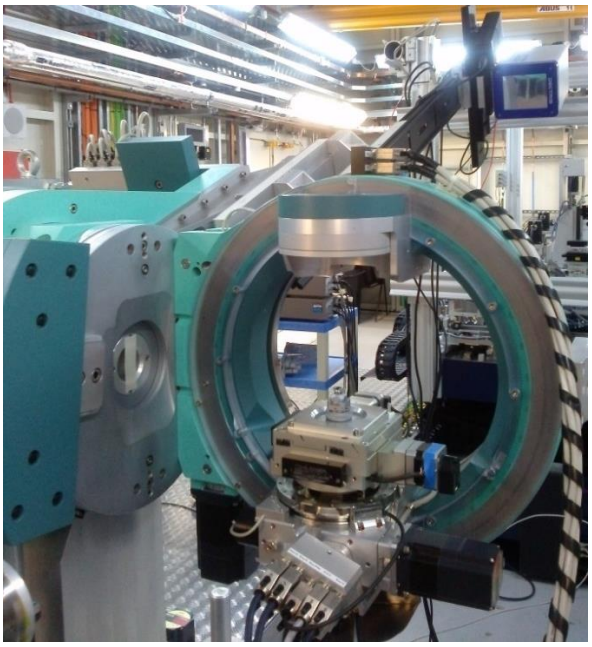

Figure 3-17 - Sample mounted on 5-circle Huber difractomter with Pilatus 300 K area detector.

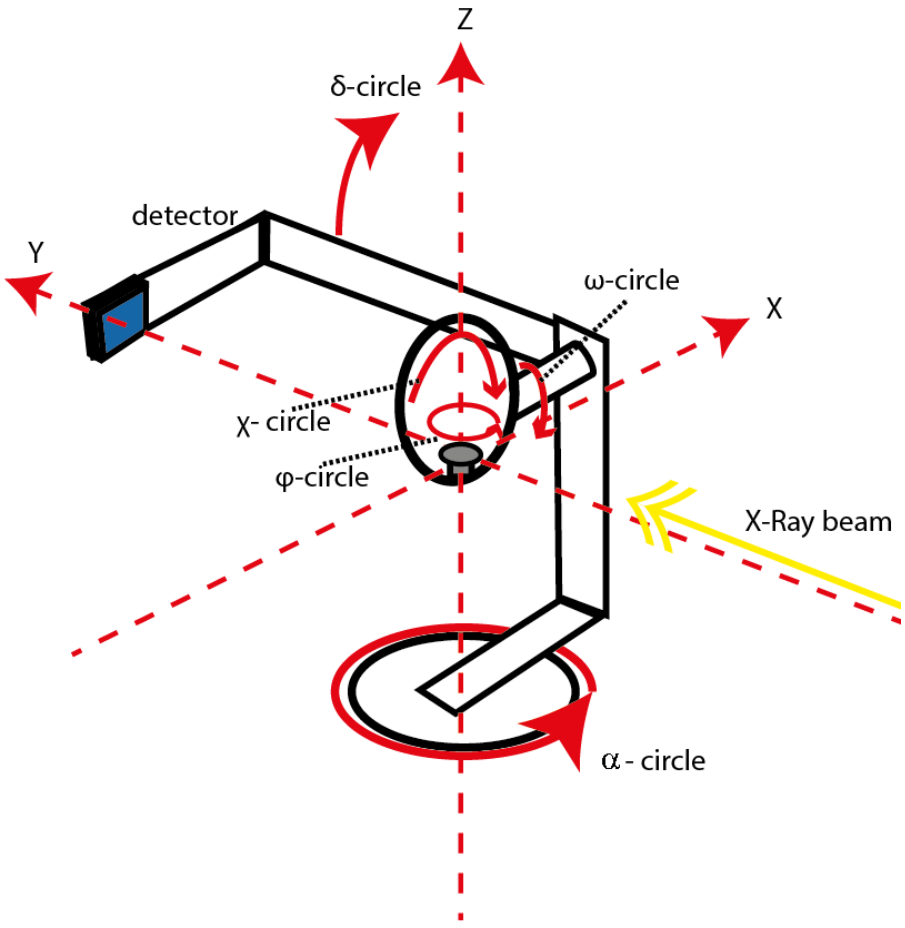

Figure 3-18 - Schematic of 5-circle diffractometer

The *X* and *Y* position is adjusted so that the X-ray beam hits the sample on the bulk material surrounding the membrane. The Si (0 0 4) peak is then found by adjusting ω and δ. The membrane edge and both incident and scattered X-rays all lie parallel to [110] crystal plane (figure 3-19).

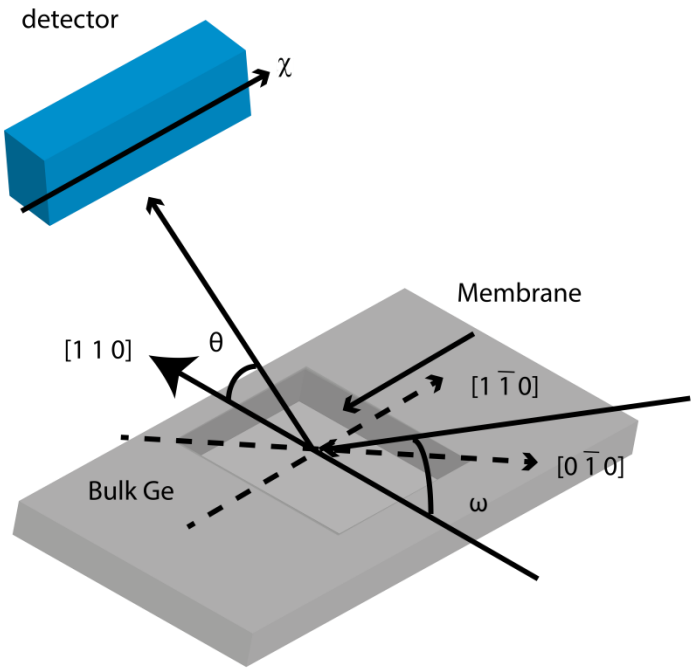

Figure 3-19 - Suspended Ge membrane with (004) scattering geometry. The edges of the membrane are aligned parallel to the <110> directions. RSMs at each point are obtained by scanning along the $[1\bar{1}0]$ and $[0\bar{1}0]$ directions.

To locate the membrane, *X* and *Y* are rastered around the expected membrane postion until the Si (0 0 4) peak disappeares. An example (0 0 4) RSM taken from the bulk material at the edge of a suspended membrane structure is given in figure 3-20. A sufficiently wide scan range was used to capture both Si and Ge (0 0 4) peaks. The Si substrate peak is fixed at $q_{\parallel} = 0 \pm 0.00003$ Å^{-1} and $q_{\perp} = 0.7365 \pm 0.00003$ Å^{-1} and is used as a reference throughout.

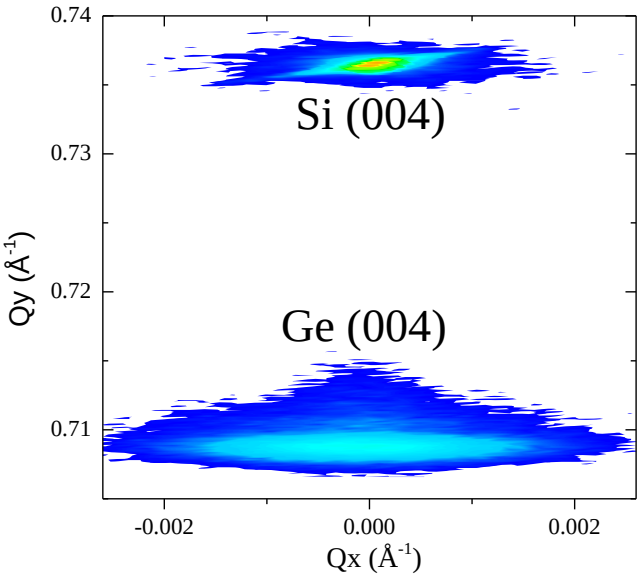

Figure 3-20 - (0 0 4) Reciprocal space map taken from bulk Ge on Si(001)

To characterise the strain along the membrane, the diffractometer is then aligned to the Ge (004) Bragg peak from the supported Ge on the frame surrounding the membrane. The detector position is adjusted so that its central scattering angle is halfway between that of the Si substrate and Ge peaks. RSMs are then measured by rotating the sample on the ω-circle around the (0 0 4) reflection.

3.6.2 Analysis of Results

For a given time interval, the Pilatus 300K detector counts incident X-ray events for each pixel. The pixels are recorded to a tagged image file format (TIFF) image, where the position corresponds to the physical pixel position on the detector and the intensity corresponds to the events counted. An example of an unprocessed TIFF

image is given in figure 3-21, where 2θ is in the vertical axis and χ in the horizontal axis.

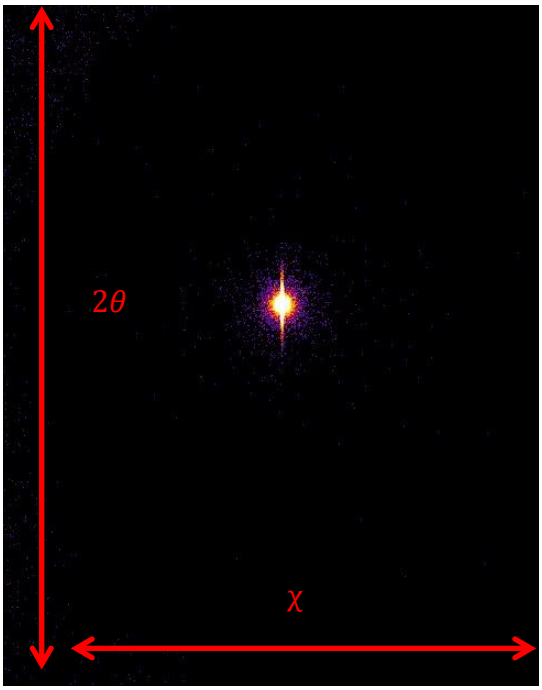

Figure 3-21 - Unprocessed tiff image from Pilatus detector showing (004) peak from a Ge membrane. The vertical axis is in the 2θ direction and the horizontal axis in the χ direction.

For speed and ease of processing, line profiles are taken from the TIFF image. To extract the peaks position in 2θ, each horizontal row of pixels are summed, giving a line profile. Example line profiles through reciprocal space taken from a single TIFF image when the detector was aligned on a (004) peak from a Ge membrane are given in figure 3-22 and figure 3-23.

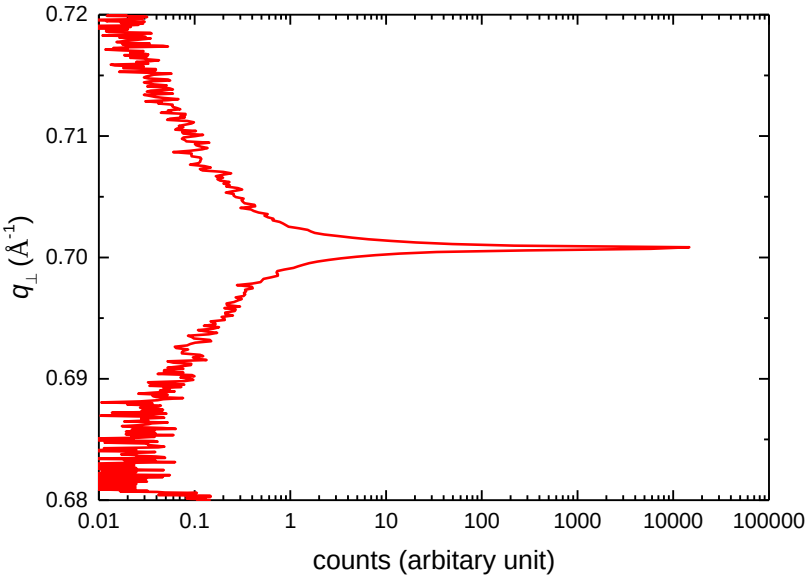

Figure 3-22 - $q_\perp$ line profile extracted from single Pilatus TIFF image with the detector aligned on a (004) peak from a Ge membrane

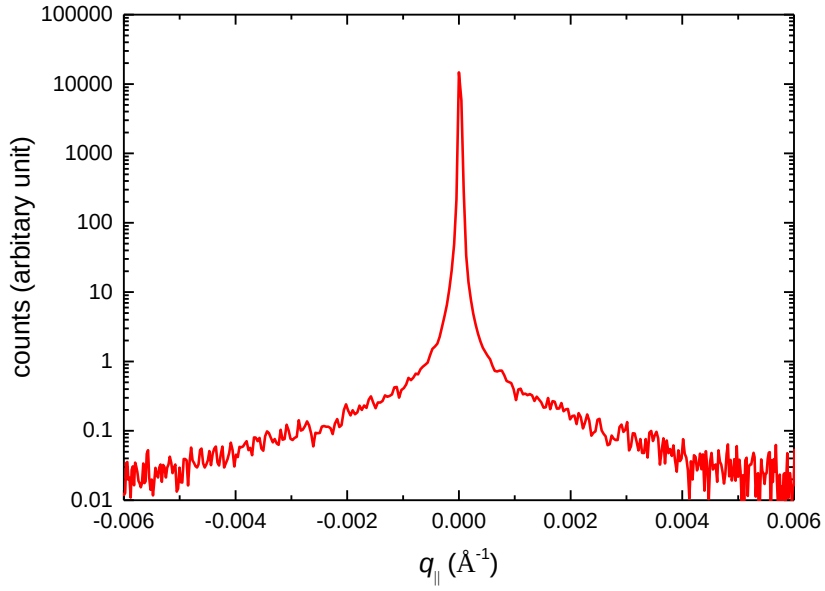

Figure 3-23 - $q_\parallel$ line profile extracted from single Pilatus TIFF image with the detector aligned on a (004) peak from a Ge membrane

The vertical pixel values from the detector need to be converted to 2θ values. Simple trigonometry gives equation 3-20, where δ is the angle from the diffractometer, p_i the detector pixel, p_c the central detector pixel (found from the direct beam condition), w the width of the detector, N the total number of pixels (619 for the 2θ direction) and L the distance between the sample and detector.

$$2\theta = \delta + \text{atan}\left(\frac{(p_i - p_c)w}{NL}\right). \qquad 3\text{-}20$$

Equations 3-21 and 3-22 [133] were then used to convert from real to reciprocal space, where λ = 1 Å and $\theta = 2\theta/2$.

$$q_\perp = \frac{4\pi}{\lambda} sin\theta cos(\omega - \theta), \qquad 3\text{-}21$$

$$q_\parallel = \frac{4\pi}{\lambda} sin\theta sin(\omega - \theta). \qquad 3\text{-}22$$

Matlab scripts are used to automate the conversion process for all scans. When the data is converted to reciprocal space, the scans are summed in the $q_\perp$ and $q_\parallel$ directions and Bragg peaks fitted with Gaussian profiles to obtain their position in $q_\perp$ and $q_\parallel$ and FWHM. An example fit is given in figure 3-24, where a Gaussian profile is fitted to a (004) Si Bragg peak in $q_\parallel$. It can be seen that the Gaussian profile gives a good fit to the peak, but does deviate slightly on the shoulders of the peaks.

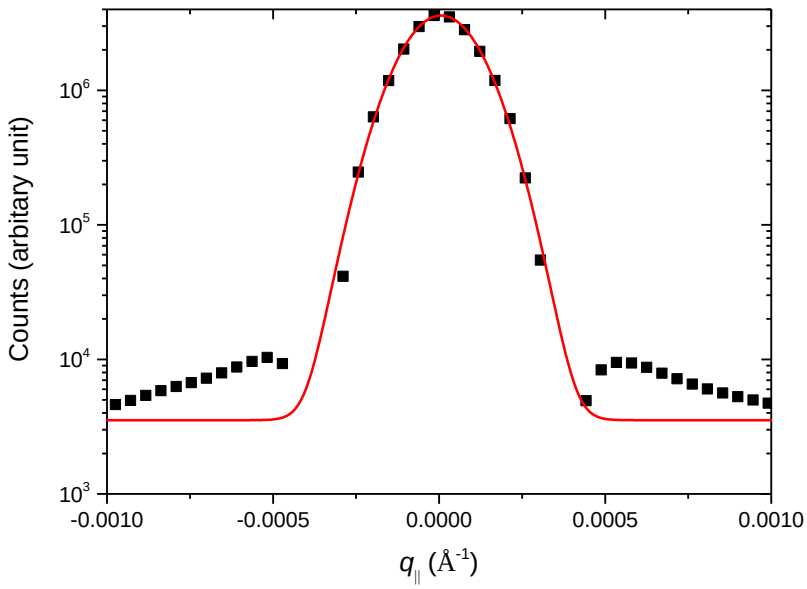

Figure 3-24- (004) Si peak in $q_{\parallel}$ (black squares) fitted with Gaussian profile (red line).

A technique for strain mapping by microfocus HR-XRD of Ge membranes using Beamline B16 at the Diamond lightsource has been presented. While synchrotron based microbeam X-ray diffraction allows a smaller sample volume to be probed than standard laboratory based X-ray diffraction, structural information is still given from a relatively large volume. Electron microscopy is able to probe a much smaller volume than both X-ray techniques and resolve some of the samples smallest features.

3.7 Transmission Electron Microscopy

In order to study small sample volumes TEM was used. The vast majority of the TEM microscopy presented in this work was performed on a JEOL 2000FX microscope operating at an accelerating voltage of 200 kV. This microscope uses a

W/LaB6 filament as the electron source and has a GATAN ORIUS 11 megapixel digital camera to record images.

3.7.1 Sample preparation

Fabricating a thin, high quality sample is essential for analysis by TEM. For a sample to be imaged by TEM, it must be sufficiently thin so that it is electron transparent, on the order of a few hundred nanometers for Si. The stages in the sample preparation process used for all TEM specimens in this work are illustrated in figure 3-25.

The wafer for analysis is first cleaved into two identical ~5x10 mm sections using a diamond scribe along the [1 0 0] direction. The pieces are glued with the growth surface face to face using two part Araldite adhesive. Similarly sized pieces of scrap Si wafer are glued to either end as supports, forming a 'sandwich structure (figure 3-25 (a, b)). The sandwich structure is held in a steel clamp which applies pressure at either side while the glue is cured at ~180^{o}C for several hours on a hot plate. To minimise the time the sample must be thinned for, a thin slice is taken of the structure using a Southbay Technology diamond saw figure 3-25 (c).

The slice is transferred to a metal block so that it can be held while it is ground. The slice is held in place on the block with melted wax, this allows the sample to be easily removed when the grinding is completed. A 8" grinding wheel at ~150 rpm is then used to grind then polish the sample to a mirror like finish with silicon carbide grinding paper (P120 grit grade to P4000). The sample is then removed from the metal block by heating the wax and attached to a glass microscopy slide with wax, polished side facing down. The sample is again ground and polished, but this time

with the intention of thinning to ~20 - 40 μm. This is very labour intensive and many samples are lost at this stage.

A copper microscopy support ring with a 1 mm by 2 mm slit is glued to the sample lamina using Araldite Rapid. The slot of the ring is glued perpendicular to the sample interface. When the Araldite has cured, a scalpel is used to scrape away the lamina not covered by the copper ring and the ring and attached lamina is freed from the glass slide by heating the wax. The sample is then cleaned in acetone [$(CH_3)_2CO$] to remove any remaining wax.

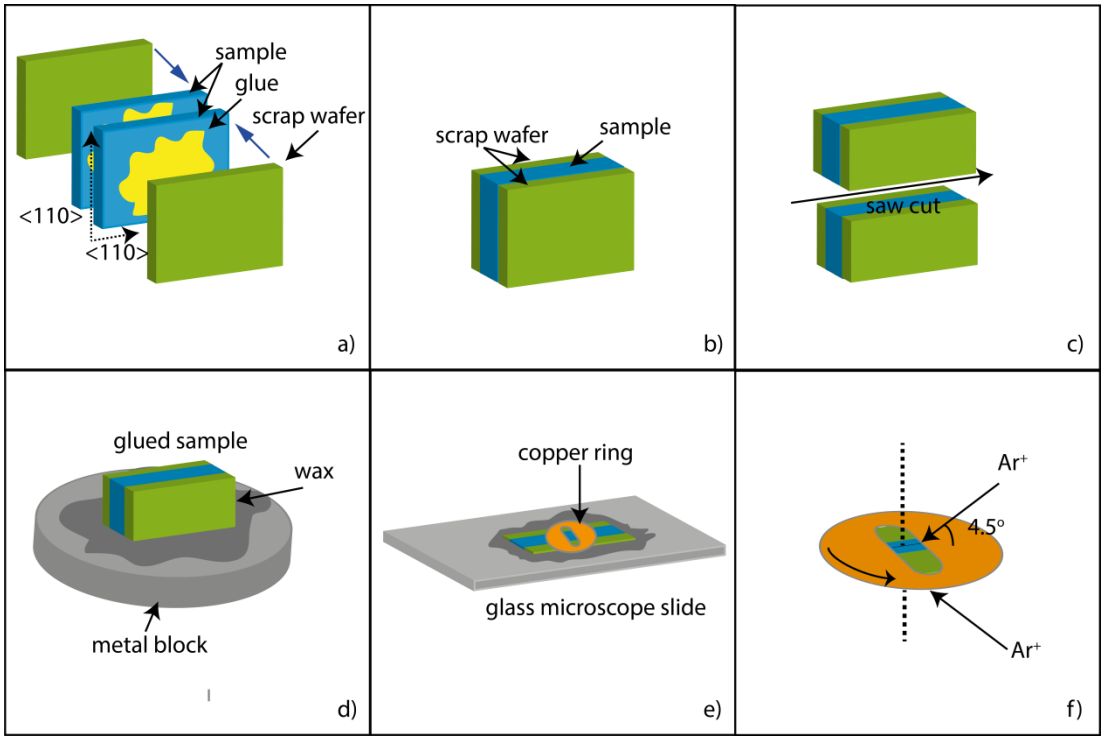

Figure 3-25 - Schematic diagrams of the stages in sample preparation for TEM. (a) Initial gluing of 'sandwich' surfaces together (b) completed 'sandwich' structure (c) diamond saw cut (d) section of sample bonded to metal block for grinding (e) ground and polished sample with copper support ring glued to surface (f) Ion beaming process

Finally the sample is thinned to electron transparency by ion milling and polishing using a Gatan 691 Precision Ion Polisher (PIPS), figure 3-25 (f). This uses two beams of argon ions accelerated with 4.5 kV potential (higher voltages can be used to speed the milling process but can damage the sample) to slowly erode the surface. The sample is continually rotated to mill the sample uniformly and the ion guns are modulated to only mill the sample perpendicular to the epilayers to avoid damaging the samples surfaces. The ion guns are set at angles of 4.5º on the copper ring side. When the sample has been perforated, it is given a final polish at a lower acceleration voltage of 2.5 kV to gently polish it. An image of a prepared sample is given in figure 3-26. The perforation can be seen at the epilayer interface and a red/yellow tinge can be observed on the left of the sample, this is due to the Si becoming translucent due to the thinness of the lamina. Looking for the red tinge is a good indicator that the sample is suitable for TEM

Figure 3-26 – Ground, polished and ion milled sample with copper support ring glued to surface

3.7.2 Imaging

A simplified schematic diagram of a transmission electron microscope is given in figure 3-27. At the top of the TEM column an electron gun is situated. This is comprised of a tungsten wire which is heated by a dc current to approximately 2700 K [134] and emits electrons into the vacuum by thermionic emission. After emission, electrons are accelerated by an electric field which is parallel to the optical axis and collimated through a hole in a metal plate.

The electrons then pass into the condenser lens system which controls the electron beam which is incident on the sample. There are generally two lenses present in a condenser lens system, the first de-magnifies the electron source and sets the spot size for the system and the second, when combined with the condenser aperture sets the angle at which the electron beam converges at the sample and the diameter of the illumination at the sample. There is also a stigmator present in the condenser lens system to correct for residual astigmatism of the C1 and C2 lenses.

Following the condenser lens system there is the sample stage. This is designed so that the sample can be introduced into the TEM column without losing vacuum by means of an airlock and so that the sample can be tilted.

The component parts below the sample stage in the TEM column are collectively known as the TEM imaging system. The role of the imaging system is to produce either a magnified image or diffraction pattern of the sample. The lens which is closest to the sample is called the objective lens. This is a powerful lens with a short focal length which requires a high current and water cooling. Since the focusing

strength of the lens is dependent on the current supplied to it, the power supply for this lens must be very stable. This lens is followed by the objective aperture, which is located at the plane where the specimens diffraction pattern is first produced. This aperture can be used to block electrons scattered above a certain angle, giving scattering contrast/diffraction contrast. The objective aperture also reduces the effects of spherical and chromatic aberration on the image. Moving down the TEM column, the next component is the selected-area aperture, also known as the diffraction aperture. The role of this aperture is to define a region of the sample from which an electron diffraction pattern is produced. It is standard for TEMs to have multiple lenses between the objective lens and the final projector lens, the combined function of these lenses can be thought of in terms of a single intermediate lens. This intermediate lens has two roles; changing the image magnification by altering its focal length in small steps, and, when the current through it is greatly reduced, producing an electron diffraction pattern on the phosphor screen/camera. Finally, at the very bottom of the TEM column is the projector lens. The role of this lens is to spread an image/diffraction pattern across the entire TEM screen.

Finally a phosphor screen converts from an electron image to a visible image. The image can then be recorded using film or a CCD. For further reading on TEM the author recommends reference [134] and for an in-depth description of the principals reference [135].

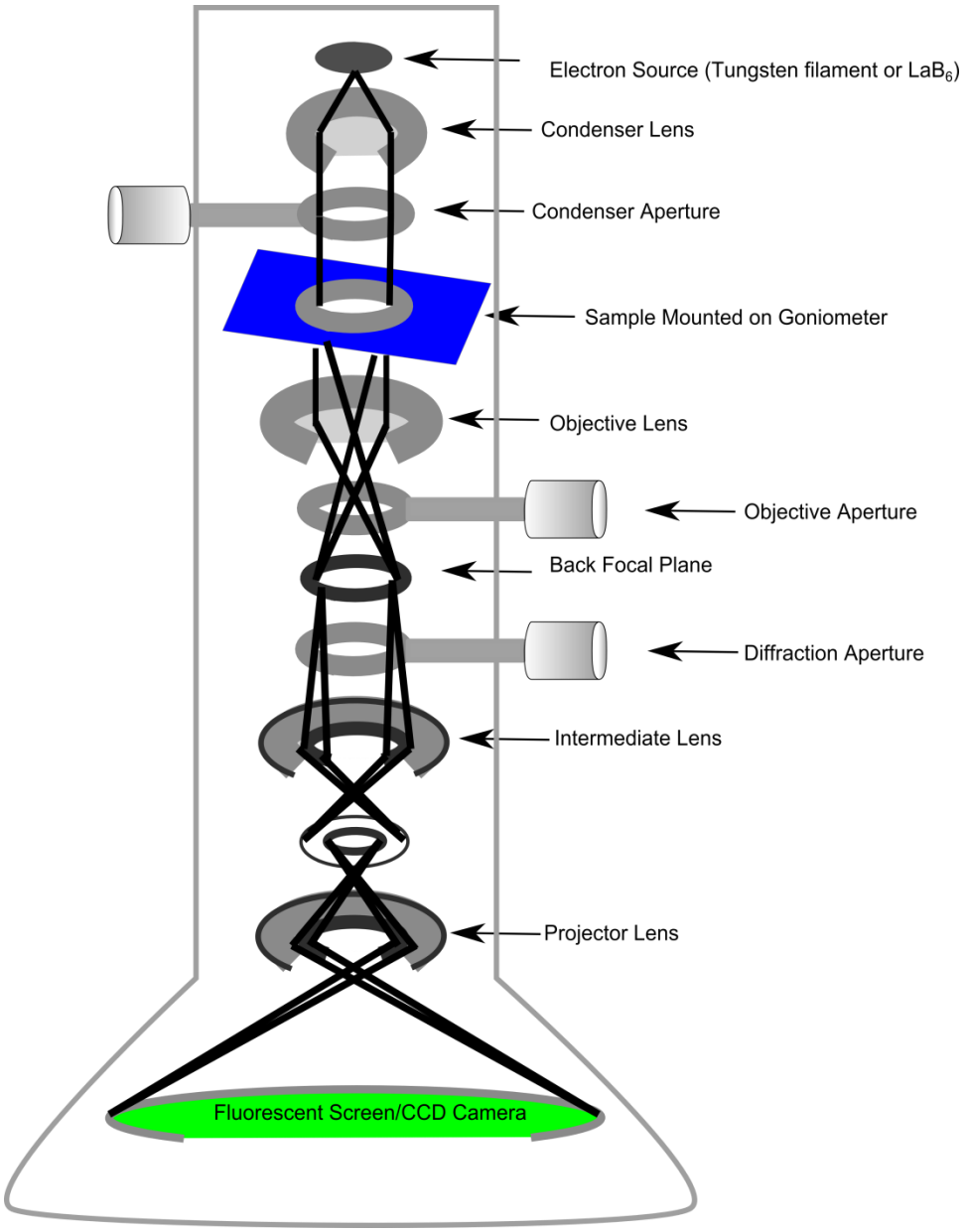

Figure 3-27 - A simplified schematic diagram of a transmission electron microscope

3.7.3 TEM Image Contrast and Diffraction

If a crystalline sample is imaged using TEM, changes in the crystal structure will change the elastic scattering diffraction condition. This in turn changes the intensity in the imaged electrons and hence gives image contrast.

As previous described, the projector lens strength can be reduced to give an electron diffraction pattern on the phosphor screen. The sample can be tilted, so that diffraction can occur from different crystal planes. The [000] direct beam is always visible. What is referred to as a two beam diffraction condition can be selected by tilting the sample so that only the direct beam and the spot from one other diffraction condition (the Bragg condition is only met for one point in the reciprocal lattice) are excited. The microscope's objective aperture can then be used to select either the direct beam, giving what is known as a bright-field image or to select a diffracted beam giving what is known as a dark-field image. This is combined with the selection of specific diffraction conditions, to give a wide variety of possibilities for sample analysis.

The strain field around dislocation causes a local bending of the crystal lattice which changes their diffraction condition and thus gives contrast in the image. If the Burgers vector (***b***) which defines the displacement of the crystal lattice is perpendicular to the diffraction condition, then the dislocation will be invisible in TEM ($g \cdot \boldsymbol{b}=0$) (figure 3-28).

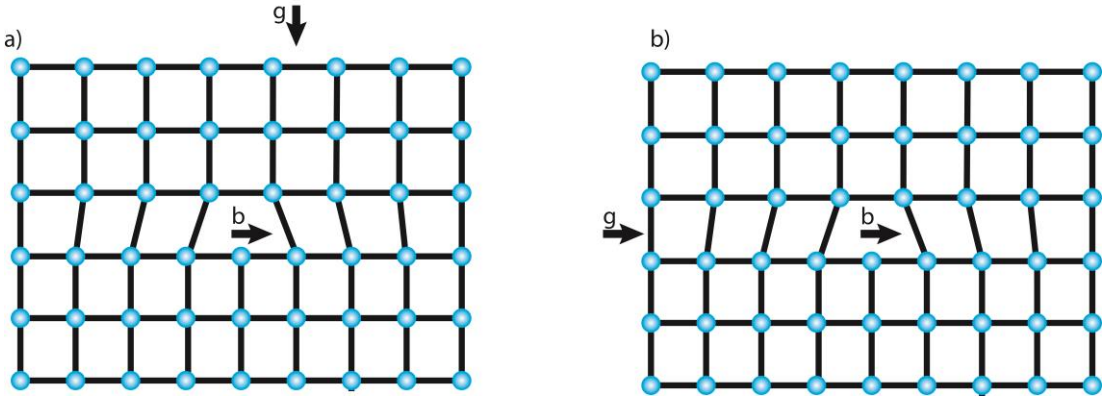

Figure 3-28 - Illustration of the dislocation invisibility criterion. In a) the dislocation is invisible due to the burgers vector being perpendicular to the diffraction condition ($g \cdot \boldsymbol{b}=0$) and in b) the dislocation is visible ($g \cdot \boldsymbol{b} \neq 0$).

If the Burgers vector of a dislocation is not known, it can be determined by what is known as $g \cdot \boldsymbol{b}$ analysis. Two non-parallel diffractions are found in which the dislocation is difficult to see, indicating $g \cdot \boldsymbol{b}=0$. It should then be possible to find $\boldsymbol{b}$. For more information on diffraction and contrast in the TEM the author recommends Williams and Carter [135].

3.7.4 Aberration-corrected TEM

Unfortunately, despite operating with electrons with extremely small wavelengths (at 200 kV, λ=0.0025 nm), the maximum resolution of conventional TEM is far from the wavelength of the electrons. The quality of the microscope's objective lens and the illumination wavelength determine one of the basic resolution limits, this is referred to as the point resolution limit and is proportional to equation 3-23 [136], where λ is the electron wavelength and C_s is the coefficient of spherical aberration. The derivation of equation 3-23 can be found in [137] by Scherzer. For a lens exhibiting spherical aberration, rays travelling parallel to the optical axis but of varying distances away from the optical axis do not converge on the same point.

$$\sim C_s^{\frac{1}{4}} \lambda^{\frac{3}{4}}. \qquad 3\text{-}23$$

It can be seen from equation 3-23 that the microscope resolution can be improved by either reducing the electron wavelength or reducing C_s. Reducing the electron wavelength requires a higher accelerating voltage which is expensive and can cause sample damage. This leaves reducing C_s, which can be achieved through the use of aberration correctors. These generate negative values of C_s and cancel the positive C_s from the microscope lenses. The use of aberration correction has greatly increased TEM resolution, with resolutions obtained now below 1 nm. For more information on aberration correction see Hetherington [136].

The superlattice structures presented in this work are comprised of layers of $Si_{1-x}Ge_x$ with only small change in Ge composition (15 %) between layers. This alloy difference is difficult to resolve with conventional TEM and gives poor contrast in images. A TEM based techniques that is able to give very good image contrast between layers of $Si_{1-x}Ge_{x,}$ with small differences in Ge composition, is high-angle annular dark field scanning transmission electron microscopy and this technique is described in the next section.

3.8 High-angle annular dark-field scanning transmission electron microscopy

Scanning transmission electron microscopy (STEM), a schematic diagram of which is given in figure 3-29, can be compared to the more frequently used scanning electron microscope (SEM). Like SEM, in STEM the optics located before the

sample are used to form an illuminating spot which is rastered over the sample. The different signals this produces are recorded using a selection of detectors as a function of the probe location on the sample surface. Unlike SEM, a thin, electron transparent sample is used which causes little beam spreading, giving the technique a resolution that is mainly determined by the size of the probe. It is possible to achieve sub Å probe sizes so atomic resolution is possible.

The technique of high-angle annular dark field (HAADF) STEM refers to a particular detector, which is positioned in the optics some distance from the sample. When the sample is not present, the detector receives no signal, hence the technique is called dark-field. When the electron probe interacts with the sample, scattered intensity is strongly related to the atomic number (Z) [138]. This is very useful for distinguishing between elements in atomic resolution images and is a distinct advantage over conventional TEM. In the cases of $Si_{1-x}Ge_{x,}$ HAADF-STEM is able to distinguish between layers with an alloy difference of 2% [139].

All HAADF-STEM is this work was performed using a JEOL ARM200F TEM. For further reading on HAADF-STEM the author recommends reference [140].

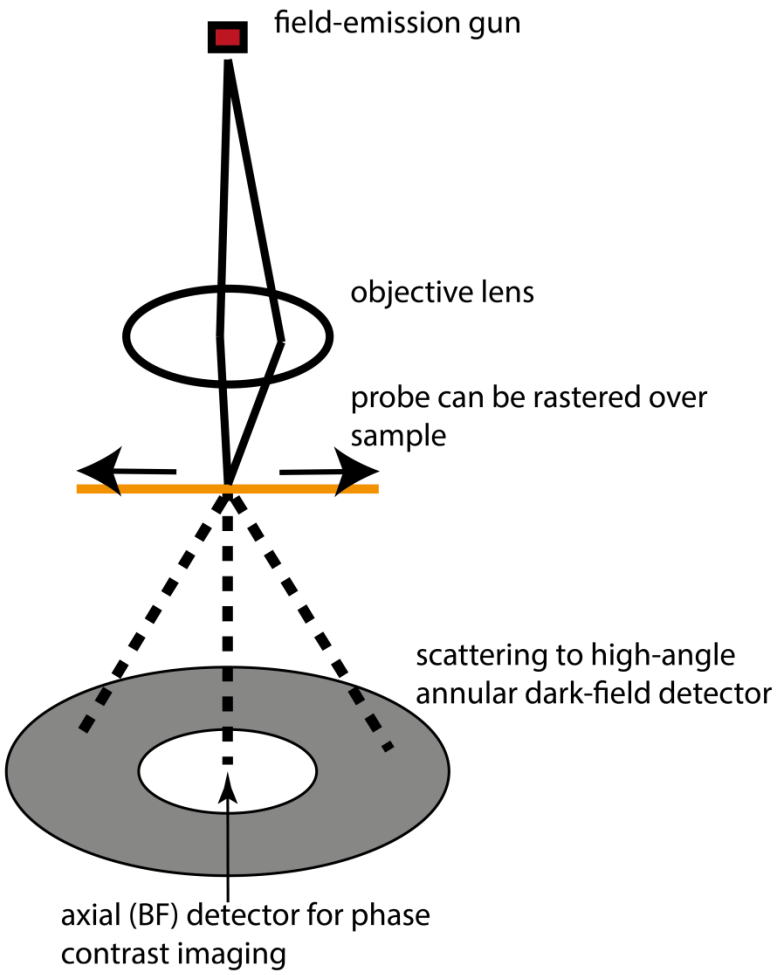

Figure 3-29 - Schematic diagram of the scanning transmssion electron microscope showing geometry of the annular dark-field (ADF) detector and the bright-field detector for phase contrast imaging. Adapted from [140]

3.9 Summary

In this chapter, a comparison of a number of complementary techniques for the materials characterisation of Si-based QCL structure is given. The parameters that can be measured with each technique are discussed. For each technique a detailed description was given, along with relevant theory.

4 Growth of Thin, Strained SiGe Layers

In this chapter low temperature (450°C) epitaxial growth of $Si_{0.4}Ge_{0.6}$/Si is presented. $Si_{0.4}Ge_{0.6}$/Si layers are grown far beyond the critical thickness predicted by the People and Bean model and their high crystalline quality is confirmed by multiple techniques. $Si_{0.4}Ge_{0.6}$ was chosen since it is a higher Ge composition than has been reported in the literature for low temperature RP-CVD grown strained layers on Si (001). The high strain, high Ge composition and good crystalline quality mean that the layers have possible applications in electronic devices. The layers also offer an opportunity to investigate the growth quality of SiGe using germane and disilane precursors by low temperature RP-CVD, the technique which will be used to grow the QCL structures presented later in this work.

4.1 Motivation

The motivation behind the work in this chapter is to produce high quality, high Ge composition, strained SiGe layers that have applications in devices such as field effect transistors (FETs) [141], quantum-well transistors [150] and optical modulators [151]. This requires comprehensive materials characterisation to show the layers have good crystal quality and are not undergoing strain relaxation.

4.2 Introduction - Low growth temperature and critical thickness

Performing growth at relatively low temperature has the following advantages in the growth of Ge/$Si_{1-x}Ge_x$ multilayers: improved interface quality, which is due to reduced Si/Ge diffusion and reduced Ge segregation and sharper dopant profiles from reduced dopant diffusion. Unfortunately, the degree to which growth

temperature can be lowered in RP-CVD is limited by greatly reduced growth rates at low temperature and by the physical limit of precursor gases requiring a certain temperature for thermal decomposition. This means that growth temperature is a compromise between growth quality and growth time. In the work on superlattice growth presented in Chapter 5, a relatively low growth temperature of 450 °C was used for all superlattice growth with the intention of achieving the highest quality possible. Few studies have explored the critical thickness for RP-CVD growth at such a low growth temperature and those that have are focused on low Ge concentration $Si_{1-x}Ge_x$ [91, 141-142]. As discussed in Chapter 2, growth at low temperature is able to extend the critical thickness, due to the kinetics of plastic deformation being reduced with lower growth temperature. Since low growth temperature was already under investigation to give high quality, multi-layer growth for superlattices, it was decided to also investigate its effect on the critical thickness of high Ge content $Si_{1-x}Ge_{x,}$ with a 60% Ge content.

It is expected that the low temperature will give rise to layers grown beyond their critical thickness and with a high level of compressive strain, which is useful in device applications. This includes electronic devices like Field Effect Transistors (FETs) where it has been observed that for pseudomorphic layers of SiGe on Si [143-144] the mobility is improved with Ge content. It is also very important to maintain the SiGe thickness around or above 10 nm in order to have a sufficiently thick layer so that material can be removed during processing, oxidation and cleaning steps, but still leave a sufficiently thick channel layer (the conducting channel region between the source and drain contacts in a FET).

4.3 Growth

The precursor flow rates were first calibrated to give an alloy concentration of $Si_{0.4}Ge_{0.6}$ for growth at 450 ˚C by using HR-XRD reciprocal space mapping on thick layers of $Si_{1-x}Ge_{x.}$ Following alloy calibration, a number of $Si_{0.4}Ge_{0.6}$/Si wafers (figure 4-1) were grown with a wide range of growth times to give a range of layer thicknesses above and below the critical thickness. The critical thickness of a layer will be marked by the beginning of strain relaxation processes that result in the introduction of a small number of dislocations at the layer/substrate interface. Characterisation techniques that are sensitive to the appearance of these defects are therefore required.

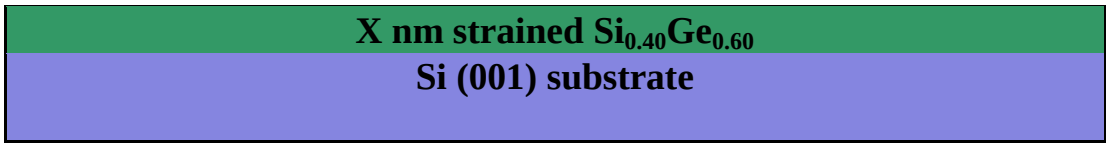

Figure 4-1 -Schematic diagram of $Si_{0.4}Ge_{0.6}$/Si(0 0 1) heterostructure grown by RP-CVD

4.4 Characterisation

4.4.1 Characterisation by XRD

Initially (004) X-ray ω-2θ scans were performed on all of the $Si_{0.4}Ge_{0.6}$/Si wafers grown. The X-ray ω-2θ scans were fitted (using the method described in section 3.5.3) to extract the $Si_{0.4}Ge_{0.6}$ layer thickness, giving values of 4.73 ± 0.04, 6.30 ± 0.04, 18.1 ± 0.06, 21.12 ± 0.08, 24.26 ± 0.09 and 27.98 ± 0.09 nm. The error in thickness measurement decreased with decreasing layer thickness since the X-ray thickness fringes become better resolved for thinner layers. The maximum error in

thickness measurement of ± 0.09 nm was seen in the thickest (24.26 nm and 27.98 nm) layers. This error is more than adequate for the critical thickness study to be performed on the layers. A layer with a long growth time did not exhibit any thickness fringes, however its thickness was estimated at ~40.6 nm by calculating a growth rate from the other layers. The X-ray ω-2θ scans for the 21.1 nm, 24.3 nm and 28.0 nm thick $Si_{0.40}Ge_{0.60}$ layers are shown in figure 4-2. For the 21.1 nm thick layer, the $Si_{0.40}Ge_{0.60}$ peak is symmetric and the thickness fringes are well defined; however, for the 24.3 nm thick layer and progressively more so for the 28.0 nm layer, the $Si_{0.40}Ge_{0.60}$ peak is asymmetric and the thickness fringes are poorly defined. The poorly defined thickness fringes are indicative of decreasing crystalline quality in the layers and the asymmetrical $Si_{0.40}Ge_{0.60}$ peak suggests a strain profile in the layers, with relaxation processes beginning to occur.

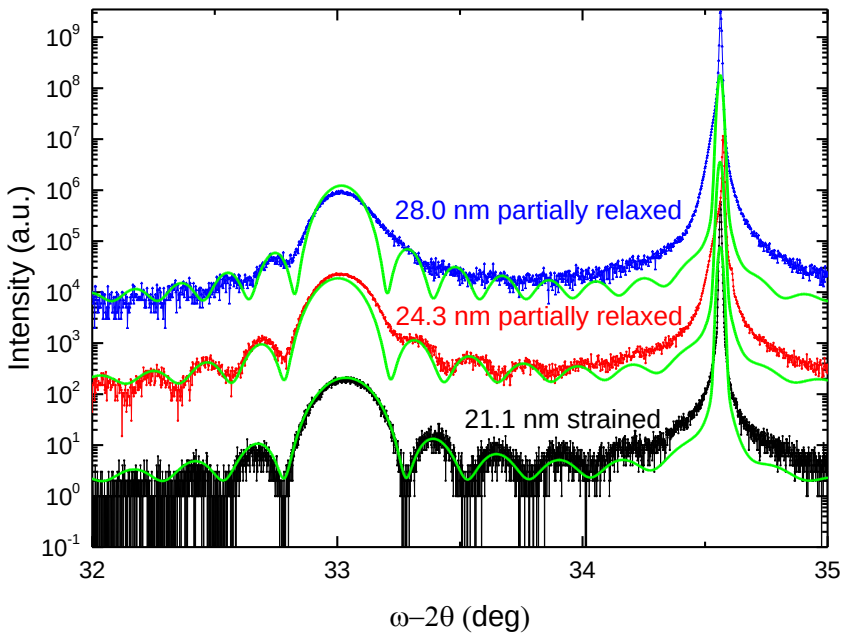

Figure 4-2 - ω-2θ XRD scans around the symmetric (004) Bragg peak for $Si_{0.4}Ge_{0.6}$ layers of increasing thickness of 21.1 nm (black), 24.3 nm (red) and 28.0 nm (blue). Simulated scans are given in green. Distinct thickness fringes can be seen in the

21.1 nm layer, but not in the 24.3 nm and 28.0 nm layers. The sharp peak on the right of each scan is from the Si substrate and is used as a reference.

Symmetric (004) RSMs and asymmetric (224) RSMs were measured for all the $Si_{0.4}Ge_{0.6}$/Si wafers grown. In figure 4-3, (004) and (224) RSMs are given for the 21.1 nm, 24.3 nm and 28.0 nm $Si_{0.4}Ge_{0.6}$ layers. The thickness fringes present in the X-ray ω-2θ scans in Figure 4-2 are also present in the RSMs, but are not as well defined. This is due to the shorter counting time and larger step size used in the RSMs due to time constraints when performing the scans (each RSM scan duration is ~24 hours). For the 21.1 nm $Si_{0.4}Ge_{0.6}$ layer, sharp, narrow peaks are observed in both the (004) and (224) RSMs. For the 24.3 nm and 28.0 nm $Si_{0.4}Ge_{0.6}$ layers, the Bragg peaks observed in both the (004) and (224) RSMs are smeared, with significant diffuse scattering occurring. The smearing suggests the presence of a strain profile in the layers with strain relaxation beginning to occur.

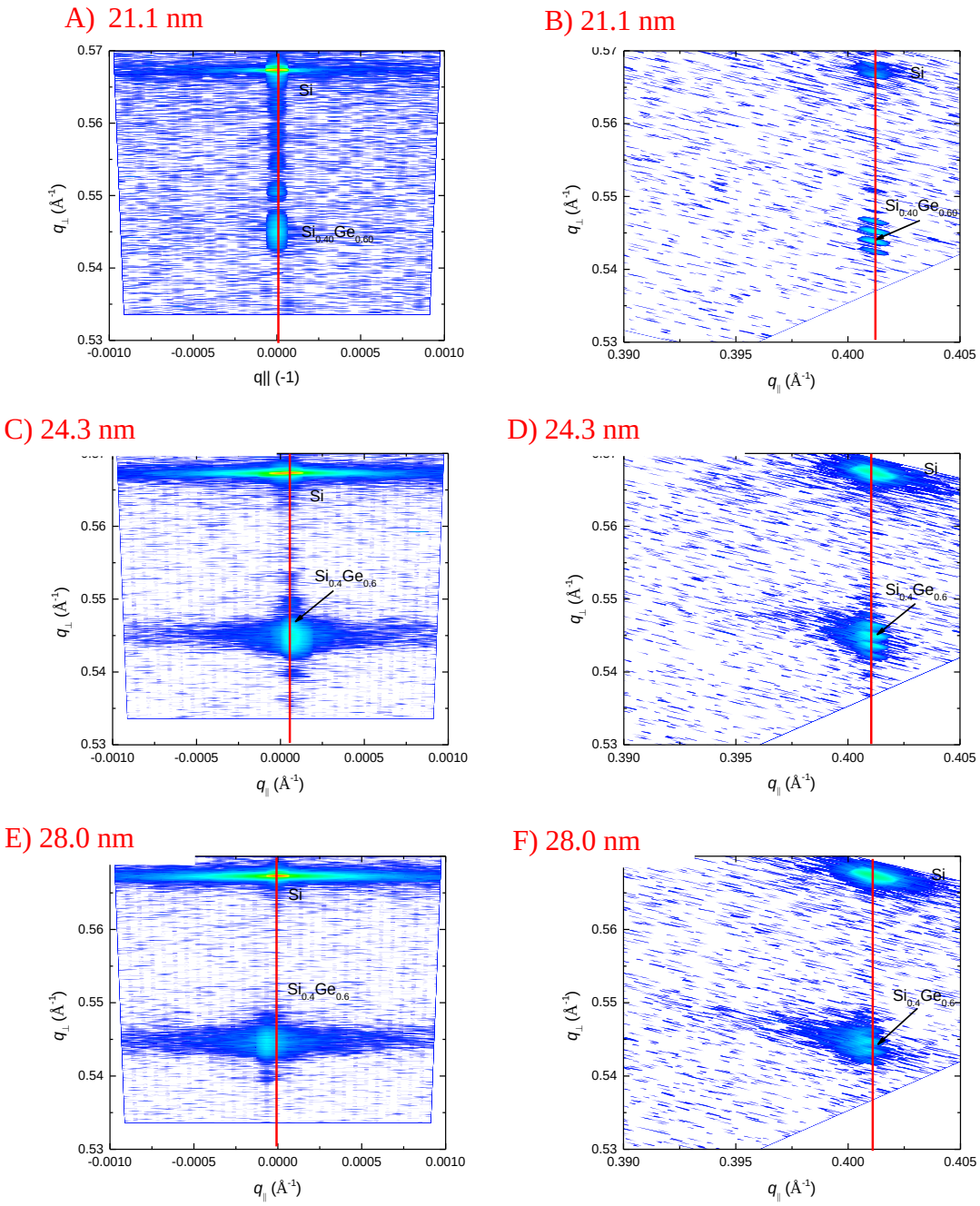

Figure 4-3 – (004) symmetric HR-XRD RSMs from A) 21 nm $Si_{0.40}Ge_{0.60}$ layer, C) 24nm $Si_{0.40}Ge_{0.60}$ layer and E) 29 nm $Si_{0.40}Ge_{0.60}$ layer. (224) asymmetric HR-XRD RSMs from B) 21 nm layer, D) 24nm layer and F) 29 nm layer.
The FWHM of the Bragg peak from the $Si_{0.40}Ge_{0.60}$ layer can be seen to increase for the layers thicker than 21 nm.

The relaxation of the $Si_{0.40}Ge_{0.60}$ layers with respect to the Si substrate, as measured from the RSMs and the FWHM of the (004) Bragg peak from the alloy layer are given as a function of layer thickness in figure 4-4. For the layers with a thickness of 28.0 nm and below, the relaxation is measured as 0% (within error), i.e. they are fully strained, however this is not supported by the FWHM of the Bragg peak, which increases quickly from the 21.1 nm layer, indicating the onset of strain relaxation.

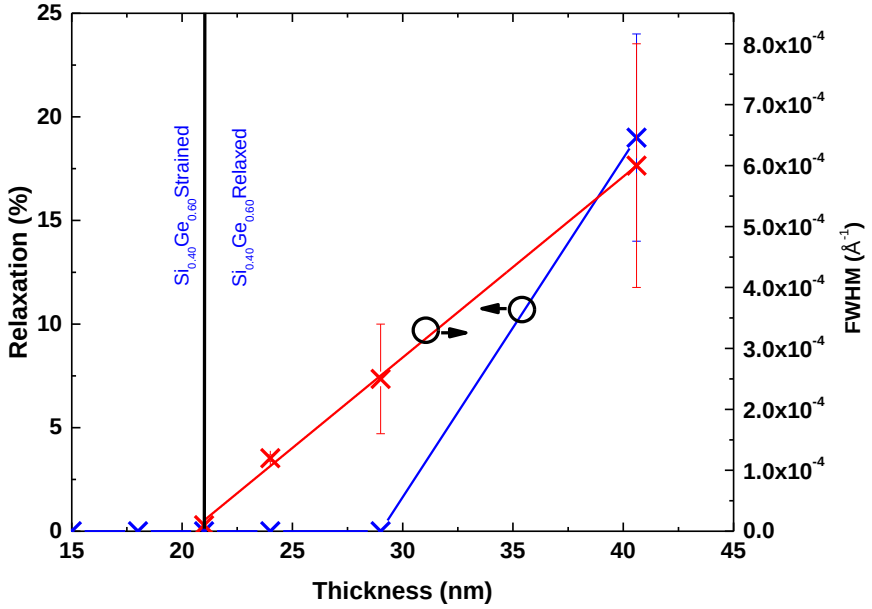

Figure 4-4 - $Si_{0.40}Ge_{0.60}$ layer relaxation with respect to the Si substrate as measured by RSM vs. layer thickness from fitted peak positions (red line and crosses) and FWHM of the $Si_{0.40}Ge_{0.60}$ layer Bragg peak from symmetrical (004) RSMs vs. layer thickness from fitted peak positions (blue line and crosses) .

4.4.2 Surface Characterisation

The wafers grown were then characterised by surface morphology measurement by AFM, since the strain field created by the introduction of dislocation into the layers is expected to have an effect on surface morphology. Tapping mode was used to

resolve the features on the thinner, smoother samples and contact mode on the rougher, thicker samples. In figure 4-5, the RMS surface roughness, as calculated from the AFM measurements, is plotted against the thickness of the $Si_{0.40}Ge_{0.60}$ layer. The RMS roughness was calculated over multiple scans to account for any inhomogeneity across the wafer. The growth starts with an RMS roughness plateaued at approximately 0.08 nm, which is comparable to the roughness of the original Si substrate. Following the plateau, the RMS sharply rises for layers thicker than 21.1 nm.

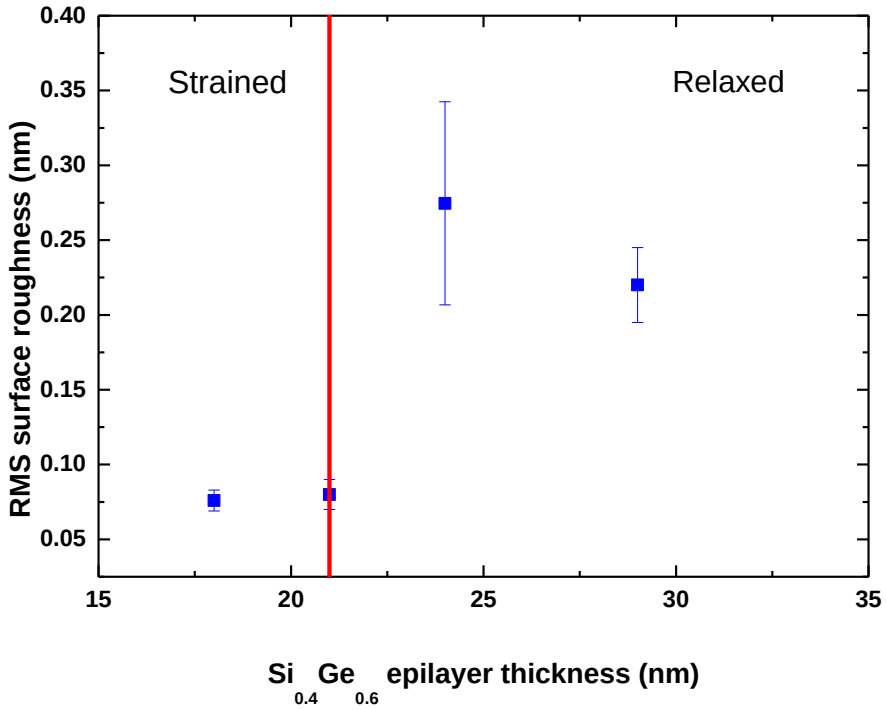

Figure 4-5 - RMS surface roughness measured by AFM plotted against epilayer thickness

Individual AFM scans are given for the 21 nm thick $Si_{0.40}Ge_{0.60}$ layer in figure 4-6 and the 24 nm $Si_{0.40}Ge_{0.60}$ layer in figure 4-7. When comparing the two scans, the large difference in vertical scale must be taken into account. The 21.1 nm thick layer

can be seen to have a relatively smooth surface, exhibiting detail with a high spatial frequency, which is most likely due to noise in the AFM. The 24.3 nm thick layer has a far rougher surface than the 21.1 nm thick layer, with a characteristic cross-hatch pattern visible.

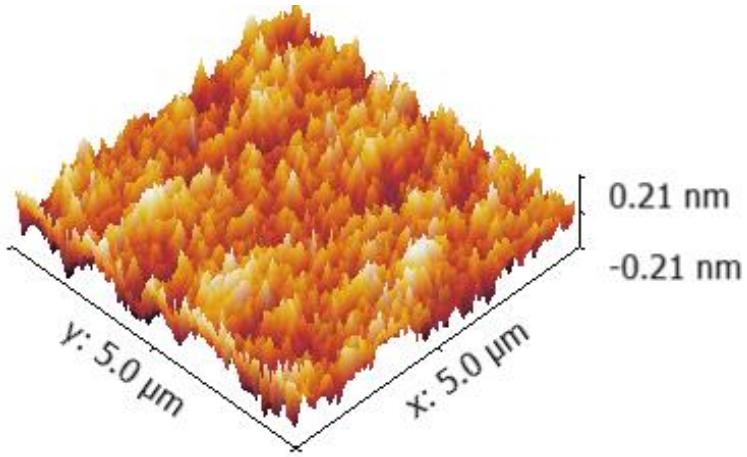

Figure 4-6 - Surface morphology for 21.1 nm layer from AFM

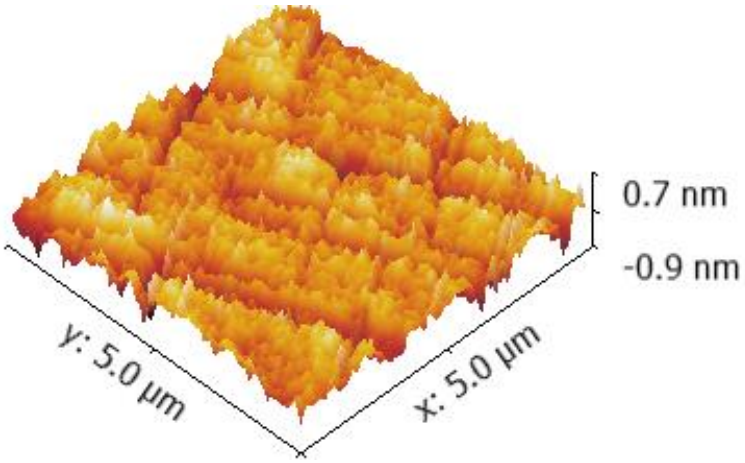

Figure 4-7 - Surface morphology for 24.3 nm layer from AFM

4.5 Discussion

The point at which the critical thickness is exceeded will be marked by the introduction of dislocations into the $Si_{0.40}Ge_{0.60}$ layer. From AFM measurements of the surface morphology, a sharp decrease in crystalline quality is seen between the

21.1 nm and 24.3 nm thick layers, indicated by an increase in surface roughness. This suggests that the critical thickness of the layer lies between 21.1 nm and 24.3 nm. Additional evidence for this conclusion comes from the cross-hatch pattern that is only visible on the surface of the 24.3 nm thick layer. The formation of the cross-hatch pattern along the two <110> directions is indicative of an underlying stress field caused by the dislocations from strain relaxation [145] and so confirms that the critical thickness has been exceeded by the 24.3 nm thick layer.

A critical thickness between 21.1 nm and 24.3 nm is confirmed by the (004) X-ray ω-2θ scans. A loss of definition in the thickness fringes of the X-ray ω-2θ scan is seen in Figure 4-2 for the 24.3 nm and 28.0 nm layers relative to the 21.1 nm layer and is due to a reduction in crystalline quality caused by strain relief through defect formation. An increase in the FWHM of the $Si_{0.4}Ge_{0.6}$ Bragg peaks for the 24.3 nm and 28.0 nm layers is also visible when compared with the 21.1 nm layer. This peak broadening is from a strain profile in the layer formed as relaxation occurs.

The critical thickness between 21.1 nm and 24.3 nm is further confirmed by HR-RSMs in figure 4-3 and figure 4-4. For the 21.1 nm layer, the symmetrical and asymmetrical RSMs show the $Si_{0.40}Ge_{0.60}$ layer is fully strained: the Bragg reflections are both narrow in the $q_{\parallel}$ direction and elongated in the $q_{\perp}$ direction, indicative of the diffraction only occurring through coherent scattering processes. However, for the 24 nm and 28.0 nm layers, the symmetrical and asymmetrical RSMs show relaxation processes are occurring in the $Si_{0.40}Ge_{0.60}$ layer. The Bragg reflections have much larger FWHM for $q_{\parallel}$, indicative of the diffraction occurring through coherent and diffuse scattering processes, which is a signature of the early stages of relaxation

processes [147]. The Bragg peaks associated with the alloy layers are also smeared suggesting a strain distribution in the layers, which also indicates the beginning of relaxation processes.

From the People and Bean model, the critical thickness for $Si_{0.4}Ge_{0.6}/Si$ is 14.5 nm. A comparison of the result from this work with relevant results from the literature and the People and Bean model for critical thickness is given in figure 4-8. It can be seen that the result from this work lies above that predicted by People and Bean and corroborates results from similar low temperature RPCVD growth by other groups.

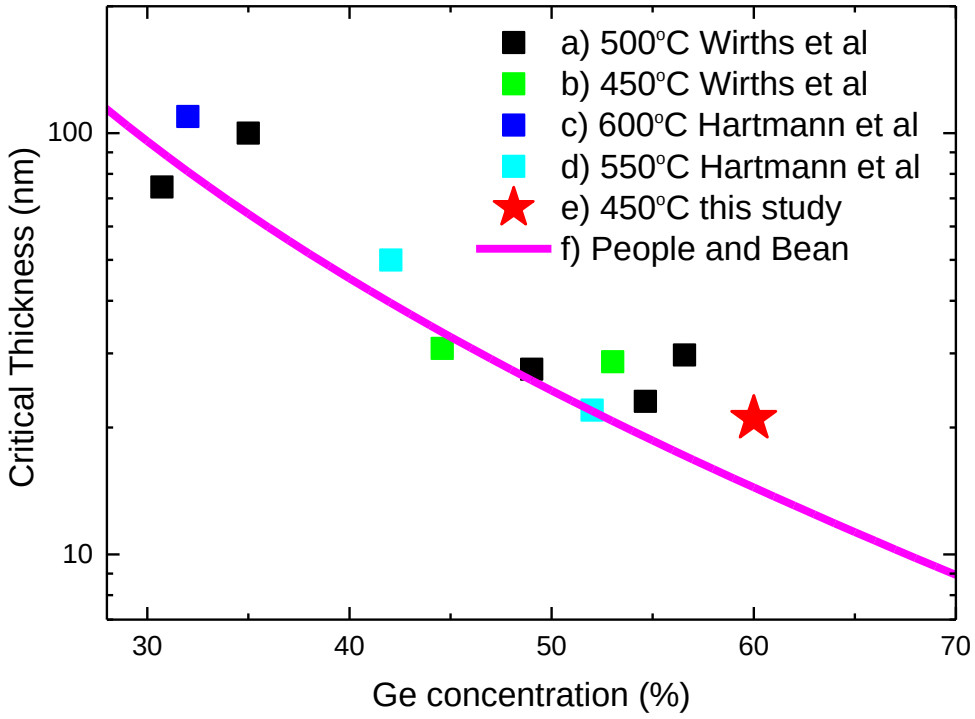

Figure 4-8 –The critical layer thickness as a function of Ge concentration for growth temperatures of 450°C, 500°C, 550°C and 600°C, a) 500°C growth by RPCVD by Wirths et al [142], b) 450° growth by RPCVD by Wirths et al [142], c) 600° growth by RPCVD by Hartmann et al [91], d) 550°C growth by RPCVD by Hartmann et al [91] e) 450°C growth by RPCVD *(this work)*, f) People and Bean critical thickness model [148-149].

The strain relaxation occurs relatively slowly for the $Si_{0.4}Ge_{0.6}$/Si layers grown in this study (figure 4-4). This is to be expected due to the high Ge composition of the layers: for higher Ge composition layers, strain energy is built up more quickly so relaxation occurs earlier during growth; since the SiGe layer is thinner when dislocations start to form there is a greater chance of dislocation blocking by the strain field of other dislocations. This increased dislocation blocking acts to slow the rate of strain relaxation for layers that have a greater strain contrast to their substrate. In reference [91] this effect was confirmed by Hartmann *et al.* for CVD grown samples by studying the relaxation rates of $Si_{1-x}Ge_x$ for a number of Ge compositions.

4.6 Summary

$Si_{0.4}Ge_{0.6}$/Si layers were grown with a wide range of thickness at a low growth temperature of 450^{o}C to determine the critical thickness for these growth conditions; the critical thickness was then confirmed using a number of techniques, all of which are in agreement. The $Si_{0.4}Ge_{0.6}$ layer was reported to be fully strained up to a thickness of 21 nm, with layers up to and including 21 nm thick being of good crystal quality and having a defect density lower than the detectable limit for the characterisation techniques used. A combination of high Ge composition, good crystal quality and high strain gives the layers possible applications in increasing performance for electronic devices such as field effect transistors (FETs) [141], quantum-well transistors [150] and optical modulators [151] due to their strain enhanced electrical properties.

5 Growth of SiGe/Ge Superlattices for Terahertz Emission

This work presented in this chapter was undertaken in collaboration with groups at the University of Leeds and the University of Glasgow. The aim of this EPSRC funded project is to work towards a Si-based QCL. Within the project, the remit for the University of Warwick is the epitaxial growth and materials characterisation of structures.

In this chapter, growth and comprehensive materials characterisation of n-type $Ge/Si_{0.15}Ge_{0.85}$ superlattices is reported. n-type $Ge/Si_{1-x}Ge_x$ are challenging to grow: in comparison to p-type $Si/Si_{1-y}Ge_y$ structures since they require a high Ge composition virtual substrate to strain balance the structure (discussed in section 2.5), n-type dopants have a higher diffusivity, and Ge has a higher diffusivity in Ge rich structures. The work presented in this chapter has many uses outside of the specific QCL project, with $Ge/Si_{0.15}Ge_{0.85}$ superlattices having a wide range of other applications such as in thermoelectric structures [152-154] and quantum-confined Stark effect modulators (QCSEs) [155-157].

Initially, growth of superlattices intended for optical measurements by the University of Glasgow are presented with full materials characterisation and a discussion of the merits of the growth quality. Growth of complex n-type QCL structures for terahertz emission are then presented, with in-depth materials characterisation. The materials characterisation performed on the superlattices includes a number of complementary techniques, HR-XRD reciprocal space mapping, X-ray ω-2θ scans, AFM, ATP,

SIMS, cross-sectional TEM and HAADF-STEM. Finally, the QCL structure growth quality is discussed, in the context of the structures performance QCLs.

5.1 Preparation for growth and growth calibration

To give accurate growth of the structures, a number of steps were carried out prior to growth, with the aim of calibrating growth rates, alloy composition and doping concentration.

5.1.1 Composition

The concentration of Ge is affected by both the precursor gas flow rates and the growth temperature. For RP-CVD at 550°C the Ge mole fraction x, has been found to follow a parabolic-like relationship given by equation 5-1 where $F(GeH_4)/F(Si_2H_6)$ is the precursor gas mass-flow ratio [78]. While the growth conditions differ from those used in this work, equation 5-1 can still be used as a guide.

$$\frac{x^2}{(1-x)} = \frac{0.47 * F(GeH_4)}{2 * F(Si_2H_6)}. \qquad 5\text{-}1$$

For each temperature used during epitaxial growth of structures, a range of partially relaxed $Si_{1-x}Ge_x$ on Si(001) substrate samples was grown. (004) and (224) XRD RSMs were then performed on all samples, from which their composition was extracted. The XRD results were used to calibrate the precursor gas flow rates to achieve a certain Ge concentration for a given growth temperature. An example is given in figure 5-1 for a sample of $Si_{1-x}Ge_x$ on Si(001) used to calibrate an intended growth of relaxed $Si_{0.05}Ge_{0.95.}$ It can be seen in figure 5-1 that for a $Si_{1-x}Ge_x$ layer

with a higher Ge composition, the $Si_{1-x}Ge_x$ peak moves away from the Si peak towards the origin of reciprocal space and the opposite for a $Si_{1-x}Ge_x$ layer with a lower composition. The layer of $Si_{1-x}Ge_x$ actually grown is 99.7±0.2 % relaxed with respect to the substrate and has a composition of x= 0.938±0.001.

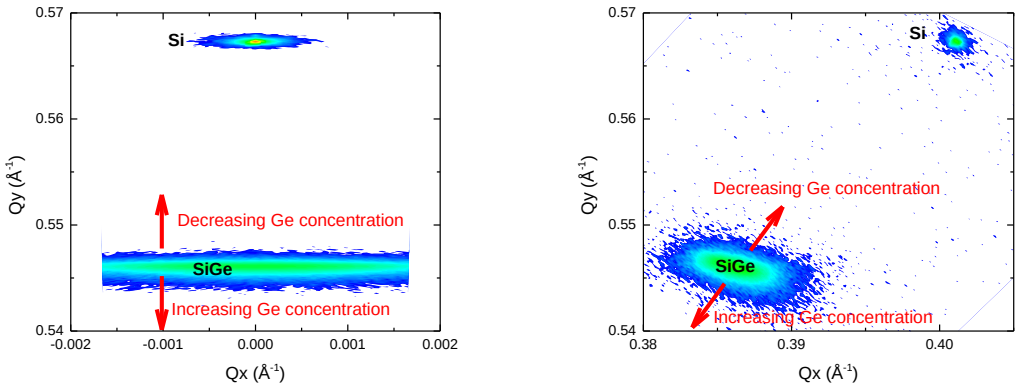

Figure 5-1 - Example of 004 (left) and 224 (right) RSMs used to calibrate precursor flows for growth of $Si_{0.05}Ge_{0.95.}$ From both RSMs SiGe composition can be determined very accurately

5.1.2 Growth rate

Growth rate is affected by growth temperature, precursor gas flow rates and the growth medium. To calibrate growth rate, a number of samples were grown, each comprised of multiple layers with alternating high and low Ge composition. The layers were grown with a progressively longer growth time through the sample (figure 5-2). Features can be seen at the layer interfaces, these are caused by strain relaxation in the structure. Cross-sectional TEM was then performed on the structure and the thickness of each layer found by taking the absolute differential of relative intensity and the results used to plot growth time vs. layer thickness (figure 5-3). The data was then fitted with a linear relationship (a linear growth rate was assumed), with the gradient giving the growth rate. It can be seen in figure 5-3 that for certain Ge concentrations/precursor gas flows, growth did not begin immediately with the

introduction of precursors. The time elapsed before growth begins is known as the 'stagnation time' or 'incubation time' and is caused by the growth needing a time to nucleate on the substrate surface. The stagnation time must be accounted for when calculating the growth time to produce a layer with a certain thickness. Stagnation time varies depending on the growth surface. For example, $Si_{0.15}Ge_{0.85}$ grown on Ge has a different stagnation time to $Si_{0.15}Ge_{0.85}$ grown on $Si_{0.05}Ge_{0.95.}$ Due to this, separate calibration samples must be grown for each different interface present in a superlattice.

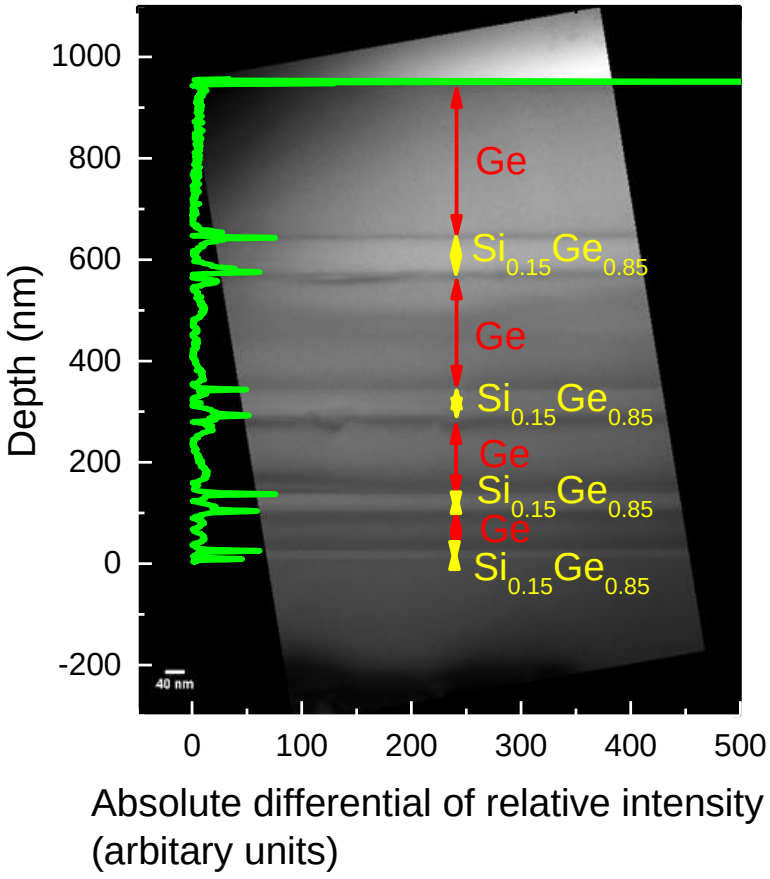

Figure 5-2 - Cross-sectional TEM micrograph of $Si_{0.15}Ge_{0.85}$ 450°C growth rate calibration structure overlaid with absolute differential of relative intensity. Features at the interfaces are dislocations formed due to exceeding critical thickness of the particular material.

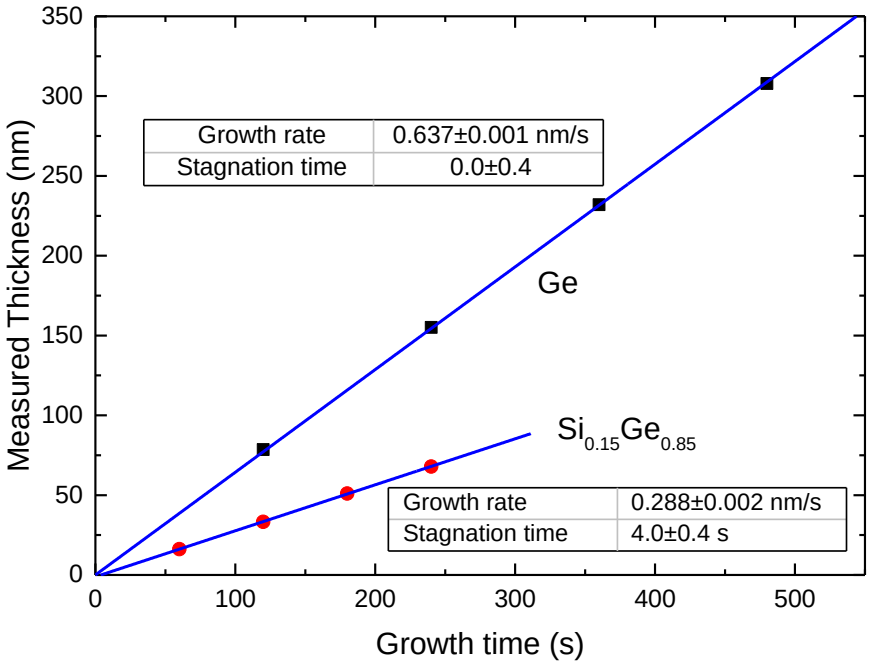

Figure 5-3 - Plot of measured thickness vs growth time for $Si_{0.15}Ge_{0.85}$ (red) and Ge (black). The points have been fitted with a linear fit (blue), which is in excellent agreement with the data. The gradient of the fit gives growth rate and the y-axis intercept gives the stagnation time.

5.1.3 Doping

To calibrate dopant concentration, samples were grown with the required Ge composition, each containing a number of steps, with the dopant gas flow increased in each step. SIMS profiles were measured for each sample, from which the dopant precursor flow required for a given level of doping can be determined. An example is given in figure 5-4 for phosphorus doping in $Si_{0.15}Ge_{0.85}$. Average dopant concentrations were calculated for plateaus. The dopant gas flow was then extrapolated for the required dopant level in the superlattice.

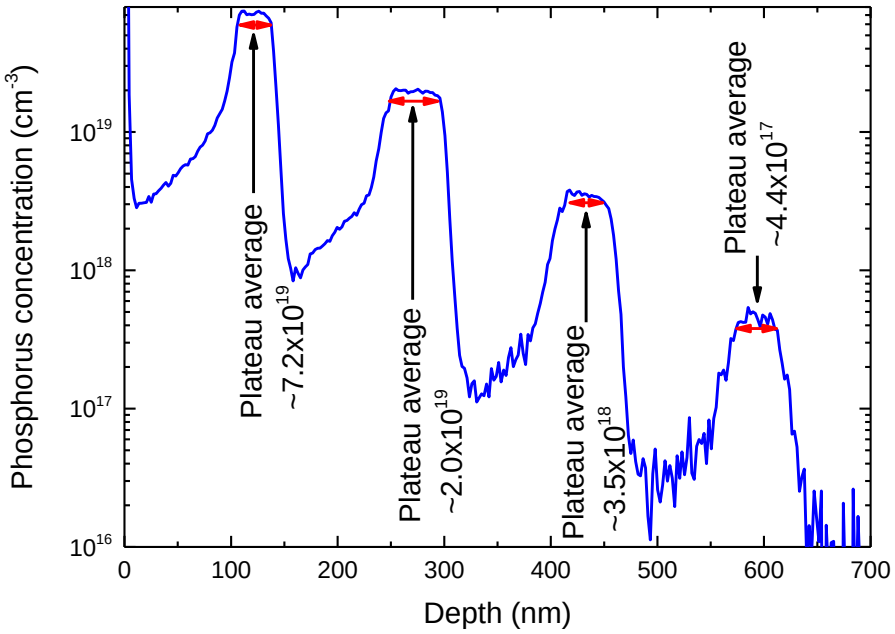

Figure 5-4 - SIMS profile for phosphorus doping in $Si_{0.15}Ge_{0.85}$ calibration sample.

Following initial calibration work, superlattice structures could be grown. The growth of two sets of superlattice structures is presented in this work, the first set are for optical measurements by collaborators and the second set are designed to function as QCLs and emit terahertz radiation. The results of the optical measurements on the first set of structures will be useful in the design of Si based QCL structures. The optical characterisation technique to be performed by collaborators on the first set is known as Fourier Transform Infrared Spectroscopy (FTIR), hence the structures are referred to as FTIR structures in this work.

5.2 FTIR Structures

5.2.1 FTIR Structures Growth Motivation

Multiple quantum well superlattice structures were proposed for growth following discussion between groups at the University of Glasgow and Leeds. The structures

are designed for characterisation using FTIR and electrical characterisation to be performed at the University of Glasgow. These techniques will be performed with the intention of characterising the intersubband transitions for the $Ge/Si_{0.15}Ge_{0.85}$ system which can be used in the design of Si-based QCLs. Similar studies have been performed on $Ge/Si_{0.20}Ge_{0.80}$ based superlattices [158].

The FTIR structures feature an n-type, high Ge content multiple QW superlattice grown on a reverse graded virtual substrate (discussed section in 2.5) with a final alloy composition of $Si_{0.05}Ge_{0.95}$. The growth was performed at low temperature to minimise Ge segregation and give sharp interfaces. This is similar to the n-type QCL structures that were grown at a later date in the project. The similarity makes them ideal preparatory structures on which to research growth techniques for the QCL structures. The QCL structures to be grown will feature a more complex active region (seven QWs in each period as opposed to one for the FTIR structures) along with a much greater thickness for the entire growth. Since the QCL structures are so large, their growth time will be extremely long, in the range of 12-60 hrs and consume large amounts of expensive precursor gas. Due to this, first perfecting growth on simpler, smaller structures such as the FTIR structures was highly useful.

5.2.2 FTIR structure design

The FTIR structure growth batch consists of six wafers, each with a different active region design. The entire structure is given in figure 5-5, with the parameters varied between samples given in table 4.

Sample Number	QW Width X(nm)	Spacer Y (nm)	Supply Z (nm)	Supply doping cm^{-3}	R Repeats of active region
11-262	**10.0**	**2.2**	**1.0**	**3.0×10^{18}**	**49**
11-263	**13.0**	**3.0**	**1.0**	**3.0×10^{18}**	**49**
11-264	**16.0**	**3.0**	**2.6**	**1.2×10^{18}**	**49**
11-265	**19.0**	**3.0**	**4.2**	**7.2×10^{17}**	**49**
11-266	**23.0**	**3.0**	**6.3**	**4.8×10^{17}**	**49**
11-267	**19.0**	**3.0**	**4.2**	**7.2×10^{17}**	**100**

Table 4- Variable parameters in FTIR structures

Figure 5-5 - Schematic diagram of FTIR layer structure

A reverse graded, high Ge composition, $Si_{0.05}Ge_{0.95}$ virtual substrate (discussed in section 2.5) was used as a platform on which to grow the structure in order to strain-

balance the superlattice. With the exception of the initial Ge seed layer, the virtual substrate was grown at a relatively high temperature, giving a high growth rate. For the remainder of the growth, the temperature was reduced to 450°C with the aim of reducing Ge segregation, improving interface quality and minimising dopant diffusion. The virtual substrate was capped with a layer of $Si_{0.05}Ge_{0.95,}$ before proceeding with the active region. The active region contains 50 or 100 repeats of Ge layers sandwiched between two $Si_{0.15}Ge_{0.85}$ spacer layers, with an additional $Si_{0.05}Ge_{0.95}$ layer with n-type doping beyond the spacer. The Ge layers are strained and form QWs with their conduction band minimum in the L-direction (section 2.1.4). The separated doped layer supplying carriers to the quantum well [159]. The active region was capped with a 100 nm $Si_{0.05}Ge_{0.95}$ layer, to prevent dopants diffusing to the surface and allow for a top metal contact without destroying the active region, then finally a 3 nm Ge layer to passivate the surface.

5.2.3 FTIR Structure structural characterisation

Following growth, comprehensive material characterisation was performed on the structures. To extract layer thickness and structure quality, cross-sectional TEM was used on the active regions of samples 11-262 to 11-267 and is shown in figures 5-6, to 5-11. The design and measured thickness of the entire active regions are summarised in table 5. It can be observed that the crystal quality is good for all FTIR structures, with no threading dislocations observed, suggesting that the TDD in the active region is low. The contrast and brightness fluctuation in the middle of the active regions (labelled in figure 5-6, since they are very pronounced in this image) are due to mechanical distortion of the sample lamina during sample preparation. For

structure 11-267, in the bottom left region of figure 5-11, what appears to be a dislocation threading arm can be seen. However since it is adjacent to the crater left by ion milling during sample preparation, it is presumed to be an artefact from sample preparation. Micrographs taken from further along the sample did not show any dislocations, but as they were further from the ion milling crater, the lamina was too thick to give good contrast to the superlattice active region. Unfortunately, contrast is poor in all micrographs, this is due to the small change in alloy (15 %) between the barriers and QW's.

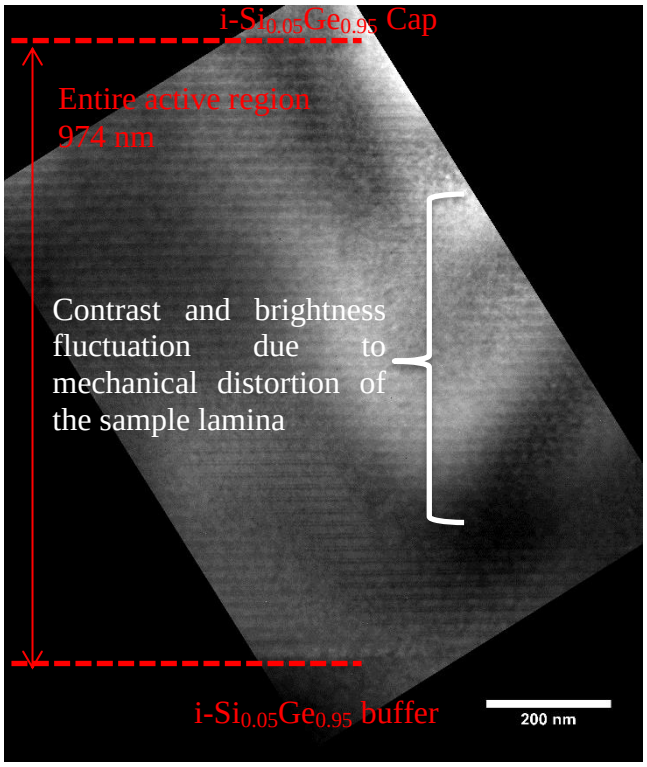

Figure 5-6 - A cross-sectional TEM micrograph of active region for sample 11-262

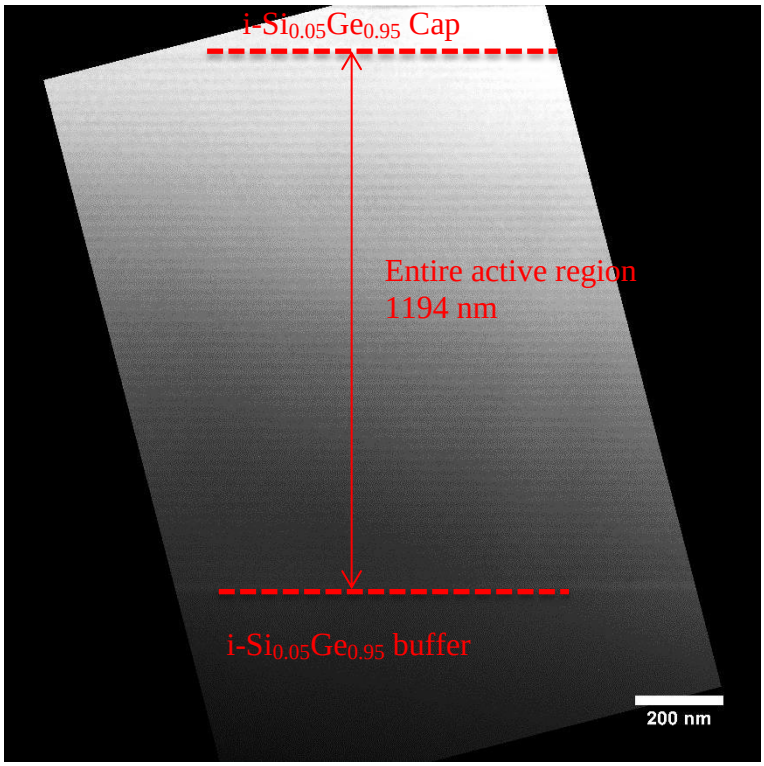

Figure 5-7 - A cross-sectional TEM micrograph of active region for sample 11-263

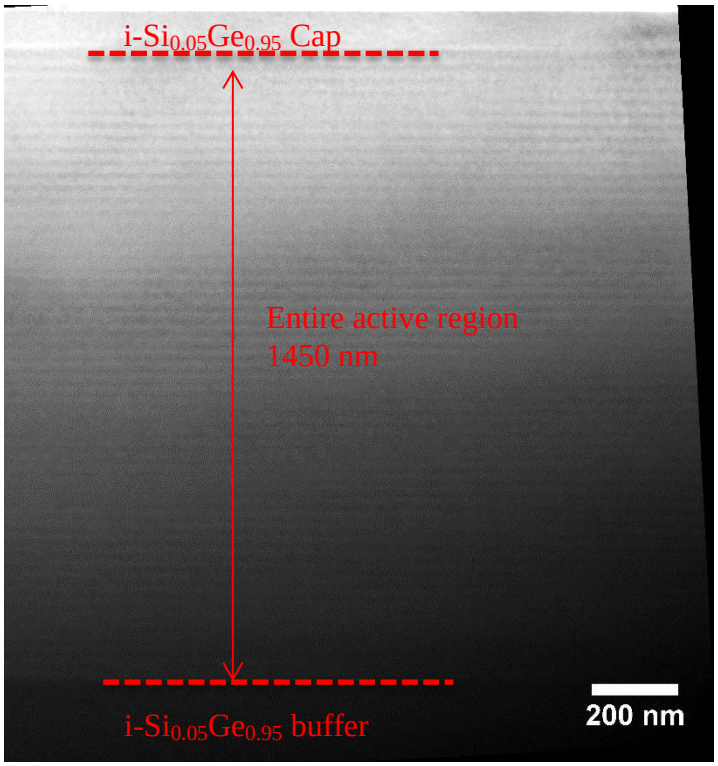

Figure 5-8 - A cross-sectional TEM micrograph of active region for sample 11-264

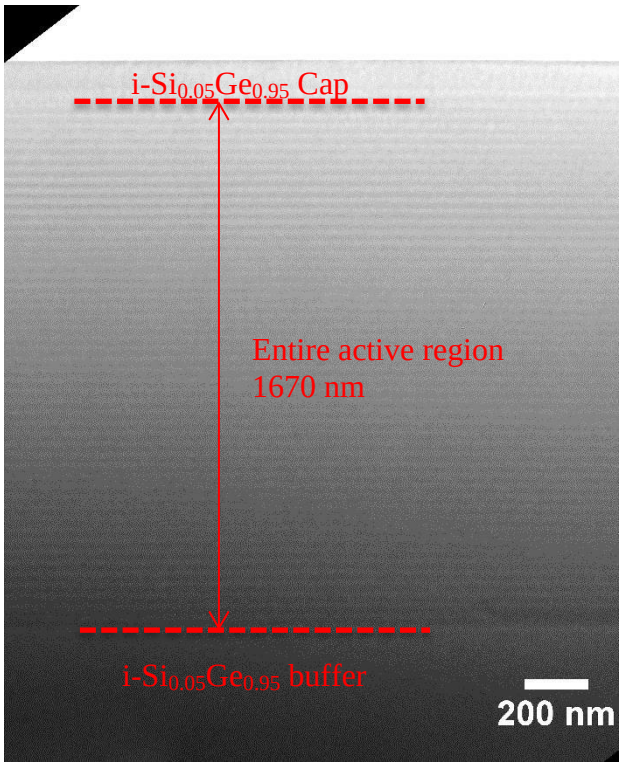

Figure 5-9 - A cross-sectional TEM micrograph of active region for sample 11-265

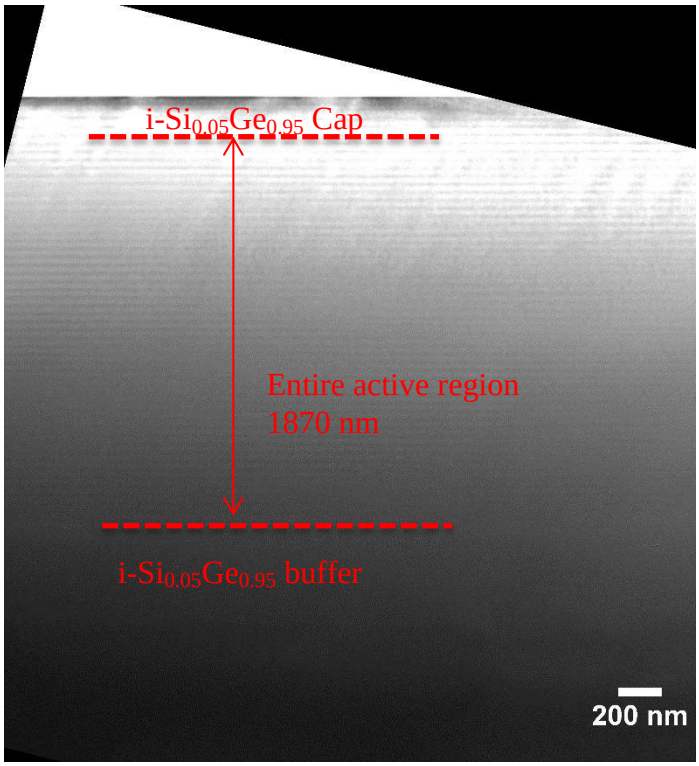

Figure 5-10 - A cross-sectional TEM micrograph of active region for sample 11-266

Figure 5-11 - A cross-sectional TEM micrograph of active region for sample 11-267

To investigate the interface quality and doping density, low energy SIMS was then performed on the structures. The Ge concentration extracted from SIMS measured on the active region is overlaid on a cross-sectional TEM micrographs in figures 5-12 to 5-17 (at a higher magnification than those given earlier) for samples 11-262 to 11-267. The thickness of each layer measured from the cross-sectional TEM are summarised in Table 5. The SIMS shows that the Ge QWs are indeed pure Ge without major Si contamination (all QW plateaus are ~100 % Ge by SIMS profile) and the correct alloy concentration has been reached in the $Si_{0.15}Ge_{0.85}$. Both the Ge/$Si_{0.15}Ge_{0.85}$ and $Si_{0.15}Ge_{0.85}$/Ge barriers are sharp, with an approximate gradient of 0.05% alloy change per nm. For the samples with the thinner supply layers, 11-262 and 11-263, a single sharp unintended peak in Ge concentration is seen at the position of the doped carrier supply layer with an alloy concentration at its peak of

approximately $Si_{0.05}Ge_{0.95}$. For the samples with the thicker supply layers, 11-264, 11-265, 11-266 and 11-267 the peak splits into two separate peaks, which are located at either side of the supply layer. Dopant concentration was also measured for all samples, but was below the dectection limit for the technique (~10^{18} cm^{-3}). The cross-sectional TEM shows that the interfaces are uniform and flat, with the mottled effect being due to sample preparation and the resolution limit of the microscope (figure 5-13). The thin dark line seen between the $Si_{0.15}Ge_{0.85}$ spacers confirms the presence of the Ge concentration spike seen in the SIMS measurement.

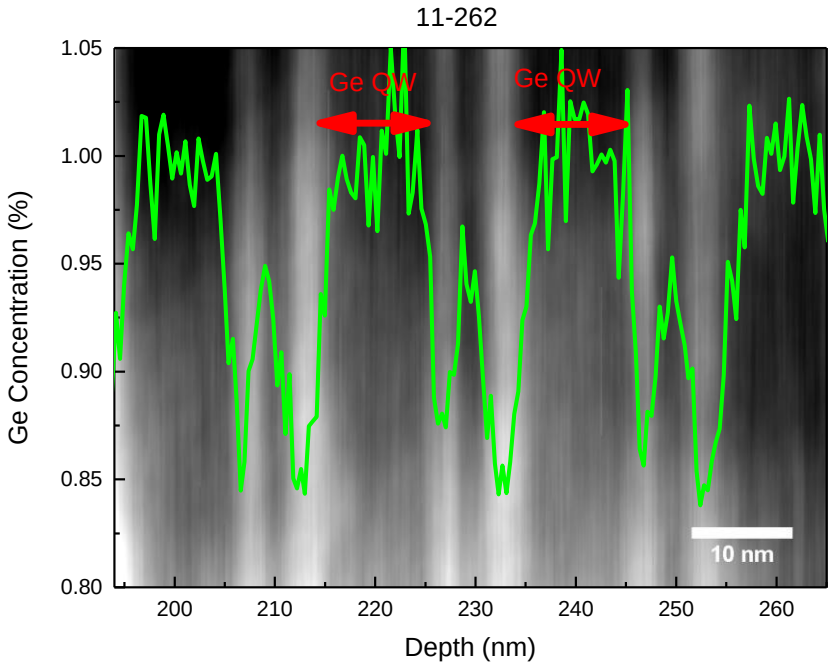

Figure 5-12 – Ge concentration SIMS profile of FTIR structure 11-262 overlaid on cross-sectional TEM micrograph

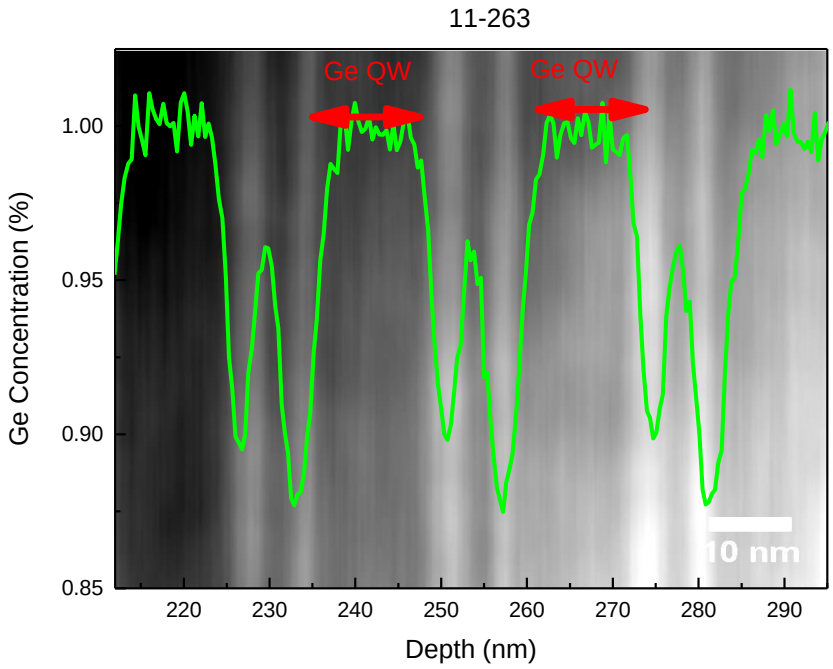

Figure 5-13 - Ge concentration SIMS profile of FTIR structure 11-263 overlaid on cross-sectional TEM micrograph.

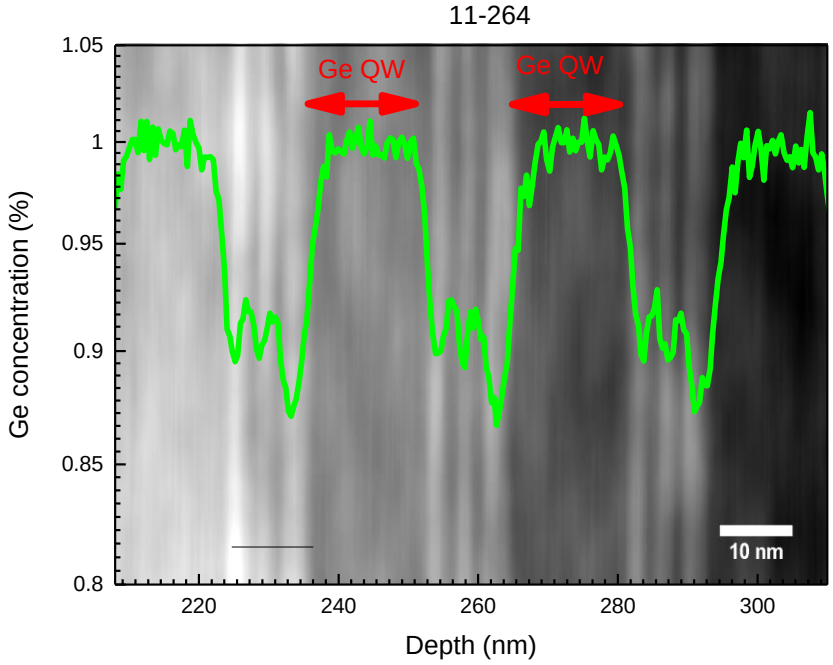

Figure 5-14 - Ge concentration SIMS profile of FTIR structure 11-264 overlaid on cross-sectional TEM micrograph.

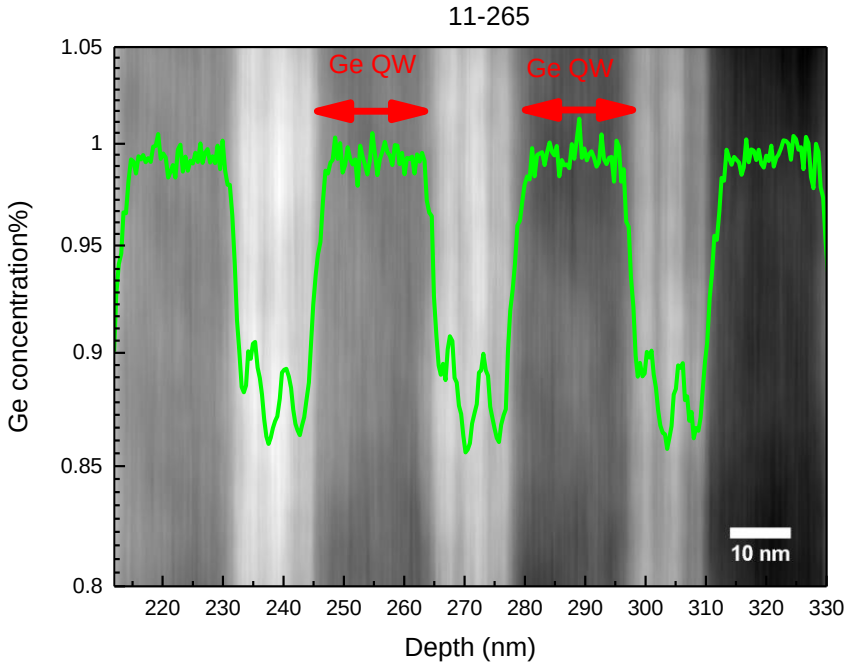

Figure 5-15 - Ge concentration SIMS profile of FTIR structure 11-265 overlaid on cross-sectional TEM micrograph.

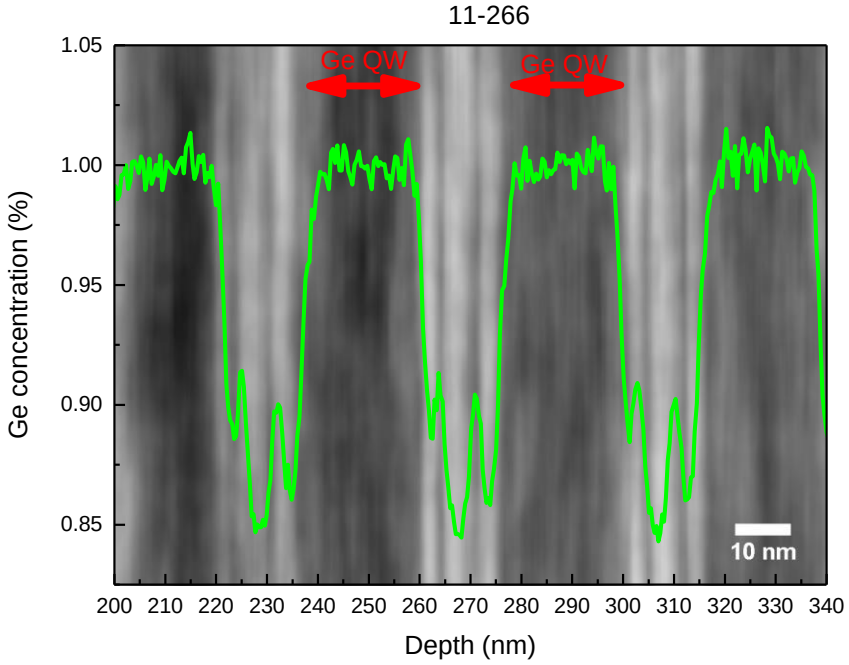

Figure 5-16 - Ge concentration SIMS profile of FTIR structure 11-266 overlaid on cross-sectional TEM micrograph.

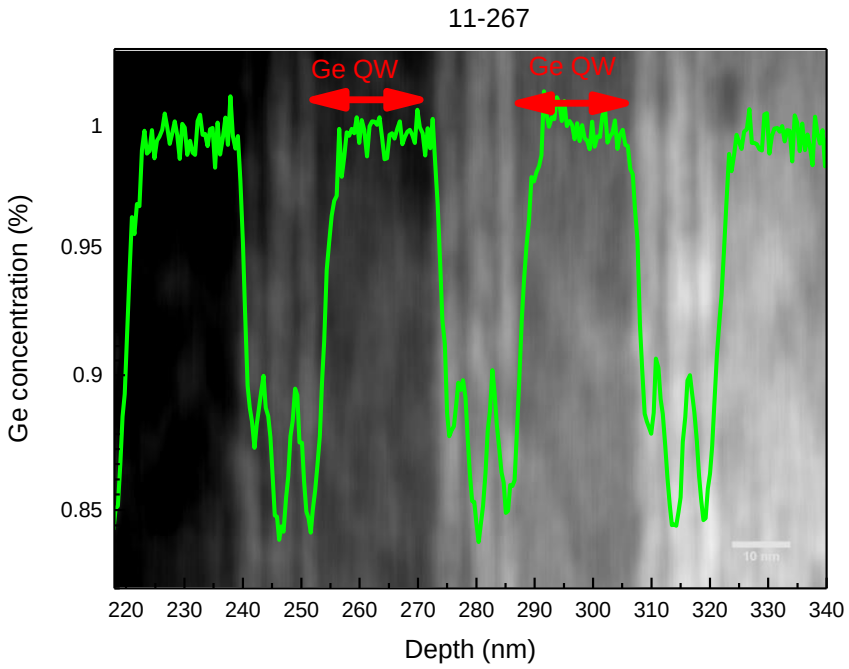

Figure 5-17 - Ge concentration SIMS profile of FTIR structure 11-267 overlaid on cross-sectional TEM micrograph

Symmetric (0 0 4) X-ray ω-2θ scans along with simulated data (the method used for simulation is given in Section 3.5.3) are given for FTIR structures 11-262 to 11-267 in figures 5-18 to 5-22. For the simulation, layer thicknesses were constrained within 2 nm of the TEM results to aid fitting. It can be seen that the experimental data closely matches the simulation. In figure 5-22, it can be seen that one of the higher order superlattice peaks to the left of the $Si_{0.05}Ge_{0.95}$ does not match the experimental data in intensity; this is likely to be due to the wrong barrier/QW ratio in the simulation (this is observable to a lesser degree in figure 5-19 and others). The measured spectrum contains over ten well defined peaks with a low FWHM. From the fitted simulation spectrum, the Ge QWs and $Si_{0.15}Ge_{0.85}$ layers were measured, with the results summarised in table 5.

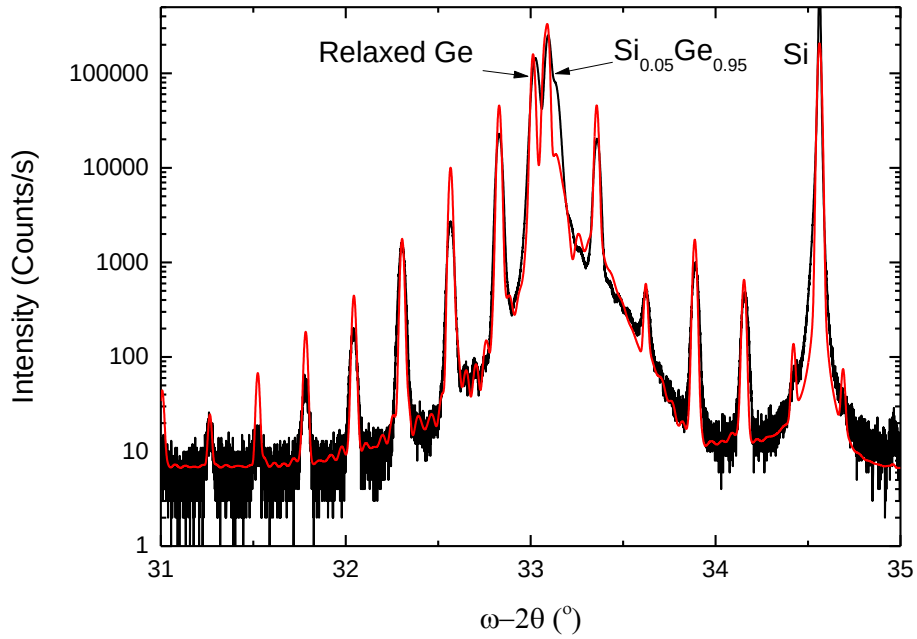

Figure 5-18 - HR-XRD (0 0 4) ω-2θ scans of FTIR superlattice structure 11-262. The measured experimental data is shown (black) along with simulated curve (red).

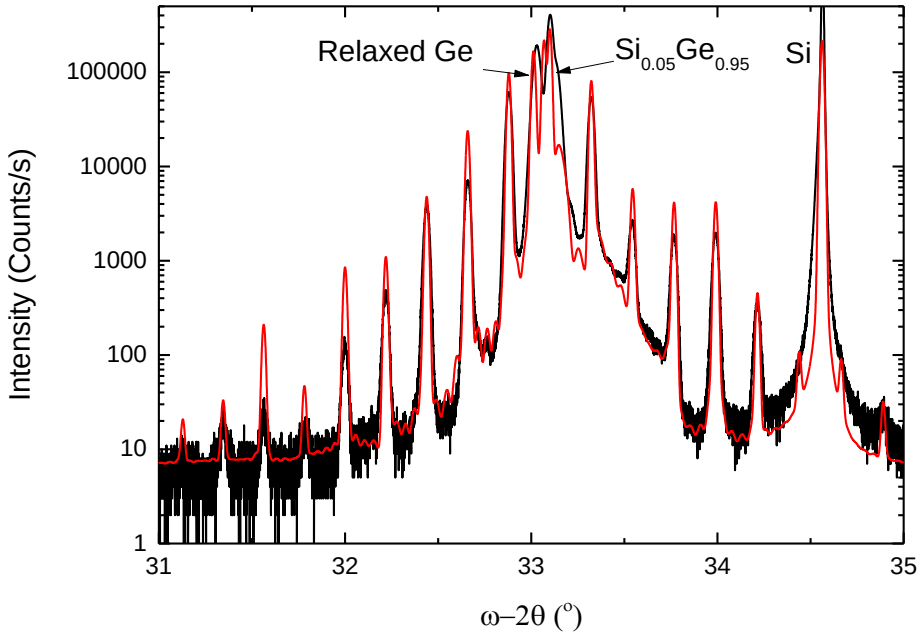

Figure 5-19 - HR-XRD (0 0 4) ω-2θ scans of FTIR superlattice structure 11-263. The measured experimental data is shown (black) along with simulated curve (red).

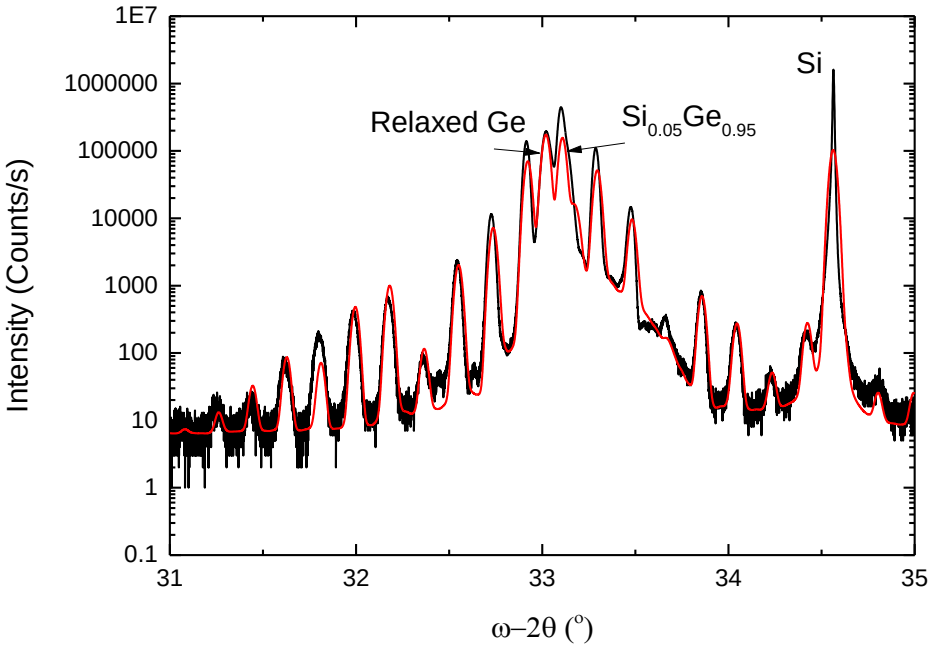

Figure 5-20 - HR-XRD (0 0 4) ω-2θ scans of FTIR superlattice structure 11-264. The measured experimental data is shown (black) along with simulated curve (red).

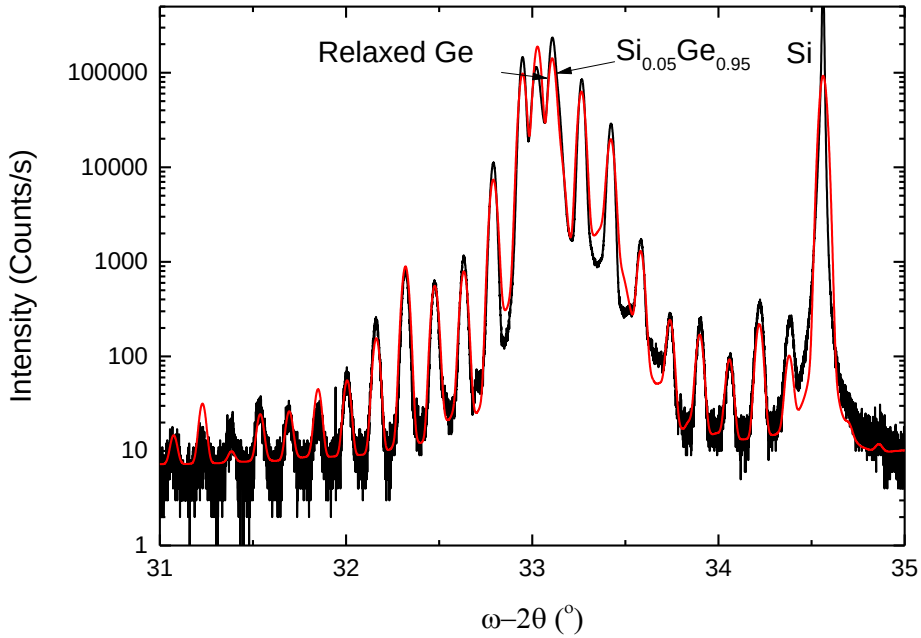

Figure 5-21- HR-XRD (0 0 4) ω-2θ scans of FTIR superlattice structure 11-265. The measured experimental data is shown (black) along with simulated curve (red).

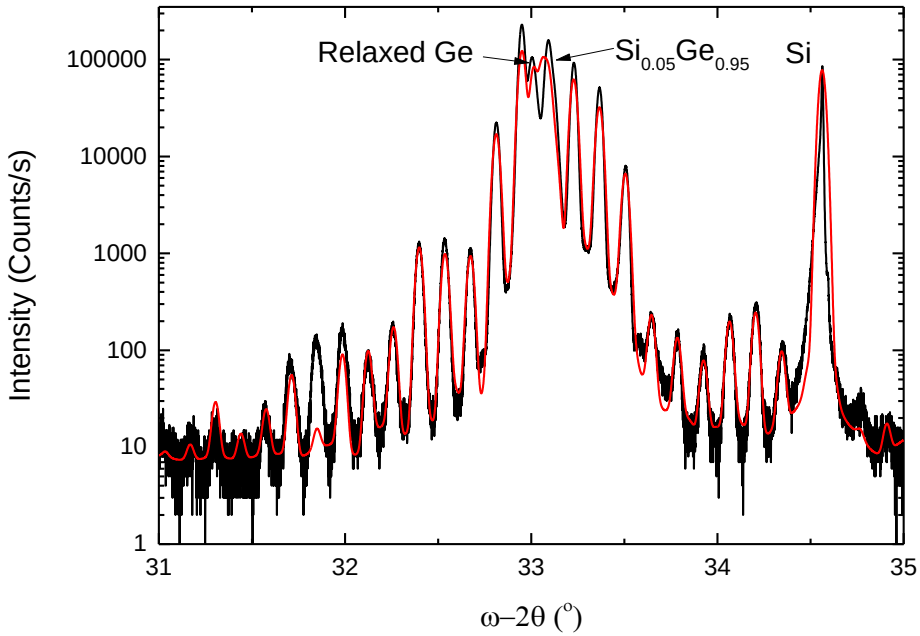

Figure 5-22 - HR-XRD (0 0 4) ω-2θ scans of FTIR superlattice structure 11-266. The measured experimental data is shown (black) along with simulated curve (red).

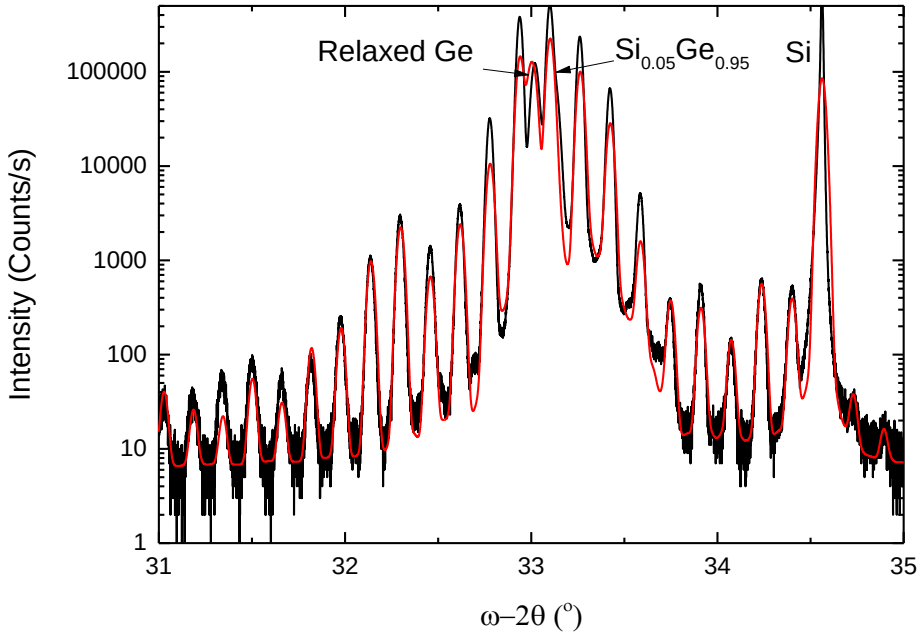

Figure 5-23 - HR-XRD (0 0 4) ω-2θ scans of FTIR superlattice structure 11-267. The measured experimental data is shown (black) along with simulated curve (red).

To investigate the surface morphology AFM was performed on the surface of FTIR structure 11-262, an example of which is given in figure 5-24. Multiple scans were taken from positions across the wafer from which the RMS surface roughness was calculated to be 2.3 ±0.5 nm. A characteristic cross-hatch pattern can be observed. It was assumed that since the growth parameters remain relatively similar for each structure the surface morphology would stay the same. Hence, the results from 11-262 can also be applied to wafers 11-263, 11-264, 11-265, 11-266 and 11-267.

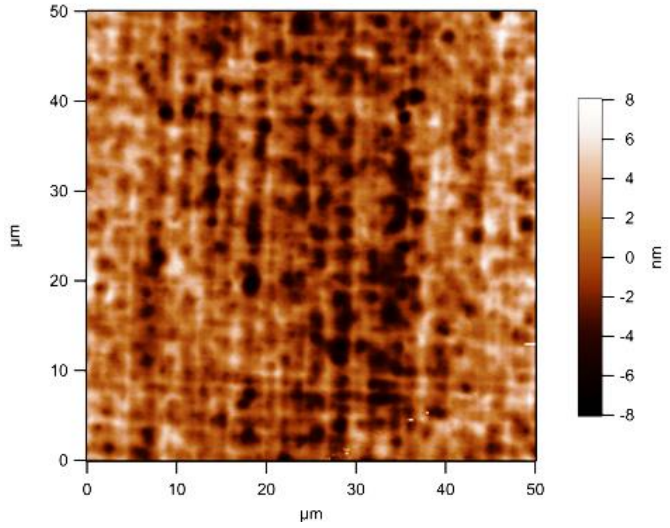

Figure 5-24 - AFM surface representation scan of FTIR superlattice structure 11-262

5.2.4 Summary of FTIR Structure characterisation

Sample Number	Active region width (nm)		QW Width X(nm)			Total SiGe layer width (nm)		
	Design	**TEM ±5 nm**	**Design**	**TEM ±0.5 nm**	**XRD ±0.5 nm**	**Design**	**TEM ±0.5 nm**	**XRD ±0.5 nm**
11-262	**800**	**974**	**10.0**	**10.9**	**10.1**	**5.4**	**9.0**	**9.9**
11-263	**1030**	**1194**	**13.0**	**14.4**	**13.2**	**7.0**	**9.3**	**10.6**
11-264	**1244**	**1450**	**16.0**	**17.2**	**17.2**	**8.6**	**10.8**	**11.0**
11-265	**1490**	**1670**	**19.0**	**19.3**	**19.7**	**10.2**	**11.6**	**13.6**
11-266	**1792**	**1870**	**23.0**	**22.7**	**23.6**	**12.3**	**13.9**	**14.4**
11-267	**2935**	**3424**	**19.0**	**20.4**	**19.9**	**10.2**	**13.6**	**12.8**

Table 5 - FTIR structure design thicknesses compared with those measured by TEM and XRD

5.2.5 Discussion

Strain-symmetrized Ge/$Si_{0.15}Ge_{0.85}$ multiple quantum well superlattice structures have been successfully grown at the low growth temperature of 450°C on a reverse linear graded SiGe/Ge/Si virtual substrate, all of which exhibit good crystalline quality.

Cross-sectional TEM on all FTIR superlattice structures grown shows no large scale roughening or dislocations, indicating a low TDD in the superlattice region. Since no strain relaxation is observed to be occurring in the superlattice then the TDD should be similar to that which is recorded for the underlying high Ge composition reverse linear graded virtual substrates, i.e. ~ $10^6 cm^{-2}$ [97-99].

The following peaks are visible in the ω-2θ scans from all the structures: the Si substrate, the relaxed Ge, the $Si_{0\rightarrow0.05}Ge_{1\rightarrow0.95}$ reverse linearly graded region of the

virtual substrate, the $Si_{0\rightarrow 0.05}Ge_{1\rightarrow 0.95}$ constant composition region, and repeated superlattice peaks from the $Ge/Si_{0.15}Ge_{0.85}$ multiple quantum wells. The repeated superlattice peaks are sharp and extend over a wide scan range, with many higher order peaks visible. This is indicative that that the superlattice is of good crystalline quality, with sharp interfaces and relatively low inter-diffusion between layers. The intensity of the superlattices peaks is strongly affected by inter-diffusion, with the peaks intensity rapidly decreasing with inter-diffusion between layers [160-161].

When the cross-sectional TEM measurement error is taken into account, the Ge QW thickness values are in good agreement with the designed structure, with a maximum variation of ~1 nm larger than the design, giving a relative error of 10% (where the relative error is defined as $= \frac{t_{tem}-t_{design}}{t_{design}} \times 100\%$). The $Si_{0.15}Ge_{0.85}$ regions have a larger deviation from the design than the Ge QWs, with a maximum variation ~3.5 nm larger than the design, giving a relative error of 66%. Unfortunately, the error in the TEM measurement is relatively large (±0.5nm), which is due to the small difference in Ge composition between the barriers and QWs giving little compositional contrast for thin regions of the sample. Multiple TEM images were taken through each of the superlattice structures and each period was found to have the same thickness within this error. This illustrates the reproducible epilayer thickness achievable with RP-CVD over a complete structure that is more than 3 µm thick. Other growth techniques such as solid-state molecular beam epitaxy (SS-MBE) can exhibit significant growth rate drift and fluctuation during growth, with cell outputs differing as much as 2% during the long growth times required to grow such a complex superlattice structure [162].

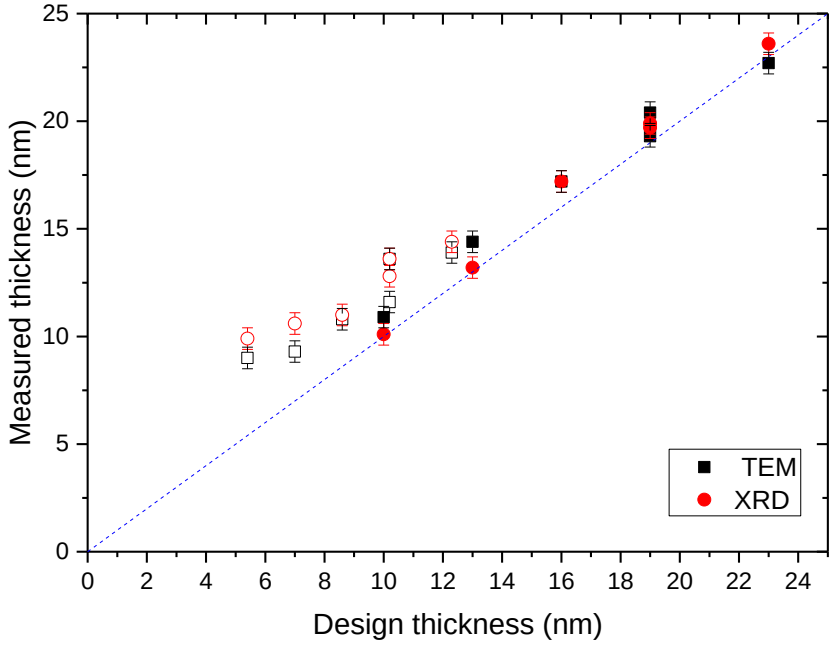

Figure 5-25 - Deviation of measured thickness from design for Ge QWs (filled) and alloy layers (open symbols) from TEM (square) and XRD (circles). The dotted blue line indicates a measured thickness equal to the design thickness.

To investigate whether the variation in grown thickness is systematic or random, the thickness values measured by TEM and by XRD are plotted against the design thickness in figure 5-25. It can be seen that TEM and XRD generally agree within experimental error. Two TEM/XRD thickness measurements not within error arise from samples 11-263 and 11-266 (figures 5-19 and 5-22). These were the X-ray scans with most pronounced difference in intensity for higher order superlattice peaks between the simulation and the measured data. This supports the theory of the wrong barrier/QW ratio in the simulations. For the thicker layers it can be seen that the measured thickness from TEM is in good agreement with the design thickness.

However, for the thinner layers, there is a systematic deviation from the intended thickness which appears to follow a linear trend. It is possible that the systematic variation is either systematic measurement artefact or a systematic growth issue. It is most likely that the variation is a systematic growth issue for the following reasons: even when the error in the measurement techniques is taken into account, the linear variation still holds; both measurement techniques agree on the linear trend; and while it cannot be used to measure individual layers, the TEM micrographs at low resolution corroborate that the active regions are thicker than intended. It is possible that the microscope will introduce systematic errors at certain magnifications, due to incorrect calibration. Since the variation is systematic, the results of the characterisation performed in this study could be used to regrow all the structures with layer thicknesses extremely close to the original design. The possible mechanism behind the non-linear growth rate is discussed in section 5.3.11.

All of the superlattice structures grown have Ge concentration spikes at the interface between the $Si_{0.15}Ge_{0.85}$ doped supply region and the $Si_{0.15}Ge_{0.85}$ spacers. This is caused by Ge surface segregation, where Ge rises to the surface of the growing crystal. The growth is interrupted before and after growing the doped region to allow for the purging and replacement of the gases in the growth chamber, during this time the Ge concentration spikes will be formed since the wafer is kept at the growth temperature during this time which will lead to of some of the Ge on the surface becoming incorporated into the crystal. For the structures with thinner supply layers of 1 nm (11-262, 11-263), only one Ge concentration spike is visible, which is because the spikes from either side of the supply layer have merged due to the small separation.

SIMS and X-ray measurements confirm the QWs are pure Ge for all the superlattice structures grown. For the $Si_{0.15}Ge_{0.85}$ regions, the correct alloy concentration has been reached outside of the Ge concentration spikes. Since the doping is below the detection limit for the SIMS measurements performed, no comment can be made on the dopant diffusion and concentration for all the structures grown. The effects of the growth variations observed on QCL operation are discussed in section 5.3.13.

5.3 Chirped Superlattice Structures

5.3.1 Chirped superlattice growth motivation

With the aim of working towards a functioning Si-based QCL structure, QCL designs were proposed by the University of Leeds. Details of the method used by the University of Leeds to design the structures can be found in references [60] and [163]. The chosen structure utilised a chirped superlattice (CSL) bound-to-continuum design (see section 2.1.2 for an explanation of the bound to continuum design). Chirping refers to a technique where the superlattice well and barrier thicknesses are varied or 'chirped' to compensate for the electric field applied to the superlattice, ensuring that the miniband edges remain at constant energy. The structures are designed to experimentally demonstrate intersubband emission, to study the effect of main quantum well size on emission frequency using an n-type Ge/SiGe on Si (001) QCL structure, and to investigate the effect of changing the size of the main quantum well on the electrical properties. The structures feature a complex seven QW active region and represent challenging epitaxial growth for the relatively immature high Ge content Ge/SiGe system. As with the previously discussed FTIR structures, growth was performed at low temperature to minimise Ge surface segregation, give sharp interfaces and reduce dopant diffusion.

5.3.2 CSL Structure design

The CSL structure growth batch consists of 3 wafers, each with a different active region design, intended show the effect of main quantum well size on emission frequency. The entire structure is given in figure 5-26, with the parameters varied

between samples given in table 6. As with the previously grown FTIR structures, a reverse graded high Ge composition $Si_{0.05}Ge_{0.95}$ virtual substrate was used as a platform on which to strain-balance the superlattices. The virtual substrate is capped with a thick (2 µm), doped bottom contact. Although a high growth temperature for the bottom contact would significantly reduce the growth time and precursor consumption, it was still grown at the lower temperature of 450°C to avoid the large dopant segregation that would otherwise occur from the relatively highly doped bottom contact.

Following the bottom contact, 50 periods of the active region superlattice were grown. The growth temperature for the QCL superlattice structure was 450°C. Each period consists of 14 layers of alternating Ge QWs and $Si_{0.15}Ge_{0.85}$ barriers. A Ge fraction of 0.85 was used for the barriers, since it gives the maximum usable conduction band offset of ~90 meV [118] between the barriers and QWs that can be used for THz QCL design. In each period, barrier #3 to quantum well #6 were n-type doped. It can be seen that it is only the size of the main Ge quantum well that varies between the structures. The periods have been strain-balanced and should have the same in-plane lattice parameter as $Si_{0.05}Ge_{0.95}$ (5.6453 Å). The strain-balance criteria was also shown to be met at the growth temperature. Following the active region, a $Si_{0.05}Ge_{0.95}$ 50nm doped top contact was grown, followed by a Ge cap.

The structures are designed to exhibit electroluminescence and the expected EL spectra has been simulated by the University of Leeds. EL can be used to demonstrate that the correct operation of the structures, even if they do not have sufficient gain to lase. Table 6 gives the frequency of the EL peak position for the

CSL QCL structures predicted from simulation, along with the bias voltage required for operation. It can be seen that the frequency decreases with increasing main QW width and lies in the mid-terahertz range.

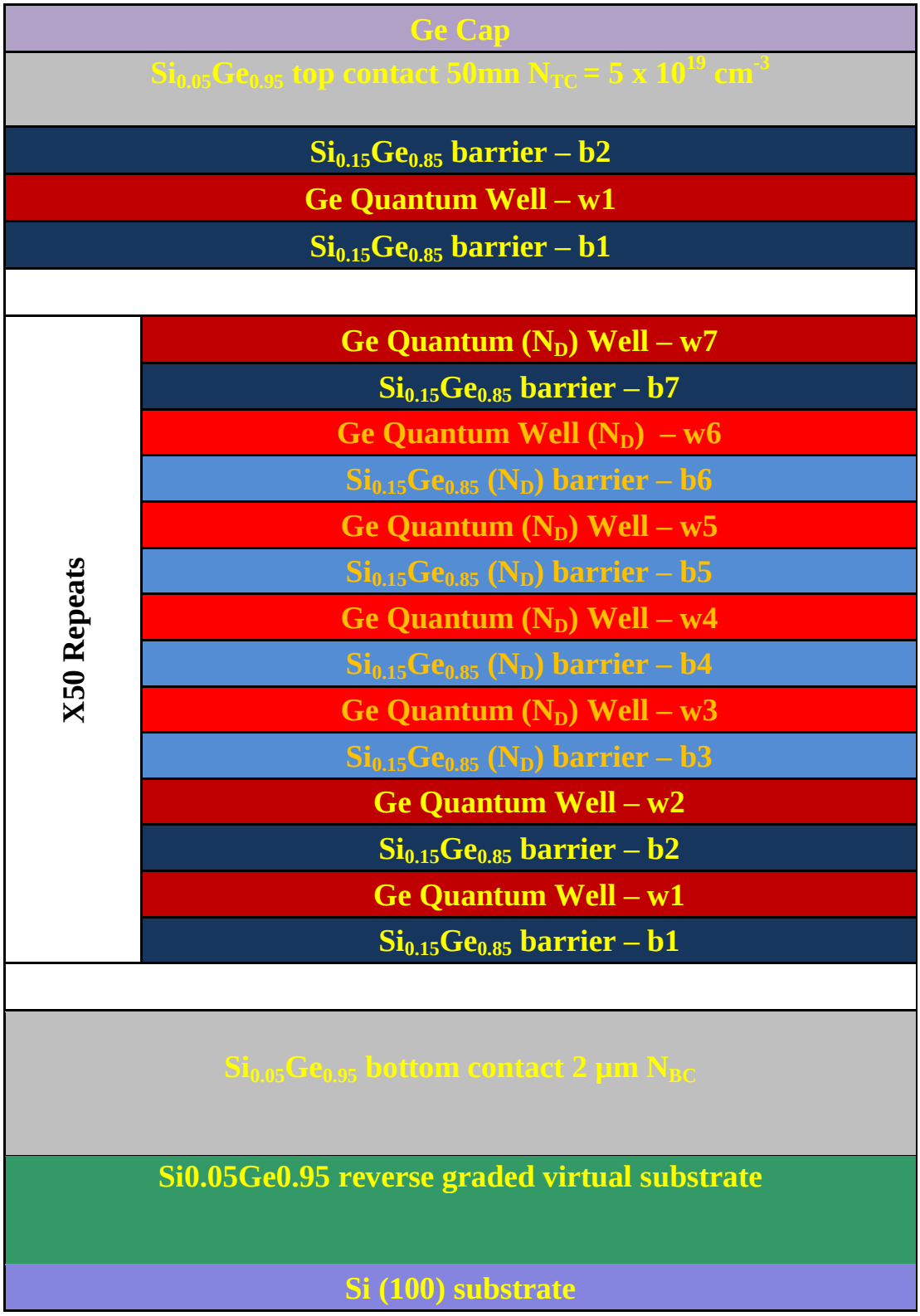

Figure 5-26 - Schematic diagram of CSL structure

Sample Number	CSL 1	CSL 3	CSL 4
b1 (nm)	**4**	**4**	**4**
w1 (nm)	**13**	**17**	**21**
b2 (nm)	**4**	**4**	**4**
w2 (nm)	**8.2**	**8.2**	**8.2**
b3 (nm)	**2.5**	**2.5**	**2.5**
w3 (nm)	**7.0**	**7.0**	**7.0**
b4 (nm)	**3.3**	**3.3**	**3.3**
w4 (nm)	**6.5**	**6.5**	**6.5**
b5 (nm)	**3.5**	**3.5**	**3.5**
w5 (nm)	**6.3**	**6.3**	**6.3**
b6 (nm)	**3.7**	**3.7**	**3.7**
w6 (nm)	**6.2**	**6.2**	**6.2**
b7(nm)	**3.9**	**3.9**	**3.9**
w7 (nm)	**6.0**	**6.0**	**6.0**
N_D (cm-3)	**$4x10^{16}$**	**$4x10^{16}$**	**$4x10^{16}$**
N_{BC} (cm-3)	**$1x10^{18}$**	**$1x10^{18}$**	**$1x10^{18}$**
EL Peak (THz)	**8.05**	**5.50**	**3.95**
Bias (kV/cm)	**4.5**	**4.5**	**4.5**

Table 6 – Barrier and layer thickness's, doping concentrations, expected emission peak position and bias for CSL structures. The main quantum well thickness's which are varied between structures are highlighted in yellow.

For strained Ge, the lowest electron energy in the conduction band occurs at the L-symmetry point of the Brillouin zone, with a significant energy gap to the higher lying Γ- and X-valleys [192]. Consequently, only L-valley electron wavefunctions are relevant to QCL operation. In figure 5-27 the L-valley conduction band profile is given for one period of the CSL 3 structure, together with the probability distribution of the electron wavefunctions. The main 17 nm wide QW, where the radiative transition occurs, is labelled and from simulation performed by the University of Leeds is expected to produce electroluminescence at a frequency of 5.50 THz. The frequency of the EL peak varies with the width of the main QW due to its width

being one of the factors determining the energy offsets between states in the QW. The wavefunctions associated with the other wells form a continuum band that enables the efficient transfer of electrons from the lower radiative state of the main QW in one period into the upper radiative state of the main QW in the next period (see section 2.1.2 for the use of a continuum band in QCL design).

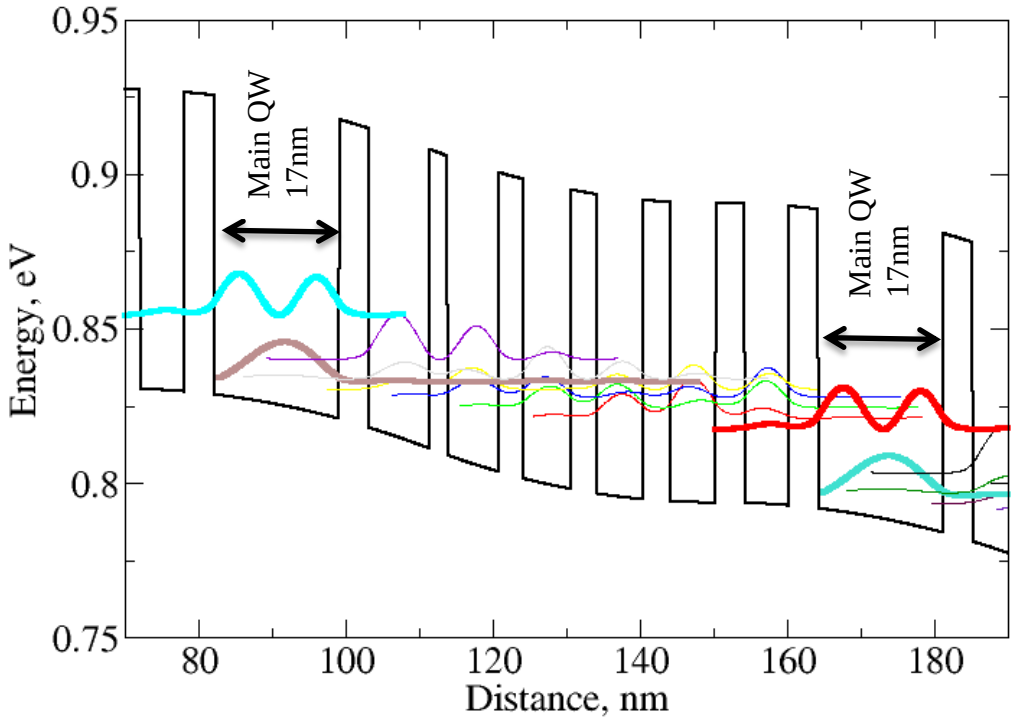

Figure 5-27 - L-valley conduction band diagram of one period of the active region for the QCL CSL 3 structure [164]. The main QW's where the radiative transition takes places are labelled, with their wave functions plotted in thick lines. The wave functions for the other wells are also plotted. A miniband is formed by the wells between the main QW'S.

5.3.3 Initial growth

Following calibration of all the necessary growth parameters, structures were grown using the parameters given in table 6 and named test-CSL 1, test-CSL 3 and test-CSL 4. The growth time was extremely long at ~ 24 hours per wafer. The fact that no issues occurred with the growth system during this time illustrated its capability in

principle to grow structures of this kind. The structural characterisation of these samples is reported in the following section.

5.3.3.1 CSL structures: initial growth

Before any structural characterisation was performed, the samples were noted to be visibly dull and hazy. Wafers with good crystal quality growth should have a mirror like finish. Dulling of the wafers surface is caused by diffuse scattering of light from an extremely rough surface. To ascertain the location in the structure at which the quality of growth was deteriorating, cross-sectional TEM was performed. In figure 5-28, cross-sectional TEM is given for the entire growth. It can be seen that the surface has extremely high roughness, with feature sizes a few microns in size. Cracks are present in the growth, extending through to the substrate. The growth/substrate interface is smooth, suggesting the issue is with growth and not a defective substrate.

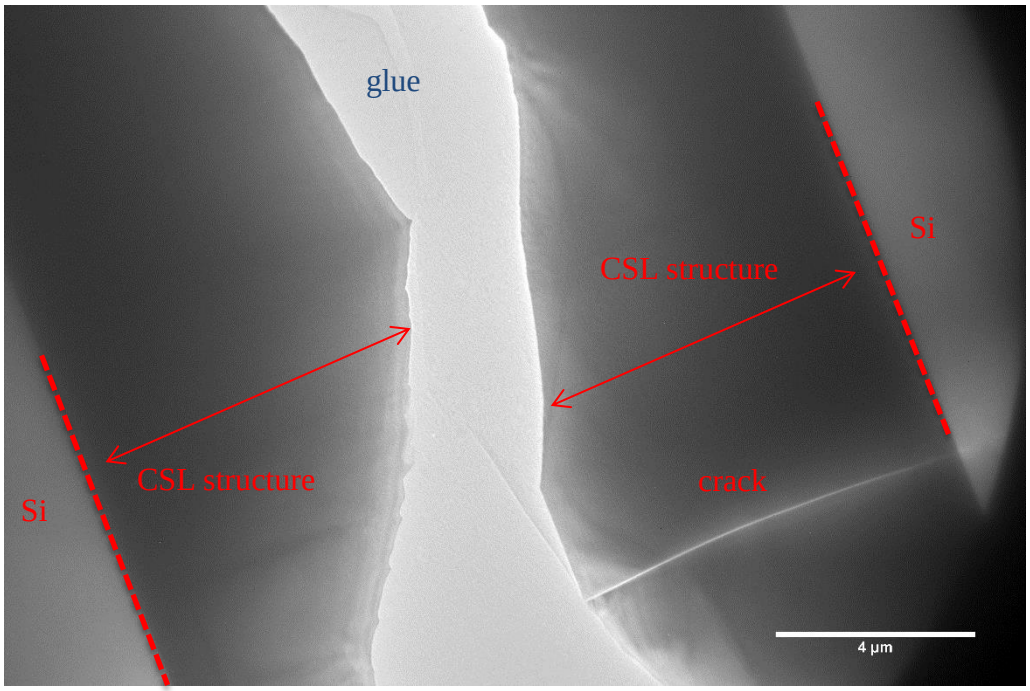

Figure 5-28- A cross-sectional TEM micrograph of initial-CSL QCL superlattice showing entire growth. Two sections of growth are visible, glued face to face during TEM sample preparation. It can be seen the growth is extremely poor quality

In figure 5-29, cross-sectional TEM is given for the bottom contact and a small section of the superlattice growth. The bottom contact/virtual substrate can be seen to be of good crystalline quality. No defects are observed in them and the interface between the bottom contact and superlattice is flat. This suggests that the defective growth is in the superlattice region.

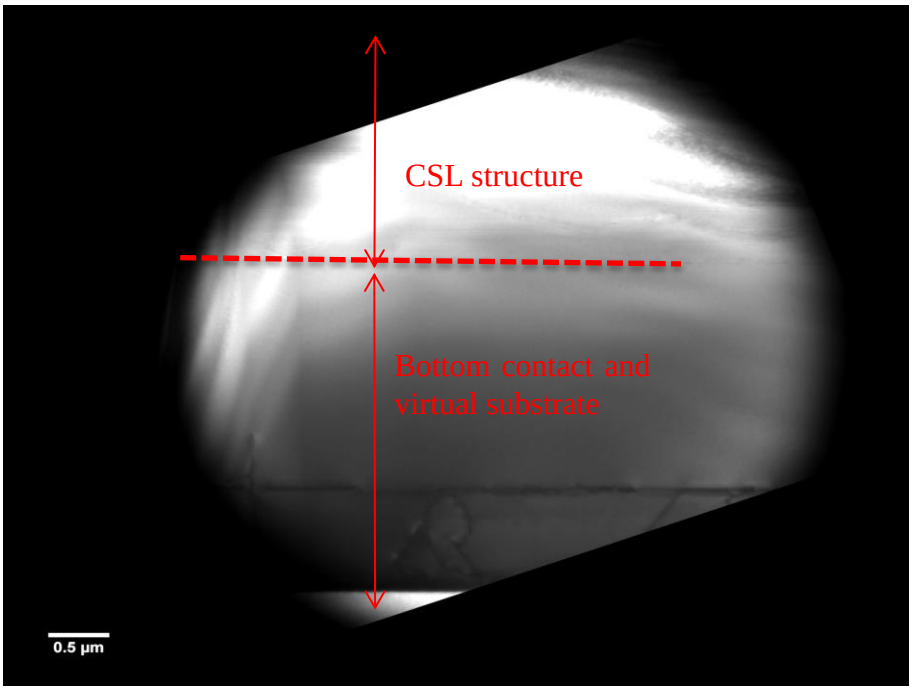

Figure 5-29 - A cross-sectional TEM micrograph of initial-CSL QCL superlattice growth showing virtual substrate, bottom contact and a small section of the superlattice growth.

In figure 5-30, cross-sectional TEM is given for the interface between the bottom contact and the superlattice. While the bottom contact is observed to be of good quality, the interface between it and the superlattice appears rough. The superlattice layers are distorted and have two boundaries running through them, possible caused by stacking faults.

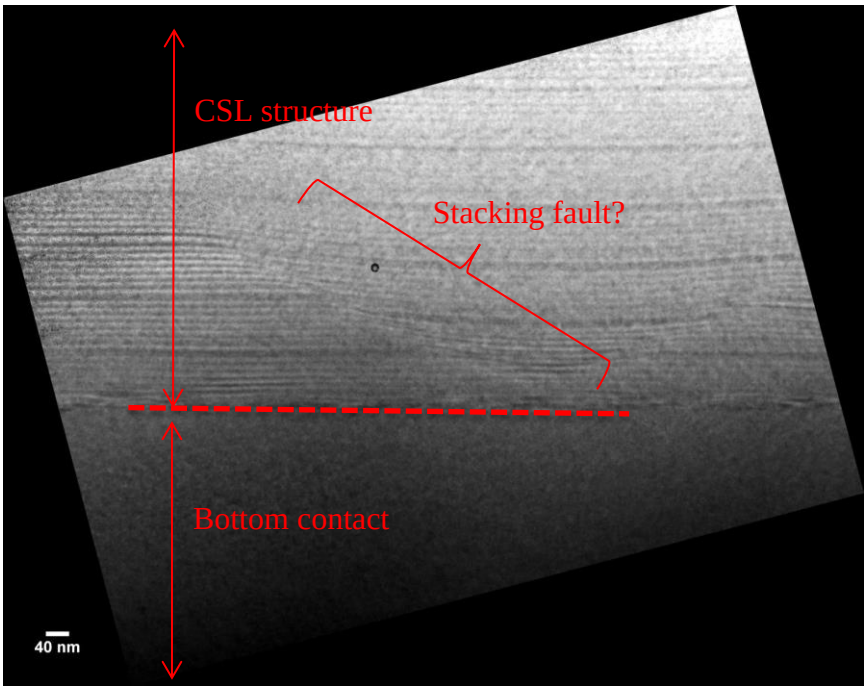

Figure 5-30- A cross-sectional TEM micrograph of initial-CSL QCL structure showing interface between the bottom contact and the superlattice.

In figure 5-31 dark-field cross-sectional TEM is given for the interface between the bottom contact and the superlattice, using the (004) diffraction condition which gives good strain contrast. The superlattice can be seen to be highly defective. The distorted superlattice regions are possibly due to dislocation pile-up.

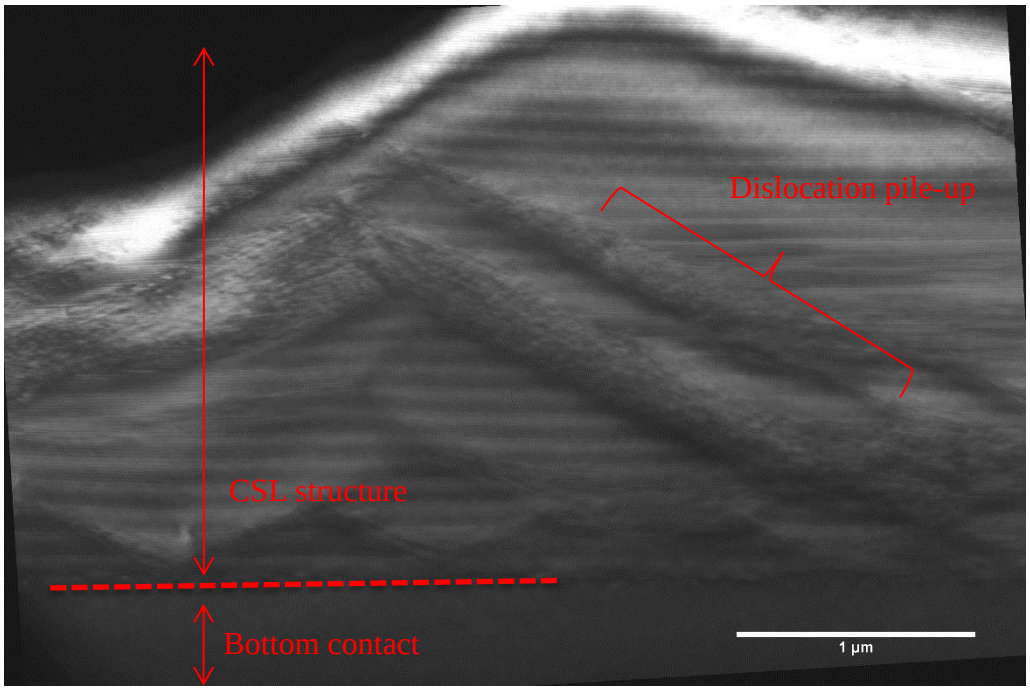

Figure 5-31 – A 004 dark field cross-sectional TEM micrograph of CSL QCL superlattice growth showing interface between the bottom contact and the superlattice.

5.3.4 Discussion

The first attempt at growing the initial-CSL structures was unsuccessful, with the superlattice regions being highly defective. The defective structures were studied by TEM to ascertain why the growth failed.

In all the TEM images, the structure exhibits good crystallinity through the virtual substrate and bottom contact. It is only at the start of the superlattice that growth deteriorates. The deterioration appears to be caused when the strain relaxes by forming dislocations. The strain relaxation could be occurring for a number of different reasons: The thickness of any individual layer in the superlattice could be exceeding its critical thickness, possibly caused by incorrect SiGe alloy

concentration giving the layers a lower than expected critical thickness. Alternatively, the superlattice could be incorrectly strain-balanced and thus have a different in-plane lattice parameter to the platform on which it is grown, in this case the $Si_{0.05}Ge_{0.95.}$

It is unlikely that any individual layer has exceeded its individual critical thickness in the superlattice. For a layer of Ge grown on $Si_{0.05}Ge_{0.95,}$ the critical thickness according to the Matthews-Blakeslee model is ~70 nm, which is far larger than the expected thickness of any Ge layer in the superlattice. This is confirmed by TEM where the entire superlattice region is observed to be defective as opposed to any individual layer. It is also unlikely that the layers have been grown with an incorrect alloy composition since the same precursor flows were used for the previously grown FTIR structures where alloy composition was measured by SIMS and XRD. This leaves incorrect strain balance as the most likely cause of the defective superlattice. This is confirmed by TEM of the structure where the defects can be observed to be forming at the bottom of the superlattice, which is symptomatic of incorrect strain balance (see section 2.4 for a discussion of superlattice strain-balance).

5.3.5 CSL Structure Strain balance

The CSL QCL superlattice is designed to be strain-balanced, with the in-plane lattice parameter matching that of $Si_{0.05}Ge_{0.95.}$ If the superlattice is not strain-balanced, then it can be treated in the same manner as an individual strained layer: If it is grown with a thickness beyond a certain critical thickness, which is determined by the lattice mismatch between the superlattice and its platform, then strain relaxation

occurs in the superlattice. To test the theory that the superlattice was not strain-balanced, intial-CSL1 structure was grown with only three periods, in the hope that this was below the critical thickness for the superlattice. It was not feasible to measure the layer thickness in the original growth because the poor crystal quality made resolving individual layers difficult.

The three-period structure was grown successfully, with good crystal quality in the superlattice. This supports the idea that the previous growth was not strain-balanced. Cross-sectional TEM of the three-period structure is given in figure 5-32. No defects can be observed in the active region and the layers are smooth with abrupt interfaces. The layer thickness was measured from the cross-sectional TEM, giving a total $Si_{0.05}Ge_{0.95}$ thickness of 37.1 ± 0.5 nm and a total Ge thickness of 59.0 ± 0.5 nm for one period. Significantly more $Si_{0.15}Ge_{0.85}$ has been grown than intended, giving the superlattice a smaller in-plane lattice parameter than the original design. The in-plane lattice parameter for the free-standing superlattice was calculated to be 5.6428 Å, which is lattice matched to a $Si_{0.06}Ge_{0.94}$ platform. However, the superlattice was grown on $Si_{0.05}Ge_{0.95,}$ which gives the superlattice a critical thickness of 450 nm from the Matthews-Blakeslee model, a thickness far exceeded in the original 50 period structure growth, explaining the observed strain relaxation.

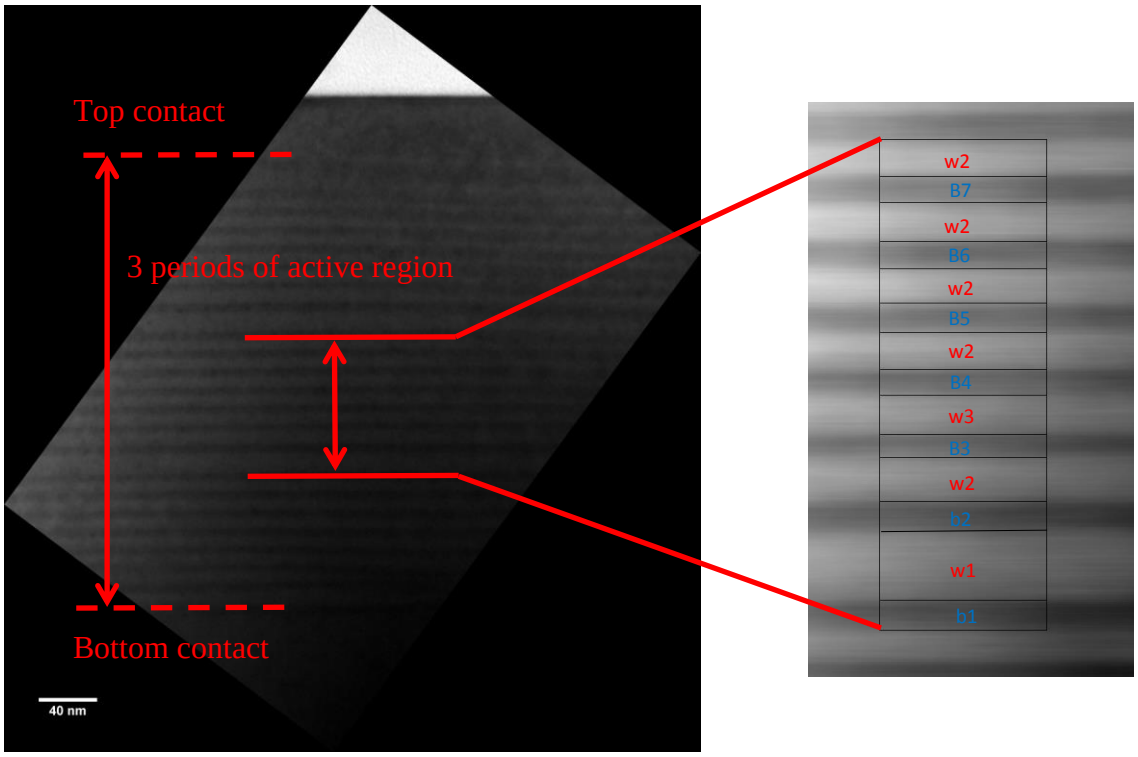

Figure 5-32 – Left - A cross-sectional TEM micrograph of initial-CSL1 QCL structure (grown with only three periods to test for incorrect layers thicknesses causing strain relaxation). The contrast is reversed (Ge is bright, SiGe is dark) due to tilt of the lamina. Right - One period of superlattice magnified from micrograph on left.

5.3.6 Successful growth

A number of growth rate calibration wafers were grown, which used thin layers for calibration as opposed to the original calibration wafers which used relatively thick layers. It was found that for thin layers, the growth rates deviate from those for thick layers (as previously noticed for the FTIR samples), with a nonlinear relationship between growth time and layer thickness. Through a process of iteration, new layer growth times were calculated for the next batch of CSL QCL structures.

Following adjustment of the layer growth times, the CSL structures were grown successfully. In this section, the structural characterisation of these structures is

reported. The successfully grown structures were named CSL 1, CSL 3 and CSL 4 and were again studied first by cross-sectional TEM to investigate the growth quality.

5.3.7 Quantum cascade laser structure CSL 1 structural characterisation

Bright-field TEM of the entire growth for structure CSL 1 is shown in figure 5-33. The contrast in the bottom half of the image is relatively low, because the wedge shape of the TEM lamina following ion beam polishing means this part of the lamina is thicker and so less transparent to electrons. It can be observed that the active region is of high quality, with all dislocations present terminating in the large bottom contact before reaching the active region.

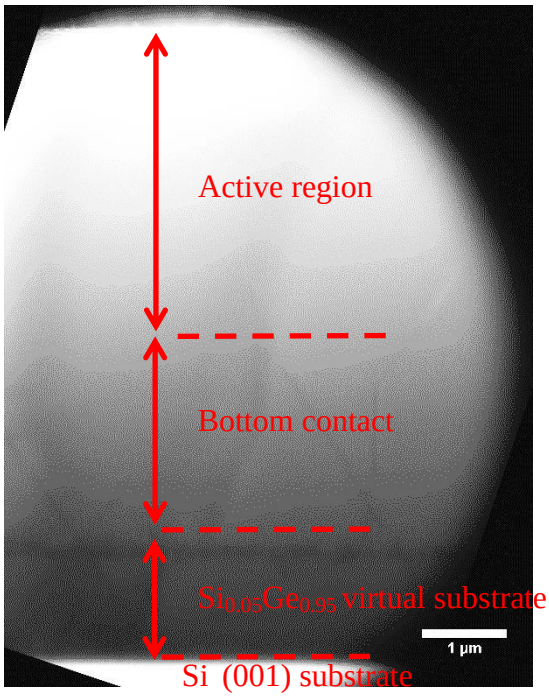

Figure 5-33 - Cross-sectional TEM micrograph of entire growth for sample 12-81, structure CSL 1

The use of conventional TEM for studying the thickness and interfaces of the layers in the active region is not ideal. The small alloy variation in the layers gives very little contrast between layers and at atomic resolution, the Ge/$Si_{0.15}SiGe_{0.85}$ layers are indistinguishable. Depending on the diffraction condition used, strain also causes contrast fluctuations, interfering with layer thickness measurements. To provide more accurate characterisation HAADF-STEM was used. HAADF-STEM gives a high Z contrast when compared with conventional TEM and has been observed to give good contrast between SiGe layers with an Ge composition difference as low as 2 % [139].

Due to the relatively large size of one period of the active region in the CSL 1 QCL structure, it was split into four sections for imaging by HAADF-STEM, as shown in figures 5-34 b) to 5-37 b). It can be seen that even at atomic resolution, HAADF-STEM gives excellent alloy contrast between the $Si_{0.15}Ge_{0.85}$ barriers and the Ge quantum wells. The interfaces are observed to be smooth with no defects. To calibrate the scale on the HAADF-STEM images, the Ge monolayer was used as an internal reference.

To extract the thickness of each layer from the images, a line profile was extracted of the relative intensity with vertical position. The differential of the relative intensity was taken and converted to an absolute value. This is referred to as the absolute differential in this study. The relative intensity and absolute differential of the relative intensity is given in figures 5-34 a) to 5-37 a). The peak positions in the absolute differential of the relative intensity plot correspond to the interface locations. Peak positions were extracted by fitting Gaussian profiles to the peaks.

It can be observed that the interfaces between layers extend over ~2 nm and that the $Si_{0.15}Ge_{0.85}$/Ge interfaces (Ge grown on top of $Si_{0.15}Ge_{0.85}$) are sharper than the Ge/$Si_{0.15}Ge_{0.85}$ interfaces ($Si_{0.15}Ge_{0.85}$ grown on top of Ge). This can be seen in the HAADF-STEM images and is also visible in the relative intensity and absolute differential of the relative intensity plots. The $Si_{0.15}Ge_{0.85}$/Ge interfaces have a higher gradient in the relative intensity plots than the Ge/$Si_{0.15}Ge_{0.85}$ interfaces and thus have peaks with a smaller FWHM in the absolute differential of the relative intensity. This suggests smearing of the Ge/$Si_{0.15}SiGe_{0.85}$ interface in the growth direction. The interfaces observed by HAADF-STEM may differ slightly from the as-grown interfaces as a result of looking through the thick TEM sample lamina (~50 nm) and due to smearing from sample preparation.

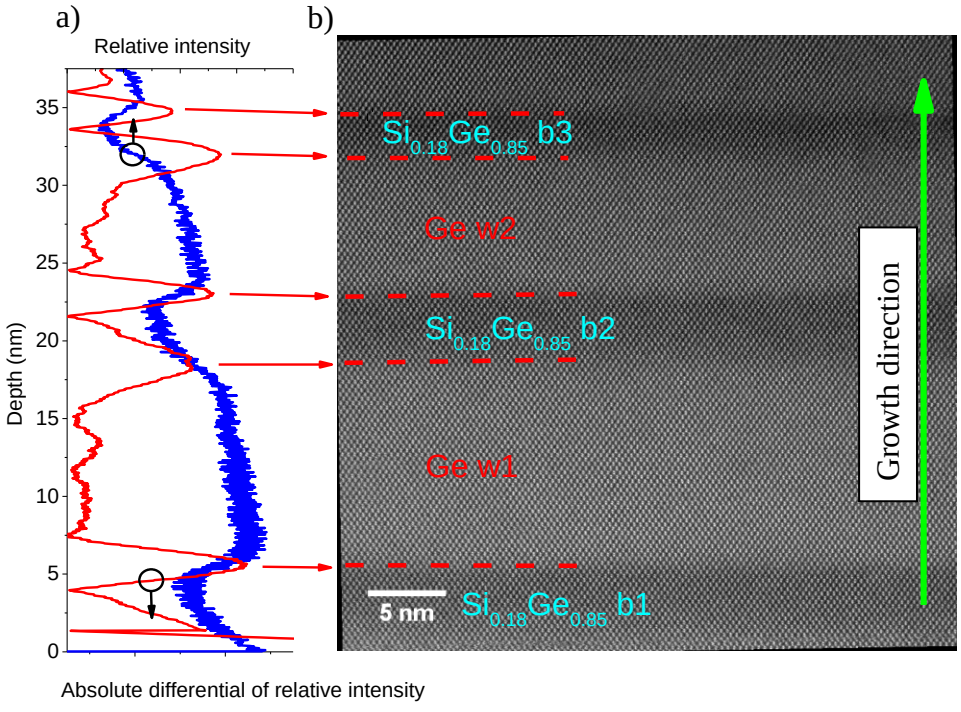

Figure 5-34 – a) Relative intensity (blue line) and absolute differential of relative intensity (red line) b) HAADF-STEM of CSL 1 QCl structure showing SiGe barriers b1 to b3.

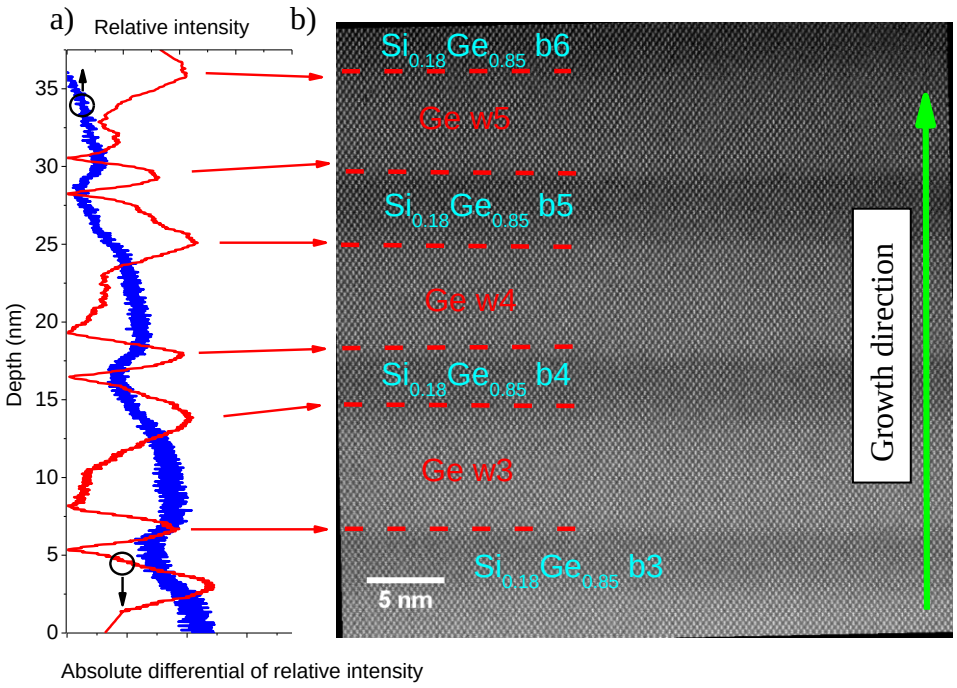

Figure 5-35 – a) Relative intensity (blue line) and absolute differential of relative intensity (red line) b) HAADF-STEM of CSL 1 QCl structure showing SiGe barriers b3 to b6.

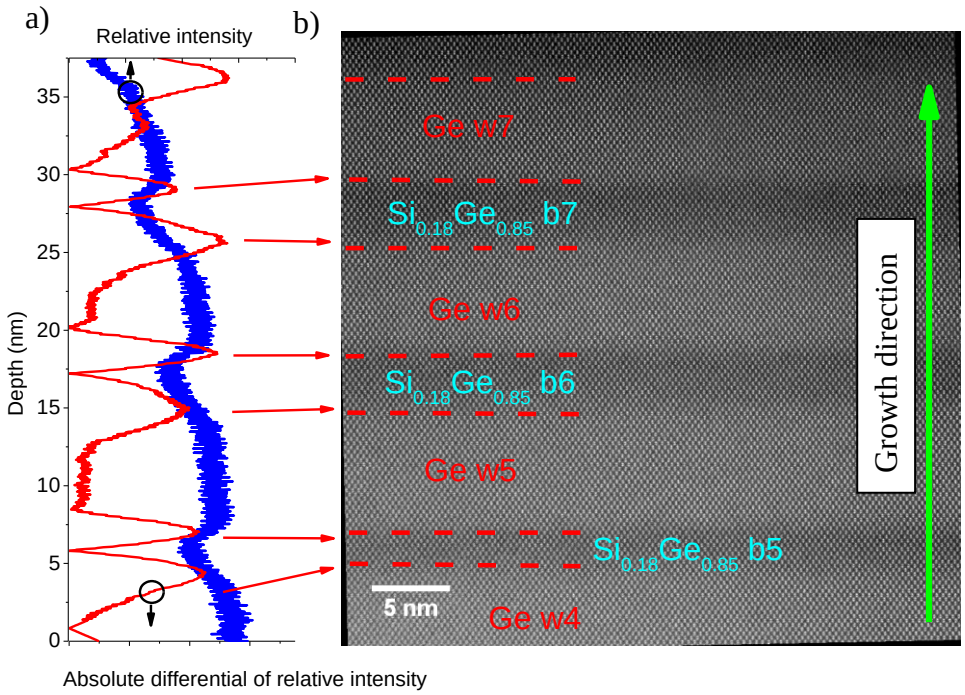

Figure 5-36 – a) Relative intensity (blue line) and absolute differential of relative intensity (red line) b) HAADF-STEM of CSL 1 QCl structure showing SiGe barriers b5 to b7.

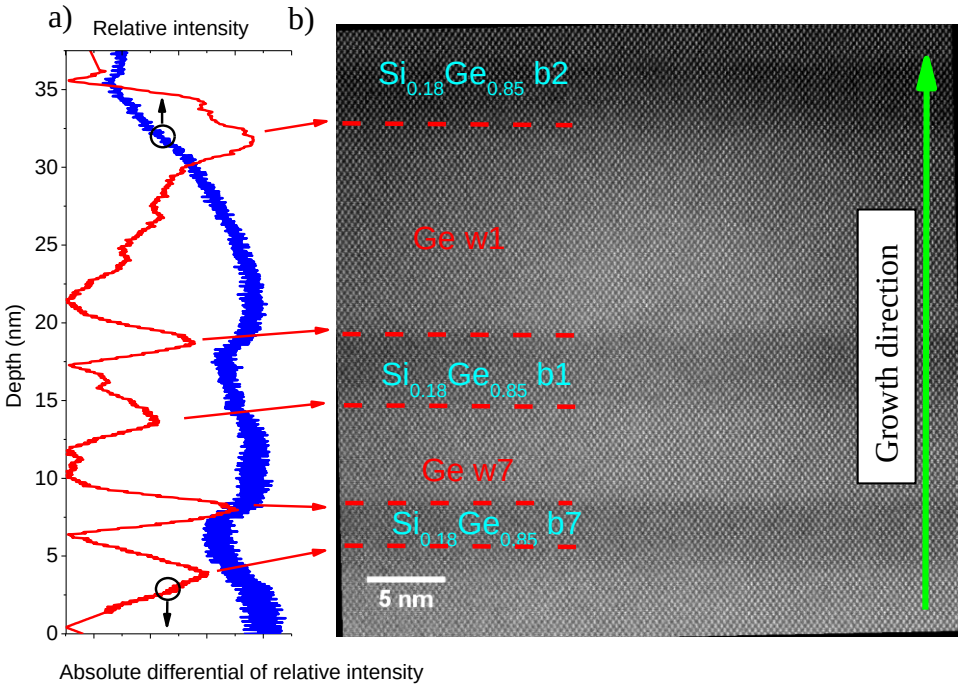

Figure 5-37- a) Relative intensity (blue line) and absolute differential of relative intensity (red line) b) HAADF-STEM of CSL 1 QCl structure showing SiGe barriers b7 to b2.

5.3.7.1 CSL1 12-81 structural characterisation by APT

In order to corroborate the QW/barrier interface quality as measured by HAADF-STEM, atom probe tomography (APT) was performed on the structures. In figure 5-38, an atom probe tomograph is given for QCL structure CSL 1. This measurement was taken at Tohoku University and full credit goes to Yasuo Shimizu, Masaki Shimodaira, Hisashi Takamizawa, Koji Inoue and Yasuyoshi Nagai. The measurement confirms that the $Si_{0.15}Ge_{0.85}$ alloy composition is correct and that pure Ge has been achieved in the QWs. On close inspection, it can be seen that the Ge QWs are smeared in the growth direction.

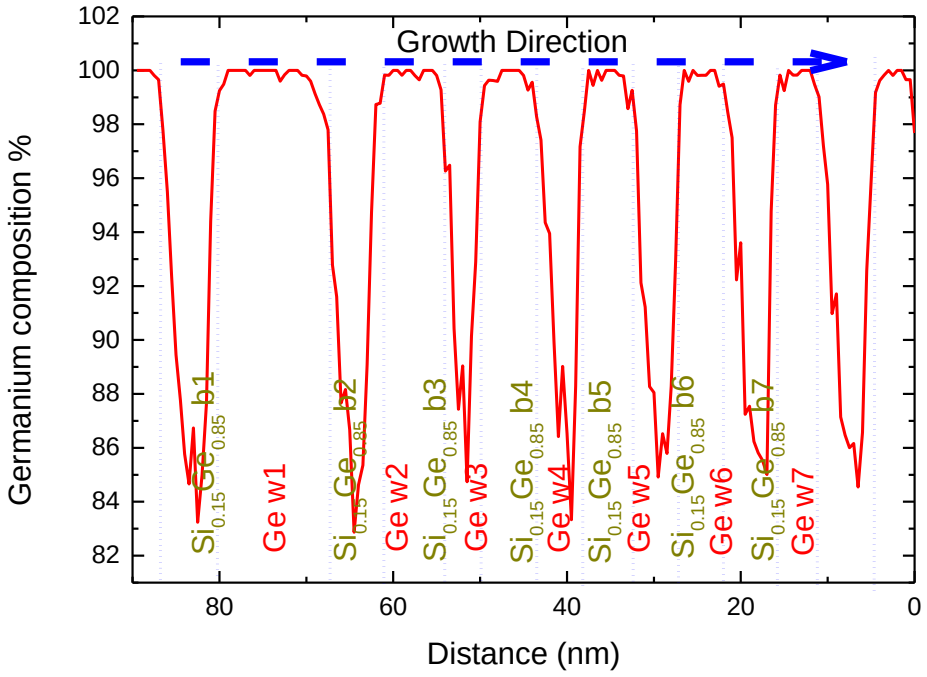

Figure 5-38 - Ge concentration profile for QCL structure CSL 1 from APT performed at Tohoku University with credit to Yasuo Shimizu, Masaki Shimodaira, Hisashi Takamizawa, Koji Inoue and Yasuyoshi Nagai.

In figure 5-39, APT is compared with HAADF-STEM relative intensity, for a single $Si_{0.15}Ge_{0.85}$ barrier, b2. It can be observed that the $Si_{0.15}Ge_{0.85}$/Ge interface is far sharper than that of the Ge/$Si_{0.15}Ge_{0.85}$ interface. The Ge/$Si_{0.15}Ge_{0.85}$ interface is ~2.9 nm and that for $Si_{0.15}Ge_{0.85}$/Ge is ~1 nm. HAADF-STEM is in good agreement with APT on the asymmetrical barrier shape. This confirms the value of HAADF-STEM in measuring interface quality and shows that the sample has not been degraded by the STEM sample preparation.

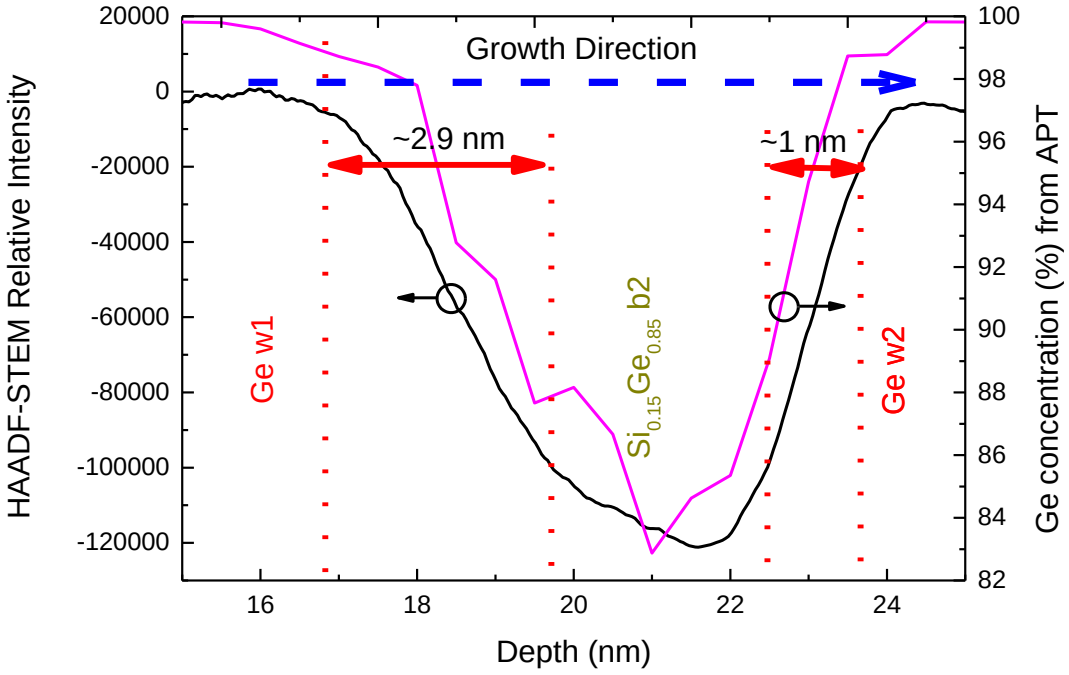

Figure 5-39 –Profile of $Si_{0.15}Ge_{0.85}$ barrier 2 from QCL structure CSL 1. APT (pink line) and relative intensity from HAADF-STEM (black line) are given for comparison. The approximate positions of the wells and interfaces are marked in dotted red lines.

The thickness of each layer in the CSL 1 QCL structure extracted using HAADF-STEM are given in table 7. The thickness of the main quantum well, W1, is in excellent agreement with the design. However, some deviation from the design thickness is seen for the thinner layers. The thickness of the entire period is in reasonable agreement with the design, having a 9% discrepancy.

Sample Number	CSL 1 Design thickness (nm)	Thickness from HAADF-STEM (nm) (± 0.2)	% error
b1 (nm)	**4.0**	**4.7**	**18**
w1 (nm)	**13.0**	**13.0**	**0**
b2 (nm)	**4.0**	**4.5**	**12**
w2 (nm)	**8.2**	**9.0**	**10**
b3 (nm)	**2.5**	**3.7**	**48**
w3 (nm)	**7.0**	**7.1**	**1**
b4 (nm)	**3.3**	**4.0**	**22**
w4 (nm)	**6.5**	**8.3**	**28**
b5 (nm)	**3.5**	**2.9**	**19**
w5 (nm)	**6.3**	**7.9**	**25**
b6 (nm)	**3.7**	**3.6**	**3**
w6 (nm)	**6.2**	**7.2**	**15**
b7(nm)	**3.9**	**3.4**	**13**
w7 (nm)	**6.0**	**6.1**	**2**
Total thickness	**78.1**	**85.2**	**9**

Table 7 - Layer thicknesses extracted from HAADF-STEM. The main QW is highlighted in yellow.

Since the phosphorus doping was below the detection limit of ATP, low energy SIMS was also performed on QCL structure CSL 1. This is presented in figure 5-40 where SIMS profiles are given showing secondary ion intensity for Si and P doping concentration. The depth resolution is very poor for both the Si and P profiles and so individual wells and barriers cannot be resolved. The peak doping value in the spikes is approximately$3 \times 10^{17}\text{atoms/cm}^{-3}$, approximately $1 \times 10^{16}\text{atoms/cm}^{-3}$ in the undoped region and approximately $5 \times 10^{16}\text{atoms/cm}^{-3}$ averaged over the doped region.

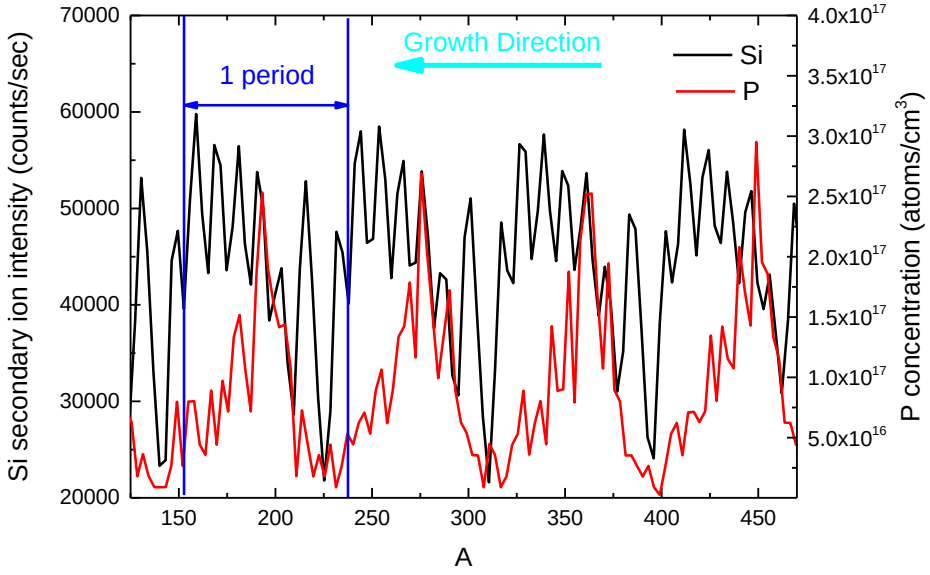

Figure 5-40 - SIMs profile showing secondary ion intensity for Si (black line) and P (red line) doping concentration

To extract the strain state of the superlattice, an ω-2θ scan was performed. In figure 5-41, the HR-XRD symmetric (004) ω-2θ scan is given for CSL 1 structure along with simulated data. The measured spectrum contains many superlattice peaks with a small FWHM. Due to the relative complexity of the superlattice period, when fitting the spectrum it was found that the fit could converge on many different permutations. To give the fit shown, it was necessary to impose limits of ± 1 nm on the fitting parameters using layer thicknesses measured by HAADF-STEM. Layer compositions were also fixed to those predetermined from prior calibration samples. However since extremely accurate layer thickness values were from HAADF-STEM, it was not necessary to extract these from the X-ray scan simulation.

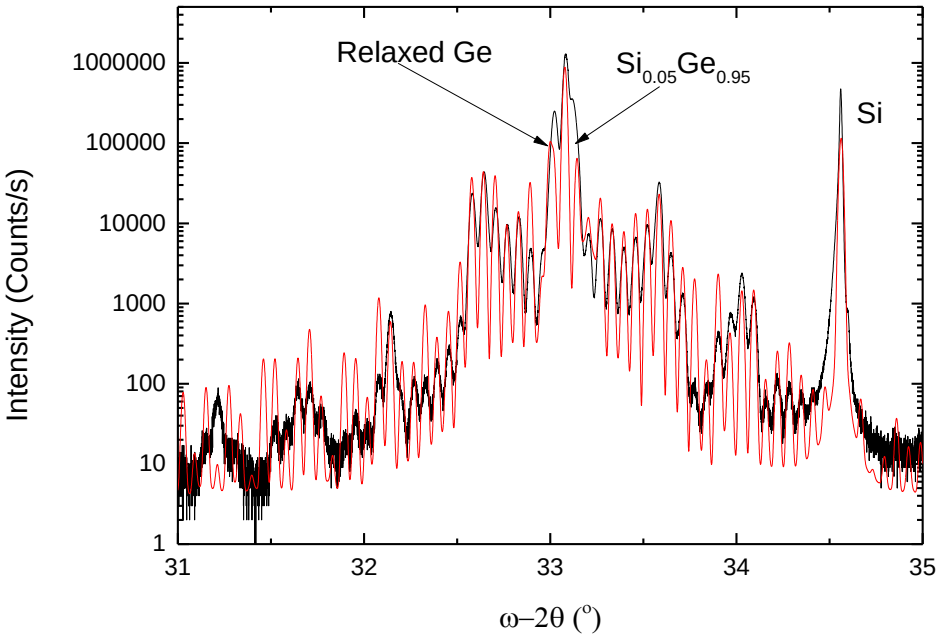

Figure 5-41 - HR-XRD (0 0 4) ω-2θ scans of QCL CSL1 superlattice structure. The measured experimental data is shown (black) along with simulated curve (red).

In addition to ω-2θ scans, symmetric (004) and asymmetric (224) RSMs were also measured for the three CSL QCL samples. Tilt can occur in superlattices and while this is not measurable by (004) ω-2θ scan, it is visible in the (004) RSM. Information on the strain state and composition can also be inferred from the RSMs.

In figure 5-42 the symmetric (004) RSM and in figure 5-43 the asymmetric (224) RSM are given for QCL structure CSL 1. In both RSMs, the Si peak is relatively weak, this is due to the thick superlattice region attenuating the beam before it reaches the substrate and is not a sign of misalignment. In the (004) RSM, figure 5-42, the red line is a guide to illustrate any tilt in the growth. If tilt is present, then the layer peaks will have a different $q_{\parallel}$ to that of the Si substrate peak and lie to the side of the red line. It can be seen that all the peaks have the same $q_{\parallel}$, indicating that

there is no tilt. In the (224) RSM, figure 5-43, the black line is a guide to illustrate 100% relaxation and the red line represents peaks from layers with the same in-plane lattice parameter as bulk $Si_{0.05}Ge_{0.95.}$ It can be seen that the $Si_{0.05}Ge_{0.95}$ buffer is fully relaxed and since all of the peaks arising from the Ge QWs and $Si_{0.15}Ge_{0.85}$ barrier layers are perfectly aligned to the red line, they must be fully strained to the $Si_{0.05}Ge_{0.95}$ buffer.

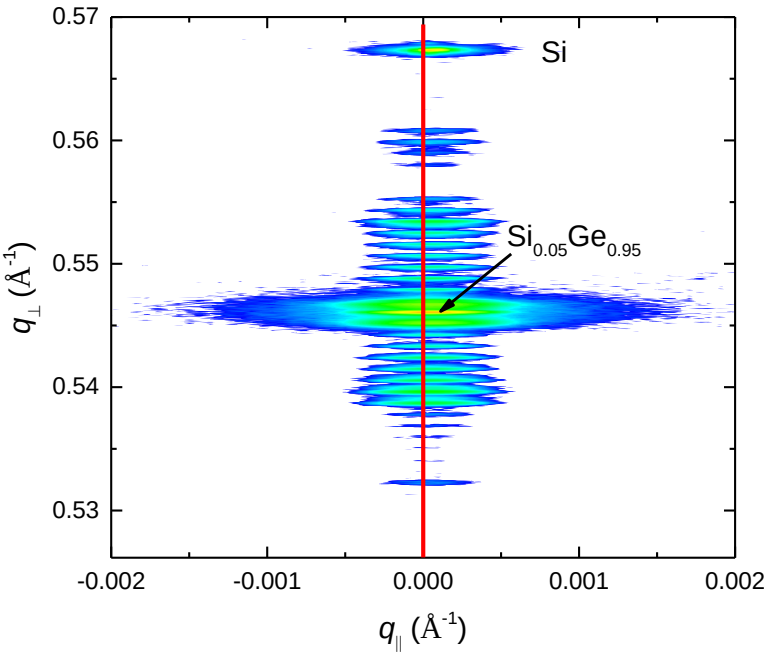

Figure 5-42 - 004 symmetrical HR-XRD RSM from QCL CSL 1 structure. The red line is given to illustrate there is no distinguishable tilt in any of the epilayers grown.

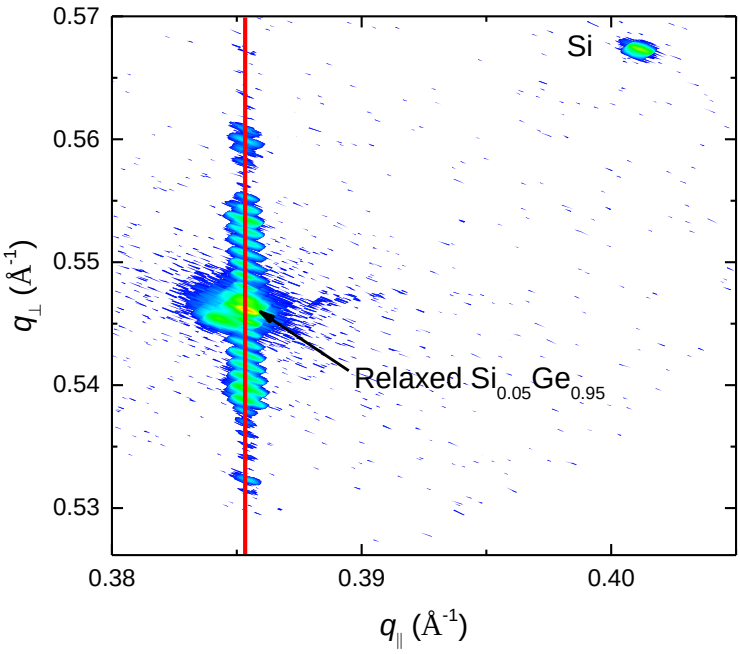

Figure 5-43 - 224 asymmetrical HR-XRD RSM from QCL CSL 1 structure. The red line going through the peak associated with the relaxed $Si_{0.05}Ge_{0.95}$ layer corresponds to the position of fully strained Ge and SiGe layers, of various Ge content, grown on a fully relaxed $Si_{0.15}Ge0._{95}$ buffer.

5.3.8 Quantum cascade laser structure CSL 3 structural characterisation

Between the three QCL structures (CSL 1, CSL 3 and CSL 4), the only growth parameter varied is the growth time of the main Ge QW, w1, and thus its thickness. Due to this, the structures are expected to be identical apart from thickness variation in the main QW and do not need as much in-depth characterisation as CSL 1. Since conventional TEM is more than adequate to measure the thick main Ge QW, HAADF-STEM was only performed on CSL 1 and conventional TEM on structures CSL 3 and CSL 4.

In Figure 5-44, a bright field TEM micrograph is given for CSL 3. The active region can be observed to be of good quality. The main Ge QW, w1 is measured to be 17.0 ±0.5 nm. This matches the design thickness of 17 nm within error.

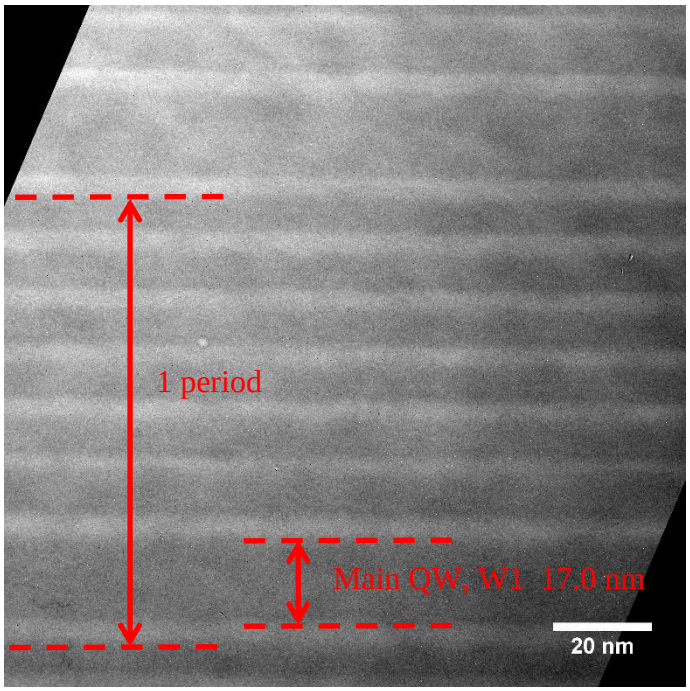

Figure 5-44 - A cross-sectional TEM micrograph showing 1 period of active region for structure CSL 2

To investigate growth uniformity across the wafer, a number of ω-2θ scans were taken with a reduced step time on a number of positions across the wafer radius, and are presented in figure 5-45. The scan positions are 5 mm, 20 mm, 30 mm and 35 mm from the wafer edge and are illustrated in Figure 5-46. ω-2θ scan superlattice peaks are very sensitive to a change in layer thickness. Any change in superlattice layer thickness across the wafer will result in a change in ω-2θ scan superlattice peak position. As can be seen in figure 5-45, the main superlattice peak positions show very little shift with position across the wafer. This implies that the thickness tolerance across the wafer in the active region is excellent, with very little variation. Again this is a very exacting test for the RP-CVD growth technology. Such

uniformity would be highly unlikely in wafers grown by other epitaxy methods, such as LEPE-CVD, which has struggled with a significant variation in layer thickness across the wafer [165] for QCL structures. This is discussed in depth in Section 5.3.12.

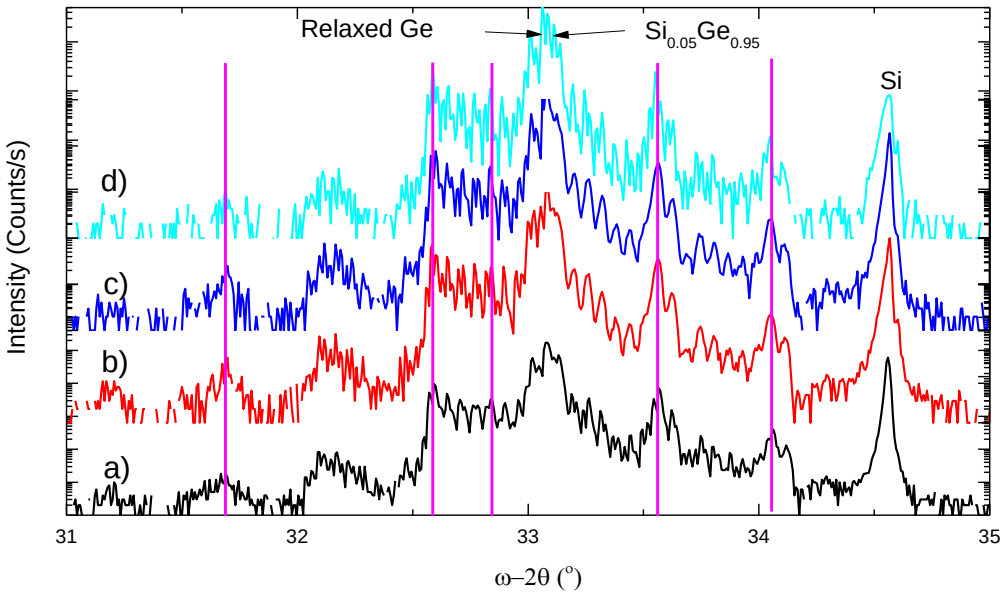

Figure 5-45 - HR-XRD (0 0 4) ω-2θ scans of QCL CSL3 superlattice structure. a) is taken from 5 mm from the wafer edge, b) 20 mm from the wafer edge, c) 30 mm from the wafer edge and d) 35 mm from the wafer edge. The pink lines drawn through major features in the ω-2θ scans are intended to highlight any peak shift between scans.

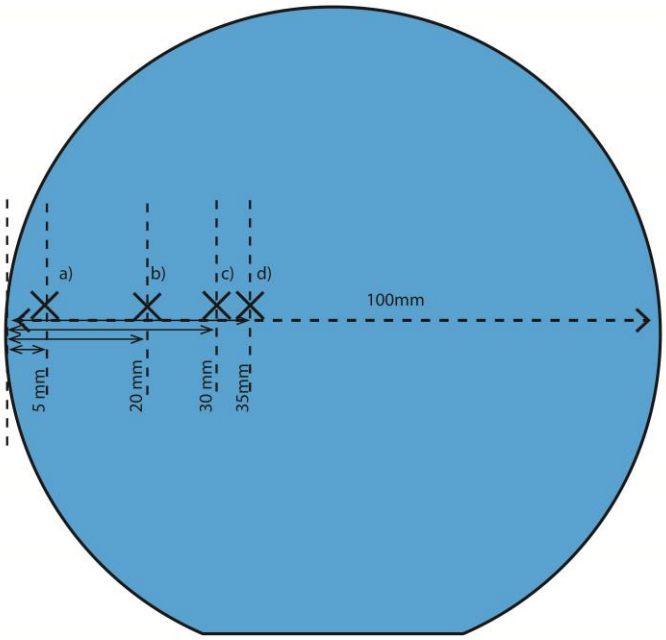

Figure 5-46 - Schematic diagram of position of ω-2θ scans on CSL 3 QCL structure wafer

In figure 5-47 the symmetric (004) RSM and in figure 5-48 the asymmetric (224) RSM are given for QCL structure CSL 3. As observed in the RSMs for QCL structure CSL 1, no tilt in the growth is seen, the $Si_{0.05}Ge_{0.95}$ buffer is fully relaxed and the Ge QWs and $Si_{0.15}Ge_{0.85}$ barriers are fully strained to the $Si_{0.05}Ge_{0.95}$ buffer.

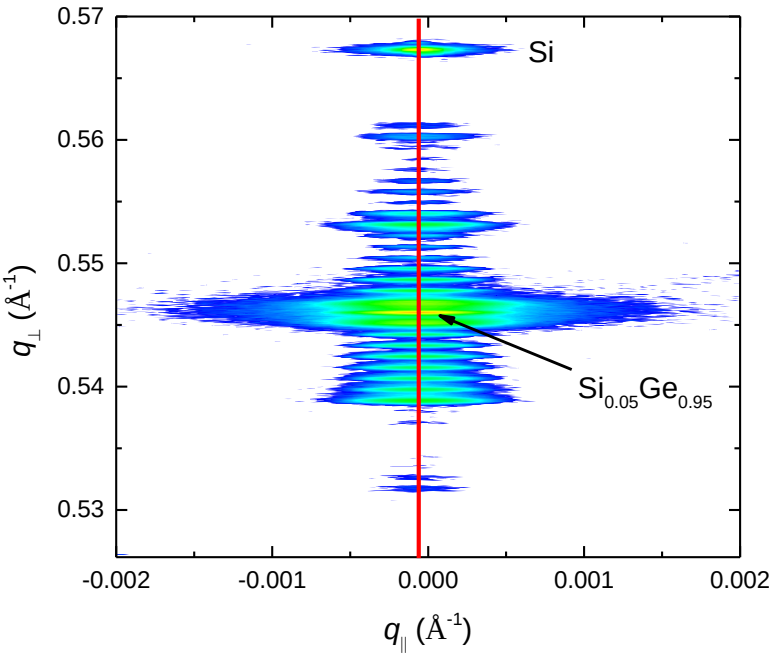

Figure 5-47 – (004) symmetrical HR-XRD RSM from QCL CSL 3 structure. The red line is given to illustrate there is no distinguishable tilt in any of the epilayers grown.

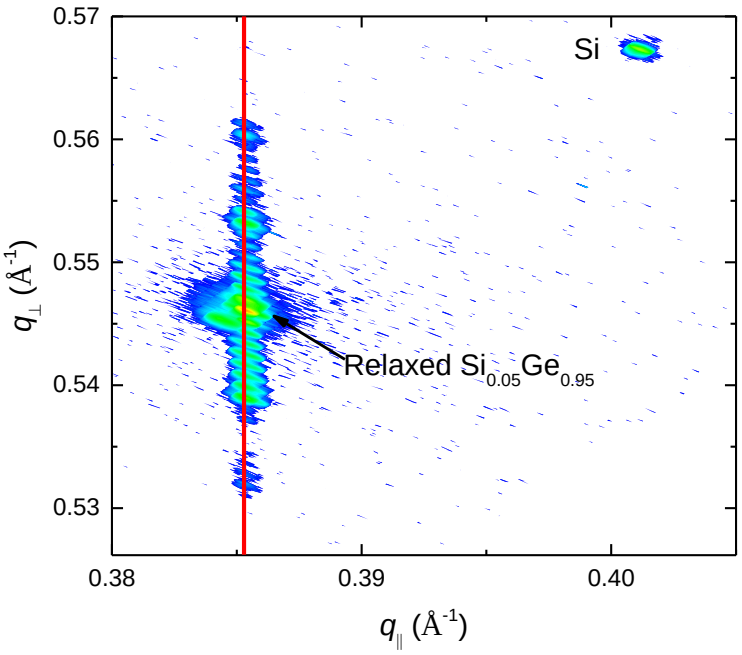

Figure 5-48 – (224) asymmetrical HR-XRD RSM from QCL CSL 3 structure. The red line going through the peak associated with the relaxed $Si_{0.05}Ge_{0.95}$ layer corresponds to the position of fully strained Ge and SiGe layers, of various Ge content, grown on a fully relaxed$Si_{0.15}Ge0._{95}$ buffer.

5.3.9 Quantum cascade laser structure CSL 4 structural characterisation

In figure 5-49, a bright-field TEM micrograph is given for CSL 4. The active region can be observed to be of good quality. The main Ge QW, w1 is measured to be 20.6 ±0.5nm, this matches the design thickness of 21 nm within error.

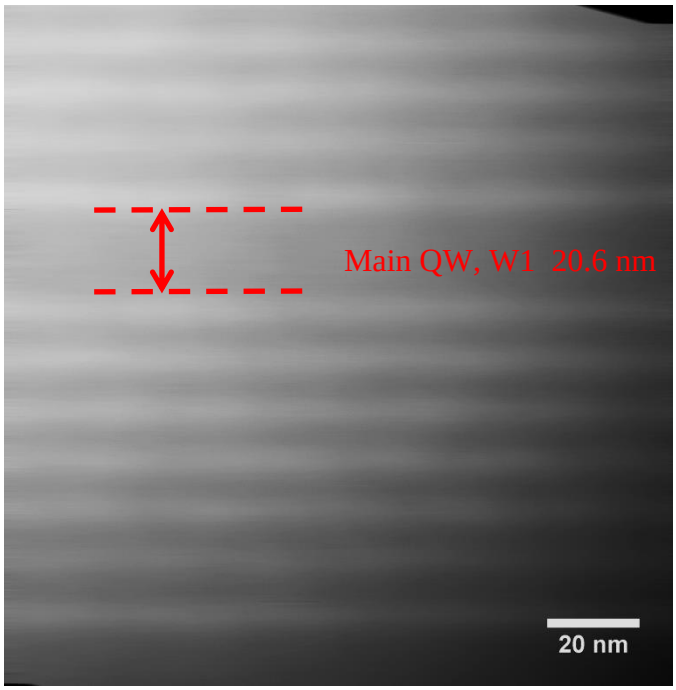

Figure 5-49 - A cross-sectional TEM micrograph showing 1 period of active region for structure CSL 4

In figure 5-50, the HR-XRD symmetric (004) ω-2θ scan is given for the CSL 4 structure (black line) along with simulated data (red line). It can be seen that the measured spectrum contains multiple superlattice peaks with a low FWHM, indicating sharp interfaces between layers. As with fitting previous scans, it was

necessary to impose limits of ± 1 nm on the fitting parameters using layer thickness values measured by TEM.

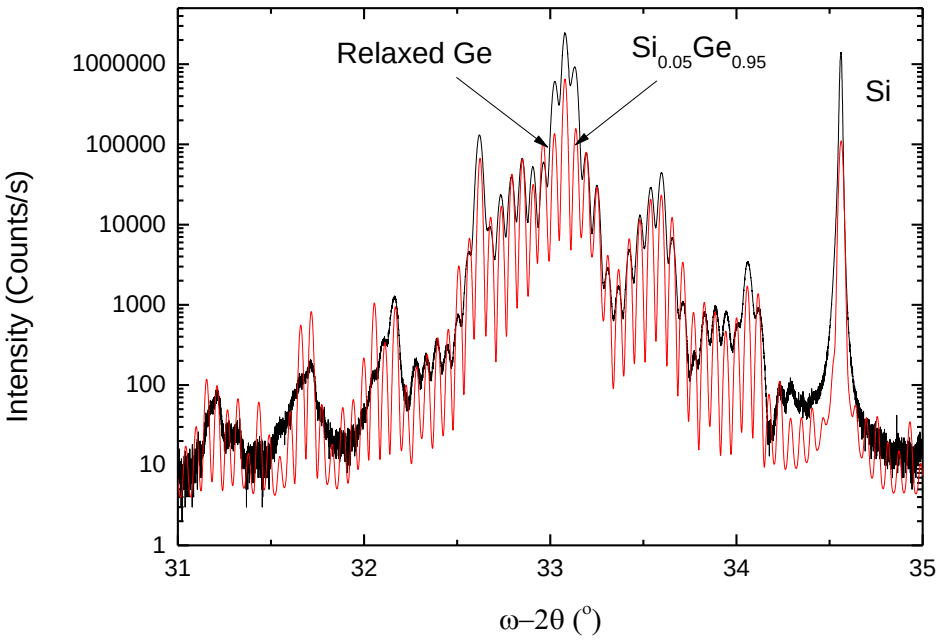

Figure 5-50 - HR-XRD (0 0 4) ω-2θ scans of QCL CSL4 superlattice structure. The measured experimental data is shown (black) along with simulated curve (red).

In figure 5-51 the symmetric (004) RSM and in figure 5-52 the asymmetric (224) RSM are given for QCL structure CSL 4. As with the previous two structures, no tilt in the growth is seen, the $Si_{0.05}Ge_{0.95}$ buffer is fully relaxed and the Ge QWs and $Si_{0.15}Ge_{0.85}$ barriers are fully strained to the $Si_{0.05}Ge_{0.95}$ buffer.

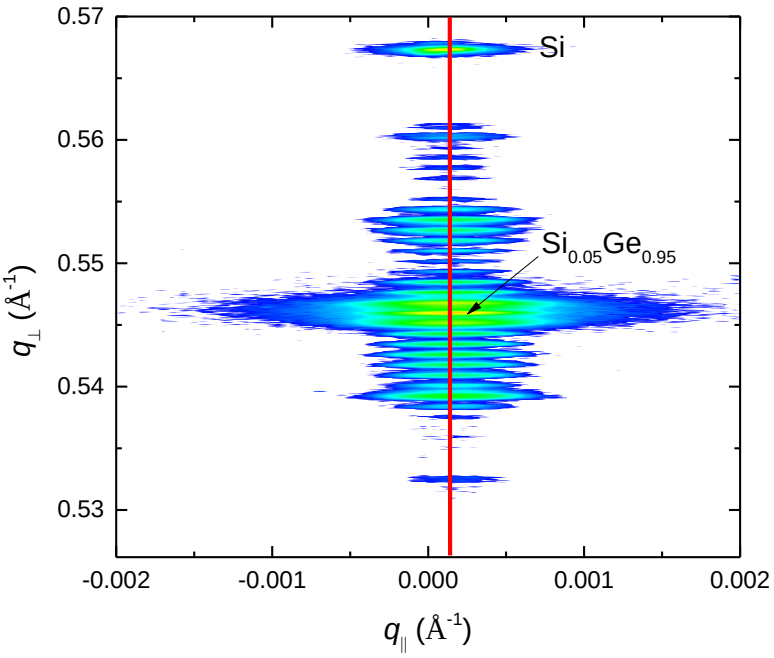

Figure 5-51 - 004 symmetrical HR-XRD RSM from QCL CSL 4. The red line is given to illustrate there is no distinguishable tilt in any of the epilayers grown.

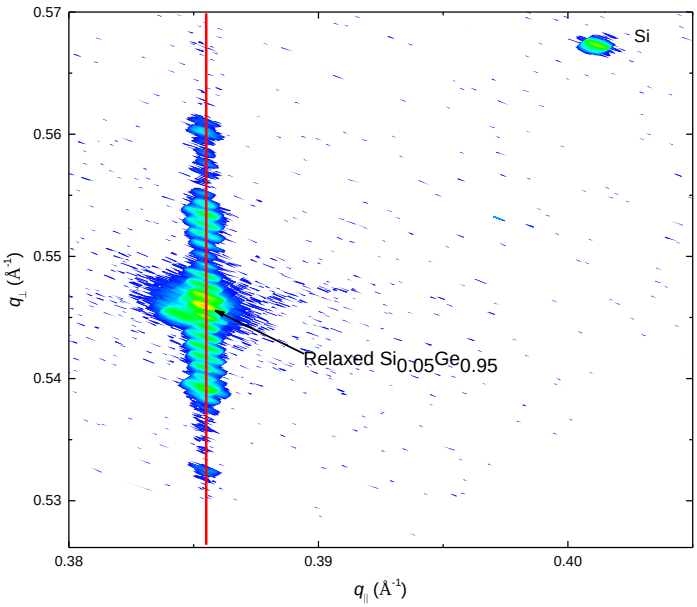

Figure 5-52 - 224 asymmetrical HR-XRD RSM from QCL CSL 4. The red line going through the peak associated with the relaxed $Si_{0.05}Ge_{0.95}$ layer corresponds to the position of fully strained Ge and SiGe layers, of various Ge content, grown on a fully relaxed$Si_{0.15}Ge_{0.95}$ buffer .

5.3.10 Surface characterisation of CSL 4 by AFM

Finally, to investigate the surface morphology, AFM was performed on the surface of QCL structure CSL 4. It was assumed that with the growth parameters staying the same for each structure, apart from the width of the main quantum well, the surface morphology would be the same for each structure. Hence the results from CSL 4 can also be generalised to CSL 1 and CSL 3. The surface of CSL 4 is shown in figure 5-53. 20x20 µm AFM scans were used due to the length scale of the roughness. Three scans were taken from position across the wafer from which the RMS surface roughness was calculated to be 3.4 ± 0.5 nm.

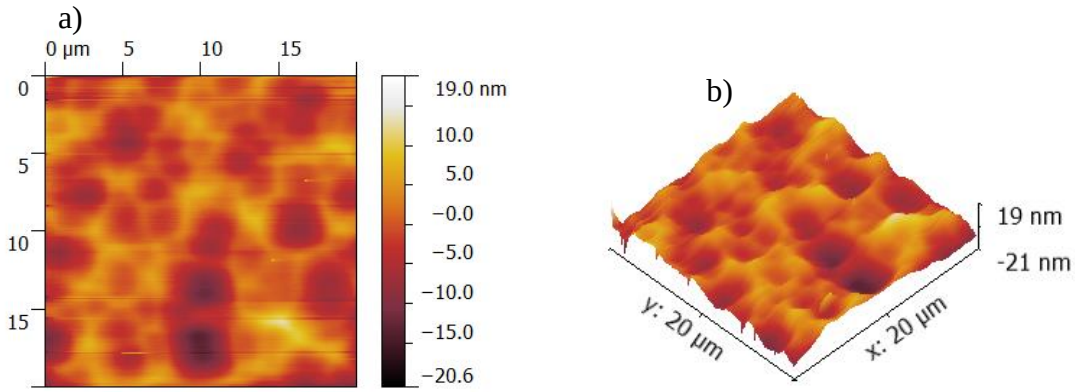

Figure 5-53 - a) AFM surface representation scan of QCL structure CSL 4 b)The same scan of QCL structure CSL 4 in 3D.

5.3.11 Discussion

Following adjustment of the growth times for the superlattice layers, QCL structures CSL 1, CSL 3 and CSL 4 were successfully grown. The structures demonstrate the

feasibility of RP-CVD grown high Ge composition n-type QCL structures on reverse linearly graded virtual substrates.

In all three structures, the active region is of good crystalline quality, with no threading dislocations seen by cross-sectional TEM. The structures are fully strain-balanced, with no layer tilt. The Ge content of the buffer matches that of the designed value. A low surface roughness was measured for the structures of 3.4 ± 0.5 nm, which matches that of the reverse graded buffer used as a platform for the superlattice growth (3 nm) to within the experimental uncertainty [99]. While defect etching has not been performed on the samples, since no strain relaxation has occurred in the superlattice region, the TDD should be no higher than that of the reverse graded buffer used as a platform for the superlattice growth, ~ $10^6 cm^{-2}$ [97, 99].

The Ge wells in the superlattice have an asymmetrical profile, with sharper interfaces of ~1 nm on the $Si_{0.15}Ge_{0.85}$/Ge interface than that of the Ge/$Si_{0.15}Ge_{0.85}$ interface of ~2.9 nm. This profile is indicative of Ge surface segregation and possibly diffusion. Similar asymmetrical profiles have been observed in the literature [61-62,166]. When designing future QCL structures using similar growth parameters, this segregation and diffusion must be taken into account.

The thickness tolerance of the thicker layers in the superlattice is excellent; with all of the main Ge QWs matching that of the design within measurement error. This illustrates that with careful calibration of growth parameters RP-CVD is capable of reproducible growth of layers with precision of a few monolayers which corroborates

previous work by this group [167]. Unfortunately, in the thinner superlattice layers, the grown thicknesses are less accurate. As observed in the initial QCL structure growth, for thin layers the growth rates are non-linear. These non-linear growth rates can be explained by Ge segregation. Hydrogen desorption is the rate limiting process for low temperature CVD growth. As Ge on the surface lowers the hydrogen desorption barrier, the $Si_{1-x}Ge_x$ growth rate will increase with surface Ge fraction [168]. Since significant Ge surface segregation is seen in the structures, it is likely that this is causing the non-linear growth rates and hence the thicker than expected $Si_{0.15}Ge_{0.85}$ layers. The Ge segregation enhanced growth rate is also presumed to be responsible for the initial CSL QCL growth failing.

Growth rate enhancement from Ge surface segregation has been previously reported in the literature [169-171]. In reference [172], it is shown to affect the thickness of layers in SiGe superlattice's grown by gas source MBE using disilane and germane; however, its effect on the layer thicknesses in a complicated thin layer superlattice such as the CSL QCLs has not been reported. It is also likely that an increased growth rate due to Ge surface segregation caused the larger than intended $Si_{0.15}Ge_{0.85}$ regions in the FTIR structures reported on earlier in this chapter.

With repeated iteration of the growth parameters it will be possible to reduce the thickness error in the thinner layers. Since the deviation in growth rate is caused by Ge surface segregation, reducing this segregation should also result in the growth rate tending towards a linear relationship. The Ge surface segregation is the limiting factor in the quality of the structures grown and for an increase in the structure quality the Ge segregation must be reduced.

5.3.12 Comparison to Literature

Since comprehensive materials characterisation of RP-CVD grown n-type QCL structures has not previously been reported in the literature, direct comparison is difficult. Also many of the structural characteristics critical to QCL operation, such as layer thickness tolerance and layer interface quality, are rarely reported. Ge/SiGe thermoelectric structures [153], Si/SiGe QCL structures [165,173], Ge/SiGe stark effect modulators [156, 157] and Ge/SiGe multiple quantum well structures that can be used for comparison of the structural characteristics.

Early p-type QCL structures were all grown by MBE, which does not require high temperature for precursor decomposition and is therefore able to grow at low temperature and minimise the Ge surface segregation. The growth rate can also be monitored *in situ*, giving accurate control of layer thickness.

The Ge surface segregation has only been previously reported in two MBE grown p-type QCL structures [61-62]. However, Ge surface segregation will have occurred in all SiGe QCL structures grown to date even if not reported. In reference [61], a 12 period p-type QCL structure was grown at 350 °C by MBE directly onto a Si(001) substrate, with no virtual substrate. The structures consist of Si barriers and SiGe QWs, with a varying Ge alloy concentration of around 30%. TEM measurements of the SiGe QWs gave a roughness of ≤ 2 monolayers (0.3 nm) for the lower interface but 3 to 4 monolayers (0.6 nm) for the upper interface, indicative of Ge surface segregation. This is significantly lower than that reported in this work and is most likely to be due to the low growth temperature of 350°C. It is also possible that there

was a significant error in the measurement of the interface roughness/surface segregation when compared to this work due to the inaccuracy of conventional TEM for measuring interface quality. In reference [62] a 15 period p-type QCL structure with SiGe QWs having a maximum Ge content of 43% was grown at 480°C by MBE. It is reported that the upper QW interface is noticeable poorer quality than the lower interface, but no quantitative value is given for the interface quality. Little information is given in the literature for MBE grown p-type QCL structure thickness tolerances; so comparison is difficult.

Recent p-type QCL structures have been grown by low-energy plasma-enhanced chemical vapour deposition (LEPE-CVD) [65,165]. This growth method uses low energy plasma focused onto the substrates surface to give fast growth rates while retaining abrupt interfaces [174], ideal for growth of large QCL superlattice structures. The fast growth rate is due to the plasma generating reactive radicals and quickly removing surface hydrogen, which limits growth rate in low temperature CVD processes [175].

In reference [165] a 100 period p-type QCL structure with SiGe QWs having a Ge content of $Si_{0.5}Ge_{0.5}$ was grown at 550°C by LEPE-CVD using SiH_4, GeH_4 and B_2H_6 precursor gases. The superlattice structure was grown on a virtual substrate with a final composition of $Si_{0.65}Ge_{0.35.}$ Large variation across the wafer was seen in the thickness of superlattice layers; this is in contrast with the work presented here where no significant variation was seen. The superlattice period in the centre of the LEPE-CVD grown wafer has a design and measured thickness of 40.6 nm and 53 nm, respectively, giving an error of 31% for one period. This is far larger than the

thickness error reported in this work, where the superlattice period in the centre of the wafer has a design thickness and measured thickness of 78.1 nm and 85.2 ± 0.2 nm, respectively, giving an error of just 9 % for one period. Away from the centre of the wafer the plasma intensity drops dramatically, which leads to LEPE-CVD layer thickness varying by factors of two or three across a 100 mm diameter wafer. No value was given for the Ge surface segregation in this structure; however, from the TEM image given, the QWs can be seen to have a broad, rounded profile, indicative of very high Ge surface segregation. It is possible that the removal of the surface hydrogen by plasma in LEPE-CVD prevents the hydrogen acting as a surfactant and results in higher Ge surface segregation. Threading dislocations were observed in the LEPE-CVD grown QCL structure, in contrast to the structures presented in this work where none were seen. This comparison to the quality of the most recently grown p-type SiGe QCL structures confirms the capability of RP-CVD in QCL structure growth.

Ge segregation has also been reported in multi-layer thermoelectric structures, where is has been suggested to actually improve the performance of the thermoelectric device [176]. Since the Ge/SiGe system has applications in thermoelectric structures [154,177-178,] the accurate profiling of the Ge segregation reported in this work might have applications in the design of future thermoelectric devices.

5.3.13 Comparison to theory

In reference [179] the effects of variation in interface quality on SiGe-based QCLs are studied for different SiGe materials systems. This is investigated by performing

simulated annealing on a barrier sandwiched between two QWs, giving the barrier a diffuse profile. The diffusion at the barrier is sufficiently degraded that the two QWs begin to merge into a single well is then calculated. The diffusion is characterised by an interdiffusion length $L_d = (Dt)^{1/2}$, where D and t are the diffusion coefficient (in units of m^2s^{-1} and time respectively) [180]. It is shown that the Ge rich n-type system used for the structures grown in this work is the most tolerant to interdiffusion, with a maximum $L_d = 3.31$ nm before the QW's begin to merge. The maximum interdiffusion length is approximately $L_d \sim 1.5$ nm for the structures grown in this work, showing that there is potential to grow a functioning Ge rich n-type Si-based QCLs using the growth techniques described in this work .

In reference [181] the effects of variations in the thickness of barriers and QWs on the EL from Ge/SiGe CSL QCLs are reported by the University of Leeds, using the same simulation method as discussed in Section 5.3.1 used to design the CSL QCL structures of the current study. The results were then used to give an estimation of the maximum tolerable thickness variation in growth. Tolerable growth thickness variations were found for 6, 7 and 8 well QCL designs. In figure 5-54, the maximum gain is plotted against bias for the 7 QW CSL design, grown in this work. The gain must be larger than the losses for any lasing to be observed. It can be seen in figure 5-54 that as the thickness deviates futher from the design the gain decreases rapidly. The average thickness variation measured is 15 %. It can be seen that the thick, main Ge QWs in the structures all have a thickness error between design and growth of far less than 5%. This suggests that the layer thickness variations seen are due to incorrect growth rate calibration and not due to random error. With further growth rate calibration, factoring in the increase in growth rate due to Ge surface

segregation and the additional non-linear growth rate variation that particularly affects thin layers, it will be possible to reduce the thickness error to a similar value to that of the main Ge QWs. This shows RP-CVD has the potential for QCL structure growth with the higher tolerances necessary for a lasing QCL device.

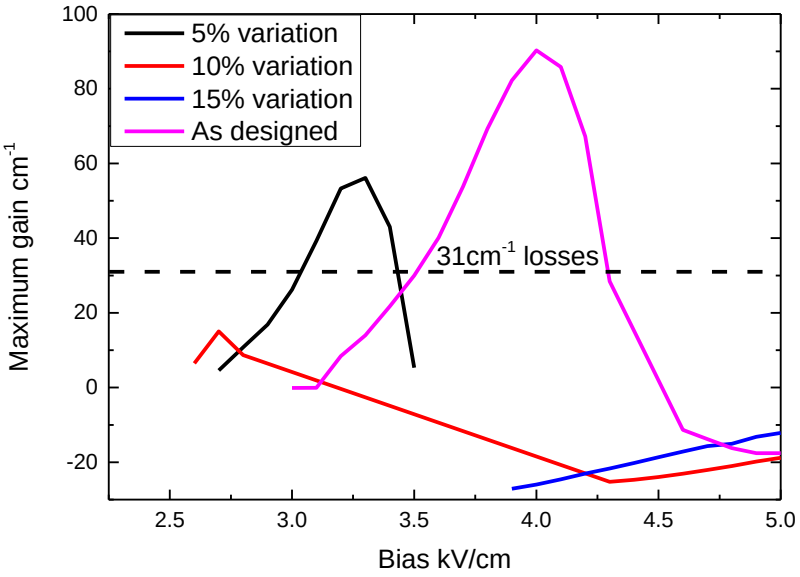

Figure 5-54 - Peak gain of 7 QWs per period CSL QCL design versus bias and growth thickness variation. Adapted from [181].

5.4 Summary

The growth of challenging n-type Ge/$Si_{0.15}Ge_{0.85}$ QCL structures by RP-CVD has been presented. Initially, the superlattices were of poor quality with strain relaxation occurring. This is due to the superlattice not being correctly strain balanced due to incorrect layer thicknesses. Through iteration of the growth times, the layer thicknesses were brought closer to the design and the structures were strain-balanced, allowing high quality growth of the entire superlattices with no strain relaxation. Following successful growth, comprehensive materials characterisation was

performed on the superlattices, including HR-XRD reciprocal space mapping, X-ray ω-2θ scans, AFM, ATP, SIMS, cross-sectional TEM and HAADF-STEM.

The successfully grown structures, along with results of their characterisation, have been passed to collaborators who will fabricate devices from the structures. When preliminary measurements have been made, it will be possible to refine growth parameters and the design of structures; however, this is outside the time frame of this study.

6 Suspended Ge structures

In this chapter, fabrication and detailed materials characterisation of flat, single crystal Ge membranes is presented. The fabrication method is compatible with integrated-circuit (IC) wafer scale processing and is able to produce membranes of variable thickness [182], with both 112 ± 5 nm and ~700 nm demonstrated. Using micro-diffraction, performed at Beamline B16 at the DIAMOND Light Source, multiple reciprocal space maps were obtained over the membrane with a real-space resolution of ~4 μm. From these reciprocal space maps, strain distribution, thickness (for the 112 ± 5 nm membrane only) and crystalline tilt were calculated. A small symmetric strain variation across the membrane was found for the 112 ± 5 nm membrane; however, if the membranes are to be used as a platform for further growth, this strain variation is insignificant. The micro-diffraction also showed the suspended material to be of better crystalline quality than the surrounding anchored material, which is confirmed by plan view TEM and AFM. The high crystalline quality of Ge membranes gives them many applications (see section 1.5). The membranes are also highly suited to use as a platform for QCL structures because since the Si substrate is removed in the membrane fabrication process, a double metal terahertz waveguide can be fabricated on them.

6.1 Motivation

The motivation behind this chapter is the necessity for an efficient waveguide for Si-based terahertz QCL operation. The Ge membrane fabrication process presented in this chapter has the potential to form the basis of a double metal waveguide (see section 1.5). A secondary motivation is the large range of application that could

benefit from a high quality Ge membrane and knowledge of its material parameters including uniformity.

6.2 Tensile strained Ge membrane fabrication

The following outlines the fabrication of two wafers of tensile strained Ge membranes. The membrane fabrication technique is covered in detail in [182].

Epitaxial growth was performed on a double-side polished low resistivity 4" Si (001) wafers with a thickness of 300 µm. Double sided wafers were used so that epitaxial Ge layers could be grown on either side. Tensile strained membranes could then be produced with the non-membrane layer being used as an etch mask for the membrane. Ge was grown using the RP-CVD system described in section 2.3.2 with a germane precursor.

Initially, the wafers were baked at 1000 °C for 10 minutes to desorb the native oxide. For the first wafer of membranes, high quality tensile strained Ge was grown via the two temperature method (described in section 2.6) on the front of the wafer (see figure 6-1, a) to a total thickness of around 700 nm. Although the Ge layer is fully relaxed at the growth temperature of 670ºC, it acquires tensile strain as it cools to room temperature, due to the mismatch in thermal expansion coefficients between Ge and Si (for an explanation see 2.5).

To grow the compressively strained Ge layer on the underside of the substrate (figure 6-1, b), the substrate needs to be flipped in the growth chamber. This is achieved by cooling the substrate to room temperature, unloading to a nitrogen

atmosphere in a class 10 clean area, turning the wafer and then re-loading into the growth chamber. This unloading and re-loading process was carried out quickly to try to ensure the epitaxial surfaces remained hydrogen passivated. The hydrogen termination of bonds on the silicon surface will prevent oxidation of the surface (the growth rate of Ge oxide on H_2 passivated Ge can be found in [183]). This is necessary to avoid a second high temperature bake, which would affect the existing Ge growth. The 700 nm of Ge is then deposited at 400 °C. Due to the low growth temperature, strain relaxation does not fully complete and some residual compressive strain stays in the layer.

The two-temperature tensile strained Ge was intentionally grown before the compressively strained Ge on the underside of the substrate, since the tensile strained Ge requires a higher temperature than the compressively strained Ge to give a high quality final layer. For an explanation of why a high temperature is used for the growth of high quality tensile strained Ge on Si (for an explanation see section 2.5). The high temperature would otherwise cause interdiffusion at the substrate/compressively strained Ge interface.

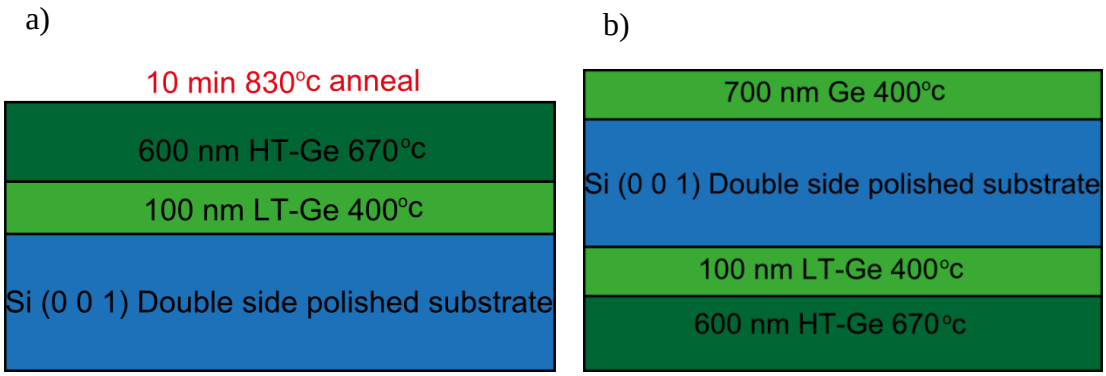

Figure 6-1 – a) Tensile strained Ge layer grown on top of wafer using two temperature method followed by an anneal. b) Wafer reversed with compressively strained layer grown.

The state of strain of both layers was measured with HR-XRD, using (004) and (224) RSMs. The compressively strained layer was found to have a relaxation (see section 2.3.5 for an explanation of layer relaxation) of 97.1 ± 0.5 % and the tensile strained layer a relaxation of 104.2 ± 0.5 %, both with respect to the Si (0 0 1) substrate.

A second wafer was grown for the fabrication of thinner tensile strained membranes with the intention of studying the effect of membrane thickness on the material properties. For the second wafer, Ge was deposited on both sides of the wafer as previously described; however, this time a thinner 400 nm etch mask layer was grown on the back of the wafer (this could be grown thinner than in the previous wafer, since it was only intended as an etch mask and so a high crystalline quality was not necessary) and a thinner 200 nm tensile strained layer on the surface with the intention of producing a thinner membrane (figure 6-2).

Figure 6-2 - Schematic diagram of Ge growth for thin membrane

An Al_2O_3 layer was deposited on the underside Ge layer with atomic layer deposition using a Picosun SUNALE$^{(TM)}$ R-150B with trimethylaluminium and H_2O. The Al_2O_3 layer was then patterned using a AZ5214E photoresist and a Karl Suss MA6 mask aligner followed by developing in AZ726 MiF then etched in a 30 °C buffered hydrofluoric acid etch. A HF:H_2O_2:CH_3COOH etch was then used to selectively etch

through the Ge to the Si, creating Si windows. The remainder of the resist was then removed and the wafer was placed in a STS Silicon ICP etcher with a Bosch process, this alternated between SF_6 & O_2 mix and C_4F_8 with a power of 15 W to remove ~275 ± 25 µm of Si. The etch depth was confirmed with optical focus variation microscopy. For the final process step, the wafer was placed in a 25% TMAH bath heated to 80 °C, with a reported Si etch rate of 0.45 ± 0.02 µm min^{-1} [184] and the wafer was etched for 420 min. This ensures that the Si was entirely removed from the top Ge layer. Interferometry was performed using a Sci-soft Filmtek 2000M reflectometer, with wavelengths 380-890nm on the supported Ge. The unintentional etch rate of the Ge was measured to be 0.18 ± 0.09 nm min^{-1}, resulting in a reduction in the thickness of the membranes compared with the as grown layer thicknesses of 200 and 700 nm. The wafer was removed from the TMAH bath, soft rinsed in de-ionised H_2O before a final soft rinse in IPA. The reason for the final IPA rinse is that IPA has a higher vapour pressure than water so it can be quickly evaporated under a gentle flow of N_2 without damaging the membrane. Approximately 50% of the membrane's survived the fabrication process. A schematic diagram for a completed thick (~700 nm) membrane is given in figure 6-3.

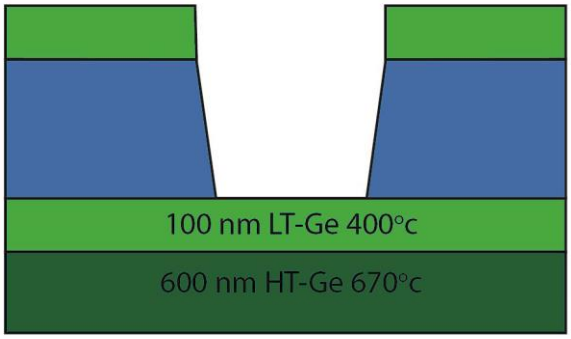

Figure 6-3 - Schematic diagram of completed tensile strained thick (~700 nm) Ge membrane

6.3 Initial membrane characterisation

6.3.1 SEM

Following fabrication, the membranes were evaluated with SEM. In figure 6-4 a) plan view SEM is given for one of the thinner membranes fabricated. A clear contrast difference is visible between the Ge membrane and its surrounding Ge on Si frame. This contrast difference is due to the membrane becoming electron transparent due to its reduced thickness. The lateral area of the membrane is measured as 3.5 mm^2. The membrane can be observed to be of good crystal quality, with no ripples or cracks. In figure 6-4 b), the cross section of a broken membrane is given. From this cross-section the thickness of the membrane is measured as approximately 56 nm, however this is likely to be inaccurate due to the membrane being tilted in the SEM field of view. The significant difference in the thickness obtained from this measurement and that from XRD given later in this section can be explained by this tilt and by anisotropy in the TMAH etch rate for the Ge across the wafer. Following basic characterisation to check the membrane is of good quality, the technique of microfocus XRD was employed to measure the material parameters of the membrane with good spatial resolution.

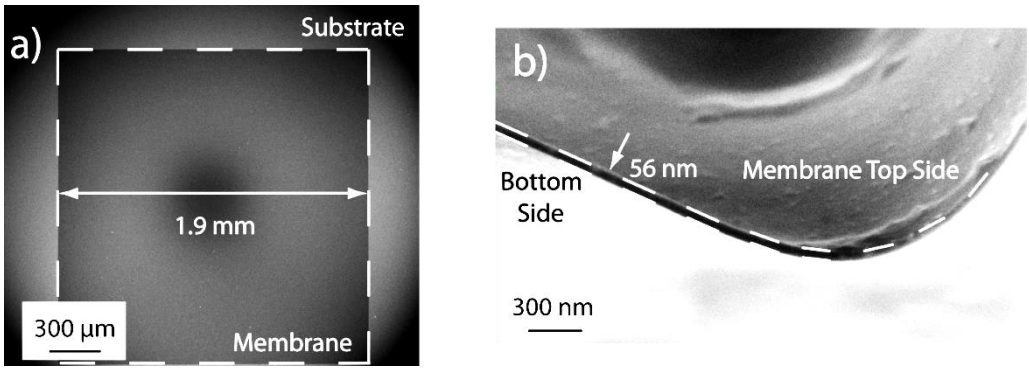

Figure 6-4 - a) SEM image taken looking perpendicular to the surface of the membrane. Electron transparency gives contrast between the membrane and the bulk, b) Side view of intentionally broken 60 nm membrane showing the dimensions of the cross section. The tilted thickness is 56 mn.

6.4 Strain mapping by microfocus XRD using Beamline B 16 at the Diamond Synchrotron of thin 112 ± 5 nm membrane

The thin membrane was characterised using microfocus XRD using Beamline 16 at the Diamond Synchrotron using the technique described in section 3.6. Individual (004) RSMs were taken every 10 µm along the $[1\bar{1}0]$ direction, and across the middle of the sample (figure 3-19).

6.4.1 Results

In figure 6-5, a (004) RSM is given for the edge of the membrane. The Ge peak has a relatively low FWHM. By contrast to the (004) RSM for Ge on the substrate, thickness fringes are present. These are visible above the Ge peak.

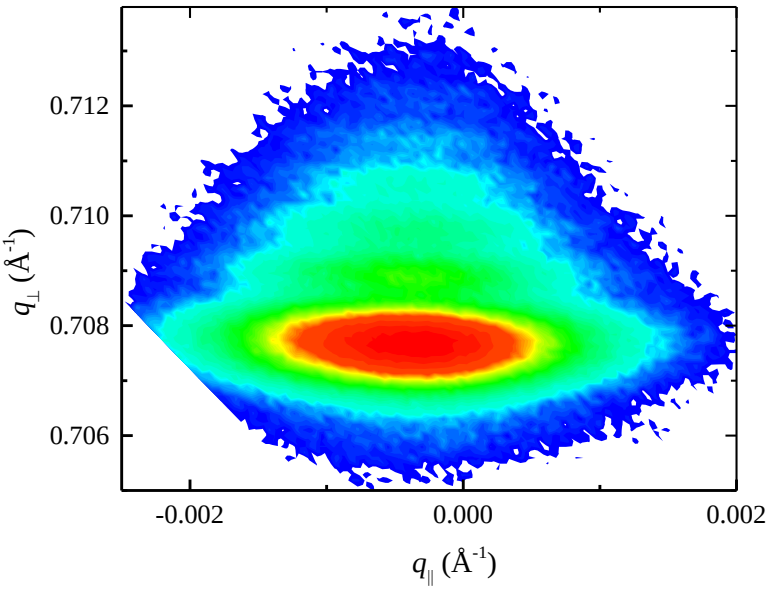

Figure 6-5 - (004) RSM taken from membrane's edge

In figure 6-5, a (004) RSM is given for the edge of the membrane. As in the (004) RSM for the edge of the membrane, the peak has a relatively low FWHM and displays thickness fringes above the Ge peak.

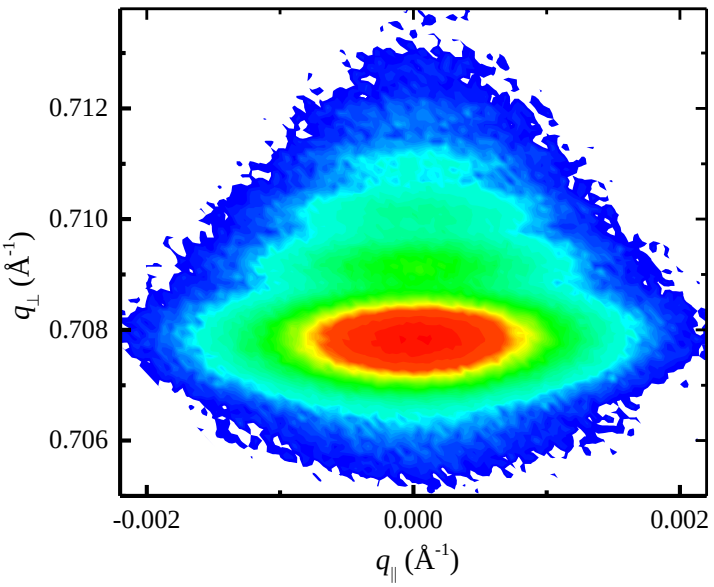

Figure 6-6 - (004) RSM from the middle of the Ge membrane

In figure 6-7, $q_{\perp}$ line profiles extracted from both suspended Ge and Ge-on-Si (001) are given. Five thickness fridges can be clearly resolved for the suspended Ge, in contrast to the Ge on Si (001) where no fridges are visible. The FWHM is also slightly smaller for the suspended Ge, which will be due to increased crystalline quality in the suspended material (good crystalline quality is indicated by high uniformity in the crystals lattice). The thickness of the tensile strained Ge membrane was calculated from the thickness fringes to be 112 ± 5 nm

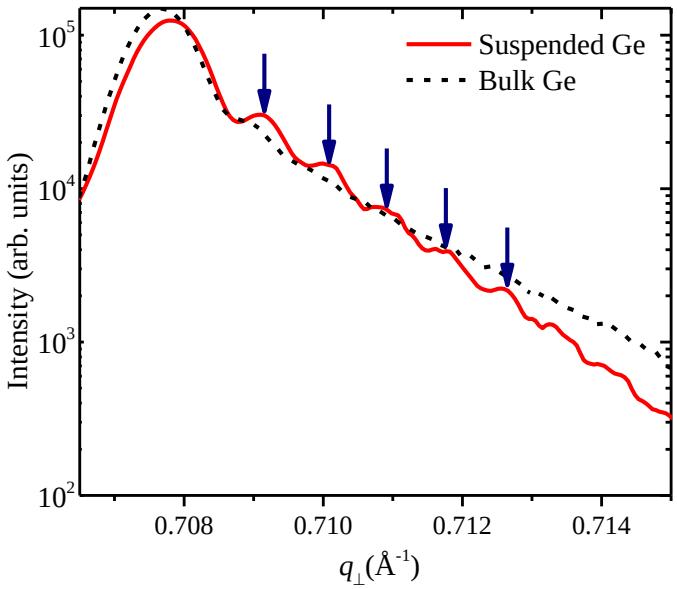

Figure 6-7 - Line profiles extracted from suspended Ge and supported Ge (004) RSMs. Thickness fringes are marked with blue arrows for the suspended Ge.

In figure 6-8, the (004) Ge Bragg peak position in $q_{\parallel}$ and peak FWHM are given as a function of position across the membrane. Initially, the Ge peak is at $q_{\parallel}$ = 0 ± 0.00003 Å^{-1} for the supported material, before sharply dropping to $q_{\parallel}$ = -0.0004 ± 0.00003 at the left membrane edge. This corresponds to a crystal tilt of ~0.035^{o} . $q_{\parallel}$ then returns to 0 Å^{-1} for the remainder of the membrane. At the right

membrane edge, some edge effects are visible but not as pronounced as that on the left membrane edge. This is due to the membrane not being mounted precisely horizontal which is also seen in the upward drift in the FWHM from left to right across the membrane. The FWHM of the peak is at its largest on the supported Ge, with an almost uniform decrease over the entire membrane.

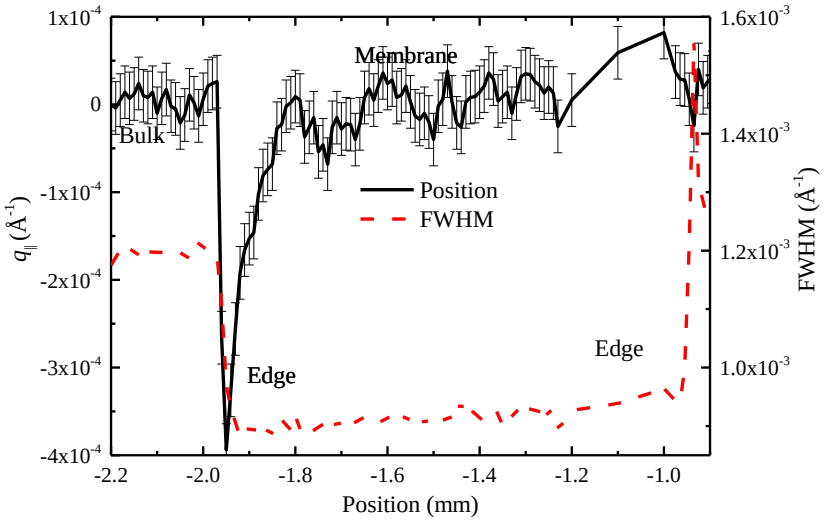

Figure 6-8 - Position (solid black line) and FWHM (dotted red line) of the (004) Ge Bragg peak as a function of position for $q_{\parallel}$.

In figure 6-9 , the (004) Ge Bragg peak position in $q_{\perp}$ and peak FWHM are given as a function of position across the membrane. For the Ge supported by Si, the Ge peak is at $q_{\perp}$ = 0.70777 ± 0.00003 Å^{-1} ($a_{\perp}$ = 5.6516 ± 0.0003 Å) with a sharp drop to $q_{\perp}$ = 0.70775 ± 0.00003 Å^{-1} ($a_{\perp}$ = 5.6517 ± 0.0003 Å) at the membrane edge. This indicates a slight reduction in the tensile strain at the edge of the membrane. There is then a gradual increase in $q_{\perp}$ towards the centre of the membrane, where at the central point $q_{\perp}$ = 0.70781 ± 0.00003 Å^{-1} ($a_{\perp}$ = 5.6512 ± 0.0003 Å). $q_{\perp}$ then gradually decreases towards the other side of the membrane.

In calculating the strain, it is assumed that the Ge behaves elastically. The bulk material has a relaxation of 103.72 ± 0.02 % with respect to the Si (001) substrate. This value was verified with lab based XRD. For the membrane, the relaxation was calculated as 103.64 ± 0.02 % for the edge and 103.91 ± 0.02 % for the middle. The in-plane strain ($\varepsilon_{\parallel}$) was calculated as 1.55(± 0.01)x10^{-3}, 1.51(± 0.01)x10^{-3} and 1.63(± 0.01)x10^{-3} for the supported Ge, membrane edge and middle. As for $q_{\parallel}$, the FWHM is at its largest on the supported Ge, with an almost uniform decrease over the entire membrane. Slight edge effects are seen at both membrane edges.

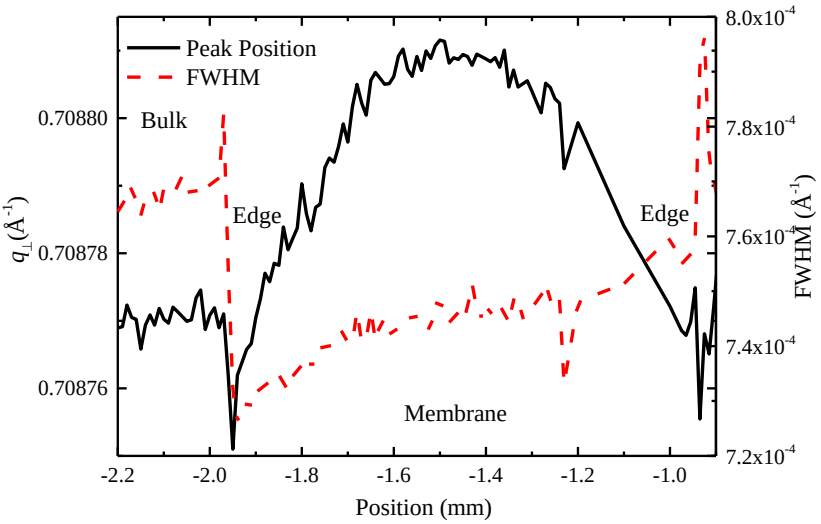

Figure 6-9 – Position (solid black line) and FWHM (dotted red line) of the (004) Ge Bragg peak as a function of position for $q_{\perp}$

While not shown here, the [1$\bar{1}$0] line profile was also taken. Peak behaviour was identical for both directions.

6.4.2 Discussion

Microfocus XRD was demonstrated to be highly suitable for strain mapping of suspended membrane structures. Information on the membrane crystal quality,

crystallographic tilt and strain was extracted with a spatial resolution of the microfocus spot size (~4 μm). The technique is non-contact and non-destructive and offers greater sensitivity to a change in lattice spacing than other techniques such as Raman Spectroscopy.

The membrane body is shown to have no lattice plane tilt, making it ideal as a platform for devices and further epitaxial growth. Tilt is observed at the edges of the membrane, this is caused by the abrupt reduction in tensile strain leading to bending of the lattice planes. Tensile strain varies over the membrane, with the highest value, 103.91%, reported in the membrane centre. The strain profile is symmetrical over the membrane. However, since the strain variation is small it should not affect optical device performance by strain-induced bandgap variation in the Ge, since it is negligible when compared to the magnitude of strain required for a functioning Ge device [185].

The FWHM of the Ge (004) peak's is significantly lower for the membrane than for the surrounding supported Ge and, since improved crystal quality is indicated by a reduction in FWHM, this suggests that the membrane is of better crystal quality than the surrounding supported Ge. When Ge is grown via the two temperature method, the strain is released via the formation of misfit dislocations in the initial low temperature Ge layer [186]. The misfit dislocations are concentrated in a dislocation at the Ge/Si interface and since this region has been removed in the membrane fabrication process during the wet etch, the crystal quality of the Ge has been improved.

As a result of removing the misfit dislocation network, thickness fringes can be seen to the side of the (004) reflection. This means the membrane thickness can be extracted by microfocus XRD. The thickness measured by XRD is almost two times that of the thickness measured by SEM on a different membrane, this is likely to be due to non-uniformity in both the Ge etch rate in the TMAH bath and the Ge growth rate across the wafer. The etch rate of TMAH is temperature dependent and so temperature variation in the etch bath will result in a large non-uniformity in the Ge thickness across the wafer.

6.5 Membrane characterisation by plan view TEM

To study the crystalline quality of the membrane and to compare it to that of the surrounding supported Ge layer, plan view TEM was performed on the membrane. Since the membrane would need to be broken to fit it in a conventional TEM sample holder, a sample holder was specially adapted for studying the membranes (figure 6-10). The crystal quality of the membrane must be studied without it being damaged, since the damage could introduce strain and additional dislocations through plastic strain relief. In conventional sample preparation for plan-view TEM, the sample is first thinned using mechanical polishing, before polishing with an ion beam. However, for the membrane this is not necessary. The membrane is sufficiently thin to be electron transparent and so needed no preparation.

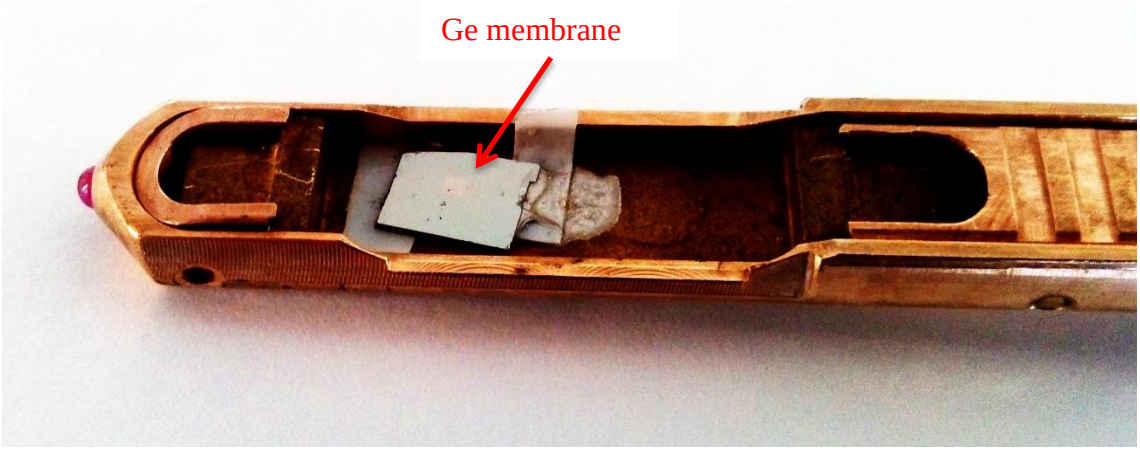

Figure 6-10 - Modified TEM Sample holder containing Ge membrane. The membrane is faintly visible due to optical transparency.

6.5.1 Results

In figure 6-11, a plan-view (PV) TEM micrograph is given from the centre of the membrane. The features observed on the membrane are threading dislocations. These were counted using ImageJ software packages "cell counting" function to give a threading dislocation density (TDD) of approximately $3x10^{9}$ cm^{-2}.

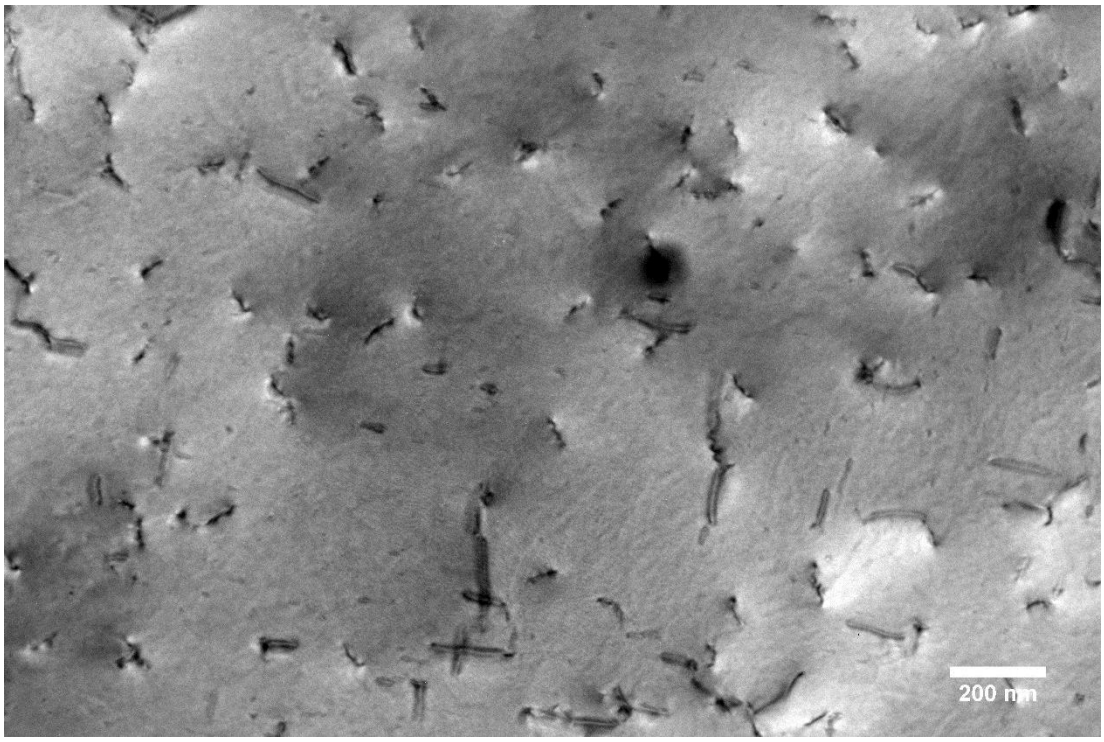

Figure 6-11 – Bright field PV-TEM micrograph taken from centre of Ge membrane.

In figure 6-12, a (220) reflection micrograph is given from the position where the membrane meets the supporting frame. The (220) reflection was chosen to give strong strain contrast, highlighting dislocations by their surrounding strain field. The top of the image is looking through the unsupported Ge membrane, the horizontal line across the image is where the membrane meets the supporting frame and the bottom of the image is looking through the supporting Si frame and the epitaxial Ge layer. Contrast is lost toward the bottom of the image due to the increasing thickness of the supporting frame. Two threading dislocations can be seen in the suspended membrane, but in the frame a dense network of dislocations can be seen. The fringes visible in the frame are thickness fringes.

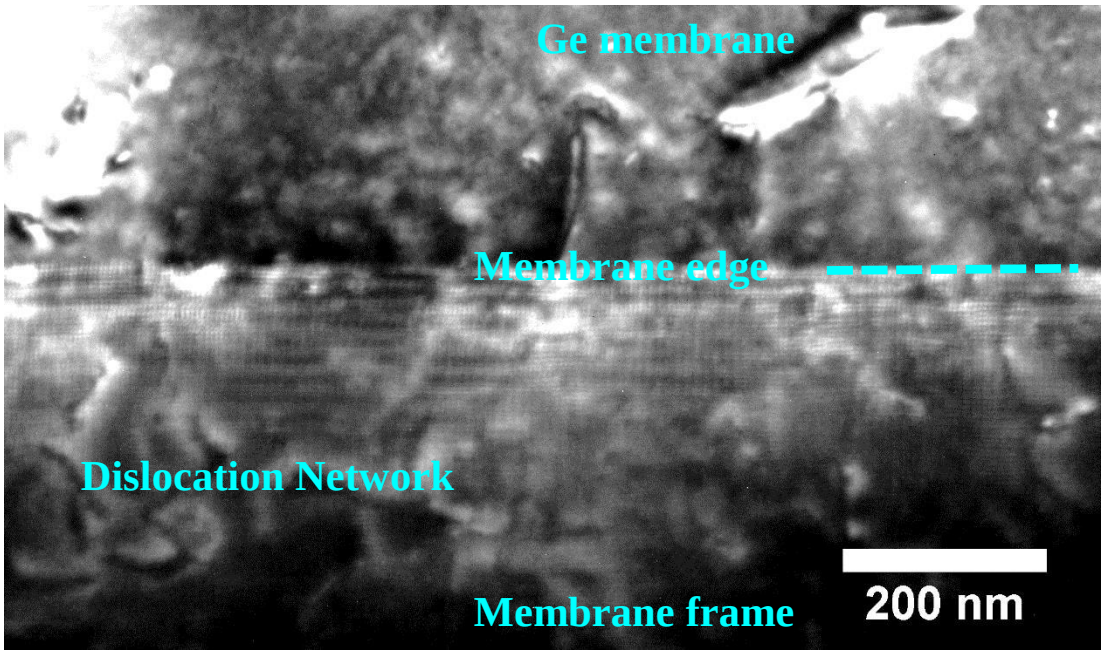

Figure 6-12 – Dark field (220) reflection PV-TEM micrograph taken from Ge membrane showing membrane, membrane edge and frame.

The membranes are ideal for study by plan-view TEM due to their electron transparency. The TDD of the membrane $3x10^{9}$ $cm^{-2,}$ is the same as the TDD for the Ge on the frame, showing that suspending the Ge has not reduced the dislocation density. Earlier it was speculated that the membrane fabrication process had removed misfit dislocation network present on the as-grown Ge. This speculation is further supported by figure 6-12, where the dislocation network can be observed on the as-grown Ge but not on the membrane. The misfit network removal means that the membrane is of better crystal quality than the as-grown Ge, since the strain field from the misfit network is no longer distorting the Ge. Removing the dislocation network also means that the membrane surface is isolated against surface to surface conduction through dislocations. In order to further investigate the effect of suspending the Ge on its materials parameters, the morphology of the membrane and support surface was measured.

6.6 Membrane surface morphology from AFM

The surface morphology was measured with an Asylum Research MFP-3D-SA AFM, operated in tapping mode. Surface morphology for the membrane edge is given in figure 6-13, showing both the suspended Ge of the membrane and the supported Ge on the frame. When a line profile is taken over the membrane's edge, a drop in height of ~2.5 nm is observed. Approximately 45-50 μm from the edge the height recovers to that of the average. For the frame, an RMS roughness of 2.66 ± 0.05 nm was measured. A lower RMS roughness of 2.16 ± 0.16 nm was measured for the membrane.

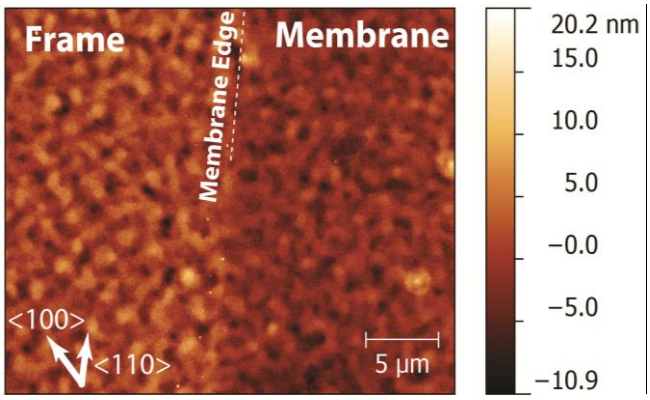

Figure 6-13 - Tapping mode AFM of the Ge membrane at its edge.

The height drop at the edge of the membrane explains the tilt observed by X-ray and the reduction in RMS roughness on the membrane suggests that the change in internal stress of Ge layer has affected its surface. There are two possibilities for the stress change that has affected the surface morphology, that associated with the increase in tensile strain for the suspended material or the stress associated with the

removed misfit dislocation network. Dislocations have a stress field and it is possible that this was distorting the surface.

6.7 Strain mapping by microfocus XRD using Beamline B 16 at the Diamond Synchrotron of thick ~700 nm membrane

The thick (~700 nm) membrane was also characterised using microfocus XRD using Beamline 16 at the Diamond Synchrotron using the technique described in section 3.6. While the thin membrane was optically transparent which made it easy to locate on the sample stage, the thicker, ~700 nm was not easily visible. To aid its location on the sample stage L-shaped alignment trenches were milled at each membrane corner using a focussed ion beam scanning electron microscope (FIB-SEM). These alignment trenches are shown in the SEM micrograph given in figure 6-14. Multiple line scans comprising many individual (004) RSMs were taken along the $[1\bar{1}0]$ direction across a portion of the membrane. Over the main body of the membrane, RSMs were measured every $100\,\mu m$, however in regions over two membrane corners they were measured every $10\,\mu m$. This was done to measure any small features present at the membrane's corners. The RSMs were then combined to give line profiles across the centre of the membrane and maps of both the in-plane strain ($\varepsilon_{\parallel}$) and peak FWHM. It was only possible to complete a map of this kind for the thicker membranes due to the duration of the synchrotron time taken to produce the map being relatively long (~2 days).

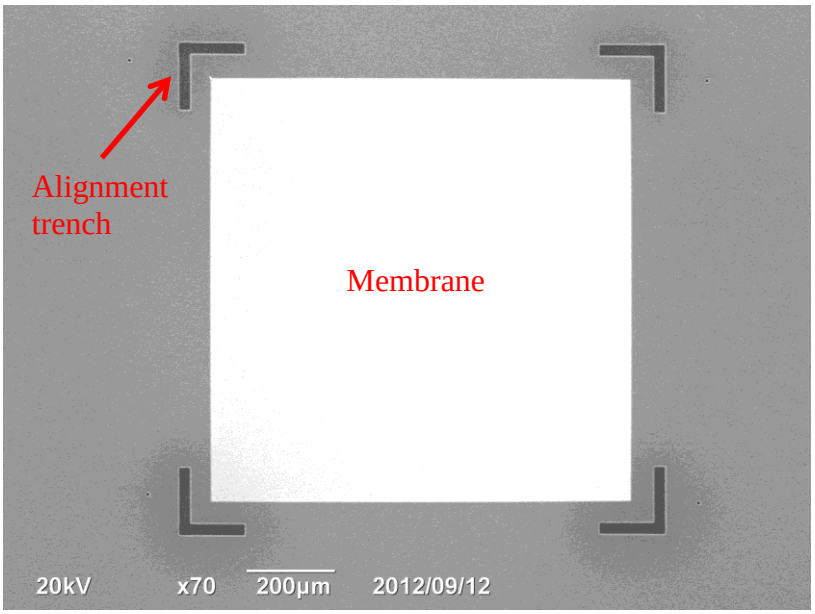

Figure 6-14 – SEM micrograph showing ~700 nm membrane with L shaped alignment trenches at its corners

In figure 6-15, a (004) RSM is given from the centre of the thick ~700 nm membrane. In contrast to the (004) RSM from the centre of the thinner membrane no thickness fringes are visible.

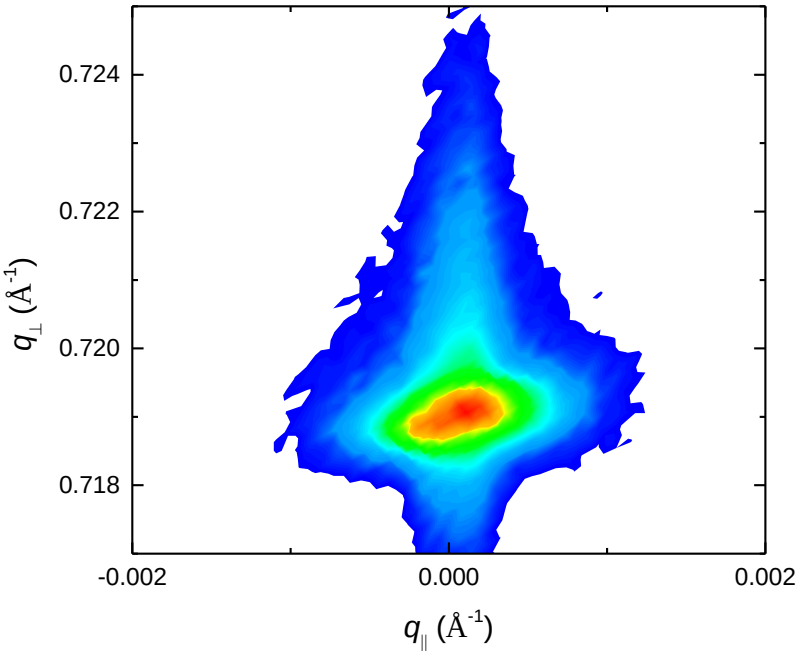

Figure 6-15 - (004) RSM from the middle of the thick ~700 nm Ge membrane.

In figure 6-16, the (004) Ge Bragg peak position in $q_{\parallel}$ and peak FWHM are given as a function of position across the thick ~700 nm membrane. The variation in $q_{\parallel}$ is due to reaching the resolution limit of the technique and is within the error of the technique; apart from small edge effects, $q_{\parallel}$ can be considered to remain constant over the membrane. As with the thinner membrane, the FWHM of the peak is at its largest on the supported Ge, with an almost uniform decrease over the entire membrane.

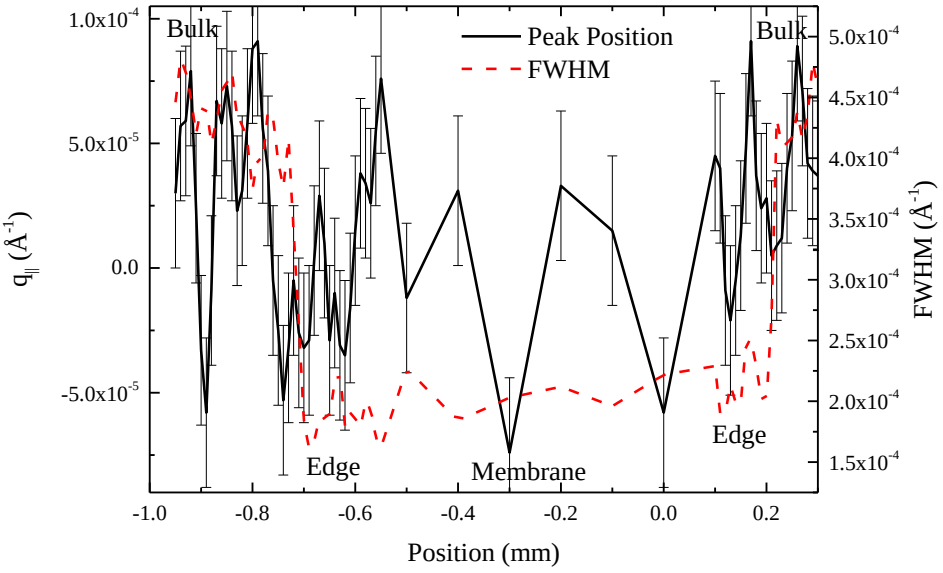

Figure 6-16 - Position (solid black line) and FWHM (dotted red line) of the (004) Ge Bragg peak as a function of position for $q_{\parallel}$

In figure 6-17, the (004) Ge Bragg peak position in $q_{\perp}$ and peak FWHM are given as a function of position across the thick ~700 nm membrane. As with the peak position in $q_{\parallel}$, variation in $q_{\perp}$ is due to reaching the resolution limit of the technique and within the error of the technique, $q_{\perp}$ can also be considered to remain constant over

the membrane and bulk material. This indicates that the tensile strain and relaxation is the same for the membrane and the as-grown Ge.

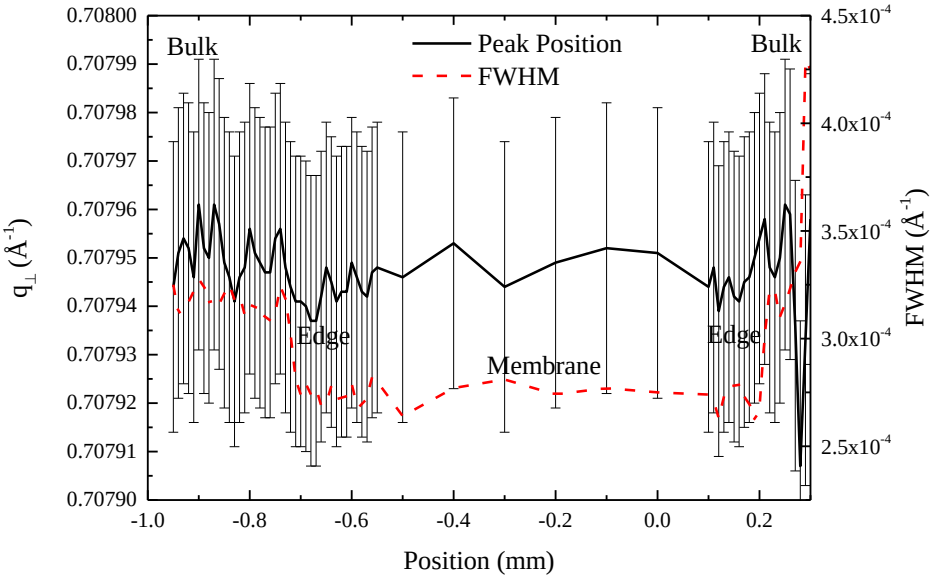

Figure 6-17 - Position (solid black line) and FWHM (dotted red line) of the (004) Ge Bragg peak as a function of position for $q_{\perp}$

In figure 6-18 a), the FWHM of the (004) Ge Bragg peak as a function of *x* and *y* sample stage position is given. The dotted black line is guide to the position of the membrane and the black dots are the position of the individual RSMs. The FWHM of the (004) Bragg peakis significantly reduced when compared to the bulk material. The reduction in FWHM can be seen to be uniform over the membrane. Sharp increases for the FWHM are see in the alignment trenches.

In figure 6-18 b) Strain calculated from the (004) Bragg peak position as a function of x and y sample stage position is given. The position of the alignment trenches is also marked. The strain can be seen to be uniform over both the

membrane, its edges and the bulk material, with the only change seen in the alignment trenches.

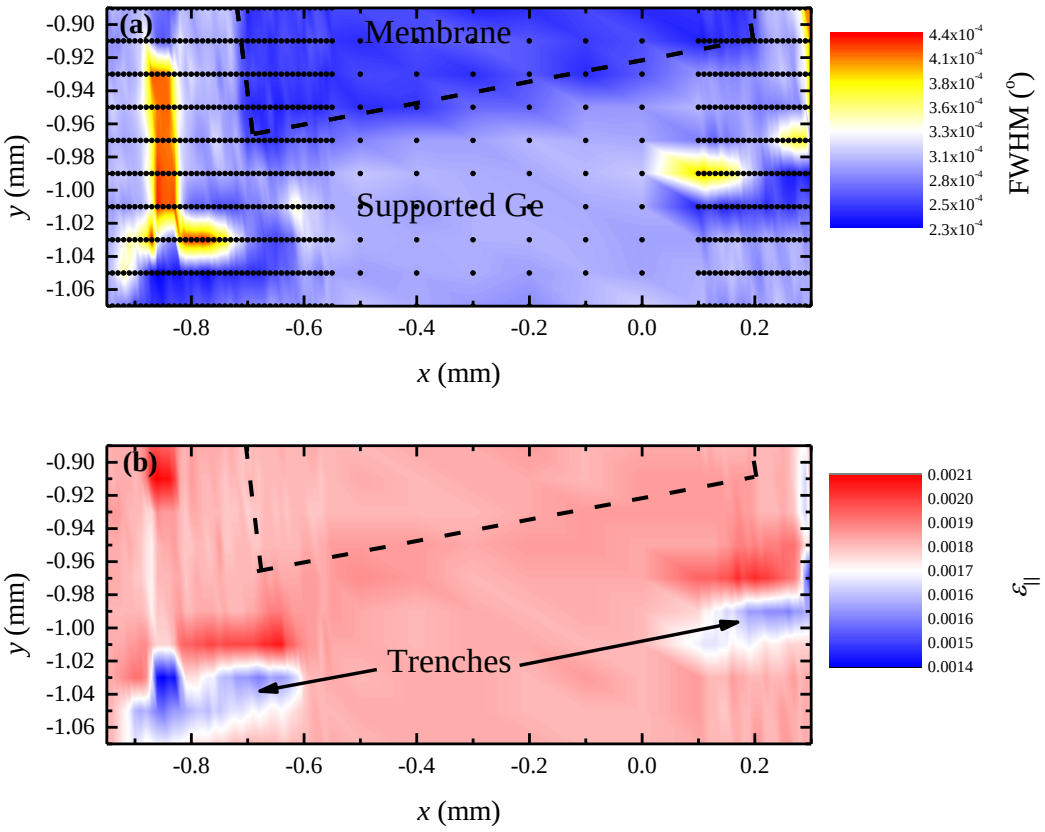

Figure 6-18 – a) FWHM of the (004) Ge Bragg peak as a function of position for $q_{//}$. The black dots indicate positions of individual RSMs b) The in-plane strain ($\varepsilon_{\parallel}$) strain calculated from (004) bragg peak position

As for the previous thinner membrane, microfocus XRD is highly suitable for determining material properties with good spatial resolution. It is also demonstrated how, with sufficient beam time, *x*-*y* maps of material properties can be measured for large (~mm^2) areas of suspended structures.

Since, within the error of the technique, the membranes have both minimal strain fluctuation and lattice plane tilt they are highly suitable as a platform for devices and

further epitaxial growth. This is an improvement over the thinner membrane which has a small but measureable variation in strain variation and some tilt at its edges. Like the thinner membrane, a reduction in the FWHM is seen in the suspended region which is indicative of an improvement in crystal quality. This can be attributed to removing the misfit dislocation network at the Ge/Si interface during the membrane fabrication, as previously discussed.

The thickness of the membrane could not be accurately determined by the method used for the previous thinner membrane due to a lack of thickness fringes being present in any of the RSMs on the membrane. This is due to the membrane being too thick to produce observable thickness fringes and not attributed to crystal quality.

6.8 Summary

The fabrication and characterisation of single crystal Ge membranes with two different thicknesses (~700 nm and 112 ± 5 nm) is presented. Micro-diffraction, performed at Beamline B16 at the DIAMOND Light Source is used to study the crystal properties of the membranes with a real space resolution of the microfocus spot size (~4 μm). For the thinner 112 ± 5 nm membrane, RSMs were taken as a line across the central portion of the membranes and, for the thicker ~700 nm membrane, multiple lines of RSMs were measured, from which *x*-*y* maps were constructed for the crystal properties of the membrane's.

Micro-diffraction revealed the membranes to have a higher crystalline quality than the surrounding supported Ge. This was also confirmed by AFM and plan view TEM. While a small symmetric strain variation across the membranes was found for the thinner membrane, it is insignificant in the context of using the membranes as a platform for further growth.

The membranes have potential as growth platforms for Si-based QCL structures since they can easily be converted into double-metal terahertz waveguides by backside metallisation due to the removal of the Si substrate. A membrane could either be fabricated from an entire QCL structure or there is the possibility that the QCL structure could be grown on a Ge membrane after it is released from the substrate. While the second method is preferable because it offers a platform for growth with improved crystal quality, it will be the most challenging; if the membrane is to be returned to the CVD growth chamber for regrowth, care must be taken during the membranes fabrication not to introduce contaminates; the membrane will need cleaning to remove any native oxide removed prior to regrowth, while for a standard Si substrate a bake in the growth chamber is used to remove native oxide, this cannot for used for membranes since they will be damaged by the high temperature; supporting a thick QCL structure may stress the thin membrane causing it to bow or break.

7 Conclusions and further work

In this chapter, the study is concluded and possibilities for further work are discussed for each of the main areas of study presented in this thesis, the growth of thin, strained SiGe layers, the growth of Si-based QCL superlattice structures and the fabrication of suspended Ge structures.

7.1 Conclusions

It is possible that the largest challenge facing the development of a Si-based QCL is that of the demand placed on epitaxial growth [59]. It is hoped that this study is a significant step in meeting this challenge, with the highlight being the growth and characterisation of challenging n-type $Ge/Si_{0.15}Ge_{0.85}$ QCL structures by RP-CVD. Comprehensive materials characterisation was performed on the superlattices, including HR-XRD reciprocal space mapping, X-ray ω-2θ scans, AFM, APT, SIMS, cross-sectional TEM and HAADF-STEM. The structures and the material characterisation have been given to collaborators who will perform additional characterisation and fabricate devices, the results of which will be used to further refine the growth process with the aim of producing a working Si-based QCL. $Ge/Si_{0.15}Ge_{0.85}$ superlattice structures also have uses in devices such as thermoelectrics, [152-153,177-178], and other optoelectronic devices like quantum confined stark effect modulator, [156-157] so this study also has applications outside of the QCL project.

It was found that Ge segregation and, possibly, Si-Ge interdiffusion are the limiting factors in the quality of the structures grown, causing smearing at the interfaces between layers and non-linear growth rates in thinner layers. This is a useful finding for the growth of future structures, since steps can be taken to reduce the Ge segregation, giving structures with improved quality.

It is highly likely that a working Si-based QCL: will eventually be fabricated and the author believes it will be in the n-type $Ge/Si_{0.15}Ge_{0.85}$ system explored in this work. This speculation comes from the simulation of n-type $Ge/Si_{0.15}Ge_{0.85}$ QCLs showing the structures to have gain close to that produced by simulated III-V QCL devices [10] and from the major hurdle of challenging heteroepitaxy being met to an extent by this work.

The QCL structures were grown at a low temperature of 450 ^{o}C to minimise Ge surface segregation, give sharp interfaces and reduce dopant diffusion. Growth at low temperature by RP-CVD has been shown to extend the critical thickness of SiGe layers on Si due to the suppression of relaxation processes. $Si_{0.4}Ge_{0.6}/Si$ layers grown past the critical thickness predicted by the People and Bean model are presented and the high crystal quality of the layers is confirmed by multiple techniques. The high strain, high Ge composition and good crystal quality makes the layers ideal for use in devices such as FETs.

In addition to the work on n-type $Ge/Si_{0.15}Ge_{0.85}$ QCLs, results are also presented in this study for the characterisation of high quality Ge membranes. Membranes of both 112 ± 5 nm and ~700 nm thickness were fabricated and comprehensively

characterised. Micro-diffraction, performed at Beamline B16 at the DIAMOND Light Source is used to characterise the membranes, giving the strain, membrane thickness, crystalline tilt and crystalline quality as a function of position over the membranes. The membranes show an increase in crystal quality over the surrounding material. The high quality of the membranes gives them many possible applications.

7.2 Further work

7.2.1 Critical thickness

As was demonstrated in Chapter 4, that RP-CVD growth at low temperature (450˚C) can yeild $Si_{1-x}Ge_x$/Si layers beyond their predicted critical thickness with no strain relaxation occurring. Since in Chapter 4 this was demonstrated for layers with a composition of $Si_{0.4}Ge_{0.6,}$ a higher Ge composition than for similar studies previously reported in the literature, the logical progression for this work is to repeat the study for SiGe layers with an even higher Ge composition. Since it is the low growth temperature which is held responsible for the extended critical thickness, a study could also be performed by measuring the critical thickness of SiGe layers grown in the limits of low temperature as a function of temperature.

The fully strained $Si_{0.4}Ge_{0.6}$ layers presented in Chapter 4 can be described as metastable. For metastable layers, the onset of strain relaxation is retarded by the energy in the layer being below the barrier of dislocation nucleation and the slow motion of misfit dislocations [187]. If the $Si_{0.4}Ge_{0.6}$ layers are annealed beyond a certain temperature, strain relaxation will begin. Ascertaining the thermal budget that the layers can withstand would be very useful to ascertain the maximum temperature

the layers can withstand during devices processing. An annealing study could be carried out on the layers using an X-ray diffractometer with a heated stage and performing ω-2θ scans while annealing the layers

7.2.2 Growth of SiGe/Ge Superlattices for Terahertz Emission

At the time of writing, the samples grown in this section have been delivered to collaborators for further characterisation (in the case of the FTIR structures) and fabrication into devices (in the case of the CSL QCL structures). The results from this will then be used to look at how the growth can be modified to improve the device performance.

The surface segregation of Ge was the biggest contributor to both the variation in layer thickness and interface quality and the structural quality could be greatly improved by reducing it. This could be achieved by growing at a lower temperature, which is challenging due to the reduced growth rate at lower temperature. It could also be reduced by exploring other precursor gases for the structure growth. In [106], it was found that the level of Ge segregation does not depend on the carrier gas (H_2,N_2) nor growth temperature for the 350–500 °C range, and it is solely the Si precursor that determines the amount of Ge segregation.

A different QCL design could also improve the chances of lasing. The structures grown in this work feature seven QWs per period, but as is shown in figure 7-1, eight period designs offer a greater tolerance to variation in growth thickness. For seven well designs a maximum variation of 5% in layer thickness is permissible, but this increases to 10% for an eight well design.

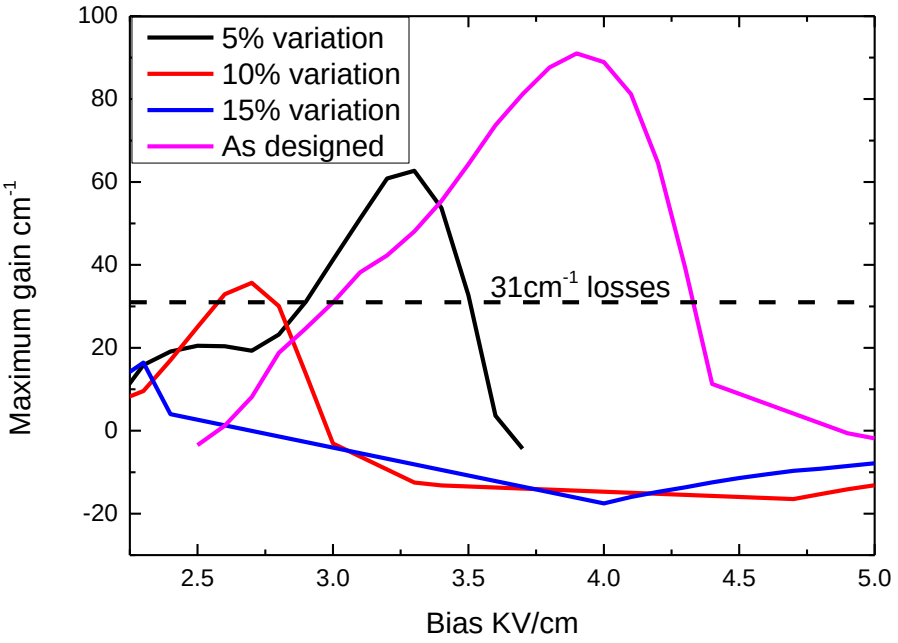

Figure 7-1-Peak gain of 8 QWs per period CSL QCL design versus bias and growth thickness variation. Adapted from [104]

7.2.3 Ge Membranes

The next step with the Ge membranes in the context of the QCL project is to fabricate a suspended superlattice structure. With the etching away of the virtual substrate and metal deposition on top and bottom on the structure, a double metal waveguide can then be formed. Microbeam XRD can be used to look at the strain in the structure after it is suspended, as was demonstrated in chapter 6.

To improve the quality of the virtual substrate underlying the superlattices, regrowth on the membrane could also be investigated. Since the suspension increases the crystal quality of the Ge it is likely this will improve the quality of the virtual substrate.

8 Overall Summary

Progress has been made towards a Si-based terahertz QCL. Complex n-type QCL structures for terahertz emission have been grown and in-depth materials characterisation presented. The structures and materials characterisation results have been delivered to collaborators. Following fabrication and testing of devices by collaborators, it is hoped that the growth can be adjusted to produce lasing from a Si-based terahertz QCL structure. Alongside the QCL structure development, work on a method to produce Ge membranes and map their material properties using microbeam XRD has been shown. The membranes have many applications, including as the foundation of a Si-based QCL waveguide. Finally, growth of thin, strained, high quality SiGe on Si that would be suitable for device applications is presented.

9 References

[1] M. Tonouchi, "Cutting-edge terahertz technology," *Nat Photon*, vol. 1, no. 2, pp. 97–105, Feb. 2007.

[2] K. Humphreys, J. P. Loughran, M. Gradziel, W. Lanigan, T. Ward, J. A. Murphy, and C. O'Sullivan, "Medical applications of terahertz imaging: a review of current technology and potential applications in biomedical engineering," in *The 26th Annual International Conference of the IEEE Engineering in Medicine and Biology Society*, San Francisco, CA, USA, pp. 1302–1305.

[3] C. Longbottom, D. A. Crawley, B. E. Cole, D. D. Arnone, V. P. Wallace, and M. Pepper, "Potential uses of terahertz pulse imaging in dentistry: caries and erosion detection," 2002, vol. 4610, pp. 109–112.

[4] C. Yu, S. Fan, Y. Sun, and E. Pickwell-MacPherson, "The potential of terahertz imaging for cancer diagnosis: A review of investigations to date," *Quant. Imaging Med. Surg.*, vol. 2, no. 1, p. 33, 2012.

[5] V. P. Wallace, A. J. Fitzgerald, E. Pickwell, R. J. Pye, P. F. Taday, N. Flanagan, and T. Ha, "Terahertz pulsed spectroscopy of human basal cell carcinoma," *Appl. Spectrosc.*, vol. 60, no. 10, pp. 1127–1133, 2006.

[6] R. M. Woodward, V. P. Wallace, R. J. Pye, B. E. Cole, D. D. Arnone, E. H. Linfield, and M. Pepper, "Terahertz pulse imaging of ex vivo basal cell carcinoma," *J. Invest. Dermatol.*, vol. 120, no. 1, pp. 72–78, 2003.

[7] J. F. Federici, B. Schulkin, F. Huang, D. Gary, R. Barat, F. Oliveira, and D. Zimdars, "THz imaging and sensing for security applications—explosives, weapons and drugs," *Semicond. Sci. Technol.*, vol. 20, no. 7, pp. S266–S280, Jul. 2005.

[8] A. G. Davies, A. D. Burnett, W. Fan, E. H. Linfield, and J. E. Cunningham, "Terahertz spectroscopy of explosives and drugs," *Mater. Today*, vol. 11, no. 3, pp. 18–26, 2008.

[9] J. Y. U., "Conceptual Design of a Table-top Terahertz Free-electron Laser," *J. Korean Phys. Soc.*, vol. 59, no. 51, p. 3251, Nov. 2011.

[10] D. J. Paul, "The progress towards terahertz quantum cascade lasers on silicon substrates," *Laser Photonics Rev.*, vol. 4, no. 5, pp. 610–632, Sep. 2010.

[11] P. H. Siegel, "Terahertz technology," *Microw. Theory Tech. IEEE Trans. On*, vol. 50, no. 3, pp. 910–928, 2002.

[12] B. S. Williams, "Terahertz quantum-cascade lasers," *Nat. Photonics*, vol. 1, no. 9, pp. 517–525, 2007.

[13] G. Scalari, C. Walther, M. Fischer, R. Terazzi, H. Beere, D. Ritchie, and J. Faist, "THz and sub-THz quantum cascade lasers," *Laser Photonics Rev.*, vol. 3, no. 1–2, pp. 45–66, Feb. 2009.

[14] B. S. Williams, S. Kumar, Q. Hu, and J. L. Reno, "High-power terahertz quantum-cascade lasers," *Electron. Lett.*, vol. 42, no. 2, pp. 89–91, 2006.

[15] L. Ajili, G. Scalari, J. Faist, H. Beere, E. Linfield, D. Ritchie, and G. Davies, "High power quantum cascade lasers operating at $\lambda \simeq 87$ and 130 μm," *Appl. Phys. Lett.*, vol. 85, no. 18, p. 3986, 2004.

[16] G. I. Haddad, J. R. East, and H. Eisele, "Two-Terminal Active Devices for Terahertz Sources," *Int. J. High Speed Electron. Syst.*, vol. 13, no. 02, pp. 395–427, Jun. 2003.
[17] S. A. Lynch, S. S. Dhillon, R. Bates, D. J. Paul, D. D. Arnone, D. J. Robbins, Z. Ikonic, R. W. Kelsall, P. Harrison, and D. J. Norris, "Si-based electroluminescence at THz frequencies," *Mater. Sci. Eng. B*, vol. 89, no. 1, pp. 10–12, 2002.
[18] S. A. Lynch, R. Bates, D. J. Paul, D. J. Norris, A. G. Cullis, Z. Ikonic, R. W. Kelsall, P. Harrison, D. D. Arnone, and C. R. Pidgeon, "Intersubband electroluminescence from Si/SiGe cascade emitters at terahertz frequencies," *Appl. Phys. Lett.*, vol. 81, no. 9, p. 1543, 2002.
[19] R. Bates, S. A. Lynch, D. J. Paul, Z. Ikonic, R. W. Kelsall, P. Harrison, S. L. Liew, D. J. Norris, A. G. Cullis, W. R. Tribe, and D. D. Arnone, "Interwell intersubband electroluminescence from Si/SiGe quantum cascade emitters," *Appl. Phys. Lett.*, vol. 83, no. 20, p. 4092, 2003.
[20] "Coherent Inc. Coherent in the News." [Online]. Available: http://www.coherent.com/Literature/. [Accessed: 26-Jul-2014].
[21] "Backward Wave Oscillator (BWO), Terahertz (THz)." [Online]. Available: http://www.insight-product.com/submmbwo3.htm. [Accessed: 19-Nov-2013].
[22] I. S. Gregory, C. Baker, W. R. Tribe, M. J. Evans, H. E. Beere, E. H. Linfield, A. G. Davies, and M. Missous, "High resistivity annealed low-temperature GaAs with 100 fs lifetimes," *Appl. Phys. Lett.*, vol. 83, no. 20, p. 4199, 2003.
[23] B. Williams, S. Kumar, Q. Hu, and J. Reno, "Operation of terahertz quantum-cascade lasers at 164 K in pulsed mode and at 117 K in continuous-wave mode," *Opt. Express*, vol. 13, no. 9, pp. 3331–3339, 2005.
[24] B. N. Murdin, "Far-infrared free-electron lasers and their applications," *Contemp. Phys.*, vol. 50, no. 2, pp. 391–406, 2009.
[25] M. J. W. Rodwell, M. Le, and B. Brar, "Correction to 'InP Bipolar ICs: Scaling Roadmaps, Frequency Limits, Manufacturable Technologies' [Feb 08 271-286]," *Proc. IEEE*, vol. 96, no. 4, p. 748, 2008.
[26] E. R. Brown, J. R. Söderström, C. D. Parker, L. J. Mahoney, K. M. Molvar, and T. C. McGill, "Oscillations up to 712 GHz in InAs/AlSb resonant-tunneling diodes," *Appl. Phys. Lett.*, vol. 58, no. 20, p. 2291, 1991.
[27] H.-W. Hübers, S. G. Pavlov, and V. N. Shastin, "Terahertz lasers based on germanium and silicon," *Semicond. Sci. Technol.*, vol. 20, no. 7, pp. S211–S221, Jul. 2005.
[28] E. R. Mueller, "Optically-Pumped THz Laser Technology," *Coherent-DEOS Prod. Note*, pp. 1–10, 2001.
[29] Y.-S. Lee, *Principles of terahertz science and technology*, 1st ed. New York, NY: Springer, 2008.
[30] R. Kohler, A. Tredicucci, F. Beltram, H. E. Beere, E. H. Linfield, A. G. Davies, D. A. Ritchie, R. C. Iotti, and F. Rossi, "Terahertz semiconductor-heterostructure laser," *Nature*, vol. 417, no. 6885, pp. 156–159, May 2002.
[31] A. Valavanis, J. Zhu, J. Freeman, L. Li, L. Chen, A. G. Davies, E. H. Linfield, and P. Dean, "Terahertz quantum cascade lasers with >1 W output powers," *Electron. Lett.*, vol. 50, no. 4, pp. 309–311, Feb. 2014.
[32] C. J. Glassbrenner and G. A. Slack, "Thermal conductivity of silicon and germanium from 3 K to the melting point," *Phys. Rev.*, vol. 134, no. 4A, p. A1058, 1964.

[33] J. S. Blakemore, "Semiconducting and other major properties of gallium arsenide," *J. Appl. Phys.*, vol. 53, no. 10, p. R123, 1982.

[34] M. Virgilio, M. Ortolani, M. Teich, S. Winnerl, M. Helm, D. Sabbagh, G. Capellini, and M. De Seta, "Combined effect of electron and lattice temperatures on the long intersubband relaxation times of Ge/Si<i>x</i>Ge<math><msub><mrow></mrow><mrow><mn>1</mn><mo>−</mo><mi>x</mi></mrow></msub></math> quantum wells," *Phys. Rev. B*, vol. 89, no. 4, Jan. 2014.

[35] G. Sun, L. Friedman, and R. A. Soref, "Intersubband lasing lifetimes of SiGe/Si and GaAs/AlGaAs multiple quantum well structures," *Appl. Phys. Lett.*, vol. 66, no. 25, p. 3425, 1995.

[36] L. Ying, N. Horiuchi-Ikeda, and H. Hirayama, "Ag–Metal Bonding Conditions for Low-Loss Double-Metal Waveguide for Terahertz Quantum Cascade Laser," *Jpn. J. Appl. Phys.*, vol. 47, no. 10R, p. 7926, 2008.

[37] B. S. Williams, S. Kumar, H. Callebaut, Q. Hu, and J. L. Reno, "Terahertz quantum-cascade laser at $\lambda \approx 100$ μm using metal waveguide for mode confinement," *Appl. Phys. Lett.*, vol. 83, no. 11, p. 2124, 2003.

[38] Q. Wang and W. H. Ko, "Modeling of touch mode capacitive sensors and diaphragms," *Sens. Actuators Phys.*, vol. 75, no. 3, pp. 230–241, 1999.

[39] S. T. Cho, K. Najafi, and K. D. Wise, "Internal stress compensation and scaling in ultrasensitive silicon pressure sensors," *Electron Devices IEEE Trans. On*, vol. 39, no. 4, pp. 836–842, 1992.

[40] S. T. Cho, K. Najafi, C. L. Lowman, and K. D. Wise, "An ultrasensitive silicon pressure-based flowmeter," in *Electron Devices Meeting, 1989. IEDM'89. Technical Digest., International*, 1989, pp. 499–502.

[41] K. Suzuki, K. Najafi, and K. D. Wise, "A 1024-element high-performance silicon tactile imager," *Electron Devices IEEE Trans. On*, vol. 37, no. 8, pp. 1852–1860, 1990.

[42] A. P. Perez-Marín, A. F. Lopeandía, L. Abad, P. Ferrando-Villaba, G. Garcia, A. M. Lopez, F. X. Muñoz-Pascual, and J. Rodríguez-Viejo, "Micropower thermoelectric generator from thin Si membranes," *Nano Energy*, vol. 4, pp. 73–80, Mar. 2014.

[43] T. A. Kwa, P. J. French, R. F. Wolffenbuttel, P. M. Sarro, L. Hellemans, and J. Snauwaert, "Anisotropically etched silicon mirrors for optical sensor applications," *J. Electrochem. Soc.*, vol. 142, no. 4, pp. 1226–1233, 1995.

[44] S. . Utteridge, V. . Sashin, S. . Canney, M. . Ford, Z. Fang, D. . Oliver, M. Vos, and E. Weigold, "Preparation of a 10 nm thick single-crystal silicon membrane self-supporting over a diameter of 1 mm," *Appl. Surf. Sci.*, vol. 162–163, pp. 359–367, Aug. 2000.

[45] J. M. Hartmann, "Reduced pressure chemical vapor deposition of Ge thick layers on Si(001) for 1.3–1.55-μm photodetection," *J. Appl. Phys.*, vol. 95, no. 10, p. 5905, 2004.

[46] J. Liu, R. Camacho-Aguilera, J. T. Bessette, X. Sun, X. Wang, Y. Cai, L. C. Kimerling, and J. Michel, "Ge-on-Si optoelectronics," *Thin Solid Films*, vol. 520, no. 8, pp. 3354–3360, Feb. 2012.

[47] J. Liu, X. Sun, R. Camacho-Aguilera, L. C. Kimerling, and J. Michel, "Ge-on-Si laser operating at room temperature," *Opt. Lett.*, vol. 35, no. 5, p. 679, Feb. 2010.

[48] R. R. King, D. C. Law, K. M. Edmondson, C. M. Fetzer, G. S. Kinsey, H. Yoon, R. A. Sherif, and N. H. Karam, "40% efficient metamorphic GaInP / GaInAs / Ge multijunction solar cells," *Appl. Phys. Lett.*, vol. 90, no. 18, p. 183516, 2007.

[49] R. M. Sieg, J. A. Carlin, J. J. Boeckl, S. A. Ringel, M. T. Currie, S. M. Ting, T. A. Langdo, G. Taraschi, E. A. Fitzgerald, and B. M. Keyes, "High minority-carrier lifetimes in GaAs grown on low-defect-density Ge/GeSi/Si substrates," *Appl. Phys. Lett.*, vol. 73, no. 21, p. 3111, 1998.

[50] S. Kazarinov, "Possibility of amplification of electromagnetic waves in a semiconductor with a superlattice," *Sov. Phys. Semicond.*, vol. 5, p. 707.

[51] Valavanis, Alexander, "n-type silicon-germanium based terahertz quantum cascade lasers," University of Leeds, 2009.

[52] M. Helm, E. Colas, P. England, F. DeRosa, and S. J. Allen, "Observation of grating-induced intersubband emission from GaAs/AlGaAs superlattices," *Appl. Phys. Lett.*, vol. 53, no. 18, p. 1714, 1988.

[53] J. Faist, F. Capasso, D. L. Sivco, C. Sirtori, A. L. Hutchinson, and A. Y. Cho, "Quantum Cascade Laser," *Science*, vol. 264, no. 5158, pp. 553–556, Apr. 1994.

[54] G. Scamarcio, "High-Power Infrared (8-Micrometer Wavelength) Superlattice Lasers," *Science*, vol. 276, no. 5313, pp. 773–776, May 1997.

[55] J. Faist, D. Hofstetter, M. Beck, T. Aellen, M. Rochat, and S. Blaser, "Bound-to-continuum and two-phonon resonance, quantum-cascade lasers for high duty cycle, high-temperature operation," *Quantum Electron. IEEE J. Of*, vol. 38, no. 6, pp. 533–546, 2002.

[56] J. Faist, M. Beck, T. Aellen, and E. Gini, "Quantum-cascade lasers based on a bound-to-continuum transition," *Appl. Phys. Lett.*, vol. 78, no. 2, p. 147, 2001.

[57] P. Dean, M. Salih, S. P. Khanna, L. H. Li, N. K. Saat, A. Valavanis, A. Burnett, J. E. Cunningham, A. G. Davies, and E. H. Linfield, "Resonant-phonon depopulation terahertz quantum cascade lasers and their application in spectroscopic imaging," *Semicond. Sci. Technol.*, vol. 27, no. 9, p. 094004, Sep. 2012.

[58] D. J. Paul, "Si/SiGe heterostructures: from material and physics to devices and circuits," *Semicond. Sci. Technol.*, vol. 19, p. R75, 2004.

[59] R. W. Kelsall, V. T. Dinh, P. Ivanov, A. Valavanis, L. J. M. Lever, Z. Ikonic, P. Velha, D. Dumas, K. F. Gallacher, D. J. Paul, J. Halpin, M. Myrnov, and D. R. Leadley, "(Invited) Germanium/Silicon Heterostructures for Terahertz Emission," *ECS Trans.*, vol. 50, no. 9, pp. 763–771, Mar. 2013.

[60] T. V. Dinh, A. Valavanis, L. J. M. Lever, Z. Ikonić, and R. W. Kelsall, "Extended density-matrix model applied to silicon-based terahertz quantum cascade lasers," *Phys. Rev. B*, vol. 85, no. 23, Jun. 2012.

[61] G. Dehlinger, "Intersubband Electroluminescence from Silicon-Based Quantum Cascade Structures," *Science*, vol. 290, no. 5500, pp. 2277–2280, Dec. 2000.

[62] I. Bormann, K. Brunner, S. Hackenbuchner, G. Zandler, G. Abstreiter, S. Schmult, and W. Wegscheider, "Midinfrared intersubband

electroluminescence of Si/SiGe quantum cascade structures," *Appl. Phys. Lett.*, vol. 80, no. 13, p. 2260, 2002.

[63] L. Diehl, S. Menteşe, E. Müller, D. Grützmacher, H. Sigg, U. Gennser, I. Sagnes, Y. Campidelli, O. Kermarrec, D. Bensahel, and J. Faist, "Electroluminescence from strain-compensated $Si_{0.2}Ge_{0.8}$/Si quantum-cascade structures based on a bound-to-continuum transition," *Appl. Phys. Lett.*, vol. 81, no. 25, p. 4700, 2002.

[64] S. A. Lynch, S. S. Dhillon, R. Bates, D. J. Paul, D. D. Arnone, D. J. Robbins, Z. Ikonic, R. W. Kelsall, P. Harrison, and D. J. Norris, "Si-based electroluminescence at THz frequencies," *Mater. Sci. Eng. B*, vol. 89, no. 1, pp. 10–12, 2002.

[65] D. J. Paul, G. Matmon, L. Lever, Z. Ikonic, R. Kelsall, D. Chrastina, G. Isella, H. Von Känel, E. Müller, and A. Neels, "Si/SiGe Bound-to-Continuum Quantum Cascade Emitters," 2008, vol. 16, pp. 865–874.

[66] K. Driscoll and R. Paiella, "Design of n-type silicon-based quantum cascade lasers for terahertz light emission," *J. Appl. Phys.*, vol. 102, no. 9, p. 093103, 2007.

[67] K. Driscoll and R. Paiella, "Silicon-based injection lasers using electronic intersubband transitions in the L valleys," *Appl. Phys. Lett.*, vol. 89, no. 19, p. 191110, 2006.

[68] A. Valavanis, T. V. Dinh, L. J. M. Lever, Z. Ikonić, and R. W. Kelsall, "Material configurations for n-type silicon-based terahertz quantum cascade lasers," *Phys. Rev. B*, vol. 83, no. 19, p. 195321, 2011.

[69] D. De Salvador, M. Petrovich, M. Berti, F. Romanato, E. Napolitani, A. Drigo, J. Stangl, S. Zerlauth, M. Mühlberger, F. Schäffler, G. Bauer, and P. Kelires, "Lattice parameter of Si1-x-yGexCy alloys," *Phys. Rev. B*, vol. 61, no. 19, pp. 13005–13013, May 2000.

[70] H. Stöhr and W. Klemm, "Über Zweistoffsysteme mit Germanium. I. Germanium/Aluminium, Germanium/Zinn und Germanium/Silicium," *Z. Für Anorg. Allg. Chem.*, vol. 241, no. 4, pp. 305–323, 1939.

[71] C. D. Thurmond, "Equilibrium Thermochemistry of Solid and Liquid Alloys of Germanium and of Silicon. I. The Solubility of Ge and Si in Elements of Groups III, IV and V," *J. Phys. Chem.*, vol. 57, no. 8, pp. 827–830, 1953.

[72] F. X. Hassion, A. J. Goss, and F. A. Trumbore, "On the Germanium-Silicon phase diagram," *J. Phys. Chem.*, vol. 59, no. 10, pp. 1118–1119, 1955.

[73] N. Armour and S. Dost, "Seed Production and Melt Replenishment for the Czochralski Growth of Silicon Germanium," *Acta Phys. Pol. A*, vol. 124, no. 2, pp. 198–212, Aug. 2013.

[74] *Silicon-germanium (SiGe) nanostructures: production, properties and applications in electronics*. Cambridge, UK: Philadelphia, PA : Woodhead Publishing, 2011.

[75] M. E. Levinshteĭn, S. L. Rumyantsev, and M. Shur, Eds., *Properties of advanced semiconductor materials: GaN, AlN, InN, BN, SiC, SiGe*. New York: Wiley, 2001.

[76] W. Martienssen and H. Warlimont, Eds., *Springer handbook of condensed matter and materials data*. Heidelberg ; New York: Springer, 2005.

[77] J. Humlíček, A. Röseler, T. Zettler, M. G. Kekoua, and E. V. Khoutsishvili, "Infrared refractive index of germanium-silicon alloy crystals," *Appl. Opt.*, vol. 31, no. 1, pp. 90–94, 1992.

[78] J. M. Hartmann, V. Benevent, J. F. Damlencourt, and T. Billon, "A benchmarking of silane, disilane and dichlorosilane for the low temperature growth of group IV layers," *Thin Solid Films*, vol. 520, no. 8, pp. 3185–3189, Feb. 2012.
[79] T. R. Bramblett, Q. Lu, T. Karasawa, M.-A. Hasan, S. K. Jo, and J. E. Greene, "Si(001)2×1 gas-source molecular-beam epitaxy from Si2H6: Growth kinetics and boron doping," *J. Appl. Phys.*, vol. 76, no. 3, p. 1884, 1994.
[80] L. H. Hall, "The Thermal Decomposition of Germane," *J. Electrochem. Soc.*, vol. 119, no. 11, pp. 1593–1596, 1972.
[81] D. W. Greve, "Growth of epitaxial germanium-silicon heterostructures by chemical vapour deposition," *Mater. Sci. Eng. B*, vol. 18, no. 1, pp. 22–51, 1993.
[82] D. Hull and D. J. Bacon, *Introduction to dislocations*. Oxford: Butterworth-Heinemann, 2011.
[83] J. P. Hirth, *Theory of dislocations*, 2nd ed. Malabar, FL: Krieger Pub. Co, 1992.
[84] D. C. Houghton, D. D. Perovic, J.-M. Baribeau, and G. C. Weatherly, "Misfit strain relaxation in GexSi1−x/Si heterostructures: The structural stability of buried strained layers and strained-layer superlattices," *J. Appl. Phys.*, vol. 67, no. 4, p. 1850, 1990.
[85] W. A. Jesser and D. Kuhlmann-Wilsdorf, "On the Theory of Interfacial Energy and Elastic Strain of Epitaxial Overgrowths in Parallel Alignment on Single Crystal Substrates," *Phys. Status Solidi B*, vol. 19, no. 1, pp. 95–105, 1967.
[86] F. C. Frank and J. H. van der Merwe, "One-Dimensional Dislocations. I. Static Theory," *Proc. R. Soc. Math. Phys. Eng. Sci.*, vol. 198, no. 1053, pp. 205–216, Aug. 1949.
[87] J. W. Matthews and A. E. Blakeslee, "Defects in epitaxial multilayers*:: I. Misfit dislocations," *J. Cryst. Growth*, vol. 27, pp. 118–125, 1974.
[88] Y. B. Bolkhovityanov, O. P. Pchelyakov, and S. I. Chikichev, "Silicon – germanium epilayers: physical fundamentals of growing strained and fully relaxed heterostructures," *Phys.-Uspekhi*, vol. 44, no. 7, pp. 655–680, Jul. 2001.
[89] J. C. Bean, "GexSi1−x/Si strained-layer superlattice grown by molecular beam epitaxy," *J. Vac. Sci. Technol. Vac. Surf. Films*, vol. 2, no. 2, p. 436, 1984.
[90] F. R. N. Nabarro, *Theory of crystal dislocations*. Oxford: Clarendon P, 1967.
[91] J. M. Hartmann, A. Abbadie, and S. Favier, "Critical thickness for plastic relaxation of SiGe on Si(001) revisited," *J. Appl. Phys.*, vol. 110, no. 8, p. 083529, 2011.
[92] I. J. Fritz, "Role of experimental resolution in measurements of critical layer thickness for strained-layer epitaxy," *Appl. Phys. Lett.*, vol. 51, no. 14, p. 1080, 1987.
[93] C. Claeys, *Extended defects in Germanium : fundamental and technological aspects*, 1. Ed. Berlin: Springer, 2009.
[94] M. Mazzerla, E. Griinbaum2b, K. W. J. Barnhamc, J. Barnesc, and P. R. Griffinc, "ELSEVIER Materials Science and Engineering B42 (1996) 43-51," *Mater. Sci. Eng. Solid-State Mater. Adv. Technol.*, vol. 42, pp. 43–51, 1996.
[95] J. H. Li, Z. H. Mai, and S. F. Cui, "X-ray analysis of strain relaxation in strained-layer superlattices," *J. Appl. Phys.*, vol. 76, no. 2, p. 810, 1994.

[96] N. J. Ekins-Daukes, K. Kawaguchi, and J. Zhang, "Strain-Balanced Criteria for Multiple Quantum Well Structures and Its Signature in X-ray Rocking Curves †," *Cryst. Growth Des.*, vol. 2, no. 4, pp. 287–292, Jul. 2002.

[97] V. A. Shah, A. Dobbie, M. Myronov, D. J. F. Fulgoni, L. J. Nash, and D. R. Leadley, "Reverse graded relaxed buffers for high Ge content SiGe virtual substrates," *Appl. Phys. Lett.*, vol. 93, no. 19, p. 192103, 2008.

[98] X.-C. Liu, M. Myronov, A. Dobbie, R. J. H. Morris, and D. R. Leadley, "High-quality Ge/Si $_{0.4}$ Ge $_{0.6}$ multiple quantum wells for photonic applications: growth by reduced pressure chemical vapour deposition and structural characteristics," *J. Phys. Appl. Phys.*, vol. 44, no. 5, p. 055102, Feb. 2011.

[99] V. A. Shah, A. Dobbie, M. Myronov, and D. R. Leadley, "Reverse graded SiGe/Ge/Si buffers for high-composition virtual substrates," *J. Appl. Phys.*, vol. 107, no. 6, p. 064304, 2010.

[100] H. von Känel, M. Kummer, G. Isella, E. Müller, and T. Hackbarth, "Very high hole mobilities in modulation-doped Ge quantum wells grown by low-energy plasma enhanced chemical vapor deposition," *Appl. Phys. Lett.*, vol. 80, no. 16, p. 2922, 2002.

[101] L. Colace, G. Masini, F. Galluzzi, G. Assanto, G. Capellini, L. Di Gaspare, E. Palange, and F. Evangelisti, "Metal–semiconductor–metal near-infrared light detector based on epitaxial Ge/Si," *Appl. Phys. Lett.*, vol. 72, p. 3175, 1998.

[102] Y. H. Xie, G. H. Gilmer, C. Roland, P. J. Silverman, S. K. Buratto, J. Y. Cheng, E. A. Fitzgerald, A. R. Kortan, S. Schuppler, M. A. Marcus, and others, "Semiconductor surface roughness: Dependence on sign and magnitude of bulk strain," *Phys. Rev. Lett.*, vol. 73, no. 22, pp. 3006–3009, 1994.

[103] R. Kube, H. Bracht, J. L. Hansen, A. N. Larsen, E. E. Haller, S. Paul, and W. Lerch, "Composition dependence of Si and Ge diffusion in relaxed Si[sub 1−x]Ge[sub x] alloys," *J. Appl. Phys.*, vol. 107, no. 7, p. 073520, 2010.

[104] E. Hüger, U. Tietze, D. Lott, H. Bracht, D. Bougeard, E. E. Haller, and H. Schmidt, "Self-diffusion in germanium isotope multilayers at low temperatures," *Appl. Phys. Lett.*, vol. 93, no. 16, p. 162104, 2008.

[105] B. Vincent, R. Loo, W. Vandervorst, J. Delmotte, B. Douhard, V. K. Valev, M. Vanbel, T. Verbiest, J. Rip, B. Brijs, T. Conard, C. Claypool, S. Takeuchi, S. Zaima, J. Mitard, B. De Jaeger, J. Dekoster, and M. Caymax, "Si passivation for Ge pMOSFETs: Impact of Si cap growth conditions," *Solid-State Electron.*, vol. 60, no. 1, pp. 116–121, Jun. 2011.

[106] B. Vincent, W. Vandervorst, M. Caymax, and R. Loo, "Influence of Si precursor on Ge segregation during ultrathin Si reduced pressure chemical vapor deposition on Ge," *Appl. Phys. Lett.*, vol. 95, no. 26, p. 262112, 2009.

[107] J. Nyéki, C. Girardeaux, G. Erdélyi, A. Rolland, and J. Bernardini, "Equilibrium surface segregation enthalpy of Ge in concentrated amorphous SiGe alloys," *Appl. Surf. Sci.*, vol. 212–213, pp. 244–248, May 2003.

[108] D. A. Grützmacher, T. O. Sedgwick, A. Powell, M. Tejwani, S. S. Iyer, J. Cotte, and F. Cardone, "Ge segregation in SiGe/Si heterostructures and its dependence on deposition technique and growth atmosphere," *Appl. Phys. Lett.*, vol. 63, no. 18, p. 2531, 1993.

[109] Digital Instuments, "Veeco Training Manual." 2000.

[110] Q. Zhong, D. Inniss, K. Kjoller, and V. B. Elings, “Fractured polymer/silica fiber surface studied by tapping mode atomic force microscopy,” *Surf. Sci.*, vol. 290, no. 1–2, pp. L688–L692, Jun. 1993.
[111] R. J. H. Morris, M. G. Dowsett, R. Beanland, A. Dobbie, M. Myronov, and D. R. Leadley, “Overcoming Low Ge Ionization and Erosion Rate Variation for Quantitative Ultralow Energy Secondary Ion Mass Spectrometry Depth Profiles of $Si_{1-x}Ge_x$/Ge Quantum Well Structures,” *Anal. Chem.*, vol. 84, no. 5, pp. 2292–2298, Mar. 2012.
[112] E. W. Müller, “The Atom-Probe Field Ion Microscope,” *Rev. Sci. Instrum.*, vol. 39, no. 1, p. 83, 1968.
[113] A. Cerezo, P. H. Clifton, M. J. Galtrey, C. J. Humphreys, T. F. Kelly, D. J. Larson, S. Lozano-Perez, E. A. Marquis, R. A. Oliver, G. Sha, and others, “Atom probe tomography today,” *Mater. Today*, vol. 10, no. 12, pp. 36–42, 2007.
[114] M. K. Miller, K. F. Russell, K. Thompson, R. Alvis, and D. J. Larson, “Review of Atom Probe FIB-Based Specimen Preparation Methods,” *Microsc. Microanal.*, vol. 13, no. 06, pp. 428–436, Dec. 2007.
[115] D. Bowen, *High resolution X-ray diffractometry and topography*. Taylor & Francis, 1998.
[116] M. Birkholz, *Thin film analysis by X-ray scattering*. Weinheim ;[Chichester: Wiley-VCH ;;John Wiley distributor], 2006.
[117] D. Bowen, *X-ray metrology in semiconductor manufacturing*. Boca Raton: CRC/Taylor & Francis, 2006.
[118] Adam CAPEWELL, “Novel Grading of Silicon Germanium for High Quality Virtual Substrates.”
[119] Vishal Ajit Shah, “Reverse Graded High Content (x>0.75) Si1-xGex Virtual Substrates.”
[120] J. Stangl, C. Mocuta, A. Diaz, T. H. Metzger, and G. Bauer, “X-Ray Diffraction as a Local Probe Tool,” *ChemPhysChem*, vol. 10, no. 17, pp. 2923–2930, Dec. 2009.
[121] C. Mocuta, J. Stangl, K. Mundboth, T. Metzger, G. Bauer, I. Vartanyants, M. Schmidbauer, and T. Boeck, “Beyond the ensemble average: X-ray microdiffraction analysis of single SiGe islands,” *Phys. Rev. B*, vol. 77, no. 24, Jun. 2008.
[122] M. Hanke, M. Dubslaff, M. Schmidbauer, T. Boeck, S. Schöder, M. Burghammer, C. Riekel, J. Patommel, and C. G. Schroer, “Scanning x-ray diffraction with 200 nm spatial resolution,” *Appl. Phys. Lett.*, vol. 92, no. 19, p. 193109, 2008.
[123] D. Chrastina, G. M. Vanacore, M. Bollani, P. Boye, S. Schöder, M. Burghammer, R. Sordan, G. Isella, M. Zani, and A. Tagliaferri, “Patterning-induced strain relief in single lithographic SiGe nanostructures studied by nanobeam x-ray diffraction,” *Nanotechnology*, vol. 23, no. 15, p. 155702, Apr. 2012.
[124] C. E. Murray, A. Ying, S. M. Polvino, I. C. Noyan, M. Holt, and J. Maser, “Nanoscale silicon-on-insulator deformation induced by stressed liner structures,” *J. Appl. Phys.*, vol. 109, no. 8, p. 083543, 2011.
[125] N. Hrauda, J. Zhang, E. Wintersberger, T. Etzelstorfer, B. Mandl, J. Stangl, D. Carbone, V. Holý, V. Jovanović, C. Biasotto, L. K. Nanver, J. Moers, D. Grützmacher, and G. Bauer, “X-ray Nanodiffraction on a Single SiGe

Quantum Dot inside a Functioning Field-Effect Transistor," *Nano Lett.*, vol. 11, no. 7, pp. 2875–2880, Jul. 2011.

[126] T. Etzelstorfer, M. J. Süess, G. L. Schiefler, V. L. R. Jacques, D. Carbone, D. Chrastina, G. Isella, R. Spolenak, J. Stangl, H. Sigg, and A. Diaz, "Scanning X-ray strain microscopy of inhomogeneously strained Ge micro-bridges," *J. Synchrotron Radiat.*, vol. 21, no. 1, pp. 111–118, Jan. 2014.

[127] K. J. S. Sawhney, I. P. Dolbnya, M. K. Tiwari, L. Alianelli, S. M. Scott, G. M. Preece, U. K. Pedersen, R. D. Walton, R. Garrett, I. Gentle, K. Nugent, and S. Wilkins, "A Test Beamline on Diamond Light Source," 2010, pp. 387–390.

[128] "Diamond Light Source - Materials - Beamline Schematic." [Online]. Available: http://www.diamond.ac.uk/Beamlines/Materials/B16/schematic.html. [Accessed: 06-Feb-2015].

[129] A. Snigirev, V. Kohn, I. Snigireva, and B. Lengeler, "A compound refractive lens for focusing high-energy X-rays," *Nature*, vol. 384, no. 6604, pp. 49–51, Nov. 1996.

[130] S. D. Rhead, J. E. Halpin, V. A. Shah, M. Myronov, D. H. Patchett, P. S. Allred, V. Kachkanov, I. P. Dolbnya, J. S. Reparaz, N. R. Wilson, C. M. Sotomayor Torres, and D. R. Leadley, "Tensile strain mapping in flat germanium membranes," *Appl. Phys. Lett.*, vol. 104, no. 17, p. 172107, Apr. 2014.

[131] V. Kachkanov, I. Dolbnya, K. O'Donnell, K. Lorenz, S. Pereira, I. Watson, T. Sadler, H. Li, V. Zubialevich, and P. Parbrook, "Characterisation of III-nitride materials by synchrotron X-ray microdiffraction reciprocal space mapping," *Phys. Status Solidi C*, vol. 10, no. 3, pp. 481–485, Mar. 2013.

[132] Dectris, "Technical Specification and Operating Procedure - PILATUS 300K." .

[133] G. Bauer, J. Li, and E. Koppensteiner, "X-ray reciprocal space mapping of heterostructures," *J. Cryst. Growth*, vol. 157, no. 1–4, pp. 61–67, Dec. 1995.

[134] R. F. Egerton, *Physical principles of electron microscopy an introduction to TEM, SEM, and AEM*. New York: Springer Science+Business Media, 2005.

[135] D. B. Williams and C. B. Carter, *Transmission electron microscopy: a textbook for materials science*. New York; London: Springer, 2009.

[136] C. Hetherington, "Aberration correction for TEM," *Mater. Today*, vol. 7, no. 12, pp. 50–55, 2004.

[137] O. Scherzer, "The Theoretical Resolution Limit of the Electron Microscope," *J. Appl. Phys.*, vol. 20, no. 1, p. 20, 1949.

[138] S. J. Pennycook, "Z-contrast stem for materials science," *Ultramicroscopy*, vol. 30, no. 1–2, pp. 58–69, Jun. 1989.

[139] A. Du, L. Tang, Y. Wang, and C. Cheng, "The application of HAADF-STEM in SiGe materials," in *Physical and Failure Analysis of Integrated Circuits, 2005. IPFA 2005. Proceedings of the 12th International Symposium on the*, 2005, pp. 159–162.

[140] P. W. Hawkes, *Advances in imaging and electron physics. Volume 113 Volume 113*. San Diego; San Francisco: Academic Press, 2000.

[141] "High strain embedded-SiGe via low temperature reduced pressure chemical vapor deposition," *Thin Solid Films*, vol. 520, no. 8, pp. 3175–3178, Feb. 2012.

[142] S. Wirths, D. Buca, A. T. Tiedemann, P. Bernardy, B. Holländer, T. Stoica, G. Mussler, U. Breuer, and S. Mantl, "Low temperature RPCVD epitaxial growth of Si1−xGex using Si2H6 and Ge2H6," *Solid-State Electron.*, vol. 83, pp. 2–9, May 2013.

[143] T. Ghani, M. Armstrong, C. Auth, M. Bost, P. Charvat, G. Glass, T. Hoffmann, K. Johnson, C. Kenyon, J. Klaus, and others, "A 90nm high volume manufacturing logic technology featuring novel 45nm gate length strained silicon CMOS transistors," in *Electron Devices Meeting, 2003. IEDM'03 Technical Digest. IEEE International*, 2003, pp. 11–6.

[144] S.-J. Kim, J.-Y. Baek, T.-H. Shim, H.-J. Lee, J.-G. Park, K.-S. Kim, and W.-J. Cho, "Hole Mobility Enhancement in Strained SiGe Grown on Silicon-on-Insulator p-MOSFETs," *J. Korean Phys. Soc.*, vol. 53, no. 4, pp. 2171–2174, Oct. 2008.

[145] H. Chen, Y. Li, C. Peng, H. Liu, Y. Liu, Q. Huang, J. Zhou, and Q.-K. Xue, "Crosshatching on a SiGe film grown on a Si(001) substrate studied by Raman mapping and atomic force microscopy," *Phys. Rev. B*, vol. 65, no. 23, May 2002.

[146] P. D. Healey, K. Bao, M. Gokhale, J. E. Ayers, and F. C. Jain, "X-ray determination of the dislocation densities in semiconductor crystals using a Bartels five-crystal diffractometer," *Acta Crystallogr. Sect. A*, vol. 51, no. 4, pp. 498–503, 1995.

[147] T. Ulyanenkova, M. Myronov, A. Benediktovitch, A. Mikhalychev, J. Halpin, and A. Ulyanenkov, "Characterization of SiGe thin films using a laboratory X-ray instrument," *J. Appl. Crystallogr.*, vol. 46, no. 4, pp. 898–902, Jun. 2013.

[148] R. People and J. C. Bean, "Calculation of critical layer thickness versus lattice mismatch for Ge[sub x]Si[sub 1 - x]/Si strained-layer heterostructures," *Appl. Phys. Lett.*, vol. 47, no. 3, pp. 322–324, Aug. 1985.

[149] R. People and J. C. Bean, "Erratum: Calculation of critical layer thickness versus lattice mismatch for GexSi1−x/Si strained-layer heterostructures [Appl. Phys. Lett. 47, 322 (1985)]," *Appl. Phys. Lett.*, vol. 49, no. 4, p. 229, 1986.

[150] W. Yu, B. Zhang, Q. T. Zhao, D. Buca, J.-M. Hartmann, R. Luptak, G. Mussler, A. Fox, K. K. Bourdelle, X. Wang, and S. Mantl, "Hole Mobilities of Si/Si0.5Ge0.5 Quantum-Well Transistor on SOI and Strained SOI," *IEEE Electron Device Lett.*, vol. 33, no. 6, pp. 758–760, Jun. 2012.

[151] M. Takenaka and S. Takagi, "Strain Engineering of Plasma Dispersion Effect for SiGe Optical Modulators," *IEEE J. Quantum Electron.*, vol. 48, no. 1, pp. 8–16, Jan. 2012.

[152] S. Cecchi, T. Etzelstorfer, E. Müller, A. Samarelli, L. Ferre Llin, D. Chrastina, G. Isella, J. Stangl, J. M. R. Weaver, P. Dobson, and D. J. Paul, "Ge/SiGe Superlattices for Thermoelectric Devices Grown by Low-Energy Plasma-Enhanced Chemical Vapor Deposition," *J. Electron. Mater.*, vol. 42, no. 7, pp. 2030–2034, Jul. 2013.

[153] D. Chrastina, S. Cecchi, J. P. Hague, J. Frigerio, A. Samarelli, L. Ferre–Llin, D. J. Paul, E. Müller, T. Etzelstorfer, J. Stangl, and G. Isella, "Ge/SiGe superlattices for nanostructured thermoelectric modules," *Thin Solid Films*, vol. 543, pp. 153–156, Sep. 2013.

[154] A. Samarelli, L. F. Llin, Y. Zhang, J. M. R. Weaver, P. Dobson, S. Cecchi, D. Chrastina, G. Isella, T. Etzelstorfer, J. Stangl, E. M. Gubler, and D. J. Paul,

"Power Factor Characterization of Ge/SiGe Thermoelectric Superlattices at 300 K," *J. Electron. Mater.*, vol. 42, no. 7, pp. 1449–1453, Jul. 2013.

[155] Y.-H. Kuo, Y. K. Lee, Y. Ge, S. Ren, J. E. Roth, T. I. Kamins, D. A. B. Miller, and J. S. Harris, "Strong quantum-confined Stark effect in germanium quantum-well structures on silicon," *Nature*, vol. 437, no. 7063, pp. 1334–1336, Oct. 2005.

[156] Y.-H. Kuo, Y. K. Lee, Y. Ge, S. Ren, J. E. Roth, T. I. Kamins, D. A. B. Miller, and J. S. Harris, Jr., "Quantum-Confined Stark Effect in Ge/SiGe Quantum Wells on Si for Optical Modulators," *IEEE J. Sel. Top. Quantum Electron.*, vol. 12, no. 6, pp. 1503–1513, Nov. 2006.

[157] Yiwen Rong, Yangsi Ge, Yijie Huo, M. Fiorentino, M. Tan, T. Kamins, T. J. Ochalski, G. Huyet, and J. S. Harris, "Quantum-Confined Stark Effect in Ge/SiGe Quantum Wells on Si," *IEEE J. Sel. Top. Quantum Electron.*, vol. 16, no. 1, pp. 85–92, 2010.

[158] Y. Busby, M. De Seta, G. Capellini, F. Evangelisti, M. Ortolani, M. Virgilio, G. Grosso, G. Pizzi, P. Calvani, S. Lupi, M. Nardone, G. Nicotra, and C. Spinella, "Near- and far-infrared absorption and electronic structure of Ge-SiGe multiple quantum wells," *Phys. Rev. B*, vol. 82, no. 20, Nov. 2010.

[159] R. Dingle, H. L. Störmer, A. C. Gossard, and W. Wiegmann, "Electron mobilities in modulation-doped semiconductor heterojunction superlattices," *Appl. Phys. Lett.*, vol. 33, no. 7, p. 665, 1978.

[160] M. Meduňa, O. Caha, M. Keplinger, J. Stangl, G. Bauer, G. Mussler, and D. Grützmacher, "<title xmlns='http://www.crossref.org/xschema/1.1' xmlns:xsi='http://www.w3.org/2001/XMLSchema-instance'> Interdiffusion in Ge rich SiGe/Ge multilayers studied by *in situ* diffraction </title>," *Phys. Status Solidi A*, vol. 206, no. 8, pp. 1775–1779, Aug. 2009.

[161] N. Ozguven and P. C. McIntyre, "Silicon-germanium interdiffusion in high-germanium-content epitaxial heterostructures," *Appl. Phys. Lett.*, vol. 92, no. 18, p. 181907, 2008.

[162] A. W. Jackson, P. R. Pinsukanjana, A. C. Gossard, and L. A. Coldren, "In situ monitoring and control for MBE growth of optoelectronic devices," *Sel. Top. Quantum Electron. IEEE J. Of*, vol. 3, no. 3, pp. 836–844, 1997.

[163] A. Valavanis, L. Lever, C. Evans, Z. Ikonić, and R. Kelsall, "Theory and design of quantum cascade lasers in (111) n-type Si/SiGe," *Phys. Rev. B*, vol. 78, no. 3, Jul. 2008.

[164] P. Ivanov, A. Valavanis, Z. Ikonic, and R. W. Kelsall, "Simulated Effect of Epitaxial Growth Variations on THz Emission of SiGe/Ge Quantum Cascade Structures," *Proc SISPAD*, pp. 328 – 331, 2013.

[165] G. Isella, G. Matmon, A. Neels, E. Muller, M. Califano, D. Chrastina, H. von Kanel, L. Lever, Z. Ikonic, R. Kelsall, and others, "SiGe/Si quantum cascade structures deposited by low-energy plasma-enhanced CVD," in *Group IV Photonics, 2008 5th IEEE International Conference on*, 2008, pp. 29–31.

[166] A. Benedetti, D. J. Norris, C. J. D. Hetherington, A. G. Cullis, D. J. Robbins, and D. J. Wallis, "Strain and Ge concentration determinations in SiGe/Si multiple quantum wells by transmission electron microscopy methods," *J. Appl. Phys.*, vol. 93, no. 7, p. 3893, 2003.

[167] "Control of epilayer thickness during epitaxial growth of high Ge content strained Ge/SiGe multilayers by RP-CVD," *J. Cryst. Growth*, vol. 318, no. 1, pp. 337–340, Mar. 2011.

[168] R. Q.-M. Ng, E. S. Tok, and H. C. Kang, “Disilane chemisorption on Si[sub x]Ge[sub 1−x](100)-(2×1): Molecular mechanisms and implications for film growth rates,” *J. Chem. Phys.*, vol. 131, no. 4, p. 044707, 2009.

[169] E. S. Tok, N. J. Woods, and J. Zhang, “RHEED and SIMS studies of germanium segregation during growth of SiGe/Si heterostructures; a two-site exchange model with growth rate dependence,” *J. Cryst. Growth*, vol. 209, no. 2, pp. 321–326, 2000.

[170] M.-H. Xie, J. Zhang, A. Lees, J. M. Fernandez, and B. A. Joyce, “Surface segregation during molecular beam epitaxy: the site-blocking effects of surfactant atoms,” *Surf. Sci.*, vol. 367, no. 2, pp. 231–237, Nov. 1996.

[171] N. Ohtani, S. M. Mokler, M. H. Xie, J. Zhang, and B. A. Joyce, “RHEED investigation of Ge surface segregation during gas source MBE of heterostructures,” *Surf. Sci.*, vol. 284, no. 3, pp. 305–314, Mar. 1993.

[172] J. M. Hartmann, J. Eymery, and V. Calvo, “Large and small angle x-ray scattering studies of Si/SiGe superlattices grown by gas-source molecular beam epitaxy,” *Semicond. Sci. Technol.*, vol. 17, no. 3, p. 198, 2002.

[173] X. B. Li, J. H. Neave, D. J. Norris, A. G. Cullis, D. J. Paul, R. W. Kelsall, and J. Zhang, “Growth and structural characterisation of Si/SiGe heterostructures for optoelectronic applications,” *Opt. Mater.*, vol. 27, no. 5, pp. 855–858, Feb. 2005.

[174] M. Bollani, E. Müller, S. Signoretti, C. Beeli, G. Isella, M. Kummer, and H. von Känel, “Compressively strained Ge channels on relaxed SiGe buffer layers,” *Mater. Sci. Eng. B*, vol. 101, no. 1–3, pp. 102–105, Aug. 2003.

[175] M. Liehr, C. M. Greenlief, S. R. Kasi, and M. Offenberg, “Kinetics of silicon epitaxy using SiH4 in a rapid thermal chemical vapor deposition reactor,” *Appl. Phys. Lett.*, vol. 56, no. 7, p. 629, 1990.

[176] P. Chen, N. A. Katcho, J. P. Feser, W. Li, M. Glaser, O. G. Schmidt, D. G. Cahill, N. Mingo, and A. Rastelli, “Role of Surface-Segregation-Driven Intermixing on the Thermal Transport through Planar Si/Ge Superlattices,” *Phys. Rev. Lett.*, vol. 111, no. 11, Sep. 2013.

[177] A. Samarelli, L. Ferre Llin, S. Cecchi, J. Frigerio, T. Etzelstorfer, E. Müller, Y. Zhang, J. R. Watling, D. Chrastina, G. Isella, J. Stangl, J. P. Hague, J. M. R. Weaver, P. Dobson, and D. J. Paul, “The thermoelectric properties of Ge/SiGe modulation doped superlattices,” *J. Appl. Phys.*, vol. 113, no. 23, p. 233704, 2013.

[178] D. Chrastina, S. Cecchi, J. P. Hague, J. Frigerio, A. Samarelli, L. Ferre–Llin, D. J. Paul, E. Müller, T. Etzelstorfer, J. Stangl, and G. Isella, “Ge/SiGe superlattices for nanostructured thermoelectric modules,” *Thin Solid Films*, vol. 543, pp. 153–156, Sep. 2013.

[179] A. Valavanis, Z. Ikonić, and R. W. Kelsall, “Growth variation effects in SiGe-based quantum cascade lasers,” *J. Opt. Pure Appl. Opt.*, vol. 11, p. 054012, 2009.

[180] E. H. Li, B. L. Weiss, and Kwok-Sum Chan, “Eigenstates and absorption spectra of interdiffused AlGaAs-GaAs multiple-quantum-well structures,” *IEEE J. Quantum Electron.*, vol. 32, no. 8, pp. 1399–1416, Aug. 1996.

[181] P. Ivanov, A. Valavanis, Z. Ikonic, and R. W. Kelsall, “Simulated Effect of Epitaxial Growth Variations on the Gain of SiGe/Ge Quantum Cascade Lasers,” presented at the European Laser Workshop 2013.

[182] V. A. Shah, S. D. Rhead, J. E. Halpin, O. Trushkevych, E. Chávez-Ángel, A. Shchepetov, V. Kachkanov, N. R. Wilson, M. Myronov, J. S. Reparaz, R. S. Edwards, M. R. Wagner, F. Alzina, I. P. Dolbnya, D. H. Patchett, P. S. Allred, M. J. Prest, P. M. Gammon, M. Prunnila, T. E. Whall, E. H. C. Parker, C. M. Sotomayor Torres, and D. R. Leadley, "High quality single crystal Ge nano-membranes for opto-electronic integrated circuitry," *J. Appl. Phys.*, vol. 115, no. 14, p. 144307, Apr. 2014.

[183] S. K. Sahari, H. Murakami, T. Fujioka, T. Bando, A. Ohta, K. Makihara, S. Higashi, and S. Miyazaki, "Native Oxidation Growth on Ge(111) and (100) Surfaces," *Jpn. J. Appl. Phys.*, vol. 50, no. 4, p. 04DA12, Apr. 2011.

[184] O. Tabata, R. Asahi, H. Funabashi, K. Shimaoka, and S. Sugiyama, "Anisotropic etching of silicon in TMAH solutions," *Sens. Actuators Phys.*, vol. 34, no. 1, pp. 51–57, 1992.

[185] D. Nam, D. Sukhdeo, A. Roy, K. Balram, S.-L. Cheng, K. C.-Y. Huang, Z. Yuan, M. Brongersma, Y. Nishi, and D. Miller, "Strained germanium thin film membrane on silicon substrate for optoelectronics," *Opt. Express*, vol. 19, no. 27, pp. 25866–25872, 2011.

[186] L. Colace, G. Masini, and G. Assanto, "Ge-on-Si approaches to the detection of near-infrared light," *IEEE J. Quantum Electron.*, vol. 35, no. 12, pp. 1843–1852, Dec. 1999.

[187] "Strain relaxation of metastable SiGe/Si: Investigation with two complementary X-ray techniques," *J. Appl. Phys.*, vol. 111, no. 6, p. 063507, 2012.

[188] S. Takagi, "A Dynamical Theory of Diffraction for a Distorted Crystal," *J. Phys. Soc. Jpn.*, vol. 26, no. 5, pp. 1239–1253, May 1969.

[189] S. Takagi, "Dynamical theory of diffraction applicable to crystals with any kind of small distortion," *Acta Crystallogr.*, vol. 15, no. 12, pp. 1311–1312, Dec. 1962.

[190] Taupin, D, "THEORIE DYNAMIQUE DE LA DIFFRACTION DES RAYONS X PAR LES CRISTAUX DEFORMES," Bull. Soc. Fran. Miner. Cryst, vol. 87, no. 4, p. 469, 1964.

[191] J. G. Klappe and P. F. Fewster, "Fitting of rocking curves from ion-implanted semiconductors," *J. Appl. Crystallogr.*, vol. 27, no. 1, pp. 103–110, 1994.

[192] C. Kittel, *Introduction to solid state physics*, 8th ed. Hoboken, NJ: Wiley, 2005.